2020

Diffusion and reshaping of metallic nanoclusters and nanocrystals

King Chun Lai
Iowa State University

Diffusion and reshaping of metallic nanoclusters and nanocrystals

by

King Chun Lai

A dissertation submitted to the graduate faculty

in partial fulfillment of the requirements for the degree of

DOCTOR OF PHILOSOPHY

Major: Condensed Matter Physics

Program of Study Committee:
James W. Evans, Major Professor
Beate Schmittmann
Patricia A. Thiel
Alejandro Travesset-Casas
Xuefeng Wang

The student author, whose presentation of the scholarship herein was approved by the program of study committee, is solely responsible for the content of this dissertation. The Graduate College will ensure this dissertation is globally accessible and will not permit alterations after a degree is conferred.

Iowa State University

Ames, Iowa

2020

DEDICATION

I would like to dedicate this thesis to everyone came across my academic works and education, especially Prof. James Evans, Prof. Patricia Thiel for their guidance. I would also like to thank my friends and family for their support during the writing of this work.

TABLE OF CONTENTS

Page

LIST OF TABLES

LIST OF FIGURES

ACKNOWLEDGMENTS

I would like to take this opportunity to express my thanks to those who helped me with various aspects of conducting research and the writing of this thesis. First and foremost, Prof. James W. Evans for his guidance, patience and support throughout this research and the writing of this thesis. His insights have often inspired me. I would also thank Prof. Patricia A. Thiel for her help in my research and career. Furthermore, I would thank Dr. Da-Jiang Liu, Dr. Yong Han for their collaborations during my degree. I would also like to thank my committee members: Dean. Beate Schmittmann, Prof. Patricia A. Thiel, Prof. Alejandro Travesset-Casas, Dr. Xuefeng Wang for their efforts and contributions to this work. Last but not least, I would also like to thank Milan Kornjaca, Bing Li, Ana-Marija Nedic, Yihua Qiang, Dr. Victor Quito, Jyotisman Sahoo, Dr. Yuriy Sizyuk, Dr. Thais Trevisan for their companies. This work was supported by NSF grant CHE-1507223. This work was supported by the U.S. Department of Energy (DOE), Office of Science, Basic Energy Sciences, Division of Chemical Sciences, Geosciences, and Biosciences through the Ames Laboratory Chemical Physics program at the Ames Laboratory under contract number DE-AC02-07CH11358. Ames Laboratory is operated for the DOE by Iowa State University. The document number assigned to this thesis/dissertation is IS-T 3274.

ABSTRACT

Synthesis and applications of metallic nanocrystals (NCs) has been a focus of the science and engineering communities for the last twenty years. This is due to the potential impact in a wide area in applications (e.g. plasmonics, catalysis, drug delivery) and the high flexibility in design of NC shape and structure. Advances in nanoscience rely on fundamental understanding of physical properties of nanoparticles and nanostructures. Our focus is on the post-synthesis dynamics or evolution of NCs which is mediated by diffusion of atoms around their periphery. Long-range diffusion and coalescence of NCs synthesized by deposition on crystalline surfaces is observed experimentally. The process is referred as Smoluchowski Ripening (SR). Although a coarse-grained mean-field theory of the long-range diffusion provides a macroscopic understanding, features deriving from the discreteness of small size islands ($O(10)-O(10^2)$ atoms) are not captured. We performed kinetic Monte Carlo (kMC) simulations of a suitably crafted stochastic atomistic model for epitaxial 2D metal (M) NCs at various temperatures on a M(100) substrate and discovered a complex oscillatory decrease with size in diffusivity. Behavior was explained by analysis of energetic and entropic factors (the latter involving combinatorial analysis of NC configurations). For diffusion of epitaxial 3D NCs of relevance to catalysts degradation, we developed an atomistic model incorporating the first realistic description of periphery (surface) diffusion kinetics. Similar oscillatory nature in diffusivity was observed in simulation of {100}-epitaxially supported 3D NCs, and explained identifying the diffusion pathway and characterizing its energetics. The same atomistic model was applied to study: reshaping of individual NCs synthesized with non-equilibrium cubic, octahedral, etc. forms; sintering of pairs of NCs; and pinch-off of elongated nanorods. The time scale of sintering for two $\sim$ 4 nm gold nanocrystals observed in experiment is recovered in our simulation model.

CHAPTER 1. INTRODUCTION

The impact of nanoscience and nanotechnology on human society and thus on our daily lives is beyond doubt. The functionality of nanomaterials for applications often comes from the ability to synthesize artificial far-from-equilibrium structures on the nanoscale. In working or operating environments, those structures may not be static or frozen, but instead dynamic and suffer morphological changes back towards their equilibrium forms. As a consequence, functionality can decay with time. Although the time evolution of nanostructured surfaces and nanoclusters (NCs), also described as nanocrystals or nanoparticles, is of central importance in determining their shape and structural stability which impacts their utility for applications, the understanding of these phenomena is yet far from complete. Thus, our focus in this thesis is on exploration of morphological time evolution of metallic nanoclusters by crafting realistic atomistic-level stochastic models behavior of which is determined Kinetic Monte Carlo (KMC) simulations and further elucidated with appropriate analytical theory. This modeling incorporates the feature that for these systems, evolution is mediated by periphery diffusion of atoms around the nanoclusters, i.e., edge diffusion for two-dimensional (2D) epitaxial nanoclusters, and surface diffusion for three-dimensional (3D) nanoclusters. Publications on this and related topics from the Ph.D. research are listed as Ref [1–11], and submitted papers are listed as Ref. [12–14]. Each main chapter (2–6) of this thesis corresponds to a published journal article [2–6] with myself as the first author. Work excerpted from multiple other papers appears in the Appendix.

There are two basic aspects of NC evolution. The first is shape or structural evolution of individual NCs, or the coalescence or sintering of NC pairs. The second is the evolution,

and specifically the coarsening of NC arrays, which results in a decrease in the number and corresponding increase in mean size of the NCs. There are two basic pathways for coarsening: Ostwald Ripening (OR) wherein smaller NCs dissolve and transfer their atoms to larger NCs, and Smoluchowski ripening (SR) which involves NC migration and coalescence. PhD research included the first analysis characterizing OR kinetics on Au(111) surfaces published in *J. Phys. Chem. C* [7], but this was not a major focus of activities. Rather, a major focus was on aspects of Smoluchowski ripening (SR) process, and specifically the NC migration component of this process, for both single-atomic-layer 2D [2,3,11] and multilayer 3D [1, 6] epitaxial NCs. This is a key process causing degradation of 3D supported metal NC catalysts.

Figure 1.1: (a) The journal cover of article [3]. (b) The supplementary journal cover of article [1].

First, we describe our studies related to 2D epitaxial metallic NCs on low-index surfaces of the same metal (so-called homoepitaxial systems). This work was based on a stochastic atomistic-level model which was crafted to effectively capture the details of edge diffusion of atoms around the periphery of the NC (e.g., distinguishing the rate for diffusion along straight close-packed steps from that to round corners or kinks on the step edge). For the migration part of SR, the long range diffusion phenomena has been observed through scanning tunneling microscopy (STM) experiments since mid-1990's [15–19] on various sur-

faces, prompting numerous theoretical studies [20–26]. Intuitively, a nanoparticle with a larger size diffuses slower than a smaller one. Classical main-field theory [27] predicts a monotonic dependence of the diffusion coefficient $D_N \sim N^{-\beta}$ on the size N of nanoparticle, with $\beta = 3/2$ for a 2D nanoparticle on a supported facet. In Chapter 2 corresponds to an article published in *Physical Review B* [2] analyzing the diffusion behavior of 2D homoepitaxial adatom nanoislands on a metal (100) surfaces. Against expectations, we discovered complex oscillatory decay of diffusion coefficients with the size of 2D nanoislands, unanticipated in multiple previous studies. In addition to precise simulation analysis, we utilized a combinatorial analysis exploiting concepts from number theory to characterize entropic aspects of these systems and thus provide deeper understanding of observed behavior. In Chapter 3 (an article selected as a journal cover for *Journal of Physical Chemistry C* [3] which shown as Fig. 1a) we further extended our study on 2D vaccancy nanopits, to which relatively little attention has been paid. Furthermore, our simulation results are compared with experiments [16,28] for Ag(100) achieving good agreement with what we regard as the most reliable results and trends, and providing a determination of key energetic parameters for this system.

Another aspect of the evolution of 2D epitaxial NCs is their reshaping. We mentioned above coalescence or sintering as a component of the SR process. There had been extensive previous studies of this process, so it was not incorporated as part of the Ph.D. research. However, another aspect of reshaping arises since formation of 2D epitaxial NCs by deposition on surface often results in far-from-equilibrium growth shapes. These will evolve post-deposition to equilibrium shapes which are determined by a 2D version of the so-called Wulff construction (which is discussed further below in the context of 3D NCs). This evolution process had not been modeled previously for homoepitaxial deposition on metal(111) surface where triangular and even fractal far-from-equilibrium growth shapes are observed. Modeling was performed for the evolution of triangular to hexagonal equilibrium shapes and reported as part of a major review on reshaping of NCs in *Chemical Reviews* [1].

Second, we describe our studies related to 3D NCs also commonly referred to as 3D nanocrystals. As noted above, these can be synthesized with remarkable control of possibly non-equilibrium "artificial shape and structure [29,30], which enables fine tuning of functionality. However, such non-equilibrium structures tend to convert to a more energetically favorable shapes. On the nanometer scale, it is anticipated as noted above that the dominant mass transport mechanism facilitating reshaping and sintering is surface diffusion (or periphery diffusion) [31, 32]. These reshaping processes bring up a natural question: what is the equilibrium shape or energetically preferred shape of a NC under different constraints? Traditionally, the equilibrium shape of a NC is constructed through Wulff (3D) construction [33] in a continuous framework (versus a discrete atomistic frmwork). In the case of a NC supported on a substrate, a modified Wulff construction known as a Kaischew [34] (or Winterbottom) construction applies. We will present multiple applications of these approaches in the Appendix excerpted from three published papers [1,9,10]. However, these approaches are only valid in continuum (large size) regime. In a discrete nanoscale regime, the sizes corresponding most closely to these continuum Wulff shapes are often regarded as "magic sizes". Between two magic sizes, a more careful analysis of stability of nanoparticles for fcc metal NCs is given in Chapter 4 (corresponding to an article published in *Journal of Physical Chemistry C* [4]). We have identified a 49 sizes, with a total of 70 distinct closed-shell configurations between each consecutive pair of two magic sizes. Energetic and geometric features of these NCs are analyzed. Though it is not the focus of this thesis, this work also discusses the implications of our findings for "crystal fractionalization". In this process, self-assembly starting with polydisperse NCs results in a spontaneous separation into two distinct crystalline NC superlattice phases (whereas starting with NCs of a single size results in formation of a single crystalline superlattice NC phase).

Regarding the reshaping process, the path from a far-from-equilibrium metallic NC to stable equilibrium structures (like those described in Chapter 4) is modeled in Chapter 5 (corresponding to an article published in *Physical Review Materials* [5]). Again, for metal

NCs, reshaping is generally mediated by surface diffusion. There were in existence previous studies of reshaping for metallic NC using stochastic atomistic models to access time scale of seconds to tens of minutes which are often relevant for experiments. However, these used generic so-called bond-counting type formalisms to describe diffusion barriers controlling diffusion rates in the numerous local environments which can occur on NC surfaces. However, this formalism fails dramatically to accurately describe this diversity of barriers, e.g., for diffusion of atoms across various low-index facets, diffusion of atoms along step edges, and diffusion of atoms between layers and facets. Thus our work developed a stochastic model incorporating the first realistic prescription of the kinetics of surface diffusion in these numerous local environments (contrasting previous generic prescriptions). Our model was applied to analyze three different classes of reshaping processes. Reshaping of a far-from-equilibrium shapes to equilibrium Wulff shapes is studied extensively for nanocubes (which have been synthesized for many metals), but also for other simple geometric shapes which have been synthesized. In addition, we analyzed the merging of two NCs in contact (sintering), for which success was validated by recovering the time scale of Au NCs sintering observed in recent high-resolution TEM experiments [35]. This work also explored the pinch-off of elongated nanorods or nanowires, which fragmented into pieces instead of reshaping to a single compact NC with truncated octahedral equilibrium shape. In addition to the *Physical Review Material* article [5], additional analysis of reshaping was incorporated as part of the major *Chemical Reviews* article [1], for which a schematic summary of our work was selected as a supplementary Journal Cover. See Fig. 1b

In Chapter 6 (corresponding to an article published in *Nanoscale* [6]), we applied our realistic stochastic model used in the reshaping studies of Chapter 5 to analyze diffusion of epitaxially 3D supported NCs. Our model parameters are chosen to correspond to Ag. Similar systems of 3D Ag NCs has been studied on graphite [36] and other oxides surfaces [37] including MgO, Al_2O_3 and TiO_2. Specifically, our model is applicable to Ag/MgO(001), a system exhibiting cube-on-cube{100} expitaxy [38]. Given the importance of the diffusion

of supported 3D metallic NCs in the context of catalyst degradation, the size dependence of diffusivity had been considered in previous classic studies, and incorporated into modeling of the kinetics of degradation via SR. However, such work assumed a simple monotonic decay of diffusivity with size. In contrast, our simulations revealed a complex oscillatory decay with size reminiscent of, but fundamentally different in detail from that for 2D clusters described in Chapter 2 and Chapter 3. To elucidate behavior, we identified optimal diffusion pathways, which involved dissolving and reforming outer layers of facets. Then, analytic assessment of the variation of energy along such minimum energy pathways was provided, both at atomistic and coarse-grained continuum levels. This allowed determination of effective barriers for diffusion for different NC sizes which matched well our precise simulation results for diffusivity.

Finally, Chapter 7 provides overall conclusion based upon the results achieved from the multiple studies of NC evolution in this thesis.

Bibliography

[1] King C. Lai, Yong Han, Peter Spurgeon, Wenyu Huang, Patricia A. Thiel, Da-Jiang Liu, and James W. Evans. Reshaping, Intermixing, and Coarsening for Metallic Nanocrystals: Nonequilibrium Statistical Mechanical and Coarse-Grained Modeling. *Chem. Rev.*, 119(11):6670–6768, 2019.

[2] King C. Lai, Da-Jiang Liu, and James W. Evans. Diffusion of two-dimensional epitaxial clusters on metal (100) surfaces: Facile versus nucleation-mediated behavior and their merging for larger sizes. *Phys. Rev. B*, 96(23):235406, 2017.

[3] King C. Lai, Da-Jiang Liu, Patricia A. Thiel, and James W. Evans. Modeling of Diffusivity for 2D Vacancy Nanopits and Comparison with 2D Adatom Nanoislands on Metal(100) Surfaces Including Analysis for Ag(100). *J. Phys. Chem. C*, 122(21):11334–11344, 2018.

[4] King C. Lai, Xun Zha, James W. Evans, and Alex Travesset. Structure of Polydisperse fcc Nanocrystals: Implications for Crystal Fractionalization. *J. Phys. Chem. C*, 123(14):9528–9537, 2019.

[5] King C. Lai and James W. Evans. Reshaping and sintering of 3D fcc metal nanoclusters: Stochastic atomistic modeling with realistic surface diffusion kinetics. *Phys. Rev. Mater.*, 3(2):026001, 2019.

[6] King C. Lai and James W. Evans. Complex oscillatory decrease with size in diffusivity of {100}-epitaxially supported 3D fcc metal nanoclusters. *Nanoscale*, 11(37):17506–17516, 2019.

[7] Peter M. Spurgeon, King C. Lai, Yong Han, James W. Evans, and Patricia A. Thiel. Fundamentals of Au(111) Surface Dynamics: Coarsening of Two-Dimensional Au Islands. *J. Phys. Chem. C*, 124(13):7492–7499, 2020.

[8] Linxia Wang, King C. Lai, Li Huang, James W. Evans, and Yong Han. Low-index surface energies, cleavage energies, and surface relaxations for crystalline NiAl from first-principles calculations. *Surf. Sci.*, page 121532, 2019.

[9] Yong Han, King C. Lai, Ann Lii-Rosales, Michael C. Tringides, James W. Evans, and Patricia A. Thiel. Surface energies, adhesion energies, and exfoliation energies relevant to copper-graphene and copper-graphite systems. *Surf. Sci.*, 685:48–58, 2019.

[10] Ann Lii-Rosales, Yong Han, King C. Lai, Dapeng Jing, Michael C. Tringides, James W. Evans, and Patricia A. Thiel. Fabricating Fe nanocrystals via encapsulation at the graphite surface. *Journal of Vacuum Science & Technology A: Vacuum, Surfaces, and Films*, 37(6):061403, 2019.

[11] King C. Lai, James W. Evans, and Da-Jiang Liu. Communication: Diverse nanoscale cluster dynamics: Diffusion of 2D epitaxial clusters. *J. Chem. Phys.*, 147(20):201101, 2017.

[12] Dapeng Jing, Ann Lii-Rosales, King C. Lai, Qiang Li, Jaeyoun Kim, Michael Tringides, James W. Evans, and Patricia A. Thiel. Non-equilibrium growth of metal clusters on a layered material: Cu on MoS_2. *New J. Phys.*, 2020. Accepted.

[13] King C. Lai, Tyler Pleasant, Andrs Garca, and James W. Evans. Generalized hydrodynamic analysis of transport through a finite open nanopore for two-component single-file systems. *Phys. Rev. E*, 2020. (under review).

[14] J. Sebastin Manzano, Hsin Wang, Takeshi Kobayashi, Pranjali Naik, King C. Lai, James W. Evans, and Igor I. Slowing. Kinetics of the Functionalization of Mesoporous Silica Nanoparticles with Organotrialkoxysilanes. *J. Phys. Chem. C*, 2020. (under review).

[15] J.-M. Wen, S.-L. Chang, J. W. Burnett, J. W. Evans, and P. A. Thiel. Diffusion of Large Two-Dimensional Ag Clusters on Ag(100). *Phys. Rev. Lett.*, 73(19):2591–2594, 1994.

[16] Woei Wu Pai, Anna K. Swan, Zhenyu Zhang, and J. F. Wendelken. Island Diffusion and Coarsening on Metal (100) Surfaces. *Phys. Rev. Lett.*, 79(17):3210–3213, 1997.

[17] Xin Ge and Karina Morgenstern. Ehrlich-Schwoebel barrier and interface-limited decay in island kinetics on Ag(100). *Phys. Rev. B*, 85(4):045417, 2012.

[18] J. F. Wendelken, Anna K. Swan, Woei-Wu Pai, and J.-K. Zuo. Morphology and Energy Barriers in Homoepitaxial Growth and Coarsening: A Case Study for Cu(100) | Morphological Organization in Epitaxial Growth and Removal. *WORLD SCIENTIFIC*, 14:320–348, 1999.

[19] Patricia A. Thiel, Mingmin Shen, Da-Jiang Liu, and J. W. Evans. Coarsening of Two-Dimensional Nanoclusters on Metal Surfaces. *J. Phys. Chem. C*, 113(13):5047–5067, 2009.

[20] David S. Sholl and Rex. T. Skodje. Diffusion of Clusters of Atoms and Vacancies on Surfaces and the Dynamics of Diffusion-Driven Coarsening. *Phys. Rev. Lett.*, 75(17):3158–3161, 1995.

[21] Clinton DeW. Van Siclen. Single Jump Mechanisms for Large Cluster Diffusion on Metal Surfaces. *Phys. Rev. Lett.*, 75(8):1574–1577, 1995.

[22] Alexander Bogicevic, Shudun Liu, Joachim Jacobsen, Bengt Lundqvist, and Horia Metiu. Island migration caused by the motion of the atoms at the border: Size and temperature dependence of the diffusion coefficient. *Phys. Rev. B*, 57(16):R9459(R)–R9462, 1998.

[23] J. Heinonen, I. Koponen, J. Merikoski, and T. Ala-Nissila. Island Diffusion on Metal fcc (100) Surfaces. *Phys. Rev. Lett.*, 82(13):2733–2736, 1999.

[24] Greg Mills, Thomas R. Mattsson, Lone Møllnitz, and Horia Metiu. Simulations of mobility and evaporation rate of adsorbate islands on solid surfaces. *J. Chem. Phys.*, 111(18):8639–8650, 1999.

[25] Arthur F. Voter. Classically exact overlayer dynamics: Diffusion of rhodium clusters on Rh(100). *Phys. Rev. B*, 34(10):6819–6829, 1986.

[26] H. C. Kang, P. A. Thiel, and J. W. Evans. Cluster diffusivity: Structure, correlation, and scaling. *J. Chem. Phys.*, 93(12):9018–9025, 1990.

[27] K. Binder and M. H. Kalos. "Critical clusters" in a supersaturated vapor: Theory and Monte Carlo simulation. *J. Stat. Phys.*, 22(3):363–396, 1980.

[28] Xin Ge and Karina Morgenstern. Ehrlich-Schwoebel barrier and interface-limited decay in island kinetics on Ag(100). *Phys. Rev. B*, 85(4):045417, 2012.

[29] Younan Xia, Yujie Xiong, Byungkwon Lim, and Sara E. Skrabalak. Shape-Controlled Synthesis of Metal Nanocrystals: Simple Chemistry Meets Complex Physics? *Angew. Chem. Int. Ed.*, 48(1):60–103, 2009.

[30] L. D. Marks and L. Peng. Nanoparticle shape, thermodynamics and kinetics. *J. Phys.: Condens. Matter*, 28(5):053001, 2016.

[31] W. W. Mullins. Theory of Thermal Grooving. *J. Appl. Phys.*, 28(3):333–339, 1957.

[32] Jens Eggers. Coalescence of Spheres by Surface Diffusion. *Phys. Rev. Lett.*, 80(12):2634–2637, 1998.

[33] Claude R. Henry. Morphology of supported nanoparticles. *Prog. Surf. Sci.*, 80(3):92–116, 2005.

[34] R. Kaischew. Uber eine Verallgemeinerung des Wulffschen Satzes und uber die Kristallbildung auf fremden Oberflachen. *Arbeitstagung Festkrperphysik.*, 73(19):81, 1952.

[35] Jong Min Yuk, Myoungho Jeong, Sang Yun Kim, Hyeon Kook Seo, Jihyun Kim, and Jeong Yong Lee. In situ atomic imaging of coalescence of Au nanoparticles on graphene: rotation and grain boundary migration. *Chem. Commun.*, 49(98):11479–11481, 2013.

[36] I. M. Goldby, L. Kuipers, B. von Issendorff, and R. E. Palmer. Diffusion and aggregation of size-selected silver clusters on a graphite surface. *Appl. Phys. Lett.*, 69(19):2819–2821, 1996.

[37] Mingshu Chen and D. Wayne Goodman. Chapter 5 Oxide-supported metal clusters. *Chemical Physics of Solid Surfaces*, 12:201–269, 2007.

[38] Riccardo Ferrando, Giulia Rossi, Andrea C. Levi, Zdenka Kuntová, Florin Nita, Andrei Jelea, Christine Mottet, Giovanni Barcaro, Alessandro Fortunelli, and Jacek Goniakowski. Structures of metal nanoparticles adsorbed on MgO(001). I. Ag and Au. *J. Chem. Phys.*, 130(17):174702, 2009.

CHAPTER 2. DIFFUSION OF TWO-DIMENSIONAL EPITAXIAL CLUSTERS ON METAL (100) SURFACES: FACILE VERSUS NUCLEATION-MEDIATED BEHAVIOR AND THEIR MERGING FOR LARGER SIZES

A paper published in *Physical Review B*

King Chun Lai[1,2], Da-Jiang Liu[2], James W. Evans[1,2,3]

[1]*Department of Physics and Astronomy, Iowa State University, Ames, Iowa 50011, USA*

[2]*Ames Laboratory-USDOE, Iowa State University, Ames, Iowa 50011, USA*

[3]*Department of Mathematics, Iowa State University, Ames, Iowa 50011, USA*

(Received 19 June 2017; published 5 December 2017)

Abstract

For diffusion of two-dimensional homoepitaxial clusters of N atoms on metal (100) surfaces mediated by edge atom hopping, macroscale continuum theory suggests that the diffusion coefficient scales like $D_N \sim N^{-\beta}$ with $\beta = 3/2$. However, we find quite different and diverse behavior in multiple size regimes. These include: (i) facile diffusion for small sizes $N < 9$; (ii) slow nucleation-mediated diffusion with small $\beta < 1$ for "perfect" sizes $N = N_p = L^2$ or $L(L+1)$, for $L = 3, 4, ...$ having unique ground-state shapes, for moderate sizes $9 \leq N \leq O(10^2)$; the same also applies for $N = N_p + 3, N_p + 4, ...$ (iii) facile diffusion but with large $\beta > 2$ for $N = N_p+1$ and N_p+2 also for moderate sizes $9 \leq N \leq O(10^2)$; (iv) merging of the above distinct branches and subsequent anomalous scaling with $1 \leq \beta < 3/2$,

reflecting the quasifacetted structure of clusters, for larger $N = O(10^2)$ to $N = O(10^3)$; (v) classic scaling with $\beta = 3/2$ for very large $N = O(10^3)$ and above. The specified size ranges apply for typical model parameters. We focus on the moderate size regime where we show that diffusivity cycles quasiperiodically from the slowest branch for $N_p + 3$ (not N_p) to the fastest branch for $N_p + 1$. Behavior is quantified by kinetic Monte Carlo simulation of an appropriate stochastic lattice-gas model. However, precise analysis must account for a strong enhancement of diffusivity for short time increments due to back correlation in the cluster motion. Further understanding of this enhancement, of anomalous size scaling behavior, and of the merging of various branches, is facilitated by combinatorial analysis of the number of the ground-state and low-lying excited state cluster configurations, and also of kink populations.

DOI: 10.1103/PhysRevB.96.235406

2.1 Introduction

Significant long-range diffusion of large two-dimensional (2D) homoepitaxial adatom clusters on single-crystal metal (100) surfaces with sizes on the order of hundreds or even thousands of atoms was studied by scanning tunneling microscopy (STM) as early as the mid-1990's [1, 2] and also more recently [3]. It is generally accepted that cluster diffusion is mediated by periphery diffusion (PD), also described as edge diffusion, of adatoms along the steps at the periphery of the cluster. The STM studies prompted extensive atomistic lattice-gas modeling starting in the 1990's of epitaxial cluster diffusion [4–11] and of related reshaping phenomena [12–19]. This work supplemented limited earlier studies [20–22]. Mesoscale continuum Langevin theory for PD-mediated cluster diffusion has also been applied, and predicts that the diffusion coefficient for clusters of N atom satisfies $D_N \sim \sigma_{\rm PD} N^{-\beta}$ with $\beta = 3/2$,where $\sigma_{\rm PD}$ denotes the mesoscale mobility for atoms at step edges [23, 24]. Simple mean-field type atomistic-level theory for compact clusters also predicts the same size dependence as the continuum theory [25, 26]. However, significantly, the

experimentally observed size scaling exponent β for moderate cluster sizes, $N = O(10^2)$ to $O(10^3)$, is below the prediction of the continuum and mean-field theories [2, 3].

Diffusion of smaller 2D clusters with less than $\sim$ 10 atoms on metal (100) surfaces was also observed but instead by field ion microscopy [27–29], and has been interpreted with appropriate theoretical analyses [30–33]. However, diffusion of small sized clusters exhibits a distinctive irregular size dependence and Arrhenius energetics, which is readily understood, e.g., given the innate stability of 2×2 atom square clusters relative to two-atom dimers and three-atom trimers. We also mention that there have been multiple studies of 2D cluster diffusion for metal (111) and metal (110) homoepitaxial systems, and also for heteroepitaxial metal systems [34–37]. Theoretical studies, particularly for metal (111) systems, have explored concerted many-atom and off-lattice nonepitaxial mechanisms [38–41]. These latter systems are of less relevance for the current study, so we do not discuss them further.

For 2D cluster diffusion on metal (100) surfaces, there is naturally interest in the effective or overall activation barrier $E_{\rm eff}$ for the process where $D_N \sim \exp\left[-E_{\rm eff}/(k_B T)\right]$.Here, k_B denotes the Boltzmann constant, and T denotes the surface temperature. $E_{\rm eff}$ is related to the kinetic parameters in atomistic-level models including the barrier $E_{\rm e}$ to diffuse along close-packed (110) cluster step edges, and any additional barrier δ to round corners or kinks. $E_{\rm eff}$ also reflects thermodynamic parameters determined by adatom interactions, particularly the formation energy $E_{\rm form}$ to create a step edge atom from a kink atom. It was previously suggested that long-range cluster diffusion is limited by creation of edge atoms through their extraction from the core of the cluster or core breakup [1, 20], so that $E_{\rm eff} = E_{\rm e} + \delta + E_{\rm form}$ [19]. This perspective is consistent with the predictions of the mesoscale continuum Langevin theory where the activation energy for cluster diffusion corresponds to that for mobility of edge atoms $E_{\rm PD}$, where $\sigma_{\rm PD} \sim \exp\left[-E_{\rm PD}/(k_B T)\right]$ with $E_{\rm PD} = E_{\rm e} + \delta + E_{\rm form}$ [23, 24]. The latter result for $E_{\rm PD}$ has been rigorously demonstrated in the absence of a corner or kink rounding barrier [42], but it is expected to apply more

generally [43].

However, Mills *et al.* [10] noted that if cluster edges are effectively facetted, then cluster diffusion can be limited by nucleation of new edge layers on these facetted step edges. This picture leads to higher values of E_{eff} than predicted above (see Sec. 2.3), and also to a weaker dependence of D_N on N reminiscent of experimental observations. This facetted regime occurs for linear cluster sizes, $L \sim N^{1/2}$ (in units of surface lattice constant, $a = 1$), which are below the characteristic separation, $L_k \approx 1/2 \exp[\epsilon_k/(k_B T)]$, of kinks on close-packed $\langle 110 \rangle$ edges [44]. Here, ϵ_k denotes the kink creation energy. Another perspective on anomalous size scaling for diffusivity was provided by Pierre-Louis [45] ho modified the continuum Langevin theory by introducing an additional diffusion field for edge atoms. This approach also recovered weaker size scaling.

Jensen *et al.* [15] adopted an analogous nucleation-mediated picture to describe the effective barrier and anomalous size scaling for the relaxation to equilibrium of convex nonequilibrium cluster shapes. Regarding the relationship between this shape relaxation process and the long-range diffusion of clusters, it should be noted that both require nucleation of new edge layers. Furthermore, a simple relationship was proposed between the size scaling exponents for cluster diffusion and relaxation of convex shapes [46]. It was later shown that further refinement to anomalous scaling could be induced in the presence of an additional kink or corner rounding barrier [14, 17].

However, we show in this contribution that the above observations, while providing key insight into deviations from standard macroscale and mean-field theories, fall far short of providing a complete characterization of the full diversity of cluster diffusion behavior on the nanoscale. A comprehensive and precise characterization of the dependence of the cluster diffusion coefficient D_N on size N can be provided by analysis utilizing kinetic Monte Carlo (KMC) simulation of a stochastic atomistic-level lattice-gas model for cluster diffusion which incorporates an appropriate description of PD kinetics. Indeed, this approach is a key component of the current study, and reveals various size regimes with distinct behavior:

(i) facile diffusion for small sizes $N < 9$; (ii) slow nucleation-mediated diffusion with weak size scaling $\beta < 1$ for perfect "perfect" sizes $N = N_p = L^2$ or $L(L+1)$ with $L = 3, 4, ...$ having unique square or near-square ground-state shapes, and also for sizes $N_p+3, N_p+4, ...$, versus facile diffusion with strong size scaling $\beta > 2$ for sizes N_p+1 and N_p+2 for moderate sizes $9 \leq N \leq O(10^2)$; (iii) merging of these distinct branches and subsequent anomalous scaling with $1 \lesssim \beta < 3/2$, the latter reflecting the quasifacetted structure of clusters for larger $N = O(10^2)$ to $N = O(10^3)$; and (iv) classic scaling with $\beta = 3/2$ consistent with macroscopic or mean-field theories for very large $N = O(10^3)$ and above. We mainly focus elucidation of behavior in regime (ii), and to some extent regime (iii). To this end, in addition to KMC analysis, we also develop and utilize results from combinatorial analysis of cluster configurations to provide deeper insight.

In Sec. 2.2, we describe our stochastic lattice-gas model for PD-mediated cluster diffusion, and also various strategies for model analysis. In Sec. 2.3, we discuss different possible types or branches of cluster diffusion, and Sec. 2.4 present KMC results providing an overview of the variation of D_N versus N. A brief report of such behavior was recently provided for just one choice of adatom interactions and no kink rounding barrier, $\delta = 0$ [47]. Here, we consider different interactions, and finite $\delta > 0$ as well as $\delta = 0$. We also present a comprehensive analysis and interpretation of diverse aspects of this behavior, as detailed in the following sections. In Sec. 2.5, we describe the variation of the effective diffusivity, $D_N(\delta t)$, for short time increments, δt, where $D_N = \lim_{\delta t \to \infty} D_N(\delta t)$. Characterization of the variation of $D_N(\delta t)$ with δt, which reflects a strong back correlation in cluster motion, is necessary for a reliable extraction of D_N. Additional elucidation of diverse size scaling and cyclic variation of diffusivity in regime (ii), and of intermingling and merging of diffusion branches by regime (iii), is provided in Sec. 2.6 based on counting the number of ground- state and first-excited-state configurations of key classes of clusters. Conclusions are provided in Sec. 2.7.

2.2 Atomistic Model for Cluster Diffusion

2.2.1 Tailored stochastic lattice-gas model

We adopt a tailored model for PD-mediated epitaxial cluster diffusion on metal (100) surfaces, which captures the key features of these systems [16]. In our stochastic lattice-gas model, clusters of adatoms reside on a square lattice of adsorption sites with lattice constant a typically set to unity. Adatoms interact with just nearest-neighbor (NN) attractive lateral interactions of strength $\phi > 0$. They can hop to NN sites, and also to 2nd NN (2NN) sites, provided that hopping retains at least one NN adatom in the cluster. Thus this hopping dynamics preserves NN connectivity (and size) of the cluster. All hop rates have the Arrhenius form $h = \nu \exp\left[-E_{\rm act}/(k_B T)\right]$, where ν is a common attempt frequency for both NN and 2NN hops. Let $n_{\rm NN}$ denote the number of in-plane NN adatoms of the hopping adatom in its initial configuration. Then, the activation barrier $E_{\rm act}$, selected to be consistent with detailed-balance, satisfies,

$$\begin{aligned} E_{\rm act} &= E_e + (n_{NN} - 1)\phi \text{ for NN hops and} \\ E_{\rm act} &= E_e + (n_{NN} - 1)\phi + \delta \text{ for 2NN hops.} \end{aligned} \tag{2.1}$$

In this model, the edge atom formation energy equals $E_{\rm form} = \phi$. It also follows that one has activation barriers of E_e for hopping of isolated adatoms along close-packed $\langle 110 \rangle$ edges via NN hops, $E_r = E_e + \delta$ for hopping around corners or kinks via 2NN hops, $E_k = E_e + \phi$ for kink escape via NN hops, and $E_c = E_e + \phi + \delta$ for "core breakup" via 2NN hops (cf. Sec. 2.1, see Fig. 2.1). The corresponding rates are denoted h_e, h_r, h_k, and h_c, respectively. The characteristic times associated with these various hop rates are denoted $\tau_e = 1/h_e$, $\tau_k = 1/h_k$, etc. An atom can also be extracted from a straight close-packed step edge with barrier $E_{\rm extract} = E_e + 2\phi + \delta$, but this process is not prominent, and thus is not shown in Fig. 2.1.

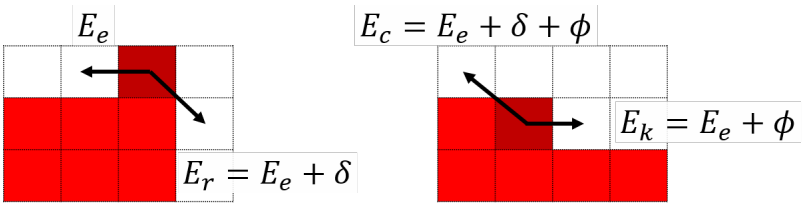

Figure 2.1: Schematic of different hopping processes in our stochastic lattice-gas model. Atoms correspond to filled red squares and available adsorption sites to empty squares.

2.2.2 Model analysis

Our focus is on analysis of the diffusion coefficient D_N for clusters of various sizes N (in atoms). To this end, it is appropriate to first define an effective time-dependent diffusion coefficient, $D_N(\delta t) = \left\langle [\delta r(\delta t)]^2 \right\rangle / (4\delta t)$, where $\delta r(\delta t)$ is the displacement in the cluster center of mass (CM) in a time interval δt, and $\langle\rangle$ is an average of data over a long trajectory. Also we set $[\delta r]^2 = \delta \mathbf{r} \cdot \delta \mathbf{r}$. Comprehensive characterization of model behavior is naturally extracted from KMC simulation. (See Fig. 2.2 for a typical cluster CM trajectory extracted from such a simulation.) The algorithm used is a standard rejection-free Bortz type algorithm. Note that in contrast to a pure random walk, $D_N(\delta t)$ is not in general constant, but can vary for shorter δt due to correlations in the walk of the cluster CM [1, 10, 22, 32]. However, $D_N(\delta t)$ plateaus for larger δt, and the conventional diffusion coefficient is obtained from $D_N = \lim_{\delta t \to \infty} D_N(\delta t) = D_N(\infty)$. Thus appropriate analysis of D_N must account for this transient behavior. For our model where $D_N(\delta t) \propto a^2 h_e$, one has that $D_N(\delta t)/D_N$ versus $h_e \delta t$, and $D_N/(a^2 h_e)$ are independent of our choice of E_e and ν, and thus h_e. For reference, choosing $E_e = 0.29$eV and $\nu = 10^{12.5}\text{s}^{-1}$ mimicking Ag/Ag(100) yields $h_e = 10^{7.6}\text{s}^{-1}$ at $300K$.

We expect $D_N(\delta t)$ to have converged to its plateau value of D_N for $\delta t > \delta t_c$, where $\left\langle [\delta r(\delta t_c)]^2 \right\rangle \sim a^2$, i.e., when the cluster of CM has moved about one lattice constant. To obtain precise D_N, we need the total length of the trajectory t_{tot} of at least $O(10^3 \delta t_c)$. Then $\left\langle [\delta r(\delta t_c)]^2 \right\rangle$ can be estimated from $O(10^3)$ statistically independent values obtained from nonoverlapping time increments of length δt_c along the trajectory. Overlapping time incre-

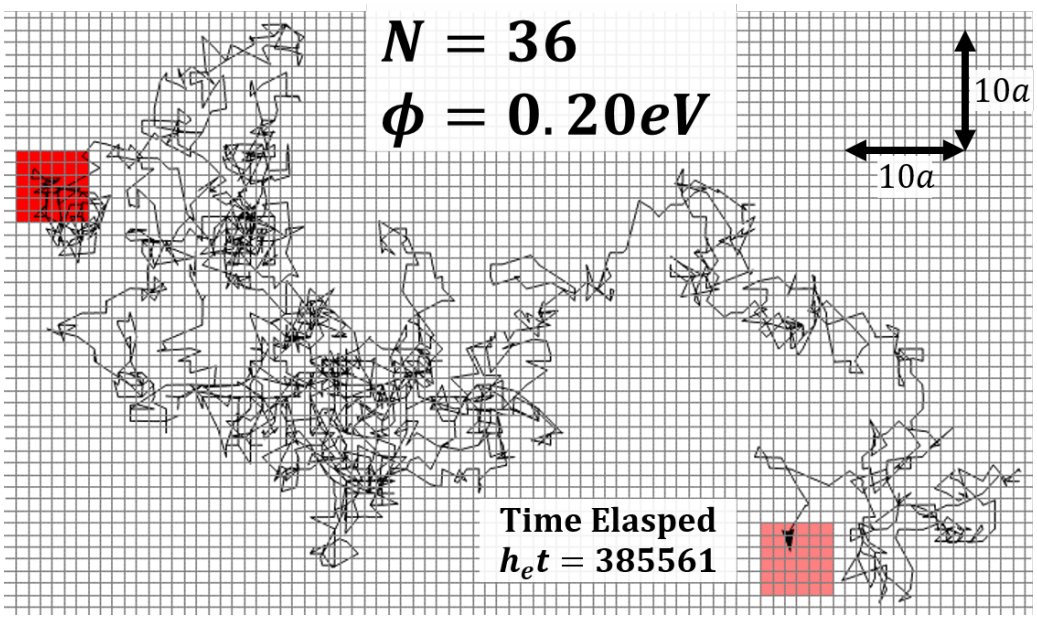

Figure 2.2: Trajectory of CM of a diffusing cluster with $N = 36$ for $\phi = 0.20$eV with $\delta = 0$ at $300K$. Start: red square. End: pink square.

ments can be used, although then the values of $[\delta r(\delta t_c)]^2$ are not completely independent. We choose $t_{\rm tot} \sim 35000\delta t_c$.

It is appropriate to note that D_N can in principle be determined exactly for any cluster size N by analysis of the linear master equations for the stochastic lattice-gas model [30,32]. These master equations track the evolution of the probability of various cluster configurations for the infinite possible number of CM positions. Let Ω_N denote the total number of distinct configurations for a cluster of size N. Then, applying a discrete spatial Fourier transform to these master equations with respect to cluster position converts them into a finite-dimensional $\Omega_N \times \Omega_N$ matrix evolution equation in transform space. One then extracts D_N from analysis of the acoustic eigenmode of this evolution matrix, and specifically from its quadratic variation for small wavenumbers. It should also be noted that the transformed $\Omega_N \times \Omega_N$ matrix encodes connectivity between cluster configurations, i.e., indicating which configurations can be directly reached from other configurations by hopping of a single edge atom. Thus the behavior of D_N also reflects this connectivity, although in a nontrivial

indirect way. Finally, we emphasize that an exact analysis utilizing this approach is only viable for relatively small clusters since Ω_N increases quickly with N. Nonetheless, it is useful to elucidate behavior in the small cluster size regime (i) (see Appendix A).

The relevance of the total number of cluster configurations Ω_N is already clear from the above discussion of exact analysis. However, one anticipates that not all configurations are equally relevant for the cluster diffusion processes, particularly at lower T. Thus, it is natural to separately analyze the number of ground-state configurations $\Omega_N(0)$, the number of first excited state configurations $\Omega_N(1)$, etc. This analysis involves nontrivial combinatorics exploiting results related to partitions of integers in number theory. Additional useful analysis will involve estimation of the number of kinks in ground state, etc., configurations. Details are provided in Appendices BD. These results will be utilized to elucidate short-time transient behavior, anomalous scaling observed for moderate sizes, and intermingling and merging of different diffusion branches.

2.3 Distinct Branches of Cluster Diffusivity for Moderate Sizes

First, we characterize of various branches or classes of cluster sizes for which distinct diffusion behavior is observed in regime (ii) of moderate clusters sizes $N = 9$ to $O(10^2)$. We close with comments on behavior for small clusters with $N < 9$.

2.3.1 Nucleation-mediated (nm) diffusion for "perfect sizes

"Perfect" sizes $N = N_p = L^2$ or $L(L+1)$, with $L = 3, 4, ...$, have unique nondegenerate ground-state shapes corresponding to perfect squares and near-square rectangles, respectively. This uniqueness does not apply for sizes $N = L(L+n)$ with $n \geq 2$ where the $L \times (L+n)$ rectangular configuration is either one of multiple ground states, or corresponds to an excited state. If $\phi/(k_BT)$ is not too small, clusters with $N = N_p$ primarily exist in their unique ground-state shapes, and are subject to nucleation-mediated diffusion. In this process, the first step is extraction of one of the four corner atoms onto a straight close-

packed ⟨110⟩ step edge, which raises the total energy by $\Delta E = +\phi$. However, typically, this atom will soon return to the more highly coordinated corner site. Thus, to initiate significant cluster restructuring leading to long-range diffusion, it is necessary that a second atom detaches from a corner and aggregates with the first atom before the first atom can return to the corner [9, 14, 16]. In this way, a step edge dimer is formed, thus potentially nucleating a new edge layer. Once this dimer is formed on one edge, subsequent atoms can migrate from kink or corner sites to complete that new edge layer.

The most direct pathway to facilitate translation of the unique ground state for $N_p = L^2$ to a different location, a key component of long-range diffusion, is shown in Fig. 2.3a. In this case, two atoms are shifted from one side of the cluster to nucleate a dimer on the opposite side. Thereafter, atoms continue to be shifted from that same side to the opposite side. After each individual atom transfer is completed, the cluster is in a different first excited state configuration with energy $\Delta E = +\phi$ above the ground state. Only when the last atom is transferred does the energy decrease again by $\Delta E = -\phi$. However, we note that there are indirect pathways leading to long-range diffusion as shown in Fig. 2.3b. Here, atoms shifted from multiple corners of the cluster whose configuration (after each atom transfer) wanders through a large number of first-excited state configurations. However, to achieve the translated ground state, multiple eroded corners must be largely reconstructed, so that, ultimately, atoms are only removed from a single side of the cluster. Significantly, we note that while long-range diffusion accesses many configurations isoenergetic with the first excited state, it requires repeatedly returning to the unique ground-state shape. Figure 2.3c shows the direct $N_p = L(L+1)$, which is analogous to that for $N_p = L^2$.

Finally, we comment on the effective barrier for nucleation-mediated diffusion of perfect clusters. An isolated edge atom extracted from the corner of a perfect core exists with low quasiequilibrium density, $n_{\mathrm{eq}} = \exp\left[-\phi/(k_B T)\right]$. Mills *et al.* [10] argued that D_N should reflect the nucleation rate $k_{\mathrm{nuc}} \sim n_{\mathrm{eq}} h_e$ to create a dimer on an outer edge. k_{nuc} is the product of the density n_{eq} times the rate h_c of extracting a second atom at the core, as

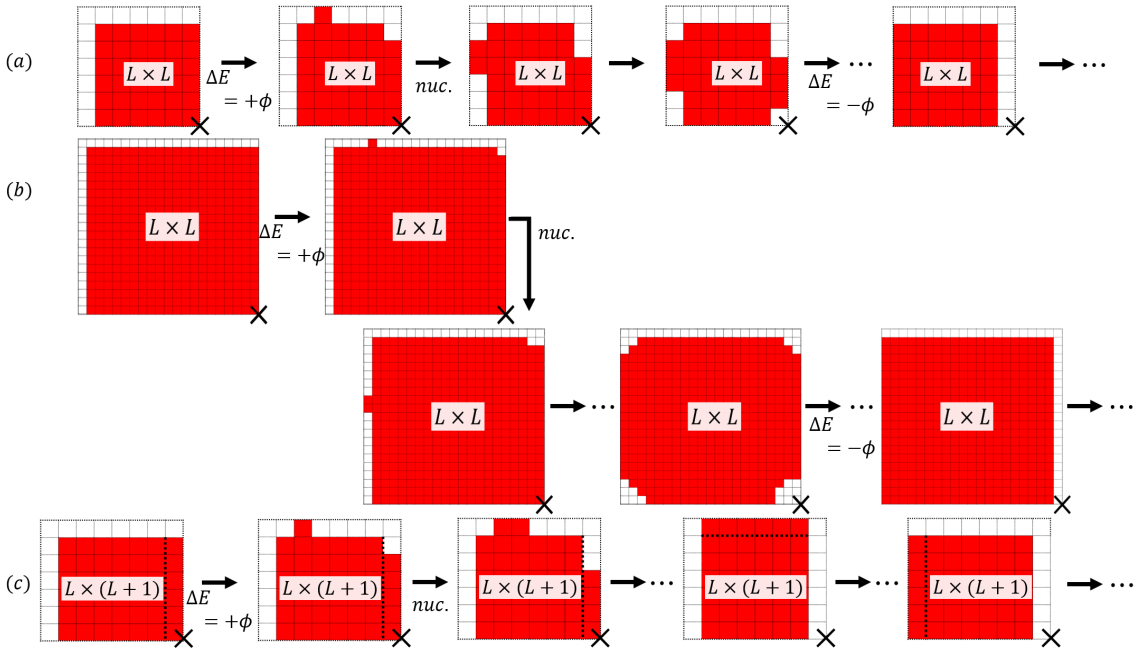

Figure 2.3: Nucleation-mediated cluster diffusion for perfect sizes $N_p = L^2$. (a) direct and (b) indirect pathways. (c) Direct pathway for perfect sizes $N_p = L(L+1)$

the extracted atom must meet the preexisting edge atom to nucleate a new step edge. Consequently, the effective barrier for cluster diffusion is given by $E_{\text{eff}} = E_e + 2\phi + \delta$ [10, 15, 17].

2.3.2 Facile (FA) cluster diffusion

For clusters of size $N = N_p + 1$ and $N = N_p + 2$, with either $N_p = L^2$ or $L(L+1)$, the edge dimer nucleation process described above for perfect clusters is not necessary for long-range cluster diffusion. For $N = N_p + 1$, we note the existence of a "special" ground-state configuration with an isolated adatom on the edge of a perfect square or rectangular core of N_p atoms. For these special configurations, the isolated edge adatom can readily diffuse around the entire cluster perimeter. For $N = N_p + 2$, "special" ground-state configurations involve an NN pair of edge atoms or edge dimer on a perfect core, where this edge dimer

can dissociate and readily reform on another edge. Either process results in no net change of energy. After transferring the isolated edge atom or dimer to new edge of the core, atoms can be transferred from another edge to complete the new edge of the core. This again leaves an isolated atom or dimer on the edge of a perfect core with shifted location.

The above scenario for $N = N_p+1$ with atoms transferred from a single edge corresponds to a direct pathway to facilitate translation of the special ground-state configuration to a different location. This direct pathway is shown in Fig. 2.4(a). However, there are indirect pathways leading to the same outcome. Analogous to the above case of perfect sizes, these indirect pathways involve shifting of atoms from multiple corners of the cluster as shown in Fig. 2.4(b) so the cluster wanders through a large number of ground-state configurations. However, to achieve the translated ground state, most of these eroded corners must be reconstructed so that atoms are only shifted from a single side of the cluster. Shifting atoms from one kink to another does not change the energy after reattachment, so as a result for either direct or indirect pathways, after each atom transfer, the system evolves through a set of configurations isoenergetic with the special ground-state configurations. The direct pathway for $N = N_p + 2$ is shown in Fig. 2.4(c).

Finally, we emphasize that while the diffusing cluster can wander through many isoenergetic configurations, long-range diffusion (if restricted to these configurations) requires that the cluster repeatedly passes through a special configuration with an isolated atom or dimer at an edge of a perfect core. This is the only way to create a new complete edge on the original perfect core. Also, we note that since diffusion of facile clusters just involves breaking atoms out of kink sites and subsequent edge diffusion, the effective cluster diffusion barrier E_{eff} is simply given by $E_{\text{eff}} = E_e + \phi + \delta$.

2.3.3 Other cases of nucleation-mediated cluster diffusion

Clusters of size $N = N = N_p + n$ with $3 \le n \le L$, for either $N_p = L^2$ or $L(L + 1)$, also exhibit nucleation-limited diffusion. The ground states for these sizes include the subclass

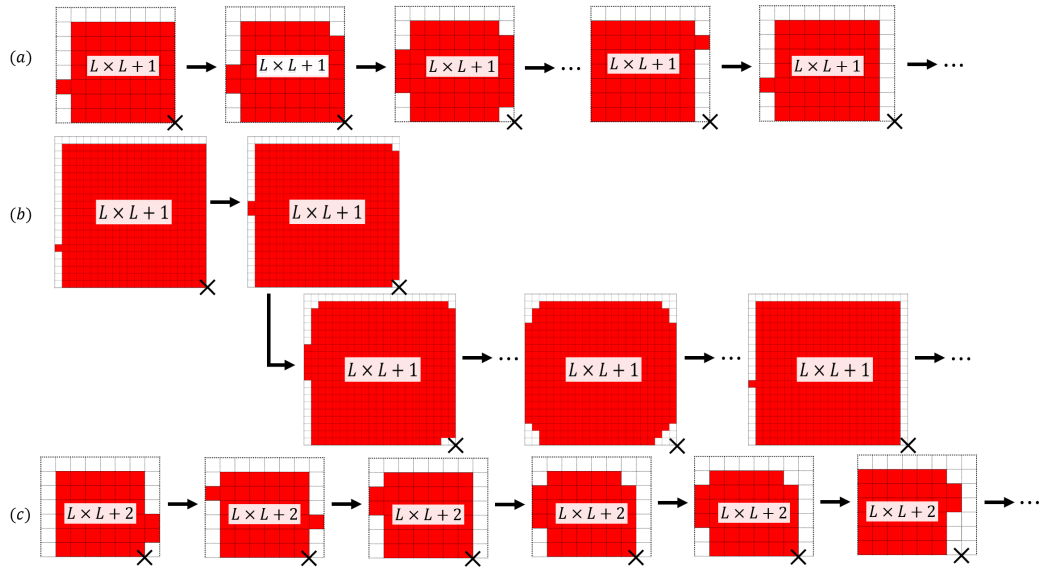

Figure 2.4: Facile cluster diffusion for sizes $N = L^2+1$: (a) direct and (b) indirect pathways. (c) Direct pathway for sizes $N = L^2 + 2$.

of configurations with a linear triple or longer string of atoms at the edge of a perfect square or rectangular core. For these configurations, adatoms can readily transfer from the opposite complete edge to that on which the string of n adatoms reside (without raising the energy after transfer), thereby completing that edge. However, this leaves behind a triple or longer string of atoms which cannot readily be transferred to another edge. Certainly, the ground states are degenerate, as starting with the above subclass of configurations, atoms can be removed from multiple corners, and added to the above mentioned string with no net change in energy. However, in any case, nucleation of a dimer on a new outer edge (i.e., on an edge outside the rectangle inscribing the ground-state configurations) is always required to facilitate long-range diffusion of the cluster CM. The same argument as used for perfect clusters indicates that the effective barrier for cluster diffusion equals $E_{\text{eff}} = E_e + \phi + \delta$.

2.3.4 Facile behavior for small sizes $n < 9$

Diffusion for all small clusters with $N < 9$ is always facile (i.e., not nucleation-mediated). For $N = 2$ or 3, cluster diffusion does not even require breaking atoms out of kink sites,

so the effective barrier is even lower than described above for facile diffusion of larger clusters. A dimer CM undergoes a pure random walk on a square grid rotated at 45° to the adsorption sites with lattice constant $a/\sqrt{2}$ hopping at rate h_r. Thus, one has $D_2 = D_2(\delta t) = 1/2a^2 h_r$ and $E_{\text{eff}} = E_e + \delta$. For a trimer, $D_3(\delta t)$ generally decreases with increasing δt to its asymptotic value, and diffusion is controlled by corner rounding so that again $E_{\text{eff}} = E_e + \delta$ [32]. Cases $N = 5 = 2 \times 2 + 1$ and $N = 7 = 2 \times 3 + 1$ fit within the category $N_p + 1$. Cases $N = 4 = 2 \times 1 + 2$, $N = 6 = 2 \times 2 + 2$, and $N = 8 = 2 \times 3 + 2$ fit within the category $N_p + 2$. Thus all these cases with $4 \leq N \leq 8$ have $E_{\text{eff}} = E_e + \phi + \delta$, and they all exhibit nonconstant $D_N(\delta t)$. (See Appendix A for an exact master equation based analysis for some of these cases.)

2.4 Cluster Diffusivity versus Size: kMC Results

2.4.1 Cluster diffusivity with no kink rounding barrier ($\delta = 0$)

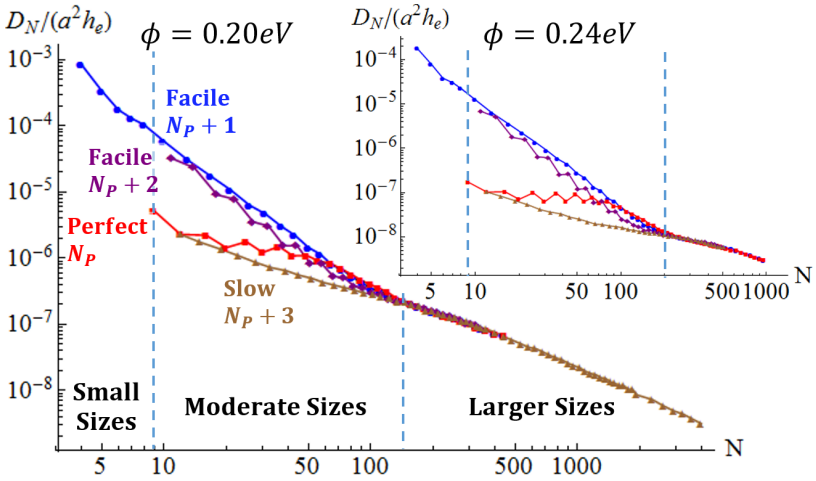

Figure 2.5: KMC results for D_N vs N with $\delta = 0$ and $\phi = 0.20$eV ($\phi = 0.24$eV in the inset) at $300K$.

We first present an overview of KMC results illustrating various size regimes and branches of D_N behavior focusing on the case $\phi = 0.2$eV and $\delta = 0$ at $300K$. See Fig. 2.5. For small sizes $N = 4$ to 8, high facile values of D_N are evident. Even higher values for $N = 1$

to 3 are not shown. For moderate sizes, $N = 9$ to $O(10^2)$, we just show for clarity only four distinctive branches: facile $N_p + 1$, facile $N_p + 2$, perfect N_p, and slow $N_p + 3$. The following key features are present: (a) initially high values and rapid decay of $D_N \sim N^{-\beta f}$ for facile $N_p + 1$ clusters up to $N \sim 82$ with large $\beta \approx 2.3$; similarly high D_N, but less regular decay for facile $N_p + 2$ clusters; (b) the lowest values and slow decay of $D_N \sim N^{\beta s}$ for sizes $N_p + 3$ for $N \sim 39 - 103$ with small $\beta \approx 0.83$; (c) very weak size dependence of D_N for perfect N_p clusters up to $N \approx 81$; perfect N_p and slow $N_p + 3$ branches merge for small $N = 12$ (and $N = 9$); (d) intermingling of D_N for perfect N_p with facile branches for $N_{\text{mingle}} \approx 43$, and subsequent transition to a rapid decrease of D_N for perfect clusters; (e) near-merging of all branches for $N \approx N_{\text{mingle}} \approx 150$. For larger sizes $N > N_{\text{merge}}$, if we write $D_N \sim N^{-\beta \text{eff}}$, the effective exponent varies slowly from $\beta_{\text{eff}} \approx 1.09$ for N just above N_{merge}, to $\beta_{\text{eff}} \approx 1.33$ for N from 5001000, to $\beta = 1.50$ (the asymptotic value for compact clusters) for N from 20003600 (see Fig. 2.6). This latter result is consistent with a kink separation $L_k = 1/2 \exp[1/2\phi/(k_B T)[\approx 24$ for $\phi = 0.20$eV, given that the asymptotic regime should apply for $N \gg (L_k)^2 \approx 570$.

It is instructive to contrast behavior for $\phi = 0.20$eV with that for $\phi = 0.24$eV retaining $\delta = 0$ at $300K$ (see the insets for Figs. 2.5 and 2.6). All of the features described above are preserved qualitatively for $\phi = 0.24$eV. However, now the deviations between the different branches for moderate sizes are enhanced, which is a natural consequence of larger values of $\phi/(k_B T)$ producing a larger difference between E_{eff} for facile and nucleation-mediated branches. Also, the approach to asymptotic behavior is significantly delayed for larger $\phi/(k_B T)$, as expected given the larger values of L_k. Specifically, for $\phi = 0.24$eV, we find that $\beta_f \approx 2.6$ up to $N \sim 101$, $\beta \approx 0.53$ for $N \sim 67-200$, $N_{\text{mingle}} \approx 81$, and $N_{\text{merge}} \approx 200250$. With regard to scaling for larger sizes, we find that $\beta_t exteff \approx 0.75$ just above N_{merge}, and $\beta_{\text{eff}} \approx 1.12$ for N from 5001000. Now $L_k = 52$ for $\phi = 0.24$eV, so we do not access the asymptotic scaling for $N \gg (L_k)^2 \approx 2700$. Naturally, choosing $\phi < 0.20$eV would minimize the difference between different branches for moderate sizes and accelerate the approach to

asymptotic behavior. However, if $\phi/(k_BT)$ is too small, the cluster connectivity constraint becomes artificial. In the limit as $\phi/(k_BT) \to 0$, the clusters become "random animals" with perimeter length proportional to size. This also results in deviations from $\beta = 1.5$ [22].

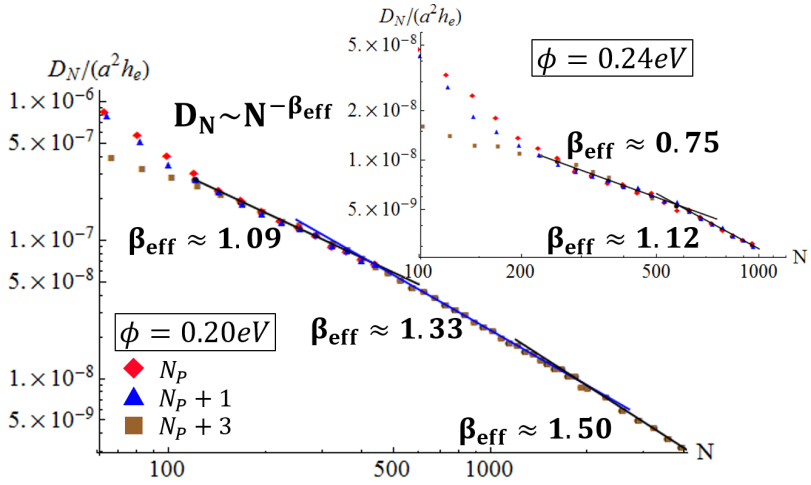

Figure 2.6: Post-merging effective scaling behavior of D_N with N for $\phi = 0.20$eV ($\phi = 0.24$eV in the inset) and $\delta = 0$ at $300K$.

Next, we consider in more detail diffusion behavior in the moderate size regime. Figure 2.7 reveals a quasiperiodic variation of D_N with $N = N_p + n$ within each cycle $n = 1$ to $n_{\max}$, where $n_{\max} = L$ for $N_p = L^2$ or $L(L+1)$. Specifically, D_N has a local maximum for $n = 1$, drops significantly for $n = 2$, and again for $n = 3$, where the latter corresponds to the lowest value within each cycle. D_N then increases within each cycle $N = N_p + n$ for increasing $n = 3, 4, 5, ..., n_{\max}$, where $N = N + n_{\max}$ recovers the next perfect size above N_p. For example, for $N_p = 30(36)$, and $N + n_{\max} = 36(42)$. Note that the length of these cycles increases for larger N, and that $N = 15, 24, 35, ...$ is the smallest value of N for which one can realize $N_p + 3, N_p + 4, N_p + 5, ...$

Interestingly, D_N values for perfect sizes for $n = n_{\max}$ within each cycle can be comparable to those for facile clusters for $n = n_{\max} + 2$. On the other hand, they are often well above D_N for $n = 3$ (the slowest clusters). This contrasts a possible perception that perfect sizes should be the slowest. Thus one might question the assignment of nucleation-mediated

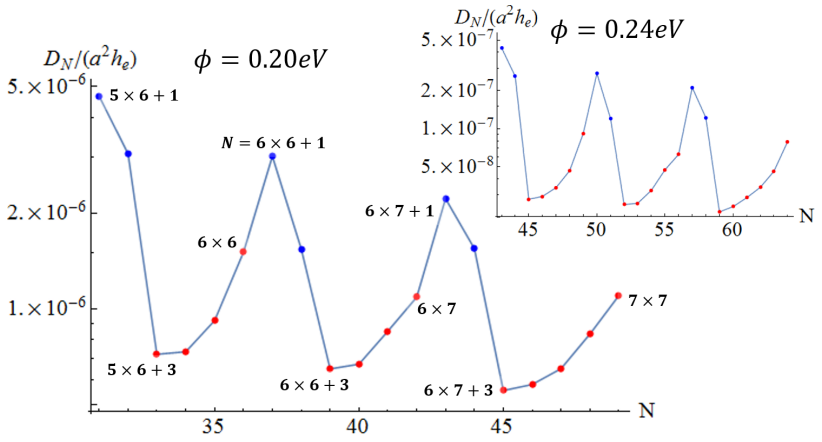

Figure 2.7: Cyclical behavior of D_N vs N between minima ($N_p + 3$) and maxima ($N_p + 1$) for $\phi = 0.20$eV and $\delta = 0$ at $300K$. Inset: $\phi = 0.24$eV.

diffusion for $n = n_{\max}$ versus facile diffusion for $n = n_{\max} + 1$. However, an Arrhenius plot for D_N versus $\phi/(k_BT)$ does show clearly the distinction between E_{act} for these classes. Typically, such Arrhenius plots plot $\ln[D_N]$ versus for fixed $1/(k_BT)$, the slope corresponding to E_{eff}. Here, instead we plot $\ln\left[D_N/(a^2h_e)\right]$ versus ϕ for fixed $T = 300K$ yielding a slope of $-n/(k_BT)$ with $n = 1$ ($n = 2$) for facile (nucleation-mediated) diffusion (see Fig. 2.8). This format is instructive for showing the extent of variation of D_N for the expected range of ϕ values for metal (100) homoepitaxial systems, and for a typical experimental temperature ($T = 300K$).

2.4.2 Cluster diffusivity with a finite kink rounding barrier ($\delta = 0.1$)

The introduction of a significant kink rounding barrier, $\delta > 0$, reduces the magnitude of D_N as a result of the increased E_{eff} described in Sec. 2.3. However, the qualitative features of the different diffusion branches for moderate sizes, and the variation of D_N versus N are the same as for $\delta = 0$. These features are shown in Fig. 2.9 for $\phi = 0.20$eV and $\delta = 0.1$eV at $300K$ (and in the inset for $\phi = 0.24$eV). A detailed characterization of the cyclical behavior of D_N versus N in the moderate size regime is shown in Fig. 2.10 where again the local maxima (minima) in D_N occur for $N = N_p + 1$ ($N = N_p + 3$). As for $\delta = 0$, D_N

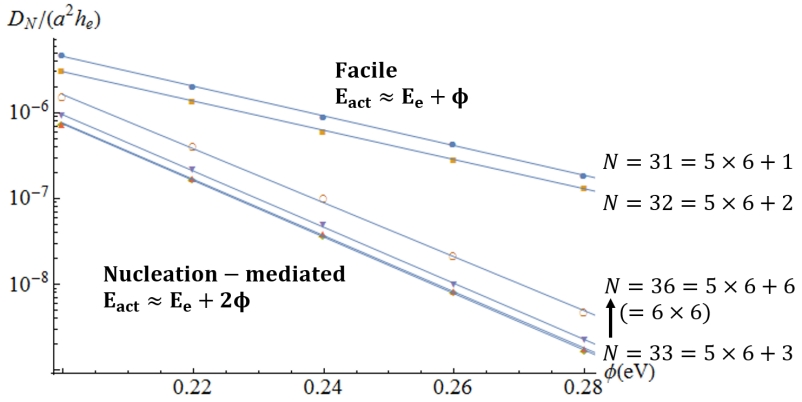

Figure 2.8: Arrhenius analysis of D_N for facile ($N_p + 1$, $N_p + 2$) and nucleation-mediated ($N_p + n$ for $n = 3, 4, ..., n_p$) sizes with $N_p = 30$ and $n_p = 6$. $T = 300K$ is fixed and ϕ is varied.

for $N = N_p + n$ for the case of perfect sizes with $n = n_{\max}$ is not so far below that for facile sizes with $n = n_{\max} + 2$, but well above that for $n = 3$. Again, we have performed an Arrhenius analysis to reveal that E_{eff} for $n = 3, 4, ...,$ and $n_textmax$ (nucleation-mediated cases) are all similar, and are clearly above those for $n = n_{\max} + 1$ and $n = n_{\max} + 2$ (facile cases).

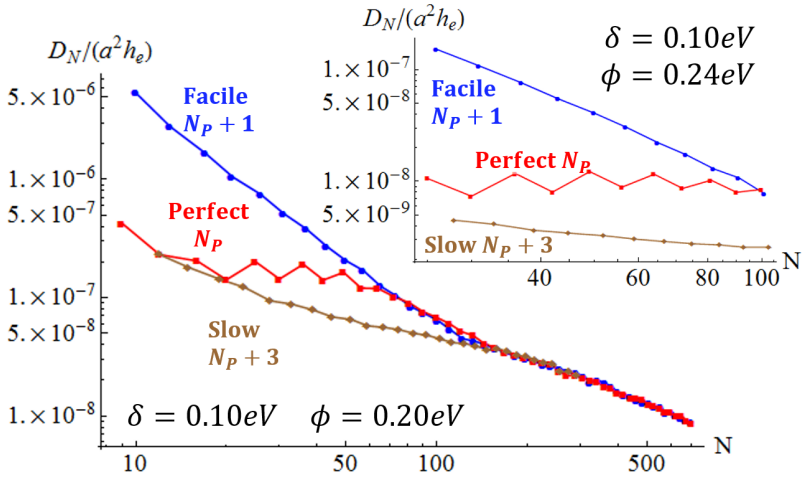

Figure 2.9: KMC results for D_N vs N with $\delta = 0.10$ and $\phi = 0.20$eV ($\phi = 0.24$eV in the inset) at $300K$.

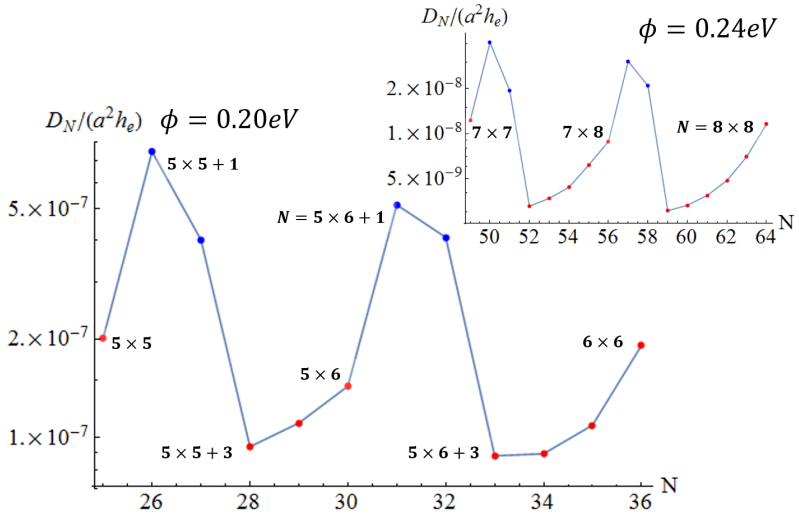

Figure 2.10: Cyclical behavior of D_N vs N between maxima $(N_p + 1)$ and minima $(N_p + 3)$ for $\phi = 0.20$eV and $\delta = 0.1$eV at $300K$. (Inset) $\phi = 0.24$eV and $\delta = 0.1$eV.

A previous study [17] indicated that introduction of a kink rounding barrier reduces the values of effective scaling exponents β_{eff}. Specifically, this should apply for regime (iii) where facile and nucleation-mediated branches have merged, but prior to the true asymptotic regime of large sizes. For $\phi = 0.20$eV at $300K$, we find that just after merging, $\beta_{\text{eff}} \approx 0.86$ for $144 \leq N \leq 325$ when $\delta = 0.1$eV (versus $\beta_{\text{eff}} \approx 1.09$ for $121 \leq N \leq 327$ when $\delta = 0$). We also find that $\beta_{\text{eff}} \approx 1.09$ for $361 \leq N \leq 677$ when $\delta = 0.1$eV (versus $\beta_{\text{eff}} \approx 1.32$ for $364 \leq N \leq 2028$ when $\delta = 0$). For $\phi = 0.24$eV, data are more limited for $\delta = 0.1$eV as the simulation is more computationally demanding. [48] However, we estimate that just after merging, $\beta_{\text{eff}} \approx 0.71$ when $\delta = 0.1$eV (versus $\beta_{\text{eff}} \approx 0.75$ when $\delta = 0$). These results confirm the proposal that increasing δ decreases β_{eff}.

2.5 Time-dependent Diffusivity and Back-correlation

The time-dependent diffusion coefficient, $D_N(\delta t) = \left\langle [\delta r(\delta t)]^2 \right\rangle / (4\delta t)$, was introduced in Sec. 2.2.2, where $\delta \mathbf{r}(\delta t)$ is the CM displacement in a time interval δ_t. The plateau value of $D_N(\delta t)$ corresponds to the conventional diffusion coefficient, $D_N = \lim_{\delta t \to \infty} D_N(\delta t) =$

$D_N(\infty)$. Thus it is important to understand the transient behavior in order to reliably assess D_N. In fact, this was essential to obtain the smooth cyclical variation of D_N shown in Sec. 2.4. Here, we consider behavior only in the absence of a kink rounding barrier, $\delta = 0$, although the basic observations and strategies of analysis apply more generally. In Fig. 2.11, we show KMC simulation results for $\delta = 0$ for the behavior of $D_N(\delta t)/D_N(\infty)$ versus $h_e\delta t$ for sizes within a single cycle $N = N_p + 1$ to $N = N_p + n_{\max}$ (cf. Sec. 2.4). As noted in Sec. 2.2.1, the form of these curves is independent of the choice of h_e. There is a strong decrease in $D_N(\delta t)$ to its plateau value $D_N = D_N(\infty)$. In Sec. 2.5.1, we estimate the short time-increment values,$D_N(\delta t \to 0)$, for special cases of perfect and facile sizes. Then, in Sec. 2.5.2, we provide further insight into the underlying back correlation in cluster motion.

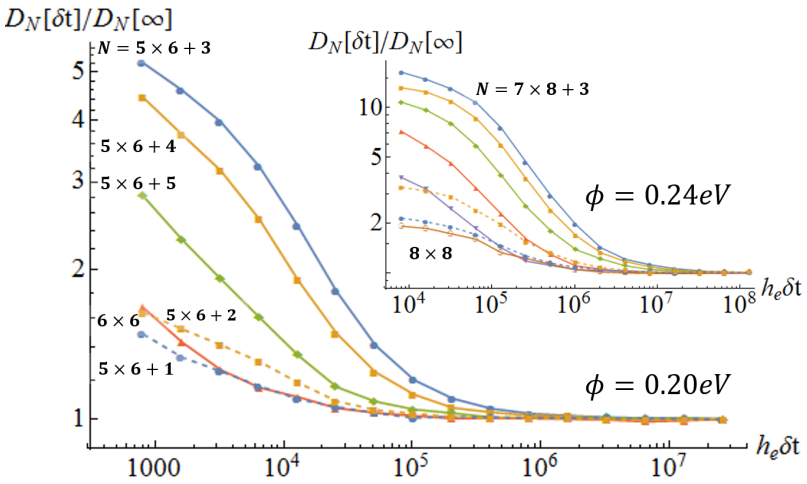

Figure 2.11: Time-dependent diffusion coefficients reflecting backward correlation in the CM motion for various cluster sizes within a cycle (see text) with $\phi = 0.20$eV (and $\phi = 0.24$eV in the inset) for $\delta = 0$ at $300K$. Here $D_N(\infty) = \lim_{\delta t\to\infty} D_N(\delta t) = D_N$.

2.5.1 Short-time behavior of $D_N(\delta t)$)

Our estimate of the value of $D_N(\delta t \to 0)$ assumes independent contributions to the mean-square displacement of the cluster CM from the short-time motion of all isolated (singly coordinated) edge atoms and all doubly coordinated kink atoms. Thus, we sum over

these contributions to obtain $D_N(\delta t \to 0)$. For short-time increments, δt, the mean-square displacement of isolated edge atoms (called "monomers" below) from their initial position satisfies $\left\langle [\delta r_e(\delta t)]^2 \right\rangle \approx 2h_e\delta t, 3h_e\delta t$, and $4h_e\delta t$ for atoms on straight close-packed steps that can make two NN hops, atoms at corners that can make one NN and one 2NN hop, and atoms that can make two 2NN hops, respectively. The latter case is rare for larger clusters, so effectively one has $2h_e\delta t \le \left\langle [\delta r_e(\delta t)]^2 \right\rangle \le 3h_e\delta t$. The mean-squared displacement of kink atoms (just called "kinks" below) from their initial position satisfies $\left\langle [\delta r_k(\delta t)]^2 \right\rangle \approx 3h_k\delta t$ for atoms that can make one NN and one 2NN hop, and $\left\langle [\delta r_k(\delta t)]^2 \right\rangle \approx 4h_k\delta t$ for corner atoms that can make two 2NN hops. Thus one has that $3h_k\delta t \le \left\langle [\delta r_k(\delta t)]^2 \right\rangle \le 4h_k\delta t$. To simplify the analysis below, we will not discriminate between the different categories of monomers and kink atoms, and will interpret $\left\langle [\delta r_e(\delta t)]^2 \right\rangle$ and $\left\langle [\delta r_k(\delta t)]^2 \right\rangle$ as suitable averages over all categories. Subsequently, we will just obtain upper and lower bounds for $D_N(\delta t \to 0)$ using the above upper and lower bounds on $\left\langle [\delta r_{e,k}(\delta t)]^2 \right\rangle$.

Before presenting our approximation for $D_N(\delta t \to 0)$, we also note that when a periphery atom is shifted by one lattice constant in a certain direction, the CM of the cluster is shifted by $1/N$ in that direction. This will produce an additional factor of $1/N^2 = 1/L^4$ in our analysis of mean-squared cluster displacement. Thus our expression for $D_N(\delta t \to 0)$ becomes

$$\begin{aligned} D_N(\delta t \to 0) & \\ & \approx \frac{1}{4N^2} \sum_i \left(n_{N,e}(i) \frac{\left\langle [\delta r_e(\delta t)]^2 \right\rangle}{\delta t} + n_{N,k}(i) \frac{\left\langle [\delta r_k(\delta t)]^2 \right\rangle}{\delta t} \right) \\ & \quad \times \frac{\exp\left[-E_i/(k_B T)\right]}{Z}, \end{aligned} \tag{2.2}$$

where $n_{N,e}(i)$ and $n_{N,k}(i)$ are the number of monomers and kinks in ith state with energy E_i, and $Z = \sum_i \exp\left[-E_i/(k_B T)\right]$ is the relevant partition function. We use this result to estimate $D_N(\delta t \to 0)$ focusing on two special cases. Further details are provided in Ref. [49].

Perfect sizes $N_P = L^2$.The ground state is unique, i.e., $\Omega_{L^2}(0) = 1$, and has a square shape with no monomers and four kinks. Thus the total contribution to $D_N(\delta t \to 0)$ from

the ground state is of order h_k/N^2, denoted $O(h_k/N^2)$. There are $4 \times (4L-2)$ first excited states where an atom is shifted from one of the four corners of the ground state and placed as a monomer on an edge, and $2 \times 4L$ first excited states with a monomer on an edge of a $(L-1) \times (L+1)$ rectangle. Thus the total number of first excited states with a monomer is $\Omega'_{L^2}(1) = (24L/8)$. The total contribution to $D_N(\delta t \to 0)$ from these states is dominated by monomer hopping and is $O(\Omega'_{L^2}(1) h_e \exp\left[-\phi/(k_B T)\right]/N^2) = O(L h_k/N^2)$, which exceeds the contribution from the ground state.

The great majority of the $\Omega_{L^2}(1)$ first excited states have no monomers, but many kinks. If $n_{L^2,k}(1)$ denotes the number of kinks in such states, then one has that $3 \leq n_{L^2,k}(1) \leq 2(1+\sqrt{2L+1})$ (see Appendix B). Despite the penalty of a Boltzmann factor of $\exp\left[-\phi/(k_B T)\right]$, the total contribution of kinks in first excited states,$O(n_{L^2,k}(1)\Omega_{L^2}(1) h_k \exp\left[-\phi/(k_B T)\right]/N^2)$, becomes comparable to those above for moderate N due to the large number of first excited states $\Omega_{L^2}(1)$. Specifically, the contribution becomes comparable when $\Omega_{L^2}(1) \exp\left[\phi/(k_B T)\right] \sim O(1)$, which occurs when $N \sim 49$ (81) for $\phi = 0.20$eV ($\phi = 0.24$eV) (see Appendix C).

Finally, we find that it is also necessary to consider contributions from the subclass of second excited states, which include a monomer. We note that the number of such states, $\Omega'_{L^2}(2) \sim 4L\Omega_{L^2-1}(1)$ (see Appendix D for a more precise analysis) is somewhat larger than $\Omega_{L^2}(1)$ for $N \sim O(10^2)$. The total contribution of such states is of order $O(\Omega'_{L^2}(2) h_e \exp\left[-2\phi/(k_B T)\right]/N^2)$, which is of the same order as the above contributions for moderate cluster sizes if one accounts for this large $\Omega'_{L^2}(2)$ and for the high monomer hop rate h_e. Combining these four types of contributions (of which the last one dominates for moderate N) yields estimates for $D_N(\delta t \to 0)$ close to simulation values as shown in Fig. 2.12 for $h_e \delta t = 1$,$\phi = 0.20$eV.

It is appropriate to note that the contributions explicitly included above correspond to exactly the configurations that arise in our picture of nucleation-mediated cluster diffusion for moderate sizes. The cluster primarily exists in the ground state, but must access first excited states in order to initiate motion. However, transitions between the numerous

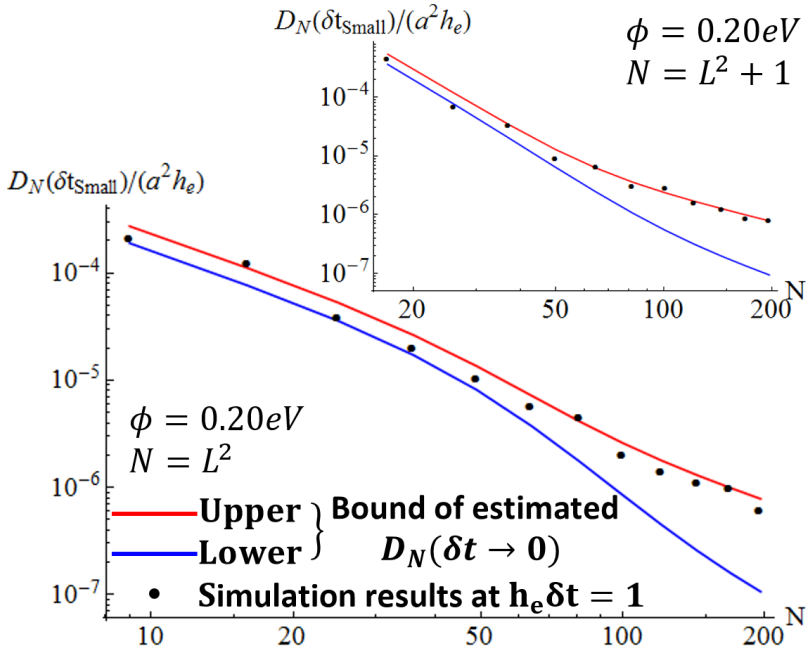

Figure 2.12: Estimated upper and lower bounds of $D_N(\delta t \to 0)$ vs simulation results for $h_e\delta t = 1$ (black dots) for $N = L^2$ (inset $N = L^2 + 1$) for $\phi = 0.20$eV and $\delta = 0$ at $300K$.

monomer-free first excited states involve second excited states with a monomer. We note that contributions from second excited states without a monomer and higher excited states are of lower order than those above since the number of relevant configurations is not substantially greater than $\Omega_{L^2}(1)$ or $\Omega'_{L^2}(2)$.

Facile clusters of sizes $N = L^2 + 1$. Here, we mimic the above analysis for perfect clusters. For $N = L^2 + 1$, there are $4L$ ground states with a monomer, i.e., $\Omega'_{L^2+1}(0) = 4L$, each of which provide a contribution $O(h_e\Omega'_{L^2+1}(0)) \sim O(h_e)$ dominated by monomer hopping. All ground states contribute by kink hopping with total contribution of order $O(n_{L^2+1,k}(0)h_k\Omega_{L^2+1}(0)) \sim O(h_e)$ for $N \geq 65$ (101) with $\phi = 0.20$eV (0.24eV), using the feature that $\Omega_{L^2+1}(0)$ grows far more quickly than $\Omega'_{L^2+1}(0)$. Note also that $n_{L^2+1,k}(0) \leq 2(1+\sqrt{2L-1})$ (see Appendix B). The third contribution comes from the first excited states with a monomer, where the number of such states satisfies $\Omega'_{L^2+1}(1) \sim 4L\Omega_{L^2}(1)$ (see Appendix D for a more precise analysis). Thus the total contribution of first excited states

is $O(h_e\Omega'_{L^2+1}(1)\exp[-\phi/(k_BT)]) \sim O(h_e)$, due to the large number of states considered, $O(\Omega'_{L^2+1}(1)\exp[-\phi/(k_BT)]) \sim O(1)$ for $N \geq 65$ (101) with $\phi = 0.20$eV (0.24eV). Combining these three contributions yields estimates for $D_N(\delta t \to 0)$ close to simulation values [see Fig. 2.12 (inset) for $h_e\delta t = 1$, $\phi = 0.20$eV]. Note that the states explicitly included above are exactly those in our picture of facile diffusion for moderate sized clusters, and other states have a lower order contribution.

Other cases and further comparison. The above analysis readily extends to other cases. For the nucleation-mediated cases, $N = N_p + n$ with $n = 3, 4, ..., n_{\max}$, we claim that $D_N(\delta t \to 0)$ will decrease from a local maximum for $N = N_p + 3$ to a local minimum for $N = N_p + n_p$ (corresponding to perfect clusters). Clusters within this class for $N = N_p+3$ have the highest ground-state degeneracy and importantly also the highest number of kinks. Consequently, the contribution from the ground states $O(n_{L^2+3,k}(0)h_k\Omega_{L^2+3}(0))$ for $N = N_p+3$ will exceed that for perfect clusters due to the substantial number of kink sites, $n_{L^2+3,k}(0) \leq 2(2+\sqrt{(}2L-5))$. The larger factor $\Omega_{L^2+3}(0)$ versus $\Omega_{L^2+n_p}(0) = 1$ does not in itself boost $D_N(\delta \to 0)$, as this factor also appears in the partition function denominator of (2.2). For $N = N_p+n$, as n increases from 3 towards n_p, the degeneracy of the ground-state and importantly the typical number of kinks decreases. Correspondingly, $D_N(\delta t \to 0)$ also decreases with increasing $n = 3, 4, ...$ Finally, comparing the above analysis for perfect and facile clusters shows that $D_N(\delta t \to 0)$ for perfect clusters is smaller roughly by a Boltzmann factor of $\exp[-\phi/(k_BT)]$ than for facile clusters.

2.5.2 Further analysis of back correlation

The substantial characteristic time δt_c, associated with the transient short-time diffusion behavior of $D_N(\delta t)$, is evident from Fig. 2.11. These data suggest $h_e\delta t_c \sim 10^5 - 10^6$ $(10^6 - 10^7)$ for $\phi = 0.20$ (0.24eV) at $300K$, at least for nucleation-mediated (NM) cluster diffusion, where the branch with $N = N_p+3$ appears to have a larger δt_c than for $N = N_p+n$ with $n > 3$. This latter feature is confirmed by a suitably rescaled version of Fig. 2.11,

which is shown in Ref. [49]. It is reasonable to expect that for NM diffusion,δt_c should reflect the characteristic time $\delta t_{\rm nuc} = 1/k_{\rm nuc}$ to nucleate a dimer on an outer edge. This implies that $h_e \delta t_c \sim h_e \delta t_{\rm nuc} \sim \exp\left[+2\phi/(k_B T)\right] \sim 10^{6.4}$ $(10^{8.0})$ for $\phi = 0.20$ (0.24eV) at $300K$ with $\delta = 0$. These crude estimates at least roughly reflect those from Fig. 2.11, and also the feature that δt_c increases with ϕ. The larger δt_c for $N = N_p + 3$ plausibly reflects the larger degeneracy of the ground state and the larger typical number of kinks for that cluster size (see Sec. 2.7), which can inhibit nucleation of new outer edges.

For facile clusters with $N = N_p + 1$ or $N = N_p + 2$, Fig. 2.11 perhaps suggests a somewhat shorter δt_c although this is not evident in the further rescaled plots in Ref. [49]. One might expect a shorter δt_c based upon the feature that nucleation is not needed so correspondingly $E_{\rm eff}$ is lower, and the long-time diffusion coefficient is higher. However, other factors, such as the high degeneracy of the ground state (see Sec. 2.7), no doubt play a role in determining δt_c.

As noted previously, assessment of transient behavior in $D_N(\delta t)$ is essential for precise determination of D_N, where precise determination becomes more demanding for longer δt_c. Thus, accurate treatment of the case $N = N_p + 3$ is most demanding, failure to do so leads to a distorted representation of the cyclical behavior of D_N versus N (see Sec. 2.7). Practically, we initially estimate that the plateau in $D_N(\delta t_c)$ is achieved for $\delta t \gg \delta^*$, where $\left\langle [\delta r(\delta t^*)]^2 \right\rangle$ is of the order of a^2 (where δt^* gives a measure of δt_c). The total length of the trajectories used to determine D_N is $t_{\rm max} \sim 35000 \delta t^*$ where data is collected only for $\delta t \gg \delta t^*$. (For reference, choosing $E_e = 0.29 eV$eV and $\nu = 10^{1.25}{\rm s}^{-1}$ for Ag/Ag(100) yields $h_e = 10^{7.6}{\rm s}^{-1}$ at $300K$, and $t_{\rm max} \sim 70000$s for $N = 59$.)

Finally, we elaborate on the interpretation of the decrease of $D_N(\delta t)$ to a plateau value as corresponding to a back correlation in the walk of the cluster. Consider the canonical model of a correlated walk with hops to NN sites on a lattice at total rate h. If $\mathbf{r}_j$ denotes the displacement of the jth hop, then the displacement of the jth hop is correlated to that of previous hops as quantified by $A(k) = \langle \mathbf{r}_j \cdot \mathbf{r}_{j-k} \rangle / \langle \mathbf{r}_1 \cdot \mathbf{r}_1 \rangle$, where $A(k) < 0$ for

back correlation. Here $\langle \mathbf{r}_j \cdot \mathbf{r}_j \rangle / \langle \mathbf{r}_1 \cdot \mathbf{r}_1 \rangle$ for all j. Adapting results for the time-dependent diffusion coefficient $D(\delta t)$ for this system into a continuous-time framework for a large number of hops yields

$$D(\delta t)/D(\delta t \to 0) = 1 + 2 \int_{0 \le u \le h\delta t} du\, A(u), \text{ so that}$$
$$A(h\delta t) = \frac{1}{2} d/ds \left[D(s)/D(0) \right] |_{s=h\delta t}, \tag{2.3}$$

Note that the magnitude of cumulative (integrated) correlation is strictly bounded by 1/2 in this formulation. Clearly, the decrease in $D_N(\delta t)$ with increasing δt shown in Fig. 2.11 corresponds to back-correlation $D_N(\delta t)$. One could extract an effective $A(u) < 0$ from the form of $A(u)$ after assigning an effective total hop rate.

2.6 Further Analysis of Diffusivity via Configuration Counting

Deeper insight into the diverse aspects of cluster diffusion behavior described in Sec. 2.4 follows from exploiting results of a combinatorial analysis of cluster configurations corresponding to ground states and first excited states. This nontrivial analysis utilizes results related to (number theoretic) partitions of integers. Details are relegated to Appendix C.

2.6.1 Anomalous scaling for facile clusters

As noted in Sec. 2.4, for facile $N_p + 1$ clusters, one finds initially high values and rapid decay of $D_N \sim N^{-\beta f}$ with large $\beta_f \approx 2.3$ ($\beta_f \approx 2.6$) up to $N \sim 82$ (101) for $\phi = 0.20$ (0.24) eV at $300K$. These exponent values are far larger than any reported in previous studies. To elucidate this behavior, recall that long-range diffusion requires that the cluster repeatedly passes through a special configuration with one edge atom on a perfect core. We suggest that the behavior of D_N reflects the possibility to wander through a large number of isoenergetic ground-state configurations far removed from the special configuration, where the number $\Omega_N(0)$ of these states increases rapidly with increasing N. After the system leaves the special configuration, let t_{ret} denote the mean-time for the system to return, where

Table 2.1: Number of isoenergetic ground-state configurations $\Omega_N(0)$ and restricted isoenergetic configurations $\Omega^*_N(0)$ for $N = L^2 + 1$.

$N = L^2 + 1$	10	17	26	37	50	65	82	101
$\Omega_N(0)$	28	80	210	504	1148	2480	5160	10360
$\Omega^*_N(0)$	28	80	202	464	988	1976	3748	6792

one expects that $D_N \sim a^2/t_{\rm ret}$. A key result of Montroll and Weiss [50] for regular lattices is that this return time is directly proportional to the size of the system, independent of dimension. This in turn suggests that $D_N \sim a^2 h_c/\Omega_N(0)$. The results presented in Table 2.1 indicate that $\Omega_N(0) \sim N^\alpha$ with $\alpha \approx 2.6$ up to $N \sim 100$, reasonably consistent with the above large β_f values (see Appendix C).

For another perspective, note that all isoenergetic states have equal population. Thus the probability $P_{\rm ret}$ that the system is in a ground state, which can directly transition to (or "return to") the special configuration, scales like $P_textret \sim 1/Omega(0)$. Then, we claim that $D_N \sim a^2 h_c P_{\rm ret}$, which recovers the above result.

The exact behavior of D_N actually depends not just on the number of isoenergetic configurations, but on their connectivity to the special configuration [30,32]. Presumably, configurations more closely connected to the special configuration should play a more significant role. This motivates analysis of the number $\Omega^*_N(0)$ of restricted isoenergetic configurations where starting from the special configuration, additional atoms are shifted to the edge with the isolated atom from just the outermost layer of the other edges. Analysis of $\Omega^*_N(0)$ data also in Table I produces a modified exponent of $\alpha \approx 2.4$, again reasonably consistent with the β_f values.

2.6.2 Intermingling of perfect and facile branches

While D_N for facile clusters decreases strongly with N for moderate sizes, the variation of D_N for perfect clusters is extremely weak. The latter behavior reflects the feature that diffusion of perfect clusters is largely controlled by the nucleation step, which depends

weakly on N, and not so much on the subsequent transfer of atoms to complete the new edge. Thus the D_N in the facile branch, which are large for smaller sizes but rapidly decreasing naturally meet and "intermingle" with the D_N of the perfect branch, which are lower for small sizes but slowly decreasing. Since D_N for the $N_p + 3$ branch are even lower than for perfect clusters and decrease with increasing N, this branch remains separate from the facile and perfect clusters at the point of intermingling.

The distinction between perfect clusters and facile (or other) classes of clusters is predicated on the feature that the former primarily exist in their ground states. However, perfect N_p clusters would have a significant probability of being in the first excited state when $\Omega_{N_p}(1)/\Omega_{N_p}(0) \approx \Omega_{N_p}(1) \approx \exp[\phi/(k_B T)]$, where again $\Omega_N(n)$ gives the number of isoconfigurations for the nth excited state for a cluster of size N, and $\Omega_{N_p}(0) = 1$. Results for $\Omega_{N_p}(1)$ determined from combinatorial analysis in Appendix C are reported in Table 2.2. For $\phi = 0.20$eV (0.24eV)), the Boltzmann factor $\exp[\phi/(k_B T)]$ 2290 (10730), and thus intermingling perfect and facile branches should occur around $N = N_{\text{mingle}} \sim 49$ (81). This prediction is consistent with the behavior shown in Fig. 2.13 where N_{mingle} is indicated by a dashed vertical line. Note that D_N for perfect (facile) clusters decreases more quickly (slowly) after intermingling.

Table 2.2: Values of $\Omega_{N_p}(1)$ for $N_p = L^2$.

$N = L^2$	26	36	49	64	81	100
$\Omega_{N_p}(1)$	496	1140	2472	5152	10352	20208

2.6.3 Mingling of all branches of cluster diffusivity

As noted above, the feature that D_N for the $N_p + 3$ branch are lower than those for perfect clusters and also that they decrease slowly with N delays merging with the perfect and facile branches. It is appropriate to note that while both N_p+1 and N_p+3 branches have a high ground-state degeneracy, this only produces strong size dependence of D_N for the former. Why? Long-range diffusion of clusters for sizes $N_p + 3$ does not require repeatedly

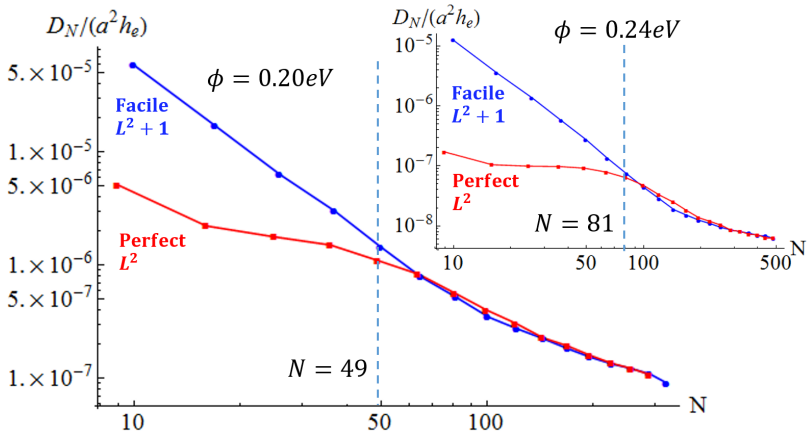

Figure 2.13: The intermingling sizes of L^2 and L^2+1 branches predicted with thermodynamics for $\phi = 0.20$eV (inset: $\phi = 0.24$eV) with $\delta = 0$ at $300K$.

passing through a single special configuration, unlike for $N_p + 1$. Thus the strong increase in the number of ground states with increasing N does not induce a strong reduction in D_N for $N + N_p + 3$.

Analogous to our assessment of intermingling and perfect branches, here we argue that the distinctive nature of $N_p + 3$ clusters (relative to $N_p + 1$) is lost when the ratio of the number of the first excited states $\Omega_{N_p+3}(1)$ to the number of ground states $\Omega_{N_p+3}(0)$ satisfies $\Omega_{N_p+3}(1)/\Omega_{N_p+3}(0) \approx \exp[\phi/(k_BT)]$. The method to count the number of isoenergetic states, $\Omega_{N_p+3}(1)$, $\Omega_{N_p+3}(0)$ is the same as that of counting $\Omega_{N_p}(1)$. Relevant results are presented in Table 2.3 (see Appendix C for details). The predicted sizes for merging, $N = N_{\text{merge}} \approx 199$ (403) for $\phi = 0.20$eV ($\phi = 0.24$eV), are indicated by dashed vertical lines in Fig. 2.14.

Table 2.3: Values of $\Omega_{N_p+3}(0)$, $\Omega_{N_p+3}(1)$ and the ratio $\Omega_{N_p+3}(1)/\Omega_{N_p+3}(0)$ for $N_p = L^2+3$.

$N = L^2+3$	147	172	199	327	364	403
$\Omega_{N_p+3}(0)$	10360	20216	38416	407968	706034	1.20×10^6
$\Omega_{N_p+3}(1)$	1.53×10^7	3.95×10^7	9.86×10^7	2.86×10^9	6.25×10^9	1.34×10^10
$\frac{\Omega_{N_p+3}(1)}{\Omega_{N_p+3}(0)}$	1475	1955	2565	7002	8847	11116

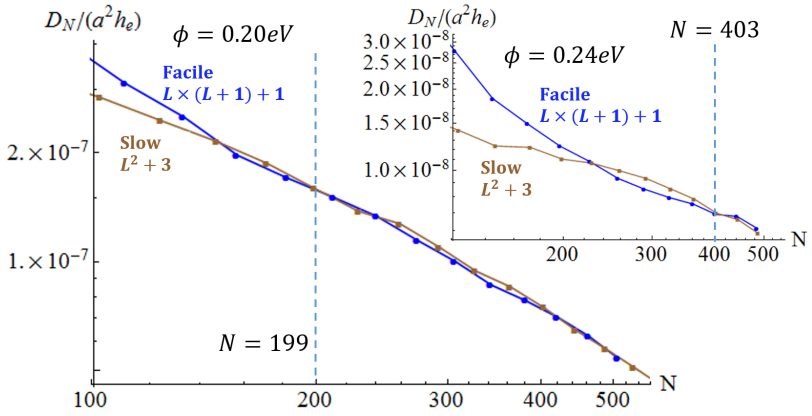

Figure 2.14: The intermingling sizes of L^2+3 and $L\times(L+1)$ branches predicted with thermodynamics for $\phi = 0.20$eV (inset: $\phi = 0.24$eV) with $\delta = 0$ at $300K$.

2.6.4 Analysis of the cyclical variation of cluster diffusivity

It is clear from Fig. 2.5 that D_N actually increases with increasing size $N = N_p + n$, within each cycle $n = 3, 4, 5, ..., n_{\max}$, where $n_{\max} = L$ for $N_p = L^2$ or $(L-1)L$ recovers a perfect cluster. A local minimum (maximum) in D_N occurs for the $n = 3$ ($n = n_{\max}+1$). We suggest that the key feature controlling this behavior is a strong decrease with increasing n in the degeneracy of the ground state from a maximum for $n = 3$ to a minimum for $n = n_{\max}$. The minimum is 1 for $N_p = L^2$, and 4 for $N_p = (L-1)L$. A larger number of degenerate ground states means a higher probability that the cluster is in a configuration with multiple atoms removed from the corners and thus many kink sites which can trap diffusing edge atoms. This makes nucleation of a new outer edge more difficult, as the lifetime of isolated atoms is reduced). Many kinks also inhibit transfer atoms to complete that new outer edge. Consequently, D_{N_p+n} increases with increasing n. We remark that oscillations in D_N versus N were observed in previous simulation studies [7,9]. However, the analysis was limited [9], e.g., perhaps giving a misimpression that perfect clusters $N = N_p$ diffuse slowest, and not recognizing that $N = N_p + 2$ (as well as $N_p + 1$) are facile.

Finally, we emphasize the substantial computational challenge in obtaining precise values for D_N particularly for $N = N_p + 3$ or $N_p + 4$. This is evident from Fig. 2.11 where one

must sample over substantially longer time intervals δt to obtain the correct asymptotic value of D_N. Lack of precision in analysis fails to produce the correct trend in D_N within each cycle. To illustrate this issue, in Fig. 2.15, we present results obtained for $D_N(\delta t$ with a small $h_e\delta t = 811$ and with a large $h_e\delta t = 12970$ for $\phi = 0.20$eV and $\delta = 0$ at $300K$ (both well below $h_e\delta t_c = 10^5 - 10^6$). Even the latter is insufficiently large to recover the correct asymptotic behavior. Such analysis gives the misimpression that the slowest diffusion occurs not for $N = N_p + n$ with $n = 3$, but for somewhat larger n.

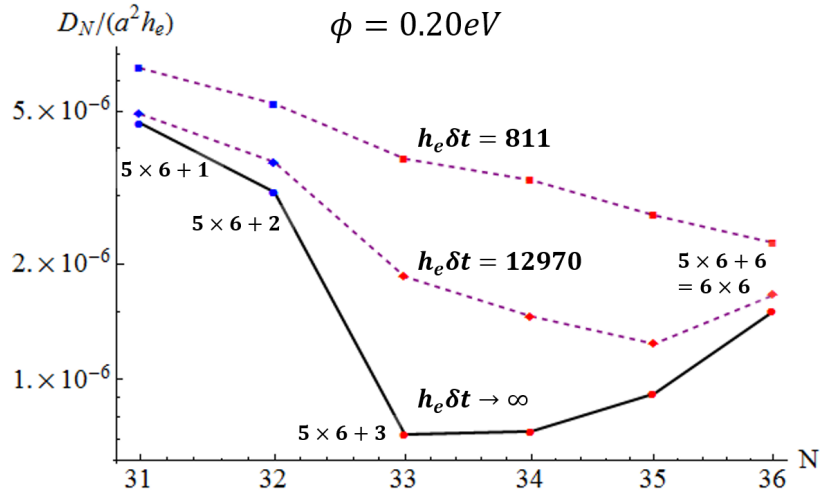

Figure 2.15: Illustration of analysis with diffusion coefficients not converged for $\phi = 0.20$eV with $\delta = 0$ at $300K$ for $31 \le N \le 36$.

2.7 Conclusions

Our precise KMC analysis of a tailored but effective model for cluster diffusion on metal (100) surfaces has revealed extraordinarily diverse behavior particularly for the regime of moderates sizes $9 \le N \le O(10^2)$. Perhaps unexpectedly, the slowest diffusion does not occur for perfect sizes $N = N_p = L^2$ or $L(L+1)$ with unique square or near-square ground-state shapes, but rather for $N = N_p + 3$. However, the slowest short-time diffusivity does occur for perfect sizes. We are able to elucidate the distinct behavior of different branches (facile, perfect, and slow) in this regime, exploiting combinatorial analysis of the number of

ground states, first excited states, etc.

Also of interest is the intermingling and merging of these branches for larger N. Combinatorial analysis was also utilized to provide insight into the intermingling and merging points essentially by determining at what cluster size thermal fluctuations or excitations smeared the distinction between various branches. As an aside, we note that another way to assess merging is based on the realization that the effective Arrhenius energy $E_{\rm eff}$ for cluster diffusion adopts a higher value, $E_{\rm eff} = E_e + 2\phi + \delta$, for nucleation-mediated diffusion for moderate sizes than in the asymptotic regime of large sizes where $E_{\rm eff} = E_e + \phi + \delta$. We have checked that for nucleation-mediated diffusion, the effective value of $E_{\rm eff}$ decreases with increasing N and is reduced to about $E_{\rm eff} = E_e + 1.5\phi + \delta$ at the point where merging occurs (see Ref. [49]).

We have not presented a comparison with experimental data. However, our results are particularly valuable in revealing the complexity of behavior for moderate sizes and the potential shortcomings in extracting size scaling exponents from data over a limited size range. We plan to apply our modeling to analyze the behavior for Ag clusters on Ag(100) where recent experimental analysis [3] has suggested somewhat lower exponent values from those determined previously [2] (but where in both cases the exponent is significantly below the classic value of $\beta = 3/2$). Also, with regard to experiment, we note that facile clusters of size $N = N_p + 1$ should be susceptible to dissociation of the isolated edge atom in the special ground-state configuration with this atom and a perfect core. However, this is only one of many isoenergetic ground states for larger N reducing this likelihood. For $N = N_p + 2$, there are no isolated edge atoms in the ground state, so this issue does not arise.

Finally, we note that basic features of results from our modeling should be more general than for cluster diffusion on metal (100) surfaces. Similar behavior is expected for metal (111) surfaces. The surprising feature that perfect clusters do not have the lowest diffusivity may even extend to supported 3D clusters. However, there are certainly other fundamental issues that remain to be addressed. For example, the degeneracy of the ground state

is important in explaining various basic features of behavior. However, if one includes more lateral adatom interactions, degeneracies can be broken, so how does this change the behavior from that of our basic model?

2.8 Acknowledgments

K.C.L. and J.W.E. were supported for this work by NSF grant CHE-1507223. They performed detailed KMC analysis and developed theoretical interpretations of the data. D.J.L. was supported by the USDOE, Office of Science, Basic Energy Sciences, Division of Chemical Sciences, Geosciences, and Biological Sciences, and his work was performed at Ames Laboratory which is operated by Iowa State University for the USDOE under Contract No. DE-AC02-07CH11358. He performed the exploratory KMC simulations revealing diverse behavior together with preliminary analysis.

2.9 Appendix A: Exact Analysis for the Small Cluster Size Regime $N < 9$

Exploiting the exact master equation analysis discussed in the text, for dimers with two linear configurations (rotated by 90^o), one finds that [32]

$$D_2 = D_2(\delta t) = (a^2/2)h_r \text{ so } E_{\text{eff}} = E_e + \delta, \tag{2.4}$$

For trimers with six distinct configurations (two linear and four bent), $D_3(\delta t)$ generally decreases with increasing δt to its asymptotic value [32]

$$D_3 = (a^2/3)h_r h_e/(h_r + h_e) \text{ so } 1/D_3 = 3a^{-2}(1/h_r + 1/h_e). \tag{2.5}$$

The latter expression confirms the obvious feature that both edge diffusion and corner rounding are required for long-range diffusion. In this case, one does not in general have perfect Arrhenius behavior except for $\delta = 0$, where $E_{\text{eff}} = E_e$. However, in practice, for typical nonzero δ, one has that $E_{\text{eff}} = E_e + \delta$. For tetramers with 19 distinct configurations,

$D_4(\delta t)$ generally decreases with increasing δt to its asymptotic value

$$D_4 = h_c h_r \left[6(h_e)^3 + 38(h_e)^2 h_r + 35 h_e (h_r)^2 + 6(h_r)^3\right] / \left\{(18h_c + h_r)\left[(h_e)^3 + 10(h_e)^2 h_r + 24 h_e (h_r)^2 + 9(h_r)^3\right]\right\}. \quad (2.6)$$

As expected, this result shows that core breakup is essential for long-range cluster diffusion. For typical values of parameters with nonzero δ, the effective barrier is given by $E_{\text{eff}} = E_e + \phi + \delta$.

Previous analysis [32] also exploited the possibility of simplified (dimensionally reduced) analysis in the limit as $h_e \to \infty$ where various configurations convert infinitely quickly between each other and may be grouped into a smaller set of quasiconfigurations. For the trimer, there are two quasiconfigurations (two linear and a single quasibent configuration), and the above result reduces to $D_2 = (a^2/3)/h_r$. For tetramers, there are five quasiconfigurations, and the above result reduces to

$$D_4 = 6a^2 h_c h_r/(18h_c + h_r), \text{ so that}$$
$$1/D_4 = (a^{-2}/6)(1/h_c + 18/h_r) \quad (2.7)$$

Results are also available for pentamers.

2.10 Appendix B: Estimating the Number of Kinks n_k in Cluster Configurations

Here, we obtain bounds on the number of kinks n_k for various cluster configurations. The lower bound can readily be determined for specific cases, and is $O(1)$. Thus we focus on estimating the upper bound in this section. First, consider removing m_1 atoms from a single corner of an otherwise perfect rectangular cluster. The number of kinks n_k is maximized if the atoms are removed to create a vacancy region as close as possible to a triangle with a 45^o diagonal (corresponding to a perfect staircase of kinks each of height a). This can be achieved exactly if $m_1 = 1+2+...+(n_k-1) = \frac{1}{2}n_k(n_k-1)$, so that $n_k = (1+\sqrt{1+8m_1})/2$.

Next, consider removing m_i atoms from the ith corner of a perfect rectangular cluster where $m_1+m_2+m_3+m_4 = m$, and where m is less than either side length of the rectangle. Then, since the above expression for n_k with atoms removed from a single corner increases sublinearly with m_1, it follows that the total number of kinks can be maximized by removing roughly equal numbers of kinks from all corners, i.e., $m_1 \approx m_2 \approx m_3 \approx m_4 \approx m/4$. Consequently, for an upper bound on the total number of kinks n_k, we replace m_1 by $m/4$ in the above expression and multiply by 4 to obtain $n_k \leq 2(1+\sqrt{1+2m})$. Considering the quantities relevant for the analysis of Sec. 2.4, we have that $m = L$ for $n_{L^2,k}(1)$, $m = L-1$ for $n_{L^2+1,k}(0)$, and $m = L-3$ for $n_{L^2+3,k}(0)$.

2.11 Appendix C: Counting of Isoenergetic Cluster Configurations

In our representation of clusters as collections of atoms, themselves represented as contiguous red squares, the energy of the cluster corresponds to its perimeter length. Consider the cluster shapes that are obtained by starting with a fully populated rectangle and then removing atoms from each corner of the cluster to form a simple "staircase" (i.e., steps at each corner are of one sign, not both). Then, the energy of these configurations is determined exactly by the perimeter length of the smallest rectangle inscribing these clusters (which corresponds to the original rectangle from which atoms were removed). This follows since the perimeter length of the inscribing rectangle and the actual cluster are equal. These observations will be useful in the following analysis.

First, we consider ground-state configurations, which have the minimum perimeter length for the prescribed number, N, of atoms. For ground states, the inscribing rectangle is either a $L_i \times L_i$ square of occupied sites, or a near-square $L_i \times (L_i+1)$ or $L_i \times (L_i+2)$ rectangle. The unique ground state for $N = L^2$ is inscribed by a square with $L_i = L$. The ground states for $N = L^2+m$ with $1 \leq m \leq L$ are inscribed by a $L_i \times (L_i+1)$ rectangle with $L_i = L$. The ground states for $N = L(L+1)$ with $1 \leq m \leq L$ are inscribed by $L_i \times L_i$ squares with $L_i = L+1$ or by $L_i \times (L_i+2)$ rectangles with $L_i = L$. Next, we consider nth

excited state configurations where the perimeter length of the cluster is increased relative to the ground state by an amount $2n$ (in units of lattice constant $a = 1$). Thus the size of the inscribing rectangle must also be increased. Specifically, the side lengths are increased by amounts n_x and n_y, where $n_x + n_y = n$ to achieve the desired perimeter length.

Thus, to evaluate the number of convex isoenergetic nth excited state configurations of a size N cluster $\Omega_N(n)$, first, one determines the different possible inscribing rectangles for the ground states. Second, one expands the side lengths of these rectangles by amounts n_x and n_y, where $n_x + n_y = n$. Third, regarding all sites in this larger inscribing rectangle as initially populated, one considers all possible ways to remove the appropriate number of atoms from the four corners of the rectangle (making sure the cluster is touching all four edges of the rectangular frame), until the final number of atoms matches the cluster size N, which we are targeting. It is instructive to provide a few examples: (i) determination of $\Omega_{L^2+3}(0)$ requires counting different possible ways to remove $L-3$ atoms from an $L\times(L+1)$ inscribing rectangle; (ii) determination of $\Omega_{L^2}(1)$ requires counting different possible ways to remove L atoms from an $L \times (L + 1)$ inscribing rectangle; and (iii) determination of $\Omega_{L^2+3}(1)$ requires counting different possible ways to remove $L - 3$ atoms from $L \times (L + 2)$ and $(L + 1) \times (L + 1)$ inscribing rectangles.

Now, we describe in detail a systematic procedure to count the number of ways of removing the appropriate number of atoms from the inscribing rectangle. We start by considering removal of m_1 atoms from one fully populated corner. The number of possibilities is identical to the number of Young or Ferrers diagrams that represents integer partition of m_1. In number theory, this integer partition is traditionally denoted by $P(m_1)$ [51]. An example for $P(m_1 = 4) = 5$ is shown in Fig. 2.16.

Next, we address the more complex challenge of counting the total number of configurations of the cluster, where one removes m_1, m_2, m_3 and m_4 atoms from each of the four corners of the inscribing rectangle, respectively, for a total of m atoms where $m = m_1 + m_2 + m_3 + m_4$. One constraint with this analysis is that removal of atoms from

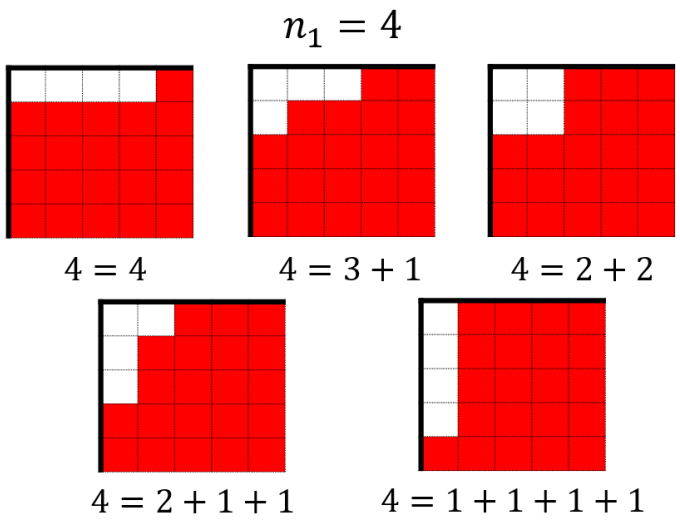

Figure 2.16: Number $P(m_1 = 4) = 5$ of possible ways to remove $m_1 = 4$ atoms from a corner illustrated by Ferrers diagrams. Partitions of 4 into strings of integers indicate the number of atoms removed from each row starting with the top row.

one corner does not interfere with removal from other corners, which requires that m is no larger than the side lengths of the inscribing rectangle. (We will comment further below on cases where this condition is not satisfied.) Subject to this constraint, the total number of configurations comes from considering the product of the corresponding integer partions, and then summing over all possible choices of m_i consistent with the constraint on the sum (and finally adjusting for any overcounting).

An example for $\Omega_{L^2}(1)$ is shown below where $m = L$ atoms are removed from an inscribing $L \times (L+1)$ rectangle.

Here, one has

$$\begin{aligned}\Omega_{L^2}(1) &= 2 \times \sum_{m_1+m_2+m_3+m_4} P(m_1)P(m_2)P(m_3)P(m_4) - (\text{over counting}) \\ &= 2 \times \sum_{m_L=0}^{L} \left[\sum_{m_l=0}^{m_L} P(m_l)P(m_L - m_l) \sum_{m_r=0}^{L=m_L} P(L - m_L - m_r) \right] \\ &\quad - (\text{over counting}).\end{aligned} \tag{2.8}$$

In the second sum, $m_L(m_R)$ gives the total number of atoms removed from the left (right) side on the inscribing rectangle, and $m_l(m_r)$ give the number of atoms removed from one corner on the left (right) side. The factor of 2 comes from a 90° rotation of the $L \times (L+1)$ rectangle, correponding to another set of discrete states. Note that "overcounting" in (2.8) includes the ground state being counted four times ($m_L = L$ and $m_l = 0$ or L) or ($m_L = 0$ and $m_r = 0$ or L). If one wishes to consider just first excited states without any monomers, then it is also necessary to subtract $4 \times (4L-2)$ states where an atom is shifted from a corner of the $L \times L$ ground-state configuration and placed on a side. One must also subtract $4L$ configurations with a monomer on the edge of a completely populated $(L-1) \times (L+1)$ rectangle.

In addition, we have analyzed $\Omega_{L^2+1}(0)$ and $\Omega_{L^2+3}(0)$, where $L-1$ and $L-3$ atoms are removed from an $L \times (L+1)$ inscribing rectangle, respectively. In these cases, the procedure described above is directly applicable. Finally, we have also analyzed $\Omega_{L^2+3}(1)$, where $2L-3$ atoms are removed from $L \times (L+2)$ or $(L+1) \times (L+1)$ inscribing rectangles. In this case, since the number of removed atoms significantly exceeds side lengths of the inscribing rectangle, significant modification is required from the formulation (2.8) used to obtain $\Omega_{L^2}(1)$ and other quantities mentioned above.

Results reported in the text for $\Omega_{L^2}(1)$, $\Omega_{L^2+1}(0)$, and $\Omega_{L^2+3}(0)$ include all states, i.e., those with monomers and those without. (See Ref. [49] for corresponding results excluding states with monomers.)

2.12 Appendix D: Counting of Excited State Configurations with One Monomer

In Sec. 2.5, we estimated number of configurations, $\Omega'_N(n)$, of clusters with N atoms corresponding to nth excited state, which include a single monomer. In some cases, this analysis was simple, e.g.,$\Omega'_{L^2+1}(0) = 4L$. However, analysis of other cases including $\Omega'_{L^2}(2)$ and $\Omega'_{L^2+1}(1)$ is nontrivial, and is thus described in more detailed below.

To estimate $\Omega'_N(n)$, we first remove the monomer, and then count the number of states $\Omega_{N-1}(n-1 \text{ or } n)$, where the appropriate choice is discussed below. For the latter, we utilize the scheme introduced in Appendix C. Next, let n_f denote the number of empty edge sites n_f with only one neighbor, which could thus accommodate a monomer. Then, it follows that

$$\Omega'_N(n) = n_f \times \Omega_{N-1}(n-1 \text{ or } n) \tag{2.9}$$

To determine n_f, we note that each kink roughly contributes two units of perimeter; it follows that the total perimeter length for clusters of size $N-1$ in the $(n-1)$th excited state is given by the sum $n_f + 2n_{N-1,k}(n-1)$, where $n_{N-1,k}(n-1)$ denotes the number of kinks in these clusters (see Appendix B).

To determine $\Omega'_{L^2}(2)$, we note that first excited states for clusters of size $N = L^2$ have configurations within a $L \times (L+1)$ inscribing rectangle. For second excited states with a single monomer, this monomer is located at the perimeter of a cluster of size $L^2 - 1$ with no monomers, but still with an $L \times (L+1)$ inscribing rectangle and which thus corresponds to a first excited state (see Fig. 2.17 for an example). Thus, one has that

$$\Omega'_{L^2}(2) \approx \Omega_{L^2-1}(1) \left[4L + 2 - 2n_{L^2-1,k}(1)\right]. \tag{2.10}$$

To determine $\Omega'_{L^2+1}(1)$, we note that ground states for clusters with size $N = L^2 + 1$ have configurations within a $L \times (L+1)$ inscribing rectangle. For first excited states with a single monomer, this monomer is located at the perimeter of a cluster of size L^2 with no monomers, but still with an $L \times (L+1)$ inscribing rectangle. The latter thus also corresponds to a first excited state. In conclusion, one has that

$$\Omega'_{L^2+1}(1) \approx \Omega_{L^2}(1) \left[4L + 2 - 2n_{L^2,k}(1)\right]. \tag{2.11}$$

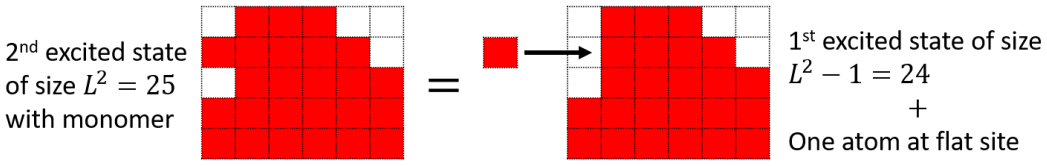

Figure 2.17: Example of an excited state with one monomer.

2.13 Supplementary Material

The Supplementary Material file contains plots with additional results from KMC simulations augmenting the main results presented in the text, details of our combinatorial analysis, and also table of values of diffusion coefficients.

Bibliography

[1] J.-M. Wen, S.-L. Chang, J. W. Burnett, J. W. Evans, and P. A. Thiel. Diffusion of Large Two-Dimensional Ag Clusters on Ag(100). *Phys. Rev. Lett.*, 73(19):2591–2594, 1994.

[2] Woei Wu Pai, Anna K. Swan, Zhenyu Zhang, and J. F. Wendelken. Island Diffusion and Coarsening on Metal (100) Surfaces. *Phys. Rev. Lett.*, 79(17):3210–3213, 1997.

[3] Xin Ge and Karina Morgenstern. Ehrlich-Schwoebel barrier and interface-limited decay in island kinetics on Ag(100). *Phys. Rev. B*, 85(4):045417, 2012.

[4] David S. Sholl and Rex. T. Skodje. Diffusion of Clusters of Atoms and Vacancies on Surfaces and the Dynamics of Diffusion-Driven Coarsening. *Phys. Rev. Lett.*, 75(17):3158–3161, 1995.

[5] Clinton DeW. Van Siclen. Single Jump Mechanisms for Large Cluster Diffusion on Metal Surfaces. *Phys. Rev. Lett.*, 75(8):1574–1577, 1995.

[6] José M. Soler. Cluster diffusion by evaporation-condensation. *Phys. Rev. B*, 53(16):R10540(R)–R10543, 1996.

[7] K. A. Fichthorn and S. Pal. *Bull. Am. Phys. Soc.*, 43:850, 1998.

[8] Alexander Bogicevic, Shudun Liu, Joachim Jacobsen, Bengt Lundqvist, and Horia Metiu. Island migration caused by the motion of the atoms at the border: Size and temperature dependence of the diffusion coefficient. *Phys. Rev. B*, 57(16):R9459(R)–R9462, 1998.

[9] J. Heinonen, I. Koponen, J. Merikoski, and T. Ala-Nissila. Island Diffusion on Metal fcc (100) Surfaces. *Phys. Rev. Lett.*, 82(13):2733–2736, 1999.

[10] Greg Mills, Thomas R. Mattsson, Lone Møllnitz, and Horia Metiu. Simulations of mobility and evaporation rate of adsorbate islands on solid surfaces. *J. Chem. Phys.*, 111(18):8639–8650, 1999.

[11] Alan Lo and Rex T. Skodje. Diffusion and evaporation kinetics of large islands and vacancies on surfaces. *J. Chem. Phys.*, 111(6):2726–2734, 1999.

[12] Hongxiao Shao, Shudun Liu, and Horia Metiu. Evolution to equilibrium of the shape of an island formed by the aggregation of adsorbed atoms. *Phys. Rev. B*, 51(12):7827–7833, 1995.

[13] Shudun Liu and Horia Metiu. A kinetic model for island shape variations under epitaxial growth conditions. *Surf. Sci.*, 405(2):L497–L502, 1998.

[14] C. R. Stoldt, A. M. Cadilhe, C. J. Jenks, J.-M. Wen, J. W. Evans, and P. A. Thiel. Evolution of Far-From-Equilibrium Nanostructures Formed by Cluster-Step and Cluster-Cluster Coalescence in Metal Films. *Phys. Rev. Lett.*, 81(14):2950–2953, 1998.

[15] P. Jensen, N. Combe, H. Larralde, J. L. Barrat, C. Misbah, and A. Pimpinelli. Kinetics of shape equilibration for two dimensional islands. *Eur. Phys. J. B*, 11(3):497–504, 1999.

[16] Nicolas Combe and Hernán Larralde. Low-temperature shape relaxation of two-dimensional islands by edge diffusion. *Phys. Rev. B*, 62(23):16074–16084, 2000.

[17] Da-Jiang Liu and J. W. Evans. Sintering of two-dimensional nanoclusters in metal(100) homoepitaxial systems: Deviations from predictions of Mullins continuum theory. *Phys. Rev. B*, 66(16):165407, 2002.

[18] José L. Iguain and Laurent J. Lewis. Relaxation kinetics in two-dimensional structures. *Phys. Rev. B*, 68(19):195407, 2003.

[19] Yong Han, Conrad R. Stoldt, Patricia A. Thiel, and James W. Evans. Ab Initio Thermodynamics and Kinetics for Coalescence of Two-Dimensional Nanoislands and Nanopits on Metal (100) Surfaces. *J. Phys. Chem. C*, 120(38):21617–21630, 2016.

[20] Arthur F. Voter. Classically exact overlayer dynamics: Diffusion of rhodium clusters on Rh(100). *Phys. Rev. B*, 34(10):6819–6829, 1986.

[21] Arthur F. Voter. Simulation Of The Layer-Growth Dynamics In Silver Films: Dynamics Of Adatom And Vacancy Clusters On Ag(100). In Michael Ray Jacobson, editor, *Modeling of Optical Thin Films*, volume 0821, pages 214 – 226. International Society for Optics and Photonics, SPIE, 1988.

[22] H. C. Kang, P. A. Thiel, and J. W. Evans. Cluster diffusivity: Structure, correlation, and scaling. *J. Chem. Phys.*, 93(12):9018–9025, 1990.

[23] S. V. Khare, N. C. Bartelt, and T. L. Einstein. Diffusion of Monolayer Adatom and Vacancy Clusters: Langevin Analysis and Monte Carlo Simulations of their Brownian Motion. *Phys. Rev. Lett.*, 75(11):2148–2151, 1995.

[24] S. V. Khare and T. L. Einstein. Unified view of step-edge kinetics and fluctuations. *Phys. Rev. B*, 57(8):4782–4797, 1998.

[25] K. Binder and M. H. Kalos. "Critical clusters" in a supersaturated vapor: Theory and Monte Carlo simulation. *J. Stat. Phys.*, 22(3):363–396, 1980.

[26] M. Rao, M. H. Kalos, J. L. Lebowitz, and J. Marro. Time evolution of a quenched binary alloy. III. Computer simulation of a two-dimensional model system. *Phys. Rev. B*, 13(10):4328–4335, 1976.

[27] G. L. Kellogg. Oscillatory Behavior in the Size Dependence of Cluster Mobility on Metal Surfaces: rh on rh(100). *Phys. Rev. Lett.*, 73(13):1833–1836, 1994.

[28] G. L. Kellogg. Field ion microscope studies of single-atom surface diffusion and cluster nucleation on metal surfaces. *Surf. Sci. Rep.*, 21(1):1–88, 1994.

[29] G. Antczak and G. Ehrlich. *Surface Diffusion: Metals, Metal Atoms, and Clusters.* Cambridge University Press, UK, 2010.

[30] U. M. Titulaer and J. M. Deutch. Some aspects of cluster diffusion on surfaces. *J. Chem. Phys.*, 77(1):472–478, 1982.

[31] Zhu-Pei Shi, Zhenyu Zhang, Anna K. Swan, and John F. Wendelken. Dimer Shearing as a Novel Mechanism for Cluster Diffusion and Dissociation on Metal (100) Surfaces. *Phys. Rev. Lett.*, 76(26):4927–4930, 1996.

[32] J. R. Sanchez and J. W. Evans. Diffusion of small clusters on metal (100) surfaces: Exact master-equation analysis for lattice-gas models. *Phys. Rev. B*, 59(4):3224–3233, 1999.

[33] O. S. Trushin, P. Salo, M. Alatalo, and T. Ala-Nissila. Atomic mechanisms of cluster diffusion on metal fcc(100) surfaces. *Surf. Sci.*, 482-485:365–369, 2001.

[34] Karina Morgenstern, Georg Rosenfeld, Bene Poelsema, and George Comsa. Brownian Motion of Vacancy Islands on Ag(111). *Phys. Rev. Lett.*, 74(11):2058–2061, 1995.

[35] Dietmar C. Schlößer, Karina Morgenstern, Laurens K. Verheij, Georg Rosenfeld, Flemming Besenbacher, and George Comsa. Kinetics of island diffusion on Cu(111) and Ag(111) studied with variable-temperature STM. *Surf. Sci.*, 465(1):19–39, 2000.

[36] Karina Morgenstern, Erik Lægsgaard, and Flemming Besenbacher. Brownian Motion of 2D Vacancy Islands by Adatom Terrace Diffusion. *Phys. Rev. Lett.*, 86(25):5739–5742, 2001.

[37] Christopher Zaum, Michael Rieger, Karsten Reuter, and Karina Morgenstern. Anomalous Scaling in Heteroepitaxial Island Dynamics on Ag(100). *Phys. Rev. Lett.*, 107(4):046101, 2011.

[38] J. C. Hamilton. Magic Size Effects for Heteroepitaxial Island Diffusion. *Phys. Rev. Lett.*, 77(5):885–888, 1996.

[39] O. U. Uche, D. Perez, A. F. Voter, and J. C. Hamilton. Rapid Diffusion of Magic-Size Islands by Combined Glide and Vacancy Mechanism. *Phys. Rev. Lett.*, 103(4):046101, 2009.

[40] Altaf Karim, Abdelkader Kara, Oleg Trushin, and Talat S. Rahman. The crossover from collective motion to periphery diffusion for two-dimensional adatom-islands on Cu(111). *J. Phys.: Condens. Matter*, 23(46):462201, 2011.

[41] Shree Ram Acharya, Syed Islamuddin Shah, and Talat S. Rahman. Diffusion of small Cu islands on the Ni(111) surface: A self-learning kinetic Monte Carlo study. *Surf. Sci.*, 662:42–58, 2017.

[42] J. Krug, H. T. Dobbs, and S. Majaniemi. Adatom mobility for the solid-on-solid model. *Z. Phys. B: Condens. Matter*, 97(2):281–291, 1995.

[43] Da-Jiang Liu, CR Stoldt, Patricia A Thiel, and James W Evans. Sintering of metal (100) homoepitaxial islands: Kink rounding barriers, modified size scaling, and experimental behavior. *MRS Online Proceedings Library Archive*, 749, 2003.

[44] Hyeong-Chai Jeong and Ellen D. Williams. Steps on surfaces: experiment and theory. *Surf. Sci. Rep.*, 34(6):171–294, 1999.

[45] O. Pierre-Louis. Continuum Model for Low Temperature Relaxation of Crystal Steps. *Phys. Rev. Lett.*, 87(10):106104, 2001.

[46] M. Eßer, K. Morgenstern, G. Rosenfeld, and G. Comsa. Dynamics of vacancy island coalescence on Ag(111). *Surf. Sci.*, 402-404:341–345, 1998.

[47] King C. Lai, James W. Evans, and Da-Jiang Liu. Communication: Diverse nanoscale cluster dynamics: Diffusion of 2D epitaxial clusters. *J. Chem. Phys.*, 147(20):201101, 2017.

[48] For $\phi = 0.24$eV at $300K$, we also find that $\beta_s = 0.37$ for $45 \leq N \leq 103$ when $\delta = 0.1$ (versus $\beta_s = 0.55$ for $67 \leq N \leq 200$ for $\delta = 0$).

[49] See Supplemental Material at http://link.aps.org/supplemental/10.1103/PhysRevB.96.235406 for further analysis of time-dependent diffusivity, of Arrhenius behavior of D_N, and for tabulated D_N values.

[50] Elliott W. Montroll and George H. Weiss. Random Walks on Lattices. II. *Journal of Mathematical Physics*, 6(2):167–181, 1965.

[51] George E Andrews and Kimmo Eriksson. *Integer partitions*. Cambridge University Press, 2004.

CHAPTER 3. MODELING OF DIFFUSIVITY FOR 2D VACANCY NANOPITS AND COMPARISON WITH 2D ADATOM NANOISLANDS ON METAL(100) SURFACES INCLUDING ANALYSIS FOR AG(100)

A paper published in *Journal of Physical Chemistry C*

King Chun Lai[1,2], Da-Jiang Liu[2], Patricia A. Thiel[2,3,4], James W. Evans[1,2,5]

[1]*Department of Physics and Astronomy, Iowa State University, Ames, Iowa 50011, USA*

[2]*Ames Laboratory-USDOE, Iowa State University, Ames, Iowa 50011, USA*

[3]*Department of Chemistry, Iowa State University, Ames, Iowa 50011, USA*

[4]*Department of Materials Science & Engineering, Iowa State University, Ames, Iowa 50011, USA*

[5]*Department of Mathematics, Iowa State University, Ames, Iowa 50011, USA*

(Received 20 December 2017; published 1 May 2018)

Abstract

Diffusion coefficients, D_N, for 2D vacancy nanopits are compared with those for 2D homoepitaxial adatom nanoislands on metal(100) surfaces, focusing on the variation of D_N with size, N. Here, N is measured in missing atoms for pits and adatoms for islands. Analysis of D_N is based on kinetic Monte Carlo simulations of a tailored stochastic lattice-gas model, where pit and island diffusion are mediated by periphery diffusion, i.e., by edge atom hopping. Precise determination of D_N versus N for typical parameters reveals a

cyclical variation with an overall decrease in magnitude for increasing moderate $O(10^2) \leq N \leq O(10^3)$. Monotonic decay, $D_N \sim N^{-\beta}$, is found for $N \geq O(10^2)$ with effective exponents, $\beta = \beta_{\text{eff}}$, for both pits and islands, both well below the macroscopic value of $\beta_{\text{macro}} = 3/2$. D_N values for vacancy pits are significantly lower (higher) than for adatom islands for moderate N in the case of low (high) kink rounding barrier. However, D_N values for pits and islands slowly merge, and $\beta_{\text{eff}} \to 3/2$ for sufficiently large N. The latter feature is expected from continuum Langevin formulations appropriate for large sizes. We compare predictions from our model incorporating appropriate energetic parameters for Ag(100) with different sets of experimental data for diffusivity at $300K$, including assessment of β_{eff}, for experimentally observed sizes N from ~ 100 to ~ 1000.

DOI: 10.1021/acs.jpcc.7b12527

3.1 Introduction

Scanning tunneling microscopy (STM) studies going back to the mid-1990s of the diffusion of large single-layer-high homoepitaxial adatom islands on metal(100) surfaces [1–4] have received extensive attention. We refer to these islands as two-dimensional (2D). The experimental studies prompted numerous theoretical analyses [5–9] which supplemented limited earlier studies. [10, 11] However, relatively little attention has been paid to the corresponding behavior for single-layer-deep 2D vacancy pits for which STM analyses were performed more recently. [12, 13] With reference to either islands or pits as clusters, the default expectation is that cluster diffusion on metal(100) surfaces is mediated by periphery diffusion (PD) of atoms around the edge of the cluster. For both islands and pits, the variation of the diffusion coefficient, D_N, with cluster size, N, is of particular interest. Here, size N is measured as the number of adatoms for islands, or missing atoms for pits. Alternatively, size can be measured by the island or pit area, $A = a^2 N$, where "a" denotes the surface lattice constant.

Macroscopic continuum Langevin theory for PD-mediated cluster diffusion predicts that

$D_N \sim \sigma_{\rm PD} N^{\beta}$ with a size-scaling exponent $\beta = \beta_{\rm macro} = 3/2$, where $\sigma_{\rm PD}$ denotes the mesoscale mobility of atoms along the step edge bordering the cluster. [14, 15] It follows that in this continuum treatment, the Arrhenius energy for $\sigma_{\rm PD}$, denoted EPD, [16, 17] should correspond to the effective barrier, $E_{\rm eff}$, for cluster diffusion. A key observation is that the macroscale continuum theory predicts identical behavior for islands and pits. A simple atomistic-level mean-field type theory [18] for PD also predicts the same size-scaling as continuum theory with $\beta = \beta_{\rm macro} = 3/2$. However, significantly, a detailed experimental study of homoepitaxial island diffusion on Ag(100) and Cu(100) surfaces at temperature $T \approx 300K$ observed exponents, $\beta_{\rm eff} \approx 1.15$ and $\beta_{\rm eff} \approx 1.25$, respectively, for moderate sizes N $= O(10^2)$ to $O(10^3)$. [2,3] These β values are distinctly below the continuum prediction. From more recent experimental studies for Ag(100), a similar scenario appears to apply for vacancy pits. [12,13] These observations prompt the current systematic theoretical analysis of the variation of D_N with N for vacancy pits, and comparison with behavior for adatom islands.

To provide further background related to this study, we note that, in contrast to metal(100) surfaces, there has been extensive analysis starting in the mid-1990s of vacancy pit diffusion on metal(111) surfaces. [19,20] The initial experimental studies for Ag(111) at $T \approx 300K$ suggested that $\beta_{\rm eff} \approx 1$ which was interpreted as a signature of cluster diffusion mediated by detachment of atoms from the pit perimeter, diffusion across the pit, and reattachment. [19] However, subsequent studies both for Ag(111) in the range $T = 279330K$ and for Cu(111) in the range $T = 318343K$ suggested a smaller $\beta_{\rm eff} < 1$ although with limited statistics, and suggested that the mechanism of pit diffusion was in fact PD. [21] Motivation for this analysis came in part from the observation that coarsening of arrays of pits on Ag(111) was mediated by cluster diffusion and coalescence, referred to as Smoluchowski ripening (SR). [19] However, Ostwald ripening (OR) tends to dominate coarsening for vacancy pits on metal(100) surfaces, except for sufficiently small mean pit sizes. [4, 12, 22] Interestingly, the opposite applies for adatom islands, i.e., OR dominates on metal(111)

surfaces, and SR on metal(100) surfaces. [2–4, 22]

Returning to our focus in the paper on modeling of cluster diffusion on metal(100) surfaces, we note that recent theoretical studies of adatom island diffusion revealed surprisingly rich behavior for moderate sizes $N \leq O(10^2)$ for realistic model parameters. [23, 24] This behavior includes distinct edge-nucleation-mediated and facile branches of diffusion with quite different size-scaling, and also a cyclical variation of D_N with N. These distinct branches merge, and oscillations disappear for larger sizes $N \geq O(10^2)$, but unconventional size-scaling persists until much larger sizes $N = O(10^3)$ for typical model parameters. In the current study, we will explore the existence of analogous behavior for vacancy pits, and compare behavior with previous results for adatom islands. However, in addition, we will apply our models to analyze and elucidate experimental data collected by different groups on pit and island diffusion for the Ag(100) system at $300K$. This will raise additional issues regarding the optimal comparison of simulation results with experimental observations.

In Section 3.2, a detailed description of our stochastic model is provided, as well as a characterization of cluster diffusion processes. An overview of simulation results and an elucidation of this behavior are presented in Section 3.3. In Section 3.4, the model is applied to analyze experimental data for Ag(100). Conclusions are provided in Section 3.5.

3.2 Stochastic Lattice-gas Model for Cluster Diffusion

3.2.1 Model details and kMC simulation of cluster diffusion

Our tailored stochastic lattice-gas model for PD-mediated 2D epitaxial cluster diffusion on metal(100) surfaces [25] involves hopping of adatoms within a single surface layer on the metal(100) substrate. These adatoms reside on a square lattice of adsorption sites with lattice constant "a", and interact with nearest-neighbor (NN) attractive lateral interactions of strength $\phi > 0$. Adatoms can hop to NN empty sites, and also to second NN (2NN) empty sites, provided that hopping retains at least one NN adatom (and with an additional mild connectivity constraint described in the Supporting Information). All hop rates have the

Arrhenius form $h = \nu \exp\left[-E_{\rm act}/(k_B T)\right]$, where ν is a common attempt frequency for both NN and 2NN hops. Let n_{NN} denote the number of in-plane NN adatoms of the hopping adatom in its initial configuration. Then, the activation barrier, $E_{\rm act}$, which is selected to be consistent with detailed balance, satisfies

$$E_{\rm act} = E_e + (n_{\rm NN} - 1)\phi \text{ for NN hops and}$$
$$E_{\rm act} = E_e + (n_{\rm NN} - 1)\phi\delta \text{ for 2NN hops.} \tag{3.1}$$

Thus, for example, one has activation barriers of the following: E_e for hopping of atoms along close-packed $\langle 110 \rangle$ step edges via NN hops; $E_r = E_e + \delta$ for hopping around corners or kinks via 2NN hops, so δ corresponds to the additional EhrlichSchwoebel or ES kink rounding barrier; $E_k = E_e + \phi (E_{k2} = E_e + \phi + \delta)$ for kink escape to a step edge via a NN (2NN) hop; and $E_{ex} = E_e + 2\phi (E_{ex2} = E_e + 2\phi + \delta)$ for extraction of an atom from the middle of a $\langle 110 \rangle$ step edge via a NN (2NN) hop. Model behavior can be determined precisely by a kinetic Monte Carlo (KMC) simulation. We utilize a standard rejection-free Bortz type algorithm.

With regard to thermodynamics, the model is equivalent to the 2D ferromagnetic Ising model on a square lattice. Typical experimental conditions correspond to $(k_B T)/\phi \approx O(10^{-1})$, far smaller than the critical value for $(k_B T)/\phi$ of 0.57 below which phase separation occurs into a 2D condensed phase and a dilute 2D gas phase. [26] The condensed phase corresponds to 2D islands (pits), and the gas phase to isolated adatoms (monovacancies), for lower (higher) submonolayer coverages. An exact expression is available for the equilibrium shape of clusters, which is the same for islands and pits, in the macroscopic limit of large size. [27] Qualitatively, these are square clusters, but with rounded corners for $T > 0$. Of particular relevance for this study is the existence of "perfect sizes" for (island or pit) clusters, $N_p = L^2$ and $N_p = L(L+1)$, for integer L, which have unique square or near-square rectangular ground state shapes, respectively, at $T = 0K$. Note that clusters of size $N = L(L+m)$ with $m \geq 2$ do not satisfy this nondegeneracy property. [23, 24]

For diffusion of adatom islands, the KMC simulation starts with a single 2D island where all adatoms are connected to at least one other adatom in the island by NN bonds. Then, the above hopping dynamics preserves NN connectivity (and thus size) of the island. In contrast, for diffusion of vacancy pits, again starting with a single 2D vacancy pit with NN connectivity, now "monomer" vacancies, corresponding to a single missing atom, can detach from the pit and diffuse through the surrounding adlayer. (Of course, monomer vacancy diffusion actually corresponds to hopping of adjacent atoms into the vacancy.) However, the equilibrium density of such monomer vacancies, $n_{\rm eq}({\rm vac}) = \exp\left[-2\phi/(k_BT)\right]$, is generally sufficiently small that, in our finite simulation system, there are rarely any detached vacancies. As a result, for simulations of both islands and pits, the cluster size is effectively constant. A special case where $n_{\rm eq}({\rm vac})$ deviates from the above result is discussed below in Section 3.2.2 and the Supporting Information (SI).

Our focus is on analysis of the diffusion coefficient, D_N, for clusters of various sizes N. To this end, it is appropriate to first define an effective time-dependent diffusion coefficient, $D_N(\delta t) = \langle [\delta r(\delta t)]\, 2\rangle / (4\delta t)$, where $\delta \mathbf{r}(\delta t)$ is the displacement in the cluster geometric centroid (GC) in a time interval δt, and $\langle\rangle$ is an average of data over a long trajectory. We have also set $[\delta r]^2 = \delta \mathbf{r} \cdot \delta \mathbf{r}$. The GC corresponds to the center-of-mass for an adatom island. For our model where $D_N(\delta t) \propto a^2 h_e$, one obtains that $D_N(\delta t)/D_N$ versus $h_e \delta t$, and $D_N/(a^2 h_e)$, are independent of our choice of E_e and ν, and thus he. Note that $D_N(\delta t)$ varies, and specifically decreases as δt increases, for shorter δt due to back-correlations in the walk of the cluster GC. [1, 9, 24] However, $D_N(\delta t)$ plateaus for larger δt, and the conventional diffusion coefficient is obtained from $D_N = \lim_{\delta t \to \infty} D_N(\delta t)$. See Figure 3.1 and additional discussion and results in the Supporting Information. Note that the short-time behavior is roughly inverted from the long-time behavior; i.e., perfect size pits have the lowest diffusivity for short-time increments, and the highest for long-time increments. This highlights the importance of accounting for these transient effects, i.e., selecting data for sufficient large $h_e \delta t$, to obtain accurate values for the true long-time diffusivity. Finally,

we will also let E_{eff} denote the effective Arrhenius energy associated with D_N, so that $D_N \sim \exp\left[-E_{\text{eff}}/(k_B T)\right]$.

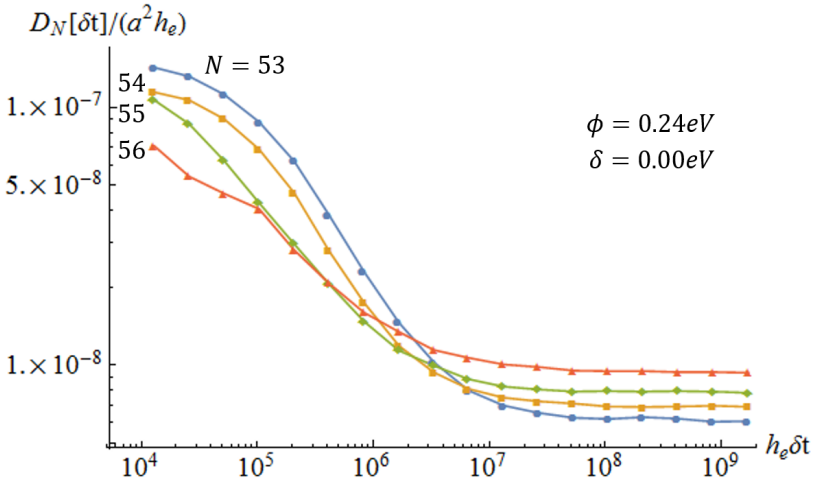

Figure 3.1: Variation of rescaled $D_N(\delta t)$ with $h_e\delta t$ for diffusion of vacancy pits with selected sizes $N = 5356$ for $\phi = 0.24$eV with $\delta = 0$ at $300K$

Certainly, the above model is simplified both in terms of thermodynamics (i.e., lateral adatom interactions) and kinetics (i.e., hop rates). For metal(100) systems, one generally expects 2NN pair attractions and bent trio repulsions to be $\sim 10\%$ of the strength of NN interactions (and weaker longer range pair and many-body interactions also exist). [28–30] The actual hopping dynamics in metal(100) systems is also more complicated than our prescription, as has been determined by a comprehensive DFT analysis of energetics at both the initial site and the transition state for hopping for general step edge configurations. [29, 30] The prescription of the diffusion rate for isolated monomer vacancies in the above model is too low, but this process is not important for the current study. Also, the model will not precisely describe hopping in some configurations, e.g., for an atom sliding out of the corner from a rectangular pit. [30] However, we claim that our simplified model captures the basic features of these systems, and is a more effective vehicle than more complex models for obtaining a fundamental understanding of the basic features of cluster diffusion behavior.

3.2.2 Vacancy pit diffusion modes and energetics

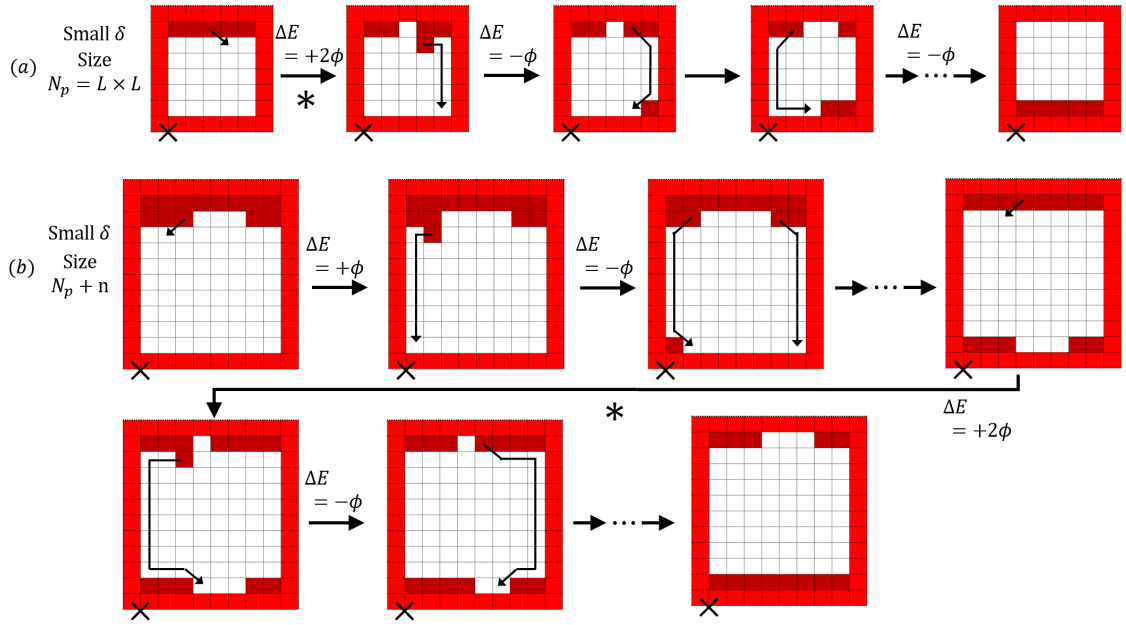

Figure 3.2: Direct vacancy pit pathways for small δ or $\delta = 0$ for sizes: (a) N_p and (b) $N_p + n$ with $n = 3$. Atoms in the top surface layer are denoted by small red squares, and vacancies by small white squares. Atoms which are moved around the periphery of the pit are denoted by darker red than those in the surrounding adlayer which are not moved. Energy changes are indicated by ΔE. Rate-determining steps are denoted by an asterisk under the horizontal arrow. The $\times$ indicates a fixed position on the surface.

We now illustrate the pathways for long-range diffusion of vacancy pits by movement of atoms around the periphery of the pit, and also indicate the associated activation barriers. Specifically, we show the steps needed to recover a prescribed initial pit shape, but with a shifted geometric centroid. This shape recovery is a key component of long-range diffusion. In Figure 3.2, we show typical "direct" diffusion pathways for the case of zero or small kink rounding barrier, δ. Figure 3.2a shows such pathways for diffusion of a pit with perfect size, $N = N_p = L^2$. We choose the initial configuration as the unique ground state, for which the typical first step is to extract an atom from some location along one of the close-packed straight edges of the pit. After the extracted atom is transferred to a corner of the

pit, the system is in a first excited state corresponding to energy change $\Delta E = +\phi$. This first rate-controlling step, indicated by an asterisk in Figure 3.2a, has the highest barrier of $E\text{act} = E_e + 2\phi + \delta$ which determines the overall or effective barrier, E_{eff}, for these pathways, as all subsequent steps have a lower barrier of $E_{\text{act}} = E_e + \phi + \delta$. Subsequent atom transfers evolve the system through a sequence of first excited state configurations, with the last transfer returning the system to the ground state after an energy change $\Delta E = -\delta$.

Figure 3.2b indicates the direct diffusion pathway for small δ for a pit size of $N = N_p + n = L^2 + n$, for integer $n < L$, where the rate-controlling step again involves extraction of an atom from a straight step edge with barrier $E\text{act} = E_e + 2\phi + \delta$. However, now this step (again indicated by an asterisk) occurs midway through the overall process. In this case, the system evolves through a sequence of ground states (after each atom transfer) before the above-mentioned step edge extraction process, and then through a sequence of first excited states until the last step, which returns the system to a ground state. Similar pathways exist for perfect sizes $N_p = L(L+1)$ with the same barrier, $E\text{act} = E_e + 2\phi$, determining $E\text{eff}$. We caution that there are other pathways, described below, which avoid corner rounding and for which naturally E_{act} does not involve δ. Thus, the actual effective barrier will depend on the relative contributions of the various pathways. We also emphasize that, for processes indicated in Figure 2, the effective barrier, E_{eff}, is higher than that predicted by the continuum Langevin formulation of $E_{\text{PD}} = E_e + \phi + \delta$.

For a *large kink rounding barrier*, δ, there is a preference for pathways which avoid 2NN kink rounding hops. Indeed, it is possible to find such pathways leading to long-range pit diffusion. Such direct pathways are shown in Figure 3.3a for $N = N_p = L^2$, and in Figure 3.3b for $N = N_p + n = L^2 + n$. For $N = N_p = L^2$, evolution is through first excited state configurations. For $N = N_p + n = L^2 + n$, evolution is initially through ground states until extraction of an atom from a pit corner, and then through first excited states. The consequences of the existence of these pathways for cluster diffusion avoiding kink rounding will be illustrated in Section 3.3 when comparing diffusivity of adatom islands and vacancy

pits. Analogous pathways avoiding kink rounding exist for $N_p = L(L+1)$. The overall barrier for all these pathways is given by $E_{\text{eff}} = E_e + 2\phi$.

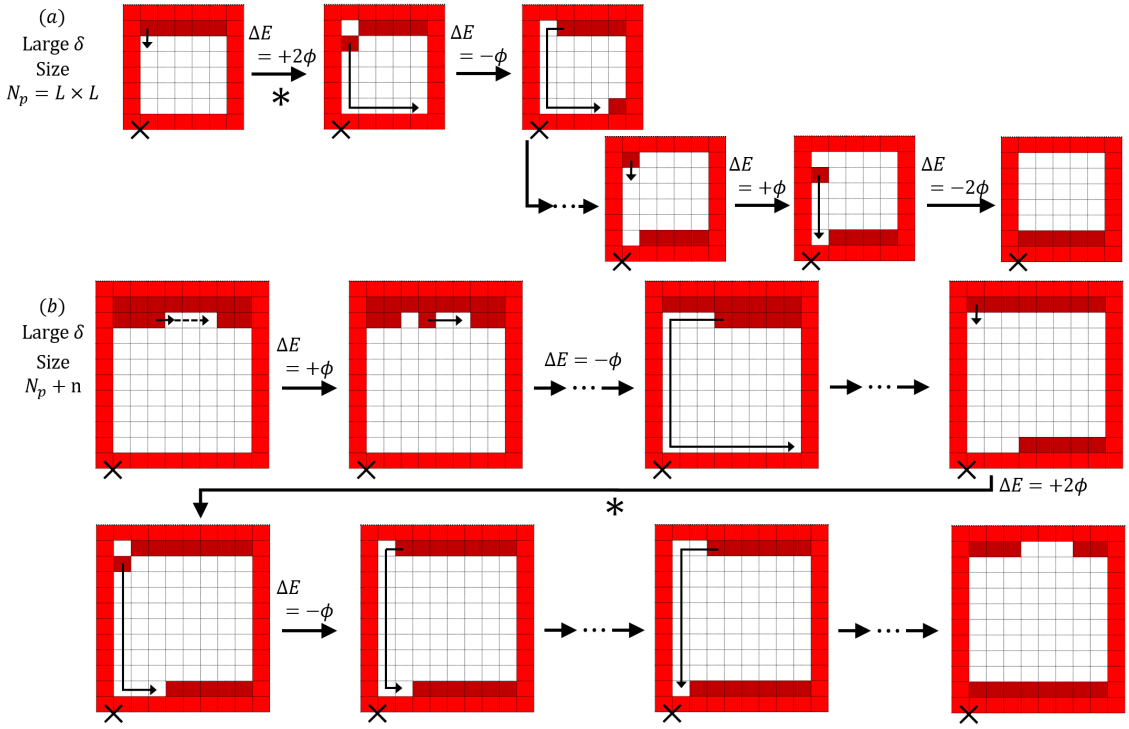

Figure 3.3: Prominent direct vacancy pit diffusion pathways for large δ for sizes: (a) N_p and (b) $N_p + n$ with $n = 3$. The format is the same as for Figure 3.2. In contrast to Figure 3.2, there are no 2NN hops of periphery atoms involved in these pathways (only NN hops).

Some other basic issues related to pit diffusion should be noted. First, in addition to the direct pathways shown above which most efficiently recover the initial configuration with a translated geometric centroid, there are also less efficient "indirect pathways". In these pathways, atoms accumulate at multiple corners of the pit. See Figure 3.4 for $N = N_p = L^2$. This means that the system accesses a large number of degenerate first excited states for $N = N_p$, and of degenerate ground states and first excited states for $N = N_p + n$. We will show in Section 3.3 that the existence of this degeneracy is important for understanding certain cyclical features of the size-dependence of diffusivity. Second, as indicated in Section

3.2.1, the equilibrium density of monomer vacancies coexisting with vacancy pits is typically given by $n_{\text{eq}}(\text{vac}) = \exp\left[-2\phi/(k_B T)\right]$. This applies in simulations with a pit of size $N = N_p$ or $N = N_p + n$ with $n > 1$ where the energy difference between the ground state of the vacancy pit and the state with a detached monomer vacancy is $\Delta E = +2\phi$. However, for size $N = N_p + 1$, this energy difference is $\Delta E = +\phi$, so one obtains that $n_{\text{eq}}(\text{vac}) = \exp\left[-\phi/(k_B T)\right]$. See the Supporting Information for further discussion. The probability that the system exists as a connected pit versus with a detached monomer also depends on system size and on the degeneracy of the connected ground states. However, this probability is negligible for all sizes but $N = N_p + 1$. Thus, results for diffusivity when $N = N_p + 1$ can be impacted by this feature.

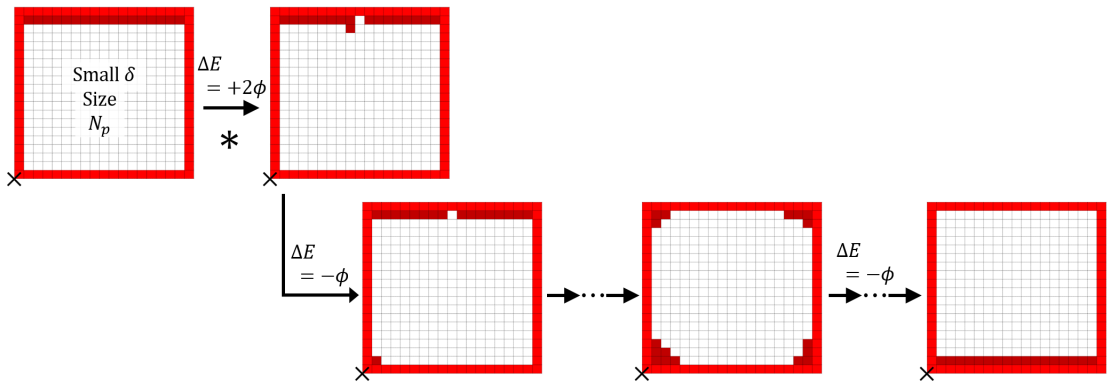

Figure 3.4: Indirect pathway for small δ for vacancy pit diffusion for size $N_p = L^2$. The format is the same as that for Figure 3.2.

3.2.3 Adatom island diffusion modes and energetics

For adatom islands, there are two distinct modes or branches of cluster diffusion. *Edge nucleation-mediated diffusion* occurs for sizes $N = N_p$. In these cases, after an atom is extracted from one of the corners of the ground state square or near-square configuration to an edge, a second atom must also be quickly extracted and join the first atom before the first atom returns to the corner. This formation of a pair of edge atoms constitutes nucleation

of a new edge of the island. Atoms can then be transferred to complete the new edge and recover a ground state with a translated geometric centroid (GC). This process of nucleation of new edges is also required for adatom islands of size $N = N_p + n$ with $n = 3, 4, ...$ In all these cases, one can show that the effective activation energy for nucleation-mediated cluster diffusion is given by $E\text{eff} = E_e + 2\phi + \delta$. In contrast, facile diffusion occurs for sizes $N = N_p + 1$ and $N = N_p + 2$. Here, the nucleation of new outer edges is not necessary. For $N = N_p + 1$, a single atom on the edge of a perfect core can easily diffuse around the core, and for $N = N_p + 2$ a dimer on the edge of a perfect core can easily dissociate and re-form on another edge. This allows facile reformation of the special configurations with a shifted GC. However, long-range diffusion does require the cluster to repeatedly transition through these special configurations. The effective activation energy for facile cluster diffusion is given by $E_{\text{eff}} = E_e + \phi + \delta$. A detailed description of behavior for adatom island diffusion is given in refs [23] and [24]. Again, continuum theory predicts an effective barrier, E_{eff}, of $E_{\text{PD}} = E_e + \phi + \delta$.

3.3 KMC Results for Pit Diffusion and Comparison with Islands

3.3.1 KMC simulation results for D_N versus N

The main part of Figure 3.5 gives an overview of the variation of vacancy pit diffusivity D_N with size N for $\phi = 0.20$eV at $T = 300K$ in the absence of a kink rounding barrier, $\delta = 0$, and also compares this behavior with that for adatom islands of N atoms. For vacancy pits with sizes below $N = O(10^2)$, we just indicate behavior for perfect sizes $N = N_p$ and sizes $N = N_p + 1$, as these provide local upper and lower bounds on diffusivity, respectively. See below. For adatom islands with sizes below $N = O(10^2)$, as in recent studies, [23, 24] we just show the following: the locally maximum diffusivity for facile sizes $N = N_p + 1$, the moderate diffusivity for perfect sizes $N = N_p$, and locally minimum diffusivity for sizes $N = N_p + 3$. It is clear that vacancy pits diffuse significantly more slowly than adatom islands when $\delta = 0$ for a broad range of sizes $N \leq O(10^3)$, but that gradual merging of

diffusivities for islands and pits is apparent for larger N. Again, the latter is expected from macroscopic continuum formulations. The inset of Figure 5 shows qualitatively similar behavior for small kink rounding barrier $\delta = 0.1$eV, but for a more restricted set of cluster sizes.

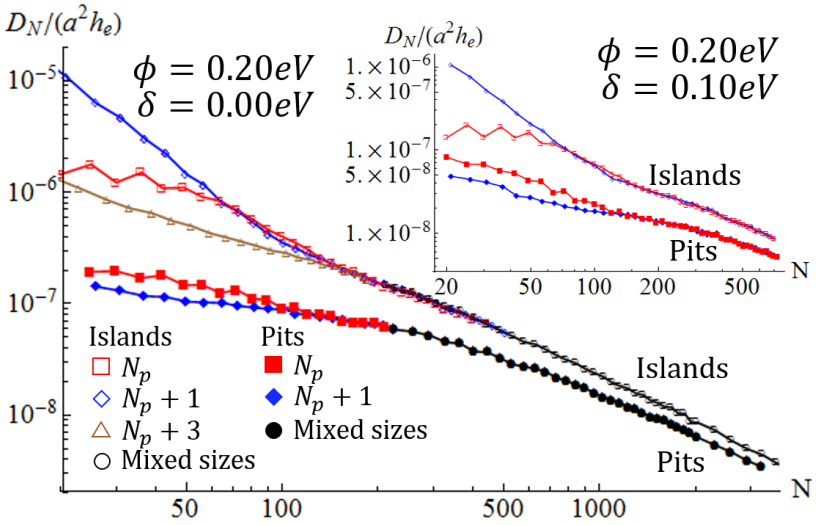

Figure 3.5: Overview of KMC simulation results for D_N versus N for vacancy pits (solid symbols) and adatom islands (open symbols) for $\phi = 0.20$eV and $\delta = 0$ at $300K$. D_N is shown only for certain special classes of sizes, often those which capture local maxima and minima. The inset shows a more limited set of data for $\phi = 0.20$eV and $\delta = 0.1$eV at $300K$.

For vacancy pits in the case of no kink rounding barrier, $\delta = 0$, a more detailed analysis reveals a cyclical variation of D_N with N for moderate sizes $N \leq O(10^2)$. This behavior is shown in Figure 3.6 for $\phi = 0.24$eV and $\phi = 0.28$eV at $300K$ focusing on a few cycles. (Larger ϕ values are chosen to amplify this behavior.) The key feature which emerges is that perfect sizes $N = N_p = L^2$ or $L(L+1)$ tend to correspond to local maxima in D_N, and sizes $N = N_p + 1$ tend to correspond to local minima. Slight deviations from this behavior are discussed in Section 3.3.2. Despite the substantial difference in diffusivity for these two classes of sizes, $N = N_p$ and $N = N_p + 1$, an Arrhenius analysis reveals that the same effective diffusion barrier, $Eact = E_e + 2\phi$, applies in both cases, recalling that here $\delta = 0$. See the Supporting Information. This contrasts behavior for adatom islands where

facile sizes $N = N_p + 1$ have higher diffusivity than perfect sizes $N = N_p$, and where these two classes of sizes have different effective diffusion barriers (at least for the moderate size regime). [23,24] We mention that identification of these oscillations either for islands or pits in experimental data would be inhibited by uncertainties in both diffusion coefficients and cluster size. This point is discussed further in Section 3.4.2.

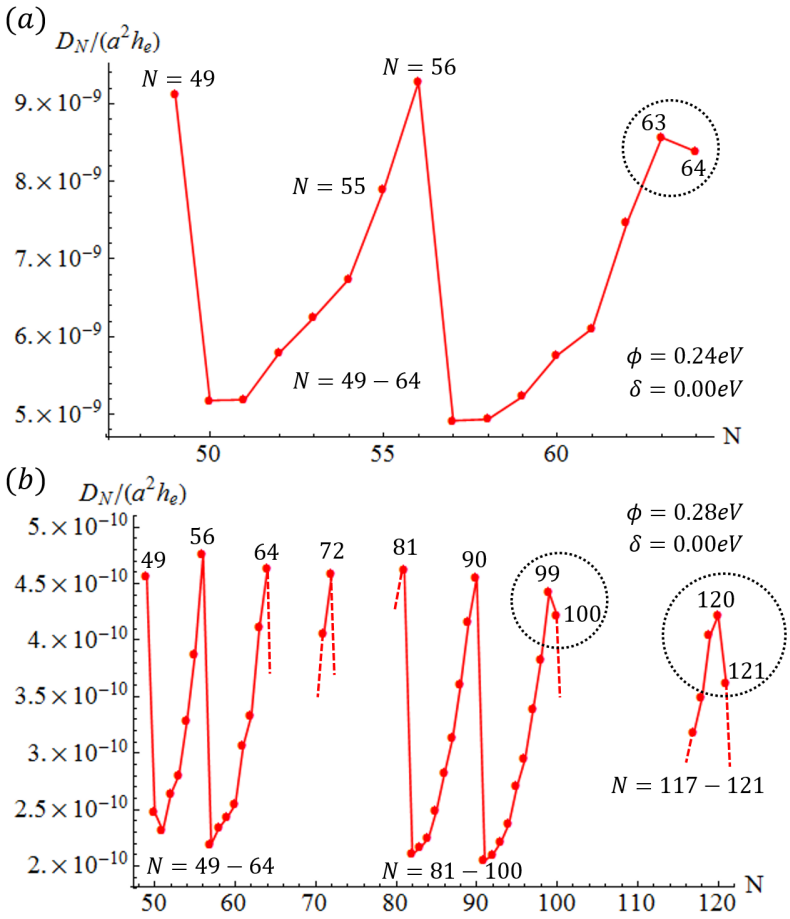

Figure 3.6: Examples of cyclic variation of D_N versus N for vacancy pits for (a) $\phi = 0.24$eV and (b) $\phi = 0.28$eV, with $\delta = 0$ at $300K$. Indicated local maxima are mainly perfect sizes, but disruption of this feature appears for larger sizes $(\cdot)$. Dashed lines are not quantitative, but just guide the eye.

Finally, we provide a more comprehensive analysis of the variation of cluster diffusivity with the strength of the kink rounding barrier, δ, for $\phi = 0.24$eV at $T = 300K$. Figure 3.7 shows $\ln\left[D_N/(a^2h_e)\right]$ versus δ for both vacancy pits and adatom islands for selected

sizes $N = N_p$ and $N_p + 1$ choosing $N_p = 64$. For vacancy pits, increasing δ above $\delta = 0$ results initially in a gradual smooth decrease in D_N, behavior which is expected since the overall efficiency in pathways involving corner rounding is reduced. However, for larger δ above about 0.15eV, D_N for pits tends to plateau, a feature which reflects the enhanced contribution and ultimately the dominance of diffusion pathways avoiding corner rounding. In contrast, D_N for adatom islands starts at higher values for small δ but decreases more quickly and persistently. This behavior for islands reflects the feature that all pathways involve corner rounding, so one finds that $D_N \sim \exp[-\delta/(k_B T)]$, at least for larger δ. Thus, while DN is smaller for vacancy pits than for adatom islands for small δ, the opposite applies for large δ with a crossover around $\delta = 0.18$eV for the parameter choices in Figure 3.7.

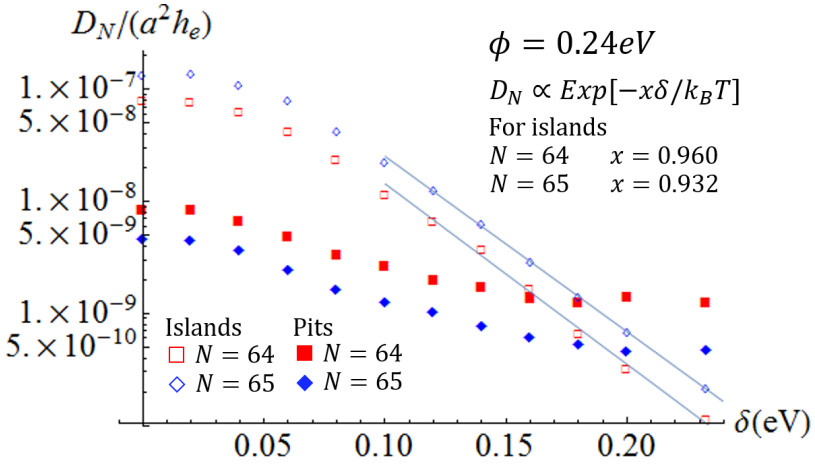

Figure 3.7: Variation of D_N with δ for perfect size $N_p = 64$ and for size $N_p + 1 = 65$ at $300K$. We also include Arrhenius fits to the data for islands for larger δ showing that $D_N \sim \exp[-\delta/(k_B T)]$

3.3.2 Further analysis of results for D_N versus N

In this subsection, we elucidate various aspects of the cluster diffusivity: asymptotic large-size behavior, cyclical behavior for moderate sizes, and finally the dependence on kink rounding barrier.

Asymptotic Large-Size Behavior

The continuum Langevin formulation reliably describes diffusion behavior for clusters with sufficiently large sizes. Since this formulation predicts identical behavior for vacancy pits and adatom islands, it follows that diffusivity for vacancy pits and adatom islands should merge for sufficiently large sizes, where both should satisfy classic size-scaling with $\beta = \beta\text{macro} = 3/2$. Previous analysis of data for adatom islands for $\phi = 0.20\text{eV}$ and $\delta = 0$ at $300K$ (using the data shown in Figure 3.5) revealed that the effective scaling exponent, β_{eff}, did achieve this asymptotic value of $\beta\text{macro} = 1.5$ for $N \geq 2300$. This is consistent with the expectation that such asymptotic behavior should be achieved for linear island sizes, $L = N^{1/2}$, well above the characteristic separation of kinks on close-packed step edges, [24] $L_k = 1/2 \exp\left[\phi/(2k_BT)\right]$, in units of "$a$". For $\phi = 0.20\text{eV}$ at $300K$, one finds that $L_k \approx 24$, so asymptotic behavior should be achieved for N well above $(L_k)^2 \approx 580$. From Figure 3.5, convergence of the effective size-scaling exponent to this asymptotic value for vacancy pits is somewhat slower with $\beta_{\text{eff}} \approx 1.32$ for $2025 \leq N \leq 3250$. Complete merging of diffusivity for pits and islands does not occur until $N = O(10^4)$, a regime not readily accessible for precise analysis from simulations.

Cyclical Variation for Moderate Sizes

A key feature of the behavior of D_N for vacancy pits shown in Section 3.3.1 is the cyclical variation. Specifically, D_N typically increases smoothly with $N = N_p + n$ for increasing $n = 1, 2, ..., n_{\max}$ from a local minimum for sizes $n = 1$ to a local maximum at $n = n_{\max}$ where $N = N_p + n_{\max}$ recovers the next largest perfect size. For example, one finds that $n_{\max} = L$ for $N_p = L^2$ or $L(L1)$, so that $N_p + n_{\max} = (L+1)L$ or L^2, respectively. To elucidate this behavior, we recall that access to the first excited state is necessary for long-range diffusion. Thus, we speculate that this cyclical increase in D_N is associated with an increased probability for the vacancy pit to be in a first excited state rather than in the ground state. To support this speculation, it is necessary to first determine the degeneracy

(i.e., the number of configurations), $\Omega_N(j)$, associated with the jth excited state of a pit with size N, at least for $j = 0$ (the ground state) and $j = 1$ (the first excited state). Then, if $P_N(j)$ denotes the probability to be in the jth excited state, it follows that the relative probability of interest is given by

$$P_N(1)/P_N(0) = \exp\left[-\phi/(k_B T)\right] \times \Omega_N(1)/\Omega_N(0). \tag{3.2}$$

Results for the variation of the key ratio, $\Omega_N(1)/\Omega_N(0)$, with N are shown in Figure 3.8. It is clear that the strong cyclical variation of this quantity correlates with the analogous cyclical variation of D_N shown in Figure 3.6.

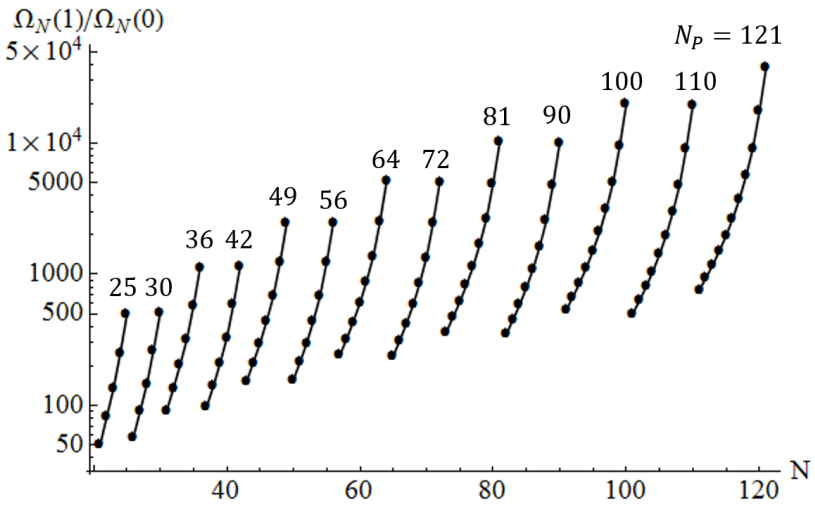

Figure 3.8: Plot of $\Omega_N(1)/\Omega_N(0)$ vs N with $N = 21 - 121$.

Determination of the results shown in Figure 3.8 for configurational degeneracy requires nontrivial combinatorial analysis. Our analysis considers pit configurations obtained by starting with a perfect rectangular pit of size exceeding N, and then adding the appropriate atoms (to reduce the size to N) to form a simple staircase in each corner. (A staircase is a step edge with kinks of one sign, and not both.) Note that the energy of all these configurations is simply determined by the perimeter length of the cluster (treating vacant sites as $a \times a$ squares) which equals that of the original inscribing rectangle. If the number of added atoms is not too large, then the configurations of different corners do not "interfere"

with each other. As a result, the total number of configurations is readily determined from knowledge of the number of configurations for a single corner with a specific number of added atoms by a suitable convolution sum over different numbers of atoms added to each of the corners. The number of configurations for a single corner can be obtained by noting that the associated configurations can be mapped onto Young or Ferrers diagrams associated with "partitions of integers" in number theory. [31] A more detailed description of this combinatorial analysis is provided in the Supporting Information, and we note that the analogous approach for the treatment of the degeneracy of island configurations is provided in ref [24].

From Figure 3.6, it is evident that there are some deviations from ideal cyclical variation of D_N with minima (maxima) at $n = 1 (n = n_{\max})$. Sometimes the local minimum occurs at $n = 2$ rather than $n = 1$, possibly due to the higher likelihood of vacancy detachment for $n = 1$ (cf. Section 3.2.2). This is evident in Figure 3.6b for $\phi = 0.28$eV and $N_p = 49$. In addition, the feature that the local maximum occurs at $n = n_{\max}$, corresponding to a perfect size, is disrupted for the larger sizes as is also evident in Figure 3.6a at $N_p = 64$ when $\phi = 0.24$eV, and in Figure 3.6b at $N_p = 100$ when $\phi = 0.28$eV. The disruption of perfect cyclical behavior is expected for sufficiently large sizes because distinct branches of behavior (e.g., for special sizes N_p versus sizes N_p+1, etc.) eventually merge. Such merging is expected to create clusters having a significant probability of being in an excited state configuration (above the $T = 0K$ ground state). [23, 24]

As indicated above for $\phi = 0.28$eV, such disruption wherein local maximum in D_N does not correspond to a perfect size first appears for $N = 100$ where $D_{N_p} = 100 < D_{N_p1} = 99$. From Table 3.1, this corresponds to $P_N(1)/P_N(0) \sim 0.4$. (Figure 3.6b shows a stronger disruption with $D_{N_p} = 121 \ll D_{N_p1} = 120$ for $\phi = 0.28$eV. Also the difference between $D_{N_p1} = 120$ and $D_{N_p2} = 119$ is much smaller than between $D_{N_p1} = 99$ and $D_{N_p2} = 98$, a precursor to more extensive disruption of cyclical behavior.) For $\phi = 0.24$eV, the criterion $P_N(1)/P_N(0) \sim 0.4$ for the onset of disruption also applies where $D_{N_p} = 64 < D_{N_p1} = 63$ as

Table 3.1: $P_N(1)/P_N(0)$ versus N at $300K$ Obtained from $\Omega_N(1)/\Omega_N(0)$

N	$\phi = 0.24\text{eV}, P_N(1)/P_N(0)$	N	$\phi = 0.28\text{eV}, P_N(1)/P_N(0)$
55	0.117	98	0.0997
56	0.233	99	0.0189
63	0.236	100	0.401
64	0.480	119	0.183
		120	0.353
		121	0.762

shown in Figure 3.6a. The criterion is also consistent with the onset of disruption evident in limited data for $\phi = 0.20\text{eV}$ shown in the Supporting Information.

Dependence on Kink Rounding Barrier

Finally, we provide brief additional comments on the δ-dependence of D_N. As noted above, behavior for adatom islands is clear as all pathways involve corner rounding, so that one has $D_N \sim \exp[-\delta/(k_BT)]$, at least for larger δ. The weaker dependence for smaller δ likely reflects the feature that in this regime the kink ES length [26] $L_\delta = \exp[\delta/(k_BT)]$ is significantly below other characteristic lengths such as kink separation, L_k, so then diffusion along close-packed step edges rather than kink rounding is rate-limiting for transport around the cluster periphery. Behavior for vacancy pits is more complicated due to a competition between pathways with and without corner rounding. However, as noted in Section 3.3.1, for large enough δ, pathways without kink rounding dominate and D_N becomes independent of δ. Direct assessment of the limiting plateau value for large δ is possible from analysis of a model where 2NN hops are strictly excluded.

3.4 Analysis of Diffusivity for Pits and Islands on Ag(100)

First, we provide some further comments on the applicability of our simplified model for the Ag(100) system with regard to equilibrium (island and pit) cluster shapes. We then discuss the presence of fluctuations and variations in experimental cluster size, and the

ramifications for comparison with simulation results for fixed cluster size. Finally, we apply our model to interpret experimental observations from three different groups for cluster diffusivity in the Ag(100) system at $300K$.

3.4.1 Equilibrium cluster shapes

As noted in Section 3.2.1 for our model with just NN interactions, a complex but exact expression is available for the equilibrium shape of clusters in the macroscopic limit of large size. [27] This limiting shape, which is identical for pits and islands, is square but with rounded corners for $T > 0$. On the other hand, for metal(100) surfaces, close-packed $\langle 110 \rangle$ / $\{111\}$ oriented steps generally have the lowest step energy, $\gamma_{\langle 110 \rangle}$; then, $\langle 100 \rangle$ / $\{110\}$ oriented kinked steps have the next highest step energy, $\gamma_{\langle 100 \rangle}$, and other orientations have significantly higher energy. Thus, it has been suggested [32] that equilibrium shapes might reasonably be regarded as octagonal being bordered by longer $\langle 110 \rangle$ close-packed steps of length $L_{\langle 110 \rangle}$, and shorter $\langle 100 \rangle$ kinked steps of length $L_{\langle 100 \rangle}$. The relative length of the two types of steps is determined from the ratio of step energies, $R = \gamma_{\langle 100 \rangle}/\gamma_{\langle 110 \rangle} \geq 1$, by solving a minimization problem for the overall step energy given a fixed cluster area. We find that this analysis reveals a critical value of $R_c = \sqrt{2}$, such that if $R \geq R_c$, then the $\langle 100 \rangle$ kinked step edges are absent, having too high an energy cost, so that the equilibrium shape is square. An early DFT analysis [32] indicated that $R = 1.20 < R_c \approx 1.414$ for Ag(100), which implies an octagonal equilibrium shape with $L_{\langle 100 \rangle}/L_{\langle 110 \rangle} \approx 0.3$. However, this analysis used slabs of limited thickness and sequentially determined the bulk energy, surface energy, and step energy for Ag. Any inaccuracy in the earlier steps can lead to more significant errors in the latter.

A more recent DFT analysis used a modified approach to avoid these issues, and found that $R = 1.39$ (1.40) using the PBE (PBEsol) functional. See the SI for ref [30]. These values are sufficiently close to Rc such that the equilibrium shape is effectively square (i.e., it includes no $\langle 100 \rangle$ kinked steps, but only $\langle 110 \rangle$ steps) at lower T. This supports the use

of our tailored model for Ag(100) for which $R = \sqrt{2}$, and which thus also exhibits square equilibrium shapes at lower T.

3.4.2 Fluctuations and variations in experimental cluster size

Over the time period of experimental observation of cluster motion required to determine diffusivity (often of a few hundred minutes), there must be some fluctuation in cluster size. In some cases, there can also be variation or drift in the mean size, but first we assume that such drift is not present. The size fluctuations are associated with detachmentattachment processes. Thus, the magnitude of the fluctuations reflects the magnitude of the overall detachment rate, noting that this must balance the overall attachment rate to preserve mean size.

For metal(100) systems, there is a separation of time scales which will serve to reduce these fluctuations. Cluster diffusion is mediated by edge diffusion, for which high rates reflect the low barrier for diffusion along close-packed step edges ($E_e \sim 0.250.29$eV for Ag). Detachment rates are much lower, being impacted by the much higher terrace diffusion barrier ($Ed \sim 0.45$eV for Ag). The effective rate disparity is even greater as periphery diffusion at least for large cluster sizes is predominantly limited by atoms breaking just one bond to escape kink sites. Consequently, in this regime, one finds that $E_{\text{eff}} = E_e + \phi + \delta$, as predicted by continuum theory. In contrast, detachment effectively requires breaking two bonds, and has an effective barrier of $E_{\text{eff}} = E_d + 2\phi$ (where we expect that δ is below ϕ). The total detachment rate, K, must balance the total attachment rate if there is no change in mean cluster size. Thus, one might adopt the expression $K \sim 4L\nu \exp\left[-(E_d + 2\phi)/(k_B T)\right]$, where L denotes the linear size of the cluster, noting that an monomer gas of density $n_{\text{eq}} = \exp\left[(-2\phi)/(k_B T)\right]$ attaches with hop rate $h_d = \nu \exp\left[-E_d/(k_B T)\right]$ uniformly along the cluster perimeter of length $\sim 4L$. For $\phi = 0.27$eV and $\nu = 10^{13}\text{s}^{-1}$, this would yield $K \sim 2\text{s}^{-1}$ at $300K$ for $N = 400$ and $L = 20$. Thus, over 100 min, there would be $M \sim$ 12000 detachment events, and size fluctuations would be on the order $\pm M_{1/2} \sim \pm 110$ for

uncorrelated detachmentattachment (i.e., large size fluctuations). However, detachment and (re)attachment are strongly correlated in the absence of an attachment barrier of atoms or vacancies to clusters, which is the case for metal(100) systems. As a result, size fluctuations will be far smaller than the above estimate. Indeed, experimental observations which track size do not reveal significant fluctuations; i.e., their magnitude is far below the estimate above.

However, the presence of (small) size fluctuations in the experiment raises the issue of the optimal processing of simulated D_N or $D_N(\text{sim})$ for fixed size to compare with experiment. The natural approach takes the normalized size distribution, P_N, centered on the mean size value, N_m, during the experimental observation period, and predicts $D_{N_m}(\text{expt})$ from a weighted average, $\sum_N P_N D_N(\text{sim})$. For large sizes (of relevance below) with smoothly decreasing $D_N(\text{sim})$ versus N, $D_N(\text{expt})$ determined in this way is effectively identical to $D_N(\text{sim})$. For smaller sizes where $D_N(\text{sim})$ oscillates with N, this process would tend to smear out the oscillations.

In experiments by our Iowa State University (ISU) group, data used to analyze island diffusivity was specifically selected to correspond to effectively constant size. This goal is facilitated by the feature that island coarsening on Ag(100) is dominated by SR. [4, 12, 22] However, for vacancy pits on Ag(100), OR tends to dominate coarsening, so there is a greater tendency for systematic slow variation in pit size over a time period of hours: larger (smaller) than average pits tend to grow (shrink). In this case, experimentally reported values of diffusivity, $D_N(\text{expt})$, naturally identify $N = N_m$ as the mean size during the observation period. At least for large cluster sizes, where both fluctuations in experimental size and oscillations in $D_N(\text{sim})$ are negligible, again it is reasonable to simply identify experimental values of diffusivity $D_N = N_m(\text{expt})$ with $D_{N_m}(\text{sim})$. See the Supporting Information for further discussion.

3.4.3 Model analysis of experimental observations for cluster diffusivity

We now apply our model to analyze and interpret experimental results for cluster diffusivity on Ag(100). The earliest study of adatom island diffusion [1] in 1994 and a subsequent study of pit diffusion [12] by the ISU group provided somewhat limited data with large uncertainties. Consequently, this data cannot by itself be used to quantify size-scaling, but it provides an assessment of the magnitude of diffusivity and is instructive when combined with other data. The ISU data also suggested that diffusivity for islands and pits of the same size is comparable. A particularly significant study of island (but not pit) diffusion by the Oak Ridge National Laboratory (ORNL) group [2] in 1997 provided extensive data from which an effective size-scaling exponent of $\beta_{\text{eff}} \approx 1.15$ was determined for a range of sizes $80 < N < 400$. ORNL values for island diffusivity were somewhat below those from the ISU study (for islands of the same size). A more recent study by Ge and Morgenstern [13] (GM) for both islands and pits again indicated that these have comparable diffusivity (for the same size), consistent with the ISU study. GM also extracted an effective exponent $\beta_{\text{eff}} \approx 0.76$ below the ORNL estimate, but found values for diffusivity significantly above both the ISU and ORNL data. These various experimental data sets are shown in Figure 3.9.

We apply the following interpretation to this somewhat inconsistent data. We propose that the ORNL data provides the most accurate estimate for the magnitude of the island diffusivity. Thus, the ISU values are somewhat elevated, and the GM values are significantly elevated, relative to the true values for cluster diffusion on a perfect flat surface. This elevation is plausibly due to intrinsic strain in the surface. Morgenstern suggested that the heavy ion bombardment producing a surface with a high step density in the GM study could have led to substantial strain. Indeed, it has been shown that ion bombardment can produce nanocavities below the surface, [33, 34] the strain field from which could impact adatom energetics on the surface. More direct evidence for the effect of strain on cluster diffusivity was provided in a study of Smoluchoswki ripening [35] (SR) of adatom islands on Ag(100).

Ripening was observed to be accelerated in a strained subregion of the surface displaying an oblong protrusion of length ~ 100 nm and maximum height ~ 0.07 nm. Modeling suggested that this acceleration in SR corresponded to a strain-induced enhancement of adatom island diffusivity by a factor of about 5. [35]

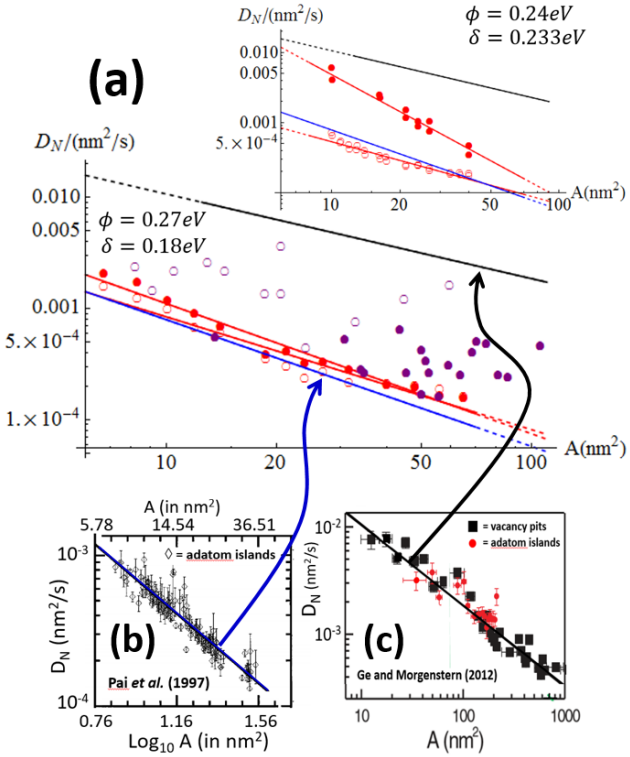

Figure 3.9: (a) KMC simulation results for pit (island) diffusion, denoted by red solid (open) symbols, versus cluster area, $A = a^2N$, at $T = 300K$ with $E_e = 0.291$eV, $\phi = 0.27$eV, and $\delta = 0.18$eV. Red lines fit KMC data with the upper lines corresponding to pits. The blue line fits ORNL island data for islands with βeff ≈ 1.15. The black line fits GM island and pit data with βeff ≈ 0.76. Solid portions of lines indicate the range of available data. Solid (open) purple symbols are ISU experimental data for pits (islands). Inset: KMC results with $E_e = 0.291$eV, $\phi = 0.24$eV, and $\delta = 0.233$eV. (b) ORNL experimental data set for islands. (c) GM experimental data sets for pits and islands. For Ag(100), one finds that $A = 0.0836N$ in nm^2.

For simulation analysis of the Ag(100) system, model parameters must be chosen appropriately. Recent successful modeling of the coalescence of pairs of Ag adatom islands on Ag(100) was based on extensive DFT analysis of pair and many-body lateral adatom inter-

actions, and also of activation barriers for periphery diffusion. [30] Using the PBEsol functional, this analysis indicated that Ee = 0.291 eV, which with $\nu = 10^{13}\text{s}^1$ yields $h_e = 10^{8.1}\text{s}^1$ at $300K$. This analysis also estimated that $\delta = 0.233$eV. While many-body interactions are non-negligible, the coalescence study concluded that, for a simplified model only including effective NN pairwise interactions, an appropriate effective strength for these is $\phi = 0.240$eV. However, we should caution that additional analysis in this study(30) indicated that the PBE functional predicts rather different and generally lower values for these energies. (However, modeling with the lower PBE energies produced too rapid coalescence.) Results for pit and island diffusivity with these parameters and $\nu = 10^{13}\text{s}^1$ are shown in the upper inset of Figure 3.9a. The island diffusivity is reasonably consistent with the ORNL observations, except that the effective exponent is somewhat lower at $\beta_{\text{eff}} \approx 0.89$. Pit diffusivity is substantially higher than island diffusivity with an effective exponent of $\beta_{\text{eff}} \approx 1.29$. This latter feature appears inconsistent with the experimental observations described above.

Our general analysis of model behavior in Section 3.3 indicates that since pit diffusivity is elevated above island diffusivity choosing $\delta = 0.233$eV above, these diffusivities will become comparable for somewhat lower δ (and that island diffusivity would dominate that for pits for even lower δ). Indeed, KMC results shown in the central frame of Figure 3.9 for $\delta = 0.18$eV and $\phi = 0.27$eV (retaining $E_e = 0.291$eV) with $\nu = 1013\text{s}^1$ reveal similar values for pit and island diffusivity, which also reasonably matches the ORNL data for islands. The corresponding effective size-scaling exponents are $\beta_{\text{eff}} \approx 1.06$ for islands and $\beta_{\text{eff}} \approx 1.17$ for pits, also quite consistent with the ORNL data. (As an aside, our change from the first to the second parameter set was guided by knowledge of the overall barrier of $E_{\text{act}} = E_e + 2\phi + \delta$ for pit diffusion and for nucleation-mediated island diffusion for moderate sizes, but $E_{\text{act}} = E_e + \phi + \delta$ for larger sizes. This prompted our increase of ϕ by 0.03eV upon decreasing δ by 0.053eV to roughly preserve E_{act} and thus the magnitude of island diffusivity matching ORNL data.)

Thus, we conclude that the modified choice of model parameters, $\delta = 0.18$eV and $\phi = 0.27$eV, better describes behavior in the Ag(100) system. This choice does not exactly match either the PBEsol or the PBE values. However, we have mentioned the significant difference between these values, reflecting limitations in DFT analysis of energetics. It is appropriate to note that this choice of δ is fairly consistent with a previous estimate of $\delta = 0.16$eV (assuming that $E_e = 0.25$eV) from modeling of comprehensive data for multilayer homoepitaxy on Ag(100) from 50 to $300K$. [36,37] The key feature in the film growth study was that the presence of a significant kink rounding barrier means that submonolayer islands become irregular at lower T below $200K$. [38] This contrasts their typical near-square shape with close-packed edges at higher T. Since the EhrlichSchwoebel barrier for a kinked step is lower than that for a close-packed step, the island shape change impacts the roughness of multilayer films. [36, 37]

3.5 Conclusions

This study has provided a comprehensive analysis of the dependence on size, N, of PD-mediated vacancy pit diffusion, D_N, on metal(100) surfaces. The analysis was based on KMC simulation of a tailored stochastic lattice-gas model appropriate for these systems. We find size-scaling for D_N deviating from predictions of macroscopic theory for a range of experimentally relevant sizes, N. In addition, strong cyclical variation of D_N with N is observed for sizes $N \leq O(10^2)$ for typical model parameters, where the "period" reflects the varying size-increment between successive "perfect" cluster sizes, N_p. Results are compared against recent comprehensive analysis of D_N versus N for adatom islands which also exhibited anomalous size-scaling and strong oscillations. However, detailed behavior differs for pits and islands: diffusivity is maximized for perfect sizes $N = N_p$ for pits versus facile sizes $N = N_p + 1$ for islands. Distinct branches of facile and nucleation-mediated diffusion with different effective barriers for moderate sizes exist for islands, but not for pits. The values of D_N can be significantly higher (lower) for islands than for pits for large (small)

kink rounding barriers, reflecting the feature that all pathways for island diffusion must overcome this barrier, but not for pit diffusion.

Our analysis of pit versus island diffusion for the Ag(100) system exploits all existing experimental data for this system. We discuss some inconsistencies in the data, but conclude that the ORNL data provides the most accurate values for DN for adatom islands, and that diffusivity for islands and pits of the same size are similar. On the basis of these interpretations, our simulation model reasonably recovers experimental behavior with the parameter choice $E_e \approx 0.29$eV, $\delta \approx 0.18$eV, $\phi \approx 0.27$eV, and $\nu = 10^{13}\text{s}^1$. Other slightly modified choices of parameters could likely also give reasonable fits to data, e.g., selecting somewhat lower values of both ϕ and ν. Finally, for the above parameter choice, we find effective size-scaling exponents of βeff ≈ 1.06 for islands and $\beta_{\text{eff}} \approx 1.17$ for pits for the relevant range of experimental sizes, quite consistent with the ORNL island diffusion data where $\beta_{\text{eff}} \approx 1.15$.

3.6 Supporting Information

The Supporting Information is available free of charge on the ACS Publications website at DOI: 10.1021/acs.jpcc.7b12527.

Connectivity constraints in the stochastic model, equilibrium monomer vacancy population, short-time diffusivity for pits, cyclic variation of diffusivity DN with size N for vacancy pits, Arrhenius behavior of DN for pits, combinatorial analysis for pit configurations, tabulated diffusivity for pits, and experimental observations regarding diffusing pits

3.7 Acknowledgments

We thank Professor Katrina Morgenstern for valuable discussions on the potential role of strain in enhancing cluster diffusivity. K.C.L., P.A.T., and J.W.E. were supported for this work by NSF Grant CHE-1507223. K.C.L. and J.W.E. performed detailed KMC analysis and developed theoretical interpretations of the data. P.A.T. provided experimental

data and insights. D.-J.L. was supported by the USDOE, Office of Science, Basic Energy Sciences, Division of Chemical Sciences, Geosciences, and Biological Sciences, and his work was performed at Ames Laboratory which is operated by Iowa State University for the US-DOE under Contract DE-AC02-07CH11358. D.-J.L. performed the initial KMC simulations comparing pit and island diffusivity.

Bibliography

[1] J.-M. Wen, S.-L. Chang, J. W. Burnett, J. W. Evans, and P. A. Thiel. Diffusion of Large Two-Dimensional Ag Clusters on Ag(100). *Phys. Rev. Lett.*, 73(19):2591–2594, 1994.

[2] Woei Wu Pai, Anna K. Swan, Zhenyu Zhang, and J. F. Wendelken. Island Diffusion and Coarsening on Metal (100) Surfaces. *Phys. Rev. Lett.*, 79(17):3210–3213, 1997.

[3] J. F. Wendelken, Anna K. Swan, Woei-Wu Pai, and J.-K. Zuo. Morphology and Energy Barriers in Homoepitaxial Growth and Coarsening: A Case Study for Cu(100) | Morphological Organization in Epitaxial Growth and Removal. *WORLD SCIENTIFIC*, 14:320–348, 1999.

[4] Patricia A. Thiel, Mingmin Shen, Da-Jiang Liu, and J. W. Evans. Coarsening of Two-Dimensional Nanoclusters on Metal Surfaces. *J. Phys. Chem. C*, 113(13):5047–5067, 2009.

[5] David S. Sholl and Rex. T. Skodje. Diffusion of Clusters of Atoms and Vacancies on Surfaces and the Dynamics of Diffusion-Driven Coarsening. *Phys. Rev. Lett.*, 75(17):3158–3161, 1995.

[6] Clinton DeW. Van Siclen. Single Jump Mechanisms for Large Cluster Diffusion on Metal Surfaces. *Phys. Rev. Lett.*, 75(8):1574–1577, 1995.

[7] Alexander Bogicevic, Shudun Liu, Joachim Jacobsen, Bengt Lundqvist, and Horia Metiu. Island migration caused by the motion of the atoms at the border: Size and temperature dependence of the diffusion coefficient. *Phys. Rev. B*, 57(16):R9459(R)–R9462, 1998.

[8] J. Heinonen, I. Koponen, J. Merikoski, and T. Ala-Nissila. Island Diffusion on Metal fcc (100) Surfaces. *Phys. Rev. Lett.*, 82(13):2733–2736, 1999.

[9] Greg Mills, Thomas R. Mattsson, Lone Møllnitz, and Horia Metiu. Simulations of mobility and evaporation rate of adsorbate islands on solid surfaces. *J. Chem. Phys.*, 111(18):8639–8650, 1999.

[10] Arthur F. Voter. Classically exact overlayer dynamics: Diffusion of rhodium clusters on Rh(100). *Phys. Rev. B*, 34(10):6819–6829, 1986.

[11] H. C. Kang, P. A. Thiel, and J. W. Evans. Cluster diffusivity: Structure, correlation, and scaling. *J. Chem. Phys.*, 93(12):9018–9025, 1990.

[12] Mingmin Shen, J.-M. Wen, C. J. Jenks, P. A. Thiel, Da-Jiang Liu, and J. W. Evans. Ripening of monolayer vacancy pits on metal surfaces: Pathways, energetics, and size-scaling for Ag(111) versus Ag(100). *Phys. Rev. B*, 75(24):245409, 2007.

[13] Xin Ge and Karina Morgenstern. Ehrlich-Schwoebel barrier and interface-limited decay in island kinetics on Ag(100). *Phys. Rev. B*, 85(4):045417, 2012.

[14] S. V. Khare, N. C. Bartelt, and T. L. Einstein. Diffusion of Monolayer Adatom and Vacancy Clusters: Langevin Analysis and Monte Carlo Simulations of their Brownian Motion. *Phys. Rev. Lett.*, 75(11):2148–2151, 1995.

[15] S. V. Khare and T. L. Einstein. Unified view of step-edge kinetics and fluctuations. *Phys. Rev. B*, 57(8):4782–4797, 1998.

[16] J. Krug, H. T. Dobbs, and S. Majaniemi. Adatom mobility for the solid-on-solid model. *Z. Phys. B: Condens. Matter*, 97(2):281–291, 1995.

[17] Da-Jiang Liu, C. R. Stoldt, P. A. Thiel, and J. W. Evans. Sintering of Metal(100) Homoepitaxial Islands: Kink Rounding Barriers, Modified Size Scaling, and Experimental Behavior. *MRS Online Proceedings Library Archive*, 749, 2002.

[18] K. Binder and M. H. Kalos. "Critical clusters" in a supersaturated vapor: Theory and Monte Carlo simulation. *J. Stat. Phys.*, 22(3):363–396, 1980.

[19] Karina Morgenstern, Georg Rosenfeld, Bene Poelsema, and George Comsa. Brownian Motion of Vacancy Islands on Ag(111). *Phys. Rev. Lett.*, 74(11):2058–2061, 1995.

[20] Karina Morgenstern. Fast scanning tunnelling microscopy as a tool to understand changes on metal surfaces: from nanostructures to single atoms. *Phys. Status Solidi B*, 242(4):773–796, 2005.

[21] Dietmar C. Schlößer, Karina Morgenstern, Laurens K. Verheij, Georg Rosenfeld, Flemming Besenbacher, and George Comsa. Kinetics of island diffusion on Cu(111) and Ag(111) studied with variable-temperature STM. *Surf. Sci.*, 465(1):19–39, 2000.

[22] J.-M. Wen, J. W. Evans, M. C. Bartelt, J. W. Burnett, and P. A. Thiel. Coarsening Mechanisms in a Metal Film: From Cluster Diffusion to Vacancy Ripening. *Phys. Rev. Lett.*, 76(4):652–655, 1996.

[23] King C. Lai, James W. Evans, and Da-Jiang Liu. Communication: Diverse nanoscale cluster dynamics: Diffusion of 2D epitaxial clusters. *J. Chem. Phys.*, 147(20):201101, 2017.

[24] King C. Lai, Da-Jiang Liu, and James W. Evans. Diffusion of two-dimensional epitaxial clusters on metal (100) surfaces: Facile versus nucleation-mediated behavior and their merging for larger sizes. *Phys. Rev. B*, 96(23):235406, 2017.

[25] Da-Jiang Liu and J. W. Evans. Sintering of two-dimensional nanoclusters in metal(100) homoepitaxial systems: Deviations from predictions of Mullins continuum theory. *Phys. Rev. B*, 66(16):165407, 2002.

[26] J. W. Evans, P. A. Thiel, and M. C. Bartelt. Morphological evolution during epitaxial thin film growth: Formation of 2D islands and 3D mounds. *Surf. Sci. Rep.*, 61(1):1–128, 2006.

[27] Craig Rottman and Michael Wortis. Exact equilibrium crystal shapes at nonzero temperature in two dimensions. *Phys. Rev. B*, 24(11):6274–6277, 1981.

[28] T. J. Stasevich, T. L. Einstein, and Sergey Stolbov. Extended lattice gas interactions of Cu on Cu(111) and Cu(001): Ab initio evaluation and implications. *Phys. Rev. B*, 73(11):115426, 2006.

[29] Yong Han, Da-Jiang Liu, and James W. Evans. Real-Time Ab Initio KMC Simulation of the Self-Assembly and Sintering of Bimetallic Epitaxial Nanoclusters: Au + Ag on Ag(100). *Nano Lett.*, 14(8):4646–4652, 2014.

[30] Yong Han, Conrad R. Stoldt, Patricia A. Thiel, and James W. Evans. Ab Initio Thermodynamics and Kinetics for Coalescence of Two-Dimensional Nanoislands and Nanopits on Metal (100) Surfaces. *J. Phys. Chem. C*, 120(38):21617–21630, 2016.

[31] George E Andrews and Kimmo Eriksson. *Integer partitions*. Cambridge University Press, 2004.

[32] O. Kurnosikov, J. H. Nietsch, M. Sicot, H. J. M. Swagten, and B. Koopmans. Long-Range Electron Interferences at a Metal Surface Induced by Buried Nanocavities. *Phys. Rev. Lett.*, 102(6):066101, 2009.

[33] O. Kurnosikov, J. H. Nietsch, M. Sicot, H. J. M. Swagten, and B. Koopmans. Long-Range Electron Interferences at a Metal Surface Induced by Buried Nanocavities. *Phys. Rev. Lett.*, 102(6):066101, 2009.

[34] Carsten Sprodowski and Karina Morgenstern. Three types of bulk impurity induced interference patterns on the (100) and (111) faces of Ne- and Ar-doped silver. *Phys. Rev. B*, 82(16):165444, 2010.

[35] C. R. Stoldt, C. J. Jenks, P. A. Thiel, A. M. Cadilhe, and J. W. Evans. Smoluchowski ripening of Ag islands on Ag(100). *J. Chem. Phys.*, 111(11):5157–5166, 1999.

[36] K. J. Caspersen, C. R. Stoldt, A. R. Layson, M. C. Bartelt, P. A. Thiel, and J. W. Evans. Morphology of multilayer Ag/Ag(100) films versus deposition temperature: STM analysis and atomistic lattice-gas modeling. *Phys. Rev. B*, 63(8):085401, 2001.

[37] K. J. Caspersen, A. R. Layson, C. R. Stoldt, V. Fournee, P. A. Thiel, and J. W. Evans. Development and ordering of mounds during metal(100) homoepitaxy. *Phys. Rev. B*, 65(19):193407, 2002.

[38] S. Frank, H. Wedler, R. J. Behm, J. Rottler, P. Maass, K. J. Caspersen, C. R. Stoldt, P. A. Thiel, and J. W. Evans. Approaching the low-temperature limit in nucleation and two-dimensional growth of fcc (100) metal films Ag/Ag(100). *Phys. Rev. B*, 66(15):155435, 2002.

CHAPTER 4. STRUCTURE OF POLYDISPERSE FCC NANOCRYSTALS: IMPLICATIONS FOR CRYSTAL FRACTIONALIZATION

A paper published in *Journal of Physical Chemistry C*

King Chun Lai, Xun Zha, James W. Evans, Alex Travesset

[1]*Department of Physics and Astronomy, Iowa State University, Ames, Iowa 50011, USA*

[2]*Ames Laboratory-USDOE, Iowa State University, Ames, Iowa 50011, USA*

(Received 6 January 2019; published 11 April 2019)

Abstract

Synthesis of nanocrystals yields polydisperse distributions, which not only implies a distribution of nanocrystal sizes, but also of shapes. Noting that the synthesis products often reflect kinetic effects and may not reflect minimum energy states, we propose that the nanocrystals (gold, silver, platinum, *etc.*) typically used in self-assembly and directed-assembly experiments consist predominantly of variations of single-crystal fcc truncated octahedra with closed shells of atoms. Between each consecutive pair of "magic number" (maximally symmetric) truncated octahedra, we identify 49 sizes with some degeneracy, for a total of 70 distinct closed-shell configurations. Energetic and geometric features of the nanocrystals for these special sizes are analyzed. Combining these results with previous theoretical models, we discuss the implications for crystal fractionalization, where polydisperse nanocrystals spontaneously phase separate into a single and multiple binary superlattices.

We show that under very general conditions, the binary superlattice phases follow the order $MgZn_2$, $CaCu_3$, AlB_2 and $NaZn_{13}$ for increasing polydispersity. Other phases are less frequent, but also possible.

DOI: 10.1021/acs.jpcc.9b00146

4.1 Introduction

Common metals such as gold, silver, copper, platinum, or palladium with bulk fcc structure can self-assembly into single-crystal fcc nanoclusters or nanocrystals (NCs). Experimental techniques are available for generating large quantities of such NCs with diameters of a few nanometers, as described, for example, in Ref. [1–7]. The outcome of all these methods is a distribution of NCs with average diameter $\langle D \rangle$ and standard deviation σ such that polydispersity $\delta \equiv \sigma / \langle D \rangle$ varies from 0.01 to 0.25 (*i.e.*, $1 - 25\%$). This polydispersity plays a significant role in NC self-assembly [8–13]. Recent experimental and theoretical work [14,15] has revealed crystal fractionalization, where polydisperse NCs crystallize into phase-separated single-component fcc superlattice domains and binary $MgZn_2$ Frank-Kasper superlattice domains. Interestingly, analogous behavior has been observed in simulations of polydisperse hard spheres [16,17]. Another intriguing example has been provided in Ref. [18], where a $MgZn_2$ phase has been assembled from single-component hydrocarbon capped Au NCs. Given the considerable polydispersity in those experiments (about 16%), it seems very likely that the emergence of the binary $MgZn_2$ superlattice phase is also the result of crystal fractionalization.

Besides a distribution of NC diameters, polydispersity implies also a distribution of NC shapes. It is the goal for this paper to characterize the Polydisperse NC Distributions (PNCD) reflecting those utilized in self-assembly experiments. We first review several experimental studies, where PNCD have been characterized, *e.g.* Ref. [2–6,19–21]. In Ref. [3], for example, it was reported that gold NCs passivated by self-assembled monolayers of straight-chain alkylthiolate molecules exhibit the shape of truncated octahedra (TO). As

described in Ref. [4], it is relatively straightforward to produce small diameter ($D_0 = 1 - 2$ nm) NCs by initiating synthesis with large thiol-to-gold ratios. Larger diameters, D, are possible by reducing the amount of alkylthiolate molecules or, for example, as described in Ref. [2], by starting with rapidly formed small diameter D_0 NCs and continuing synthesis for a reaction time, t. The latter results in a Gaussian distribution of NC sizes with mean diameter satisfying $\langle D(t)\rangle/D_0 = [(1 - D_0/D_\infty)\exp(-\gamma t) + (D_0/D_\infty)]^{-1}$, and with $\gamma \approx 0.035$ min^{-1}, and a typical saturation value of $D_\infty = 12 - 45$ nm. The standard deviation σ also follows the same time dependence. These studies serve to illustrate that these PNCD are controlled by the synthesis kinetics, and the TO shape of NCs indicates that they have a single-crystal fcc structure. The latter implies that they are not necessarily in fully-equilibrated ground states which theoretical studies indicate can be dominated by non-fcc icosohedral, decahedral, and even amorphous structures for small sizes. See the Supporting Information [3, 22–31].

The goal of this study, however, is not to characterize fully equilibrated NCs, but instead those PNCD utilized in NC self-assembly experiments. [32, 33] Again, these PNCD are intrinsically non-equilibrium distributions that reflect the kinetics of the synthesis process, and any subsequent post-synthesis processing or filtering, see Ref. [34]. Based on the above observations, our goal is to generate sets of fcc TO NCs from which we can generate PNCD mimicking those used in self-assembled experiments. These TO NCs expose (100) (square) and (111) (hexagonal) fcc faces. However, well-known symmetric regular NCs only occur for certain very sparse sizes with "magic numbers" of atoms [35]. These magic sizes (in atoms) are

$$N_a^{TO}(n) = 16n^3 + 15n^2 + 6n + 1 \ , \tag{4.1}$$

giving $N_a = 38, 201, 586, 1289, 2406, 4033, 6266, \cdots$ as the smallest possible clusters. The integer n is the edge length in unit of nearest-neighbor distance (*i.e.*, edges have $n+1$ atoms) defining both (100) and (111) facet boundaries. Less symmetric clusters were considered in Ref. [36] by defining two integers (n, m) such that n is the edge length defining the (111)

facet boundaries and $m = n - k$ those adjoining (111) and (100) facets. These are labeled $\mathrm{TO}_n^{|k|-}$ $(-4 \leq k < 0, n > 1)$ and TO_n^{k+} $(0 < k \leq 4, n > 1)$. The magic numbers are (adapted from Ref. [23])

$$N_a^{TO}(n,k) = \frac{1}{3}(3 - 11k + 15k^2 - 10k^3 + 18n - 54kn + 54k^2n + 45n^2 - 90kn^2 + 48n^3) \ . \quad (4.2)$$

It was reported that the following 5 TO^+ clusters $N_a^{TO+} = 79(n = 2), 314(n = 3)$, $N_a^{TO2+} = 140(n = 3), 459(n = 4)$ and $N_a^{TO3+} = 225(n = 4)$ showed the highest stability [36].

One obvious conclusion from the above discussion is that even considering all available TO and $\mathrm{TO}_n^{k\pm}$ sizes, there would be insufficient NCs to generate the type of almost continuous PNCD observed in experiments. Therefore, many other sizes and related shapes must be considered.

In Sec.4.2, we present a basic model for fcc NC structure and energetics. This model is used to identify ground-state closed-shell TO structures which can be used to construct a realistic PNCD. We note that our model is simpler than other studies based on more refined energetics which focus on determining ground-state NC structures amongst all fcc or non-fcc possibilities. However, just analysis of fcc structures is relevant for our application, where our model not only recovers the basic features seen in refined studies, but also provides a more direct insight into these features (e.g., by identifying an extended set of low-energy closed-shell structures). In Sec.4.3, first we characterize the basic features of these selected TO NCs. Then, we discuss how to generate PNCD mimicking experiment from our family of TO NCs, and draw upon previous theoretical analyses to discuss crystal fractionalization for these distributions. In particular, we make predictions for the specific phases expected to emerge in crystal fractionalization as a function of the polydispersity of the PNCD. This general predictive framework also serves to explain the experimental observations of Ref. [18]. Finally, conclusions are provided in Sec.4.4.

4.2 Methods

4.2.1 Model formulation

For the fcc NCs under consideration, their energies are calculated within a simple model wherein atoms interact solely with nearest-neighbor (NN) attractive interactions (or bonds) of strength ϕ. Thus, the total NC energy is simply proportional to the total number of NN bonds. The effectiveness of this description has been promoted [37] based upon a recent DFT analysis [38] assessing fcc NC energetics for various metals. It is instructive to note that the NC energy in this model can also be computed exactly from the formula

$$E(N) = \gamma_{100} A_c(100) + \gamma_{111} A_c(111) + \beta_A L_A + \beta_B L_B + 24\alpha_{vert} - \epsilon_c N. \tag{4.3}$$

Here $\gamma_{100} = \frac{2\phi}{a^2}$ and $\gamma_{111} = \frac{\sqrt{3}\phi}{a^2}$ are the surface energies of the (100) and (111) fcc faces (see supporting information, with a as the separation of NN atoms), and $A_c(100)$ and $A_c(111)$ their respective areas (defined below); $\beta_A = \frac{\phi}{a}$ and $\beta_B = \frac{0.5\phi}{a}$ are edge energies where L_A (L_B) are the total length of edges adjoining (111) and (100) facets (pairs of (111) facets); and $\alpha_{vert} = 0.25\phi$ is the energy associated with each of the 24 vertices. In Eq. 4.3, the last term with $\epsilon_c = 6\phi$ corresponds to the bulk energy contribution, while the first two terms correspond to surface energy corrections, third and fourth correspond to edge corrections to over-counting broken bonds shared by neighboring facets, and the fifth term corresponds to the vertex correction to end point of edges with finite length.

In Eq. 4.3, the length of edges is defined as the distance between vertex atoms. The area $A_c(i)$ of facets is the product of number of hollow sites on the facet and area per hollow site on a facet (a^2 for (100); $\frac{\sqrt{3}}{2}a^2$ for (111)). See Fig. 4.1a, a "hollow site" is the natural adsorption site with the atom maximally coordinated to 4[3] atoms on a (100)[(111)] facet. Both fcc and hcp hollow sites exist on a (111) facet, but only the former are populated to propagate the single-crystal fcc structure. On a (100) face, an isolated atom placed in a "hollow site" acquires a coordination of 4, while on a (111) it acquires a coordination of 3.

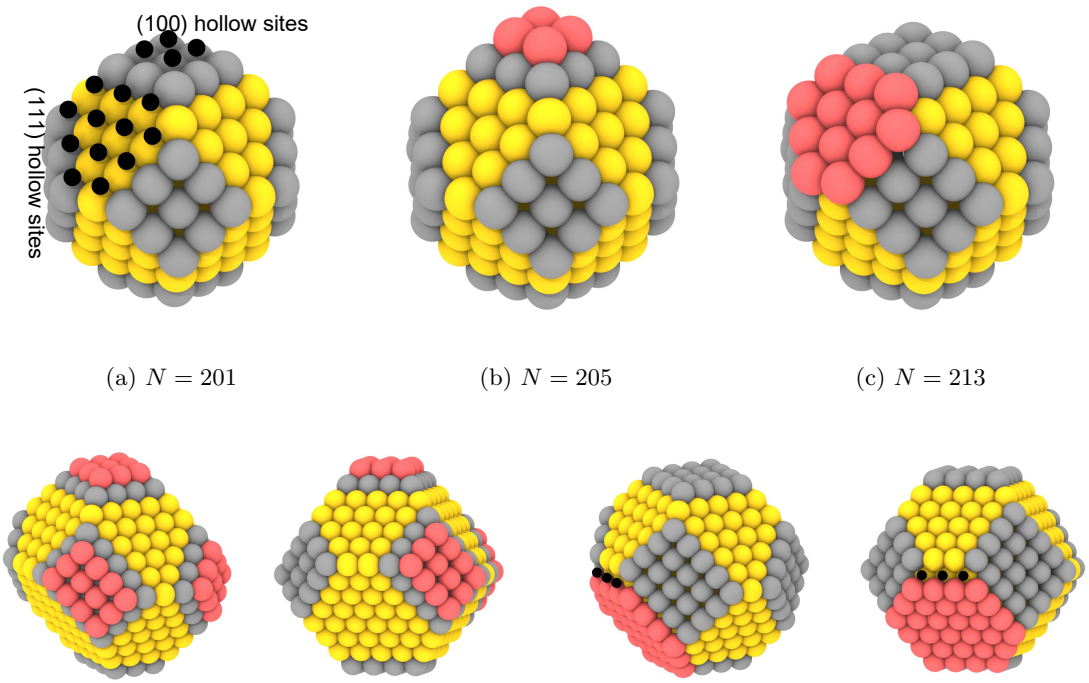

(a) $N = 201$ (b) $N = 205$ (c) $N = 213$

(d) $N = 567$ closed-shell (e) $N = 567$ open-shell

Figure 4.1: (a)–(c) show three closed-shell ground state configurations for $N = 201$, 205, and 213: (a) regular TO_{201} with hollow sites on two facets marked by black dots in smaller size; (b) TO_{205} with hollow sites on a (100) TO_{201} facet filled; (c) TO_{213} with hollow sites on a (111) TO_{201} facet filled. (d)–(e) show two configurations with $N = 567$ viewed from two angles: (d) is obtained by adding 30 atoms (marked as red) to (100) facets of $N = 537$ configuration to create a new closed-shell configuration; (e) is obtained by adding 30 atoms to a (111) facet of $N = 537$ configuration to create an open-shell configuration with 3 (111) hollow sites unfilled (marked as black smaller dots), and which we do not include in PNCD.

A simple analysis shows that the ratio of surface energies for extended (111) and (100) facets in our nearest-neighbor model satisfies

$$\frac{\gamma_{111}}{\gamma_{100}} = \frac{\sqrt{3}}{2} = 0.8660254. \tag{4.4}$$

It is natural to compare the model value Eq. 4.4 with those in a large data base of values for various metals determined from DFT analysis using the PBE functional [39]. Selected examples are shown in Table 4.1. We should note that there is some imprecision in these values partly since the PBE functional is not exact, and partly because relatively thin metal slabs were used in the analysis generating the database. For example, more extensive analysis using thicker slabs and retaining the PBE functional for Ag [40, 41] finds a ratio of 0.91 contrasting the data base value of 0.94. However, overall DFT values for the ratio Eq. 4.4 lie around the model value. Finally, we remark that effective values of ϕ for various metals can be perhaps most naturally extracted from DFT values for surface energies of the (111) facet which is dominant in NCs using the formulae listed above relating the γ's to ϕ's. These ϕ values are also listed in Table 4.1. These values were shown [37] to be quite consistent with those extracted from the above-mentioned DFT analysis [38]. However, we do emphasize that they are very different from effective values of $\phi(\text{bulk}) = \frac{E_c}{6}$ obtained by requiring ϕ recover the bulk cohesive energy, E_c [37]. As an aside, we note that the above

Table 4.1: nearest-neighbor separation a from Ref. [42, 43] ; DFT results of (100) and (111) surface energies and their ratio for different metals from Ref. [39]. The values of ϕ are obtained from $\gamma_{111} = \frac{\sqrt{3}\phi}{a^2}$.

Metal	a(Å)	γ_{111}(eV/Å^2)	γ_{100}(eV/Å^2)	$\gamma_{111}/\gamma_{100}$	$\phi(eV)$
Ag	2.89	0.048	0.051	0.94	0.232
Cu	2.55	0.082	0.092	0.89	0.308
Au	2.89	0.046	0.054	0.85	0.221
Pt	2.77	0.092	0.115	0.80	0.408
Pd	2.75	0.084	0.095	0.88	0.367

model can be naturally extended to treat twinned fcc structures such as I and Dh shapes by accounting strain energies through standard elasticity theory, see supporting information Fig. S1. For fcc shapes (TO, CO), there is no strain energy, and the model incorporating strain energy reduces to that above.

4.2.2 Criteria for constructing the PNCD

Next, we return to our central goal of constructing a PNCD for fcc NCs within our model by considering the optimal configuration for each size N with some additional restrictions. The actual PNCD will consist of NCs that meet these three conditions:

1. *Configurations maximize the number of bonds.* Fig. 4.1(a-c) shows a $N = 201$ magic size NC (Fig. 4.1a) and other ground states built from it: $N = 205$ (Fig. 4.1b) and $N = 213$ (Fig. 4.1c), showing the atoms added on red.

2. *Closed shell condition: All facets are smooth and complete.* This implies that all hollow sites within a given layer are either completely empty or filled, as is illustrated in Fig. 4.1(a-d).

3. *Degenerate ground states: If they exist, all such states must satisfy condition 2.* As an example of a doubly degenerate ground state occurs at $N = 567$, see Fig. 4.1. Fig. 4.1d satisfies both criteria 1,2, but the other ground state Fig. 4.1e has empty hollow sites as shown, and therefore violates this criterion.

The justification for the closed-shell condition (2-3) is provided by a Becker-Doering rate equation formulation analyzing the kinetics of NC formation [44–46]. This formulation accounts for reversible attachment-detachment of atoms to NCs where the ratio of the attachment to detachment rates reflects the change in NC energy according to the principle of detailed balance, *e.g.*, a small (large) decrease enhances (reduces) detachment relative to attachment rates. Thus, for closed-shell NC structures, the relatively low decrease in energy upon attaching an extra (low-coordinated) atom (see the Supporting Information), implies a high detachment rate for that atom. This suggests a kinetic enhancement of the populations of NCs with sizes corresponding to such closed-shells. It might also be noted that closed-shell configurations generally correspond to local minima in the NC energy per atom versus size. See Fig. 4.3 in Sec.4.3.

Based on the above criteria, we have devised an algorithm to generate all close-shell NCs that satisfy conditions 1-3. The algorithm proceeds by starting from a regular TO with a specific N, say 201, and sequentially adding atoms, one by one to fill facets arranging these atoms in near-square 2D arrays on incomplete facets to maintain the minimum energy for each size [47]. After a certain number of atoms are added, a complete facet is recovered leading to a larger closed-shell ground state structure satisfying all the required conditions, and which is incorporated into the PNCD. In this way, our process of generating all desired NCs mimics a situation where all shapes grow from an initial TO seed. (As an aside, we note that our algorithm has an intrinsic stability in the following sense. Even starting with a structure far from the ground state (e.g., a CO configuration), upon adding atoms the resulting structures do converge progressively towards ground-state TO structures. See the Supporting Information Fig. S1.)

4.2.3 Detailed Characterization of Closed-Shell Clusters

The TO clusters with magic sizes given by Eq. 4.1 for various n have been shown to be remarkably stable [35]. We therefore characterize the stable closed-shell configurations within the range of sizes $N_a^{TO}(n) \leq N < N_a^{TO}(n+1)$. We identify 49 N's where stable NCs exist with some degeneracy, (denoted by Ω_N,) for a total of 70 configurations, see Table 4.2. In the supporting information, we provide snapshots for all the different configurations. It follows from our results, that the configurations in the interval $[N_a^{TO}(n), N_a^{TO}(n+1))$ can be readily mapped on to those in the $[N_a^{TO}(n+1), N_a^{TO}(n+2))$ interval. For example, those in the interval $N = [201, 586)$ are mapped onto those in the interval $N = [586, 1289)$, where, for example, $N = 201, 225, 314, 459$ would be mapped to $N = 586, 637, 807, 1072$ corresponding to adding just one more atom to all edges. For this reason, it is only necessary to characterize structures within one interval, say $N = [201, 586)$. Refer to supporting information Fig. S5 for a detailed illustration, of the construction algorithm. As an aside, we note that CO are never ground states due to their large (100) facets relative to (111) facets.

Table 4.2: Table of sizes N of stable TOs in the period $(N_a^{TO}(2) \leq N < N_a^{TO}(5))$. Ω_N denotes the ground state degeneracy for size N. Note that the configurations obtained by rotational or mirror transformations are not included. The red N correspond to regular TO's; green N correspond to NCs with TO^+ or TO^- at one of the ground state(s).

$n = m = 2$									
N	Ω_N	N	Ω_N	N	Ω_N	N	Ω_N	N	Ω_N
38	1	56	1	80	1	112	1	152	2
39	1	57	2	82	1	116	2	158	1
40	2	61	1	86	1	120	1	162	1
41	3	63	1	88	1	124	2	166	3
43	1	65	1	90	2	128	3	170	2
45	1	68	1	94	3	132	2	176	1
47	1	70	2	98	1	136	1	182	1
48	2	71	2	102	1	140	2	186	1
52	1	75	1	104	2	144	1	192	1
54	1	79	1	108	1	148	1		

$n = m = 3$									
N	Ω_N	N	Ω_N	N	Ω_N	N	Ω_N	N	Ω_N
201	1	256	1	318	1	396	1	486	2
205	1	260	2	324	1	405	2	498	1
209	2	269	1	333	1	414	1	507	1
213	3	275	1	339	1	423	2	516	3
219	1	281	1	345	2	432	3	525	2
225	1	288	1	354	3	441	2	537	1
231	1	294	2	363	1	450	1	549	1
235	2	296	2	372	1	459	2	558	1
244	1	305	1	378	2	468	1	570	1
250	1	314	1	387	1	477	1		

N	Ω_N	N	Ω_N	N	Ω_N	N	Ω_N	N	Ω_N
586	1	698	1	816	1	960	1	1120	2
595	1	707	2	828	1	976	2	1140	1
604	2	723	1	844	1	992	1	1156	1
613	3	735	1	856	1	1008	2	1172	3
625	1	747	1	868	2	1024	3	1188	2
637	1	760	1	884	3	1040	2	1208	1
649	1	772	2	900	1	1056	1	1228	1
658	2	775	2	916	1	1072	2	1244	1
674	1	791	1	928	2	1088	1	1264	1
686	1	807	1	944	1	1104	1		

In counting degenerate structures, we did not include those that are related by proper or improper (mirror) rotations. Just to illustrate how the degeneracy is counted, let us consider the $N = 213$ case. There are four hollow sites on each of the six (100) facets (being filled up in Fig. 4.1b from 4.1a on the $N = 201$ cluster) and twelve hollow sites on each of the eight (111) facets (being filled up in Fig. 4.1c from 4.1a). So using $N = 201$ as a base cluster, one can construct $N = 205$ by adding four extra atoms on top of one of the (100) facets. Then by filling up two (100) facets gives $N = 209$, with degeneracy of two (filling up two perpendicular or parallel (100) facets).

We can also fill up three empty (100) facets to have $N = 213$ (giving two degenerate shapes). However, these twelve new atoms added on $N = 201$'s (100) facets can be re-grouped on one single (111) facet with same number (sixty five) of bonds formed. Thus, there is a degeneracy of three for $N = 213$.

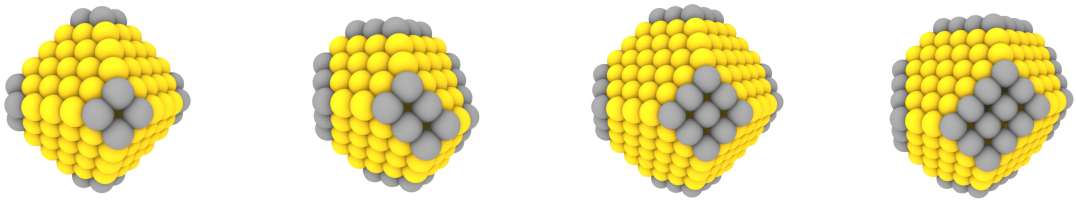

(a) $N = 225$ symmetric (b) $N = 225$ (c) $N = 459$ symmetric (d) $N = 459$

Figure 4.2: (a)–(b) show structures for $N = 225$: (a) A symmetric TO^+ closed-shell with 1068 NN bonds which is not a ground state configuration; (b) A less symmetric closed-shell configuration with 1070 NN bonds which is a ground state. (c)–(d) show structures for $N = 459$: (c) A symmetric TO^+ closed-shell configuration; and (d) a less symmetric closed-shell configuration. Both are ground states with 2304 NN bonds.

It should not be assumed that TO^{k+} configurations are automatically ground states. For example, at $N = 225$ the $(5, 2)$ TO^{3+} configuration Fig. 4.2a is not a ground state, as the more irregular configuration Fig. 4.2b has lower energy. See Supporting Information Fig. S5 for views of the ground state shown in Fig. 4.2b. Another interesting example is the

$N = 459$ configuration TO^{2+} $(n = 5, m = 3)$, which, as shown in Fig. 4.2c, has the same energy as the more irregular Fig. 4.2d.

4.3 Discussion

4.3.1 Properties for selected TO NCs

The Wulff theorem [48] establishes that the equilibrium configuration of macroscopic crystalline fcc clusters based on our model with nearest-neighbor interactions is a regular TO. Considering the N as a continuous variable, we can obtain a fit, $E_{Fit}(N)$, to the energy of regular TO in the form or a polynomial [29,31,49] in $N^{1/3}$ (where $N^{1/3}$ reflects the linear NC size) with four fitting parameters of the form

$$E_{Fit}(N) = a_0 + a_1 N^{1/3} + a_2 N^{2/3} + a_3 N. \tag{4.5}$$

This form should be compared with Eq. 4.3. These four parameters are determined by matching our calculated energies for regular TO with sizes $N = 38, 201, 586, 1289$. In this analysis, the parameters used in $E_{Fit}(N)$ are $a_0 = -1.59\phi, a_1 = 6.07 \times 10^{-2}\phi, a_2 = 7.554\phi$, and $a_3 = -6.00\phi$.

In our actual analysis, N is not continuous but rather a discrete number of atoms in the NC, and furthermore nanoscale clusters typically do not have such high symmetry as regular TO. However, it is natural to consider deviations in the actual energy E_N from that of a hypothetical regular TO with size N and energy $E_{Fit}(N)$. This discrepancy of energy per atom, $\Delta E(N) = (E_N - E_{Fit}(N))/N$ can be considered as providing a quantitative assessment of how energetically favorable a size N is relative to the hypothetical minimum energy regular TO.

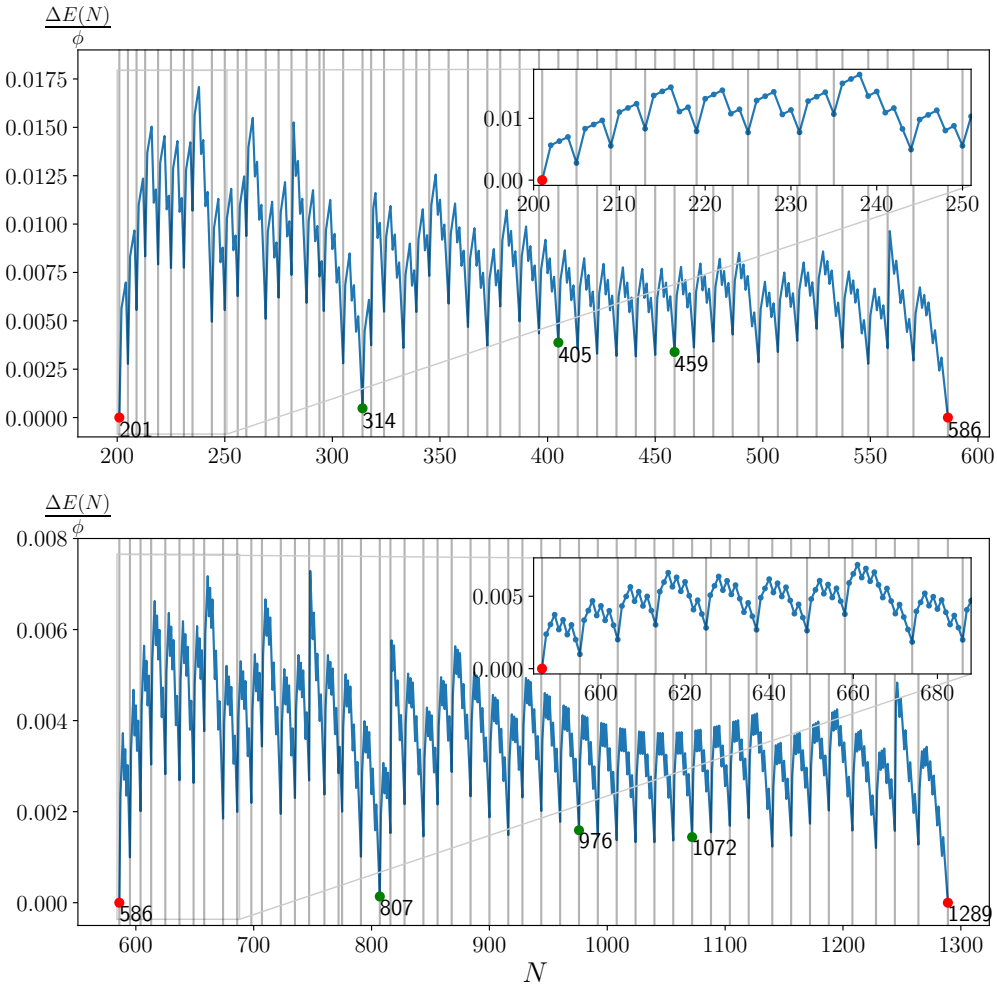

Figure 4.3: Plot of discrepancy of energy per atom with discrete N from a continuous N. The vertical grid-lines correspond to sizes with ground state(s) only in closed-shell, listed in Tab. 4.2; red dots represent N in regular TO shape, green dots represent TO^+ or TO^-. Insets are zoom-in versions of $201 \leq N \leq 250$ (upper), $586 \leq N \leq 686$ (lower).

Comprehensive results are shown in Fig. 4.3 for $\Delta E(N)$ for $201 \leq N \leq 1289$ not just for closed-shell clusters, but also for other sizes generated by our algorithm with open-shell structures constructed as described in Sec.4.2 and also in the supplementary information. A similar representation of NC energetics was applied in Ref. [29] where interactions were

described by the many-body Embedded Atom Method (EAM) and energy minimization achieved with a Monte Carlo approach, and also in other refined modeling of fcc and non-fcc ground state NCs [31, 49]. Our results show that same features can clearly be captured within our nearest-neighbor interaction model. The local minima correspond to sizes with ground state(s) only in closed-shell shape(s) - the focus of this paper. Furthermore, the pattern repeats between two regular TO magic numbers as also shown in Fig. 4.3.

One relevant measure of NC structure, particularly in the context of self-assembly, is the sphericity defined as

$$Sph = \frac{(36\pi)^{\frac{1}{3}} V^{\frac{2}{3}}}{A} \tag{4.6}$$

where A is the area and V the volume of the NC. In general, $Sph \leq 1$ with $Sph = 1$ corresponds to a perfectly spherical shape. As shown in Fig. 4.4 the clusters are quite spherical with Sph converging for large size to a value $Sph_\infty = \frac{4}{1+2\sqrt{3}} \left(\frac{\pi}{3}\right)^{\frac{1}{3}} \approx 0.90992$ corresponding to a symmetric regular TO.

The effective radius, R, of the NC may be defined by the formula (cf. Ref. [50, 51])

$$4\pi R^2 = A, \tag{4.7}$$

where A is the area of the outer surface of the NC. Within this definition, NCs of the same diameter have a single value for the surface area, and also identical grafting densities when capped with the same number of ligands. An alternative definition for radius R_V is provided by $4\pi R_V^3 = 3V$, and R_V is related to R by $\frac{R}{R_V} = \frac{1}{\sqrt{Sph}} > 1$. It will be more convenient to report NC diameters $D = 2R$ or $D_V = 2R_V$. Either choice should satisfy D or $D_V \propto N^{\frac{1}{3}}$ at large N. The small discrepancy in the exponent (0.37 vs $\frac{1}{3} \approx 0.33$) observed in Fig. 4.4 is due to the discrete sizes not fitting exactly in the continuous TO shape. The discrepancy will decrease for larger N.

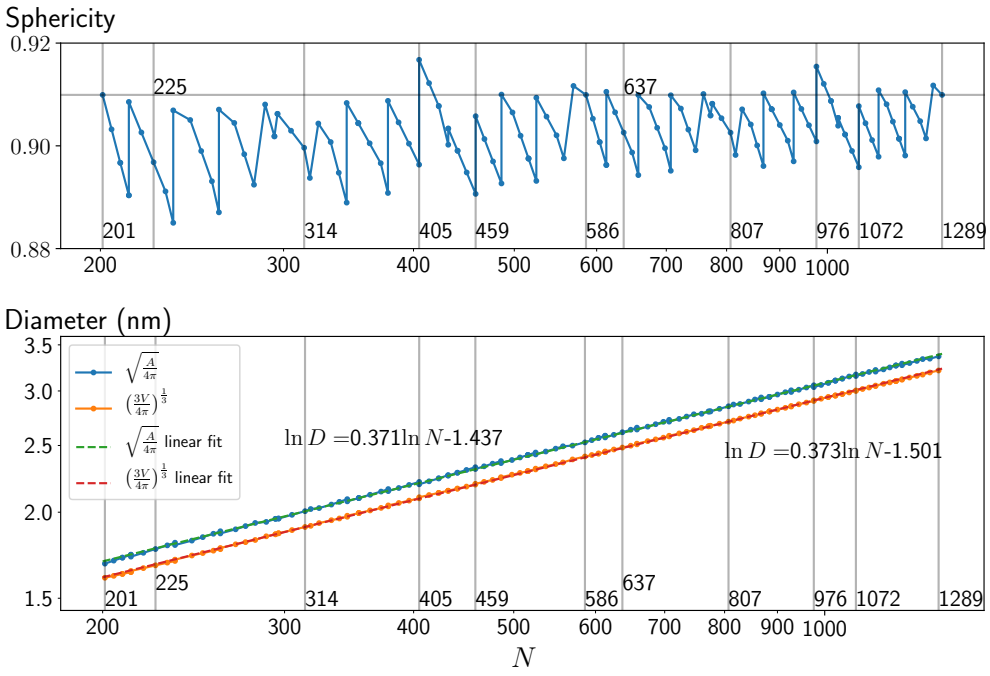

Figure 4.4: Two periods, $201 \leq N < 586$ and $586 \leq N < 1289$ are shown with some values N mentioned in discussion labeled. Sphericity: Regular TO's with area $A = \left(6 + 12\sqrt{3}\right) a^2$ and volume $V = 8\sqrt{2}a^3$ have sphericity $\frac{4}{1+2\sqrt{3}} \left(\frac{\pi}{3}\right)^{\frac{1}{3}} \approx 0.91$. Diameter: Calculated from surface area and volume assuming spherical shapes. Here we use the lattice constant 4.078 Å for Au.

4.3.2 Polydisperse NC size dDistributions and crystal fractionalization

PNCD used in the self-assembly studies of interest here are reasonably described by Gaussian distributions of diameter, D, according to

$$P(D) = \frac{1}{\sqrt{2\pi}\sigma} \exp\left(-\frac{(D - \langle D \rangle)^2}{2\sigma^2}\right) \tag{4.8}$$

where again $\langle D \rangle$ is the average diameter, σ is the standard deviation, corresponding to polydispersity $\delta \equiv \sigma / \langle D \rangle$. As a first example, we will consider mean diameters $\langle D \rangle =$ 1.68, 2.53, and 3.37 nm (using the Au lattice constant 4.078 Å), corresponding to TO

(n=2, 3, 4), with $N = 201, 586, 1289$ atoms, see Eq. 4.1. We then build NC distributions with polydispersity $\delta = 12\%$. This is done by sampling with the appropriate weight according to the Gaussian distribution of diameters from our constructed ensemble of NCs with different sizes. More specifically, this process involves sorting 350 NCs (with sizes ranging over 5 intervals between consecutive magic sizes 38 and above) by diameters, $d_1, d_2, \cdots, d_k, \cdots, d_n$, and obtain a diameter range associated with the kth NC $\Delta_k = \frac{d_{k+1}-d_{k-1}}{2}$. Then, the probability P_k of selecting the kth NC is given by $P_k \cdot \Delta_k = \Phi\left(\frac{d_{k+1}+d_k}{2}\right) - \Phi\left(\frac{d_k+d_{k-1}}{2}\right)$, where $\Phi(d)$ is the cumulative distribution function.

See Fig. 4.5 for the actual sizes and populations of NCs selected (indicated by the symbols) in the generated distribution. Note that a Gaussian distribution of diameters translates into a skewed distribution in sizes. It is clear from this plot that we have identified a sufficient number of closed-shell TO NCs to capture the quasi-continuous distribution of sizes observed in experiment. Thus, our ensembles of NCs can provide effective input for MD simulations of these systems.

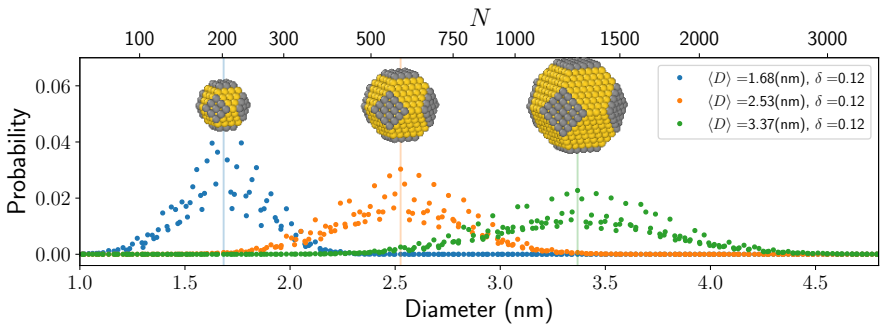

Figure 4.5: NC distributions with mean sizes around $N = 201, 586, 1289$, and polydispersity 12% sampled from our selected ground state closed-shell TO NCs.

As a relevant application, we will discuss the experiments reported by Hajiw *et al.* [18], and in this way show that the $MgZn_2$ superlattice phase is indeed the result of crystal fractionalization. The Orbifold Topological Model (OTM), described in Ref. [52, 53], provides

detailed criteria to assess the stability of binary NC superlattices (BNSLs) with different crystal structures formed by crystallization of a mixture of NCs with two different sizes. It was shown that the stability of binary structures is a function of the ratio of the two effective NC diameters, where the effective diameter is increased from the core diameter of the metallic fcc TO NC by accounting for the presence of ligands. Consideration of "vortex" configurations for the ligands is necessary for certain cases, but are not relevant in this example. In its simplest form, the fractional degree of expansion of NC diameter upon hydrocarbon ligand-capping (functionalization) is given by the Optimal Packing Model (OPM) formula [54]

$$\tau_\lambda = (1+3\lambda)^{\frac{1}{3}} \ , \tag{4.9}$$

where $\lambda = \frac{2L}{D}$ is the ratio between the maximum extended length of the ligand $L = 0.12(k+1) = 0.84$ (nm), with $k = 6$ for hexanethiol ligands, see Ref. [55] (k is the number of hydrocarbons) and the core diameter D. The effective "hard sphere" ratio of the two functionalized NCs with core diameters $D_A > D_B$ is then defined by

$$\gamma = \frac{D_B \cdot \tau_B}{D_A \cdot \tau_A} \ . \tag{4.10}$$

BNSLs appear when γ are close to critical values γ_c, which for the most relevant superlattice structures for the BNSL are given in Table 4.3, see Ref. [56] for details.

Table 4.3: Optimal values γ_c for most common BNSL structures.($\phi_c = \frac{2}{5+\sqrt{5}} \times \left(11+\sqrt{5}+2\sqrt{10(1+\sqrt{5})}\right)$)

BNSL	$MgZn_2$	$CaCu_5$	AlB_2	$NaZn_{13}$
γ_c	$\sqrt{\frac{2}{3}} \approx 0.8164$	$\frac{1+2\sqrt{19}}{15} \approx 0.6479$	$\frac{1}{\sqrt{3}} \approx 0.5774$	$\frac{1+\sqrt{\phi_c+1}}{\phi_c} \approx 0.5576$

Our formulation considers a Gaussian PNCD with mean diameter, $\langle D \rangle$, and large polydispersity, δ, which decomposes or phase separates into a central narrow Gaussian distribution corresponding to an fcc phase together with a series of BNSLs each of which corresponds to a pair of Gaussian PNCD with $\delta \leq 5\%$, and average diameters

$$D_{A/B} = (1 \pm \alpha)\langle D \rangle \quad \text{with} \quad \gamma(\alpha) = \gamma_c \ , \tag{4.11}$$

where $\gamma(\alpha)$ is given by Eq. 4.10 with the corresponding core diameters $D_{A/B}$. We point out that the diameter of the NC includes the hexanethiol ligands [18] in the OPM formula Eq. 4.10.

In Fig. 4.6, we consider a distribution of NCs with a nominal or mean diameter of $\langle D \rangle =$ 2.4 nm functionalized with hexanethiol and with a substantial $\delta = 16\%$ polydispersity, *i.e.*, the system described in Ref. [18]. We first decompose this distribution into sub-distributions of NCs, with polydispersity $\delta \leq 5\%$, forming mono-disperse fcc and $MgZn_2$ phases. The mean diameter of fcc sub-distribution is also $\langle D \rangle = 2.4$ nm, the polydispersity is 5%. The mean diameters of the two components of $MgZn_2$ phase are given by Eqs. 4.10 and 4.11, the polydispersity of component B is 5%, and the polydispersity of component A is obtained from $\delta_A = \frac{\sigma_A}{D_A}$, with $\sigma_A = \frac{\sigma_B}{2}$, (the factor 2 accounts for 2 in AB_2,) so that $\delta_{A/B} \leq 5\%$. We similarly extend this decomposition to account for other BNSL structures with larger γ's. The sum of the Gaussian distributions of the single component fcc superlattice and $MgZn_2$ phases adds up to $\sim 60.5\%$ of the original distribution, with fcc $\sim 31\%$, two components of the $MgZn_2$ phase $\sim 9.8\%$ and $\sim 19.5\%$ each. The rest NCs might be in $CaCu_5$, AlB_2, $NaZn_{13}$ phases, as shown Fig. 4.6(a–c) or amorphous. Fig.4.6 also shows the results of sampling our ensemble of closed-shell TO NCs for these individual Gaussian sub-distributions, naturally extending the procedure described above.

Upon decomposing the full NC distribution as illustrated in Fig. 4.6, it is clear that this large δ results in a significant presence of the fcc superlattice phase as well as the $MgZn_2$ BNSL. Among the other phases listed in Table 4.3, only $CaCu_5$ may appear in trace amounts. Should experiments be conducted with larger polydispersity δ, we predict that

phases at smaller γ_c would appear (see the Supplementary Information Fig. S2 for analysis of such cases with larger polydispersity).

In addition, for the decomposed distributions, Fig. 4.6 shows the closed-shell TO NCs from our ensemble which dominate not just the central narrow Gaussian distribution generating the fcc phase, but also those dominating the bimodal distributions in the wings which generate the binary phases. For the selected mean diameter $\langle D \rangle = 2.4$ nm capped with hexanethiol ligands and a large polydispersity 16%, the TO NC shown with size N = 507 dominates the fcc phase, and TO NCs shown with sizes N = 345 and 707 dominate the the $MgZn_2$ phase. This prediction could in principle be validated by detailed microscopy studies of these individual phases.

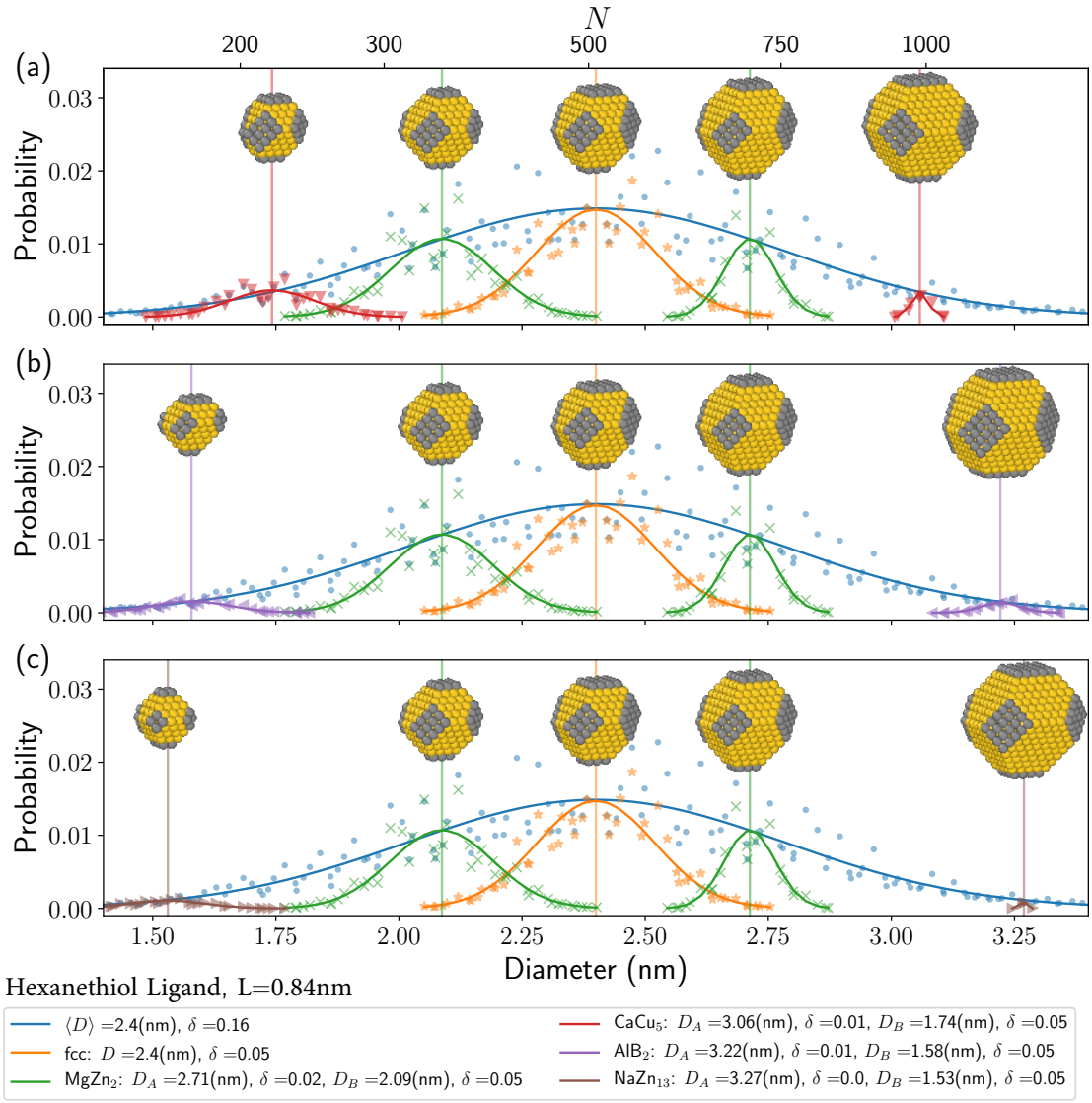

Figure 4.6: Decomposition of a Gaussian NC distribution with mean diameter $\langle D \rangle = 2.4$ nm capped with hexanethiol ligands and a large polydispersity 16%. (a) Decomposition into: a sub-distribution about $D = 2.4$ nm with polydispersity 5% forming monodisperse fcc superlattice; two sub-distributions about D_A and D_B with optimal ratio γ_c of $MgZn_2$; and an additional sub-distribution about the two diameters with optimal ratio for $CaCu_5$. (b) Same as (a) except the sub-distribution for $CaCu_5$ is replaced by one for AlB_2. (c) Same as (a) except the sub-distribution for $CaCu_5$ is replaced by one for $NaZn_{13}$. In these three cases, only $CaCu_5$ has significant population as a third minority phase.

4.4 Conclusions

In this paper, we have characterized the structure of fcc NCs constituting typical polydisperse fcc nanocrystal distributions utilized in self-assembly experiments. We have shown that in between each consecutive pair of regular truncated octahedra (with magic number sizes), there are exactly 49 sizes N, some with degeneracy, for a total of 70 distinct favorable closed-shell configurations. The full description of these configurations is given in supporting information Table S3. Although the overall polydisperse NC size distributions are kinetically controlled, the shapes of individual NCs within these distributions are close to ground state fcc structures as identified in experimental studies [28, 29, 31]. The constructed quasi-periodic sequence of sizes includes NC sizes matching those observed in mass spectroscopy, see Ref. [36]. Furthermore, the closed-shell configurations correspond to local minima of the energy per atom (Fig. 4.3), compatible with other theoretical studies [29, 31] utilizing different approaches. We therefore conclude that our results provide a realistic description of PNCD. Our generated ensemble of closed-shell fcc NC structures after appropriate functionalization (which a non-trivial task) will enable MD simulation crystal fractionalization based on these realistic polydisperse NC distributions.

Because the shapes of NCs in our ensemble are approximately spherical (see Fig. 4.4), addition of alkylthiolate ligands (for 1-6 nm diameters) will allow the resulting capped NCs to be quite accurately represented as spheres [50]. Thus, according to the proposal discussed above based on analysis for roughly spherical NCs, for increasing polydispersity, upon self-assembly one expects the appearance of a sequence of superlattice phases, see Ref. [52, 53]

$$\text{fcc/bcc} \rightarrow \text{MgZn}_2 \rightarrow \text{CaCu}_5 \rightarrow \text{AlB}_2/\text{NaZn}_{13} \rightarrow \text{Other phases: NaCl, bcc AB}_6, \textit{ etc.} \tag{4.12}$$

The polydispersity, δ, where each superlattice phase first has a significant presence may be estimated as discussed in supplementary information Fig. S3. One finds that the $MgZn_2$ superlattice phase is present in significant amounts roughly for $\delta \geq 6\%$, $CaCu_5$ for $\delta \geq 20\%$,

AlB_2 for $\delta \geq 32\%$ and $NaZn_{13}$ for $\delta \geq 36\%$. Particularly pertinent are the results of Hajiw *et al.* Ref. [18], where a $\delta = 16\%$ distribution of alkylthiolate gold NCs reported a $MgZn_2$ phase. Our results Fig. 4.6 clearly show that this $MgZn_2$ superlattice phase is the result of crystal fractionalization. What is remarkable about Ref. [18] is the high quality of the crystals reported, as the X-ray data includes more than 10 Bragg peaks. This suggests that crystal fractionalization may be a very efficient pathway to self-assembly of multiple binary phases. Further experimental evidence, including higher polydisperse samples to confirm the series in Eq. 4.12, will be necessary. We would like to emphasize that Fig. 4.6 and supplementary information Fig. S2, not only predict the crystal phases, but also the structure and shape of each of the NCs within the superlattice, as allowed by our detailed classification. This provides a test for our proposed PNCD that future experiments should be able to validate.

Experiments on aqueous dispersions of colloidal silica with high polydispersity $\delta = 18\%$ have also reported crystal fractionalization. Here, because there are no flexible capping ligands, vortices cannot develop and the possible phases are only those that are described by hard spheres [52]. Based on the sequence Eq. 4.12, at this level of polydispersity, there is the possibility of some small amounts of the $CaCu_5$ superlattice phase. We expect that further experimental studies will confirm this prediction.

Rather interestingly, Lindquist *et al.* [17] have reported crystal fractionalization for polydisperse hard spheres with $\delta = 12\%$ into a $MgZn_2$ superlattice phase, while Coslovich *et al.* [16] report an AlB_2 superlattice with a very broad distribution. These results show that such effects are highly universal, present even in the simplest of models, that is, hard spheres. The emergence of an AlB_2 superlattice for very broad distributions as described in Coslovich *et al.* [16] provides further evidence for the series in Eq. 4.12. Very recently, Bommineni et al. [57] have reported, for the first time, the $NaZn_{13}$ phase as a result of crystal fractionalization, in complete agreement with Eq. 4.12. They also report some more complex Frank-Kasper phases, which fit within existing descriptions of binary systems [56]

and will be analyzed elsewhere.

A remaining interesting question is into what structures the other possible shapes (I, Dh) will assemble. As shown in supplementary information, Fig. S1, the sphericity of Ino or Marks decahedral shapes, for example, is not that much different from TO. Still, the complexity of their shapes will make it challenging to functionalize uniformly and more likely, will result in a considerable anisotropy, which may significantly affect the optimal packing of the stable thermodynamic phases [58] as driven by shape.

4.5 Supporting Information

The Supporting Information is available free of charge on the ACS Publications website at DOI: 10.1021/acs.jpcc.9b00146.

Magic numbers and other considerations for non-fcc clusters; ratio of $\gamma_{111}/\gamma_{100}$ in our model; details of construction of ground-state NCs for any N; BeckerDoering formulation for NC populations; discussion of CO NCs; additional BNSL distributions; sphericities of NC configurations; and images of NCs and tables of cluster sizes.

4.6 Acknowledgments

A.T. acknowledges many discussions and clarification of their work with B. Pansu, I. Coropceanu, and D. Talapin. Interest and discussions are also acknowledged from S. Mallapragada and D. Vaknin. The work of A.T. and X.Z. is funded by NSF, DMR-CMMT 1606336 "CDS&E: Design Principles for Ordering Nanoparticles into Super-crystals". K.C.L. and J.W.E. were supported for analysis of 3D fcc NC structure versus size by the NSF grant CHE-1507223.

Bibliography

[1] Tadao Sugimoto. Preparation of monodispersed colloidal particles. *Advances in Colloid and Interface Science*, 28:65–108, January 1987.

[2] Ram Seshadri, G. N. Subbanna, V. Vijayakrishnan, G. U. Kulkarni, G. Ananthakrishna, and C. N. R. Rao. Growth of nanometric gold particles in solution phase. *J. Phys. Chem.*, 99(15):5639–5644, April 1995.

[3] Charles L. Cleveland, Uzi Landman, Marat N. Shafigullin, Peter W. Stephens, and Robert L. Whetten. Structural evolution of larger gold clusters. *Zeitschrift fr Physik D Atoms,Molecules and Clusters*, 40(1):503–508, March 1997.

[4] Mathew M. Maye and Chuan-Jian Zhong. Manipulating core-shell reactivities for processing nanoparticle sizes and shapes. *J. Mater. Chem.*, 10(8):1895–1901, 2000.

[5] Nikhil R. Jana, Latha Gearheart, and Catherine J. Murphy. Evidence for seed-mediated nucleation in the chemical reduction of gold salts to gold nanoparticles. *Chem. Mater.*, 13(7):2313–2322, July 2001.

[6] Shawn P. Shields, Vernal N. Richards, and William E. Buhro. Nucleation control of size and dispersity in aggregative nanoparticle growth. a study of the coarsening kinetics of thiolate-capped gold nanocrystals. *Chem. Mater.*, 22(10):3212–3225, May 2010.

[7] Nguyen T. K. Thanh, N. Maclean, and S. Mahiddine. Mechanisms of nucleation and growth of nanoparticles in solution. *Chem. Rev.*, 114(15):7610–7630, August 2014.

[8] Dmytro Nykypanchuk, Mathew M. Maye, Daniel van der Lelie, and Oleg Gang. Dna-guided crystallization of colloidal nanoparticles. *Nature*, 451(7178):549–552, 2008.

[9] Sung Yong Park, Abigail K. R. Lytton-Jean, Byeongdu Lee, Steven Weigand, George C. Schatz, and Chad A. Mirkin. DNA-programmable nanoparticle crystallization. *Nature*, 451(7178):553–556, 2008.

[10] Dmitri V. Talapin and Christopher B. Murray. PbSe Nanocrystal Solids for n- and p-Channel Thin Film Field-Effect Transistors. *Science*, 310(5745):86–89, 2005.

[11] Michael A. Boles, Michael Engel, and Dmitri V. Talapin. Self-Assembly of Colloidal Nanocrystals: From Intricate Structures to Functional Materials. *American Chemical Society*, 2016.

[12] Honghu Zhang, Wenjie Wang, Mufit Akinc, Surya Mallapragada, Alex Travesset, and David Vaknin. Assembling and ordering polymer-grafted nanoparticles in three dimensions. *Nanoscale*, 9(25):8710–8715, 2017.

[13] Honghu Zhang, Wenjie Wang, Surya Mallapragada, Alex Travesset, and David Vaknin. Macroscopic and tunable nanoparticle superlattices. *Nanoscale*, 9(1):164–171, 2016.

[14] Robert Botet, Bernard Cabane, Lucas Goehring, Joaquim Li, and Franck Artzner. How do polydisperse repulsive colloids crystallize? *Faraday Discuss.*, 186(0):229–240, 2016.

[15] Bernard Cabane, Joaquim Li, Franck Artzner, Robert Botet, Christophe Labbez, Guillaume Bareigts, Michael Sztucki, and Lucas Goehring. Hiding in Plain View: Colloidal Self-Assembly from Polydisperse Populations. *Phys. Rev. Lett.*, 116(20):208001, 2016.

[16] Daniele Coslovich, Misaki Ozawa, and Ludovic Berthier. Local order and crystallization of dense polydisperse hard spheres. *J. Phys.: Condens. Matter*, 30(14):144004, 2018.

[17] Beth A. Lindquist, Ryan B. Jadrich, and Thomas M. Truskett. Communication: From close-packed to topologically close-packed: Formation of Laves phases in moderately polydisperse hard-sphere mixtures. *J. Chem. Phys.*, 148(19):191101, 2018.

[18] Stéphanie Hajiw, Brigitte Pansu, and Jean-François Sadoc. Evidence for a C14 Frank–Kasper Phase in One-Size Gold Nanoparticle Superlattices. *American Chemical Society*, 2015.

[19] Kenji Koga, Tamio Ikeshoji, and Ko-ichi Sugawara. Size- and Temperature-Dependent Structural Transitions in Gold Nanoparticles. *Phys. Rev. Lett.*, 92(11):115507, 2004.

[20] Verena Goertz, Nico Dingenouts, and Hermann Nirschl. Comparison of Nanometric Particle Size Distributions as Determined by SAXS, TEM and Analytical Ultracentrifuge. *Part. Part. Syst. Char.*, 26(1-2):17–24, 2009.

[21] Z. W. Wang and R. E. Palmer. Determination of the Ground-State Atomic Structures of Size-Selected Au Nanoclusters by Electron-Beam-Induced Transformation. *Phys. Rev. Lett.*, 108(24):245502, 2012.

[22] F. R. Negreiros, E. A. Soares, and V. E. de Carvalho. Energetics of free pure metallic nanoclusters with different motifs by equivalent crystal theory. *Phys. Rev. B*, 76(20):205429, 2007.

[23] F. Baletto, R. Ferrando, A. Fortunelli, F. Montalenti, and C. Mottet. Crossover among structural motifs in transition and noble-metal clusters. *J. Chem. Phys.*, 116(9):3856, 2002.

[24] Charles L. Cleveland and Uzi Landman. The energetics and structure of nickel clusters: Size dependence. *J. Chem. Phys.*, 94(11):7376, 1998.

[25] Julia Uppenbrink and David J. Wales. Structure and energetics of model metal clusters. *J. Chem. Phys.*, 96(11):8520, 1998.

[26] Charles L. Cleveland, Uzi Landman, Thomas G. Schaaff, Marat N. Shafigullin, Peter W. Stephens, and Robert L. Whetten. Structural Evolution of Smaller Gold Nanocrystals: The Truncated Decahedral Motif. *Phys. Rev. Lett.*, 79(10):1873, 1997.

[27] Amanda S. Barnard, Neil P. Young, Angus I. Kirkland, Marijn A. van Huis, and Huifang Xu. Nanogold: A Quantitative Phase Map. *American Chemical Society*, 2009.

[28] Hui Li, Lei Li, Andreas Pedersen, Yi Gao, Navneet Khetrapal, Hannes Jónsson, and Xiao Cheng Zeng. Magic-Number Gold Nanoclusters with Diameters from 1 to 3.5 nm: Relative Stability and Catalytic Activity for CO Oxidation. *American Chemical Society*, 2014.

[29] J. Magnus Rahm and Paul Erhart. Beyond Magic Numbers: Atomic Scale Equilibrium Nanoparticle Shapes for Any Size. *American Chemical Society*, 2017.

[30] D. Schebarchov, F. Baletto, and D. J. Wales. Structure, thermodynamics, and rearrangement mechanisms in gold clusters—insights from the energy landscapes framework. *Nanoscale*, 10(4):2004–2016, 2018.

[31] Anna L. Garden, Andreas Pedersen, and Hannes Jónsson. Reassignment of 'magic numbers' for Au clusters of decahedral and FCC structural motifs. *Nanoscale*, 10(11):5124–5132, 2018.

[32] Ino Shozo. Epitaxial Growth of Metals on Rocksalt Faces Cleaved in Vacuum. II. Orientation and Structure of Gold Particles Formed in Ultrahigh Vacuum. *J. Phys. Soc. Jpn.*, 2013.

[33] L. D. Marks. Surface structure and energetics of multiply twinned particles. *Philos. Mag. A*, 2006.

[34] Younan Xia, Xiaohu Xia, and Hsin-Chieh Peng. Shape-Controlled Synthesis of Colloidal Metal Nanocrystals: Thermodynamic versus Kinetic Products. *American Chemical Society*, 2015.

[35] David Wales et al. *Energy landscapes: Applications to clusters, biomolecules and glasses*. Cambridge University Press, 2003.

[36] Robert L. Whetten, Joseph T. Khoury, Marcos M. Alvarez, Srihari Murthy, Igor Vezmar, Z. L. Wang, Peter W. Stephens, Charles L. Cleveland, W. D. Luedtke, and Uzi Landman. Nanocrystal gold molecules. *Adv. Mater.*, 8(5):428–433, 1996.

[37] King C. Lai and James W. Evans. Reshaping and sintering of 3D fcc metal nanoclusters: Stochastic atomistic modeling with realistic surface diffusion kinetics. *Phys. Rev. Mater.*, 3(2):026001, 2019.

[38] Luke T. Roling, Lin Li, and Frank Abild-Pedersen. Configurational Energies of Nanoparticles Based on Metal–Metal Coordination. *American Chemical Society*, 2017.

[39] Richard Tran, Zihan Xu, Balachandran Radhakrishnan, Donald Winston, Wenhao Sun, Kristin A. Persson, and Shyue Ping Ong. Surface energies of elemental crystals. *Sci. Data*, 3(1):1–13, 2016.

[40] Yong Han, Da-Jiang Liu, and James W. Evans. Quantum stabilities and growth modes of thin metal films: Unsupported and NiAl-supported Ag(1 1 0) and Ag(1 0 0). *Surf. Sci.*, 602(14):2532–2540, 2008. [Online; accessed 9. Feb. 2020].

[41] Yong Han and Da-Jiang Liu. Quantum size effects in metal nanofilms: Comparison of an electron-gas model and density functional theory calculations. *Phys. Rev. B*, 80(15):155404, 2009.

[42] John R. Rumble, David R. Lide, and Thomas J. Bruno. CRC handbook of chemistry and physics :, Feb 2020. [Online; accessed 9. Feb. 2020].

[43] The Nature of the Nucleation Process, Jan 1974. [Online; accessed 9. Feb. 2020].

[44] Vitaly A. Shneidman. Transformations of the distribution of nuclei formed in a nucleation pulse: Interface-limited growth. *J. Chem. Phys.*, 131(16):164115, 2009.

[45] Vitaly A. Shneidman. Transformations of the distribution of nuclei formed in a nucleation pulse: Interface-limited growth. *J. Chem. Phys.*, 131(16):164115, 2009.

[46] D. Turnbull and J. C. Fisher. Rate of Nucleation in Condensed Systems. *J. Chem. Phys.*, 17(1):71, 2004.

[47] King C. Lai, Da-Jiang Liu, and James W. Evans. Diffusion of two-dimensional epitaxial clusters on metal (100) surfaces: Facile versus nucleation-mediated behavior and their merging for larger sizes. *Phys. Rev. B*, 96(23):235406, 2017.

[48] G. Wulff. XXV. Zur Frage der Geschwindigkeit des Wachsthums und der Auflösung der Krystallflächen. *Zeitschrift für Kristallographie - Crystalline Materials*, 34(1-6):449–530, 1901.

[49] Jonathan P. K. Doye and Lars Meyer. Mapping the Magic Numbers in Binary Lennard-Jones Clusters. *Phys. Rev. Lett.*, 95(6):063401, 2005.

[50] Curt Waltmann, Nathan Horst, and Alex Travesset. Capping Ligand Vortices as "Atomic Orbitals" in Nanocrystal Self-Assembly. *American Chemical Society*, 2017.

[51] Tommy Waltmann, Curt Waltmann, Nathan Horst, and Alex Travesset. Many Body Effects and Icosahedral Order in Superlattice Self-Assembly. *J. Am. Chem. Soc.*, 2018.

[52] A. Travesset. Topological structure prediction in binary nanoparticle superlattices. *Soft Matter*, 13(1):147–157, 2016.

[53] Alex Travesset. Soft Skyrmions, Spontaneous Valence and Selection Rules in Nanoparticle Superlattices. *American Chemical Society*, 2017.

[54] Uzi Landman and W. D. Luedtke. Small is different: energetic, structural, thermal, and mechanical properties of passivated nanocluster assemblies. *Faraday Discuss.*, 125(0):1–22, 2004.

[55] Xun Zha and Alex Travesset. Stability and Free Energy of Nanocrystal Chains and Superlattices. *J. Phys. Chem. C*, 2018.

[56] Alex Travesset. Nanoparticle Superlattices as Quasi-Frank-Kasper Phases. *Phys. Rev. Lett.*, 119(11):115701, 2017.

[57] Praveen K. Bommineni, Nydia Roxana Varela-Rosales, Marco Klement, and Michael Engel. Complex Crystals from Size-Disperse Spheres. *Phys. Rev. Lett.*, 122(12):128005, 2019.

[58] Rose K. Cersonsky, Greg van Anders, Paul M. Dodd, and Sharon C. Glotzer. Relevance of packing to colloidal self-assembly. *PNAS*, 115(7):1439–1444, 2018.

CHAPTER 5. RESHAPING AND SINTERING OF 3D FCC METAL NANOCLUSTERS: STOCHASTIC ATOMISTIC MODELING WITH REALISTIC SURFACE DIFFUSION KINETICS

A paper published in *Physical Reviews Materials*

King Chun Lai[1,2], James W. Evans[1,2]

[1] *Department of Physics and Astronomy, Iowa State University, Ames, Iowa 50011, USA*

[2] *Ames Laboratory-USDOE, Iowa State University, Ames, Iowa 50011, USA*

(Received 27 May 2018; published 11 February 2019)

Abstract

Far-from-equilibrium evolution of metallic nanocluster shapes is highly sensitive to the atomistic-level details of surface diffusion for diverse local surface configurations. A stochastic model was developed incorporating realistic values for the multiple diffusion barriers (contrasting previous unrealistic generic prescriptions) based upon insights from homoepitaxial film growth. Kinetic Monte Carlo simulation then elucidates the conversion of Ag nanocubes to Wulff polyhedra mediated by nucleation of new 100 facets, the pinch-off of sufficiently elongated Ag nanorods, and key aspects of sintering for orientationally aligned Ag and Au nanoclusters. The time scale for sintering of Au nanoclusters observed in high-resolution transmission electron microscopy studies was also recovered.

DOI: 10.1103/PhysRevMaterials.3.026001

5.1 Introduction

Solution-phase synthesis strategies for formation of three-dimensional (3D) crystalline metallic nanoclusters (NCs) have achieved remarkable control of NC structure [1,2] enabling fine tuning of properties for applications, e.g., plasmonics or catalysis. Note that in such applications often NCs are removed from the solution-phase environment. However, NCs are intrinsically metastable, and thus are vulnerable to postsynthesis reshaping towards their equilibrium Wulff shapes. Also, ensembles of NCs can coarsen, e.g., via coalescence or sintering of mobile clusters [3, 4]. On the nanometer scale, it is anticipated that the dominant mass transport mechanism facilitating reshaping and sintering is surface diffusion (also sometimes described as periphery diffusion) [5, 6]. Assessment of the associated equilibration kinetics is important to determine robustness of the functionality of NCs. In situ high-resolution transmission electron microscopy (HRTEM) studies [7–11] are providing increasingly high-fidelity imaging of such reshaping phenomena. However, there remains a need for realistic and predictive atomistic-level modeling for a more complete understanding of some intrinsically nanoscale features of behavior.

Classic deterministic continuum treatments of reshaping, typically with isotropic surface energy and diffusivity [5, 12–14], predict that the relaxation time, $\tau_{\rm eq}$, for reshaping and sintering of macroscopic particles mediated by surface diffusion scales like $\tau_{\rm eq} \sim N^{4/3}$ for NCs of N atoms. Subsequent theoretical and experimental analyses revealed complex phenomena such as void formation near the neck region for sintering particles [6], and also pinch-off for elongated shapes [10, 15–17], both reminiscent of the Rayleigh-Plateau instability. A Langevin version of these formulations might be applied to smaller scale objects where fluctuations are more important [18]. However, it is recognized that such continuum treatments generally fail to adequately describe evolution on the nanoscale, noting that NCs are often strongly faceted [19–21]. This failure also applies for two-dimensional (2D) epitaxial metallic NCs when linear sizes are below the persistence length of straight steps, or below other characteristic lengths determined by the details of the periphery diffusion

kinetics [22–24].

Stochastic lattice-gas models analyzed by kinetic Monte Carlo (KMC) simulation can track the evolution of crystalline NCs over relevant time scales [19,21,25,26]. Such models can in principle incorporate the complex dependence of the activation barriers for hopping of surface atoms on the vast array of possible local atomic environments (e.g., hopping across facets, along straight step edges and around kinks, and between terraces and facets). However, such analyses have previously utilized generic prescriptions of these barriers, typically the so-called Initial Value Approximation (IVA) or bond counting model where the barrier is determined entirely by the coordination in the initial state before hopping [7,19,21]. IVA does satisfy detailed balance guaranteeing evolution to the correct equilibrium structure, contrasting some treatments [26]. However, it fails dramatically to capture key features of surface diffusion in fcc metal systems. See Appendix A and Supplemental Material [27]. This severe failure includes incorrectly predicting the relative values of barriers for terrace diffusion on different facets, and of the barriers for step edge versus terrace diffusion [28], and also neglecting the presence of additional one-dimensional, 2D, and 3D Ehrlich-Schwoebel (ES) barriers for rounding of kinks, descent of monoatomic steps, and transport between facets [28–30]. These detailed features of surface diffusion are important for reliable treatment of NC reshaping. This failure of IVA is also evident when comparing results from KMC simulations for the evolution of 2D epitaxial NC shapes based on IVA models with those from realistic modeling, or with scanning tunneling microscopy experiments (see Supplemental Material [27]).

Furthermore, IVA hopping barriers include an arbitrary constant. This constant is often adjusted to fit the experimental time scale for NC evolution [7] but IVA then produces unphysical barriers. Alternatively, the constant can be adjusted to fit some specific barrier, but then IVA fails to match time scales and appropriate values of other barriers.

In Sec. 5.2, we present our strategy to craft a general formalism which reliably describes barriers for diverse surface hopping processes. We will exploit extensive insights from ex-

perimental and theoretical analyses of homoepitaxial fcc metal film growth and relaxation for multiple low-index substrate orientations [28, 29] particularly for Ag [31–35]. This approach eliminates all of the deficiencies of IVA, and allows prediction of actual relaxation time scales. The latter is key for assessing robustness of metastable NC structures. In Sec. 5.3, the model is applied to analyze reshaping of Ag NCs. First, we consider evolution of Ag nanocubes [1, 36] to equilibrium Wulff shapes, which involves the erosion of 111 corner facets and nucleation of new 100 side layers. Second, the pinch-off of elongated Ag nanorods or nanowires is assessed. In Sec. 5.4, the model is applied for sintering of Ag NC pairs following orientated attachment [37, 38] identifying for aligned 100 facets distinct early-stage neck filling and late-stage nucleation-mediated reshaping regimes. In addition, the model is shown to capture the evolution and time scale observed in experimental HRTEM studies for sintering of $\sim$ 4-nm Au NCs. A summary of our analysis is presented in Sec. 5.5.

5.2 Model Formulation

We consider crystalline fcc NCs with atoms interacting via an effective nearest-neighbor (NN) attractive interaction of strength $\phi > 0$. The distance between NN atoms will be denoted by a, which also corresponds to the surface lattice constant so, e.g., $a = 0.289$nm for Ag. The effectiveness of this description is supported by recent analysis in which the energy of NCs was decomposed as a sum of energies per atom, E_n, where the E_n depend on the coordination, n, of the atom. This study demonstrated a near-linear variation of E_n with coordination n [39] consistent with a NN interaction model. We note that appropriate values of the effective interaction strength, ϕ, are typically far below those extracted from the bulk cohesive energy, E_c. For example, for Ag we will set $\phi = 0.225$eV versus $E_c/6 = 0.492$eV (where the latter reflects the feature that each bulk atom in a fcc metal can be regarded as having 12 shared bonds with neighbors). It should be noted, however, that our choice of ϕ reasonably recovers surface energies for low-index facets for various metals. See Appendix B.

In this model, the equilibrium Wulff shape of NCs is a truncated octahedron bounded by 111 and 100 facets in the macroscopic regime. The lengths of edges joining 111 facets to 100 facets ($a_{\{100\}}$), and to other {111} facets ($a_{\{111\}}$) , are equal [40]. On the nanoscale, these shapes are most closely achieved for certain magic numbers of atoms [41]. Choices with $a_{\{111\}} = a_{\{100\}}$ and with $a_{\{111\}} = a_{\{100\}} + 1$ (in units of surface lattice constant, a) correspond to local-energy minima [40]. The number of atoms, $N_W(a_{\{100\}}, a_{\{111\}})$, in the NC satisfies $N_W(3,3) = 201$, $N_W(3,4) = 314$, $N_W(4,4) = 586$, etc.

Hop rates of surface atoms are selected to have an Arrhenius form, $h = \nu \exp\left[-E_{\rm act}/(k_B T)\right]$, for NC temperature T where ν is a common attempt frequency and $E_{\rm act}$ is the activation barrier. For hopping from an initial (i) site to a final (f) unoccupied neighboring fcc lattice site, E_i and E_f denote the total interaction energy for the atom at these sites. Thus, $E_{i,f} = -n_{i,f}\phi$, for atom coordination numbers $n_{i,f}$ ranging from 1 to 11 for atoms with ≥ 1 vacant NN fcc site. $E_{\rm TS}$ denotes the total interaction energy at a transition state (TS) for hopping between these sites. Then, the activation barrier, $E_{\rm act}(i \to f)$, is given by $E_{\rm act}(i \to f) = E_{\rm TS} - E_i$, where "symmetric" $E_{\rm TS}$ is the same for forward $(i \to f)$ and reverse $(f \to i)$ transitions, thereby ensuring detailed balance. The standard IVA bond-counting choice selects constant $E_{\rm TS} = C_{\rm IVA}$, whereas an alternative Metropolis choice selects $E_{\rm act} = C_{\rm MET} + \max(E_f, E_i)$. However, we emphasize that both choices very poorly represent diffusion on fcc surfaces. See Supplemental Material [27], Ref. [28], and Appendix A. Thus, instead, our choice is a refined version of a symmetric Bronsted-Evans-Polyani form [42, 43]:

$$E_{\rm TS} = C_\alpha + 1/2(E_i + E_f), \text{ so that } E_{\rm act} = C_\alpha + 1/2(E_f - E_i), \tag{5.1}$$

where instead of the standard selection of a single C_α we will assign multiple C_α for judiciously selected classes, α, of hops. To satisfy detailed balance, forward and reverse hops are always assigned to the same class, α, and thus have the same C_α. Since NN initial and final sites have four shared NN sites, and each have another seven NN sites, the occupancy of 18 sites impacts $E_{\rm act}$.Here, we are exploiting the modeling framework developed in Ref. [44].

See Fig. 5.1(a).

We consider four basic classes of hopping: terrace diffusion on {100} facets or on {111} facets labeled by $\alpha = 100_{\rm TD}$ or $\alpha = 111_{\rm TD}$, respectively [Figs. 5.1(b) and 5.1(c)], and edge diffusion along a {100}-microfaceted A step or a {111}-microfaceted B step on a {111} facet labeled by $\alpha = 111_A$ or $\alpha = 111_B$, respectively [Figs. 5.1(d) and 5.1(e)]. It is appropriate to note that edge diffusion along a close-packed step on a {100} facet is locally equivalent to edge diffusion along an A step on a {111} facet, so these are assigned the same barrier in our modeling. Independent and separate determination of these barriers indicates that this assignment is reasonable (see Supplemental Material [27] and Ref. [28]). Similarly, in-channel terrace diffusion on a {110} facet is locally equivalent to diffusion along a B step on a {111} facet, so barriers are set equal in our modeling, which again is reasonable based upon independent analysis [28].

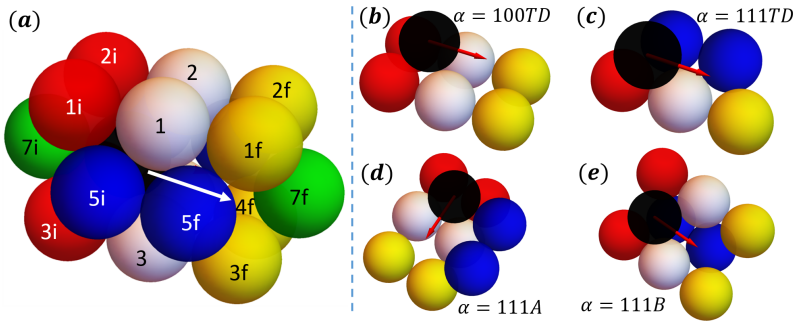

Figure 5.1: (a) 18 sites impacting black atom hopping [44]. Four sites NN to both initial (i) and final (f) sites are labeled 14. Seven additional sites NN to i (f) are labeled 1i7i (1f7f). Some sites are not visible (4, 4i, 6i, 6f). These 18 NN sites can be either filled or empty. (be) four classes of intralayer terrace and edge diffusion. NN sites in (be) which must be filled are indicated.

Each of the above basic hopping classes is divided into two subclasses. The first subclass is intralayer diffusion where both the initial and the final state are fully supported at a hollow site created by atoms in the lower supporting layer. Here, C_α adopt "base values" $C_\alpha = c_\alpha$.

We set

$$c_{100\mathrm{TD}} = 0.425\mathrm{eV},\ c_{111\mathrm{TD}} = 0.100\mathrm{eV},\ c_{111A} = 0.275\mathrm{eV}, \tag{5.2}$$
$$c_{111B} = 0.300\mathrm{eV} \text{ for Ag},$$

effectively capturing actual terrace and edge diffusion barriers for low-index Ag surfaces (in marked contrast to the IVA prescription) [28, 31–35]. One significant point is that some hopping processes involve a transition between an edge atom at the step edge (with one or more lateral neighbors) and one on the terrace (with no lateral neighbors). In this case, both forward and reverse processes are assigned to the terrace diffusion class.

The second subclass corresponds to interlayer diffusion. First, we consider cases where a fully supported atom hops out over a step edge to a site which is not fully supported. In such cases, the rate for such a hop can be impacted by ES barriers, δ_{ES}. Here, we set

$$C_\alpha = c_\alpha - m\phi/2(+\delta_{\mathrm{ES}}) \text{ for } m \text{ missing supporting atoms.} \tag{5.3}$$

The term $m\phi/2$ in C_α compensates for the feature that $1/2(E_f - E_i) = +m\phi/2$ for a perfect step with a single atom on the upper terrace, resulting in $E_{\mathrm{act}} = c_\alpha(+\delta\mathrm{ES})$ for that case. Whether or not δ_{ES} is included depends upon the details of the step edge configuration. For interlayer diffusion on a Ag{100} facet, δ_{ES} is included for $m = 2$ (descending a close-packed step), but not for $m = 1$ (descending at a kink). Why? A finite ES barrier exists for hopping down a close-packed step, but not at a kink where exchange is facile [28]. Thus, for an atom initially with no lateral NN, one has $E_{\mathrm{act}} = c_{100\mathrm{TD}}(c_{100\mathrm{TD}} + \delta_{\mathrm{ES}})$ for $m = 1$ ($m = 2$). For interlayer transport from an Ag{111} facet, δ_{ES} is included if $m = 1$, but not for $m = 2$. Why? Descent is facile from a B step or kink at an A step ($m = 2$), but not from an A step or kink at a B step ($m = 1$) [34]. In both cases, we set $\delta_{\mathrm{ES}} = 0.10\mathrm{eV}$ reasonably matching the best estimates of ES barriers for Ag [28, 32, 34]. Finally, we note again that to satisfy detailed balance, for the reverse process of an atom hopping back to a fully supported site, one assigns the same C_α as for the forward process of hopping out over the step edge.

We emphasize that our formulation for realistic kinetics is general, although one needs to revise the selection of values for C_α, ϕ, and $\delta_{\rm ES}$ for different metals. Appropriate values for Pt follow from Ref. [29], and for Au are presented in Sec. 5.4. However, the appropriate prescription for inclusion of an ES barrier can be system dependent, e.g., the details for Pt based on detailed analysis of interlayer transport for that system [29] differ from those for Ag. In the following sections, we perform extensive KMC simulations of this model to precisely characterize NC reshaping and sintering.

5.3 Reshaping of Ag Nanoclusters

5.3.1 Relaxation of Ag nanocubes to Wulff shapes

Nanocubes can have distinctive plasmonic properties given their shape, and also distinctive catalytic properties given that the exposure of {100} facets is maximized. Consequently, there is interest in stability against nanocube reshaping, as is reflected by recent HRTEM studies and associated analysis [45]. It was suggested that the barrier to shift an atom from the edge of a nanocube to the terrace was key in controlling reshaping [45]. Our analysis indicates that a more complex nucleation process controls overall shape relaxation. Complete nanocubes with {100} facets have unstable low-coordinated edges and corner and edge atoms. Thus, to mimic synthesized near-perfect nanocubes [1,36], we start with truncated Ag nanocubes where all atoms have at least six NNs. See Fig. 5.2(a) for time $t = 0$.

Below, we assess the temperature dependence and size dependence of relaxation to the Wulff shape. In Figs. 5.2(b) and 5.2(c), we monitor the "width" h_{100} (h_{111}) between the outermost {100} facets ({111}) facets) on opposite sides (corners) of the nanocube. These quantities are naturally rescaled by interlayer spacing $\left[a/\sqrt{2}\right]$ for {100} facets and layers, and $a/\sqrt{3/2}$ for {111} facets and layers] to monitor the evolution of the number of {100} and {111} layers. This definition identifies every plane with at least one atom as a layer. The evolution from a truncated nanocube to a Wulff shape involves formation of new {100} layers on the sides of the initial nanocube, and erosion or dissociation of {111} facets at the

corners. Results for larger size $N = 1584$ atoms show distinct stages in these formation and dissociation processes. Apart from the final equilibrium plateau, there is a weak plateau for h_{100} and h_{111} changing by two layers. This corresponds to the nucleation of one new layer on each {100} facet, and complete dissociation and removal of a {111} facet from each corner. Note that nucleating a layer on just one side, or removing a layer from just one corner, but not the other, is evidently a rare transient state.

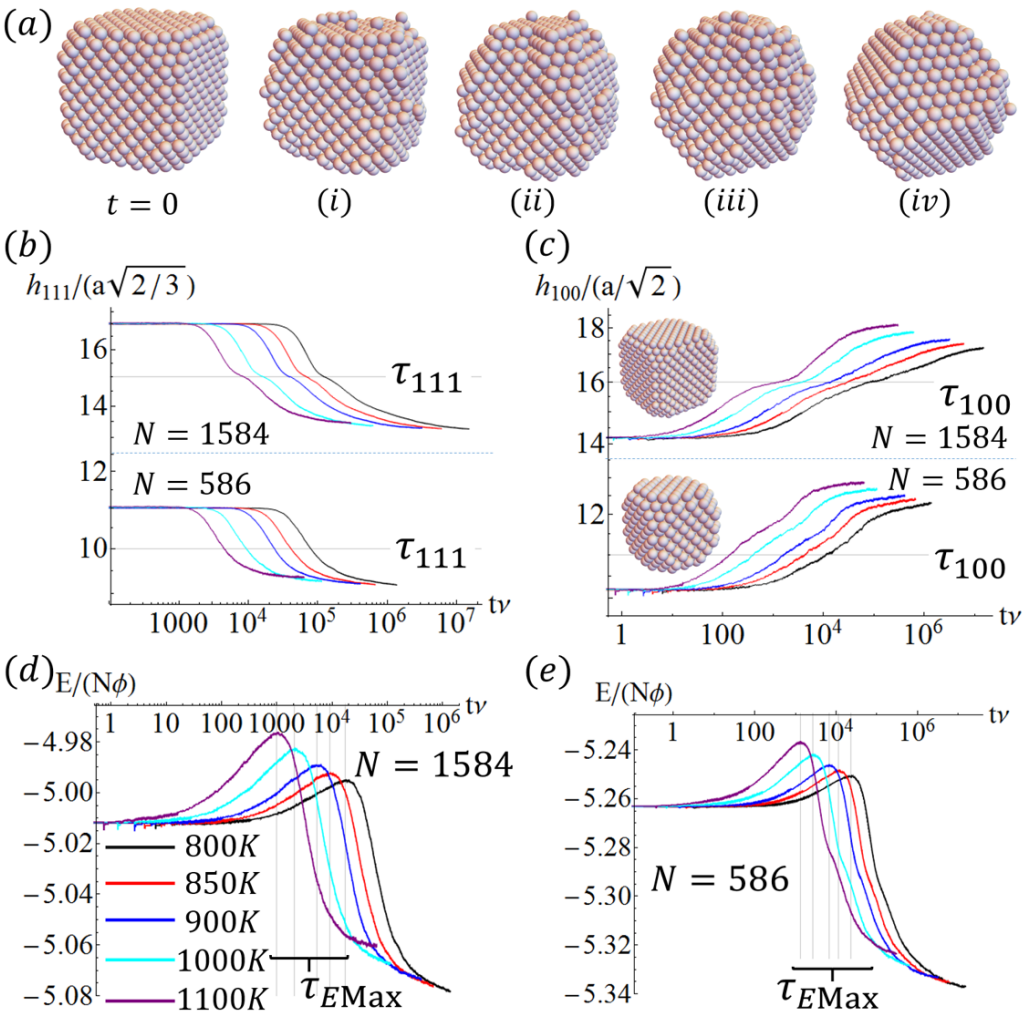

Figure 5.2: Ag nanocube reshaping: (a) Configuration snapshots ($N = 1584$,$T = 1100K$). T-dependence of time evolution of rescaled $h_{111}(t)$ in Fig. 5.2(b), rescaled $h_{100}(t)$ in Fig. 5.2(c), and of the scaled total energy in Fig. 5.2(d) and Fig. 5.2(e), for $N = 586$, 1584 averaged over 400 trials.

To assess the T dependence of the evolution, we introduce characteristic times, $\tau_{\rm relax} = \tau_{100}$ and τ_{111}, reflecting significant evolution of h_{100} and h_{111}, respectively, from their initial values [specifically, a change by two layers, as indicated in Figs. 5.2(b) and 5.2(c)]. From these characteristic times, we assess effective Arrhenius energies, $E_{\rm eff}$. For $\tau_{\rm relax} = \tau_{111}$, which characterizes dissociation of a {111} corner facet and transfer of its atoms to a {100} facet, Arrhenius analysis of KMC results for τ_{111} yields $E_{\rm act} \approx 0.7$eV. Considering the NC starting as a perfect truncated nanocube, a corner atom on the {111} facet transfers to the {100} facet via what can be regarded as a kink site on a close-packed step edge for the {100} facet. The barrier for the first step $E_{\rm act} = 0.525$eV is relatively low. However, in the second step to reach the final adsorption site on the {100} facet, which is $\Delta E = +2\phi$ above the initial site energy, the atom must surmount a barrier of energy $c_{100\rm TD}$ above the final-state energy. Thus, the overall atom transfer barrier is $E\text{eff} = c_{100\rm TD} + \Delta E = 0.875$eV, comparable to the simulation result. Note that, for higher T, entropic factors associated with thermal excitation are significant, and not incorporated in our analysis.

Atoms freed from {111} facets diffuse onto {100} facets and nucleate new {100} layers, a process characterized by $\tau_{\rm relax} = \tau_{100}$, for which Arrhenius analysis of KMC results yields a distinct and higher $E_{\rm eff} \approx 1.1$eV. Here, we naturally analyze the formation of a relatively stable square tetramer of atoms on {100} facets. Consider first the transfer of three of the 12 atoms on the initial complete {111} corner facet to a single {100} facet to form a trimer. This involves breaking a total of eight lateral bonds on the {111} facet, but forming two lateral bonds in the trimer, and increasing coordination to supporting atoms on the {100} facet for a total energy change of $\Delta E_{123} = +3\phi$. Let E_4 denote the barrier for transfer of a fourth atom from the {111} facet to the {100} facet to stabilize the trimer. This process is controlled by a last step to reach a {100} adsorption site yielding a barrier $E_4 = 0.75$eV. This implies an effective nucleation barrier of $E_{\rm eff} = E_4 + \Delta E_{123} = 1.42$eV. However, if the trimer is at the {100} facet edge so that the atom from the {111} facet can hop directly into a site with two lateral bonds forming the square tetramer, then E_4 is reduced to 0.525eV

and $E_{\text{eff}} = 1.20$ eV, reasonably consistent with simulation results.

We also track the total NC energy, E [Figs. 5.2(d) and 5.2(e)], and define a reshaping time $\tau_{\text{relax}} = \tau_{E\ \text{Max}}$ corresponding to the peak energy. Both peak and late stage E are larger for higher T due to entropic effects. Arrhenius analysis for $\tau_{E\ \text{Max}}$ yields $E_{\text{eff}} \approx 0.72$eV, coinciding with that for τ_{111}. Thus, the energy maximum corresponds to the early-stage disruption of {111} facets, E decreasing only after new {100} layers nucleate and grow.

It should be emphasized that the above results for the evolution of h_{111}, h_{100}, and E are obtained from extensive KMC simulation averaging over several hundred trials. This is necessary to minimize the effect of substantial fluctuations at the nanoscale, and to thus obtain precise results for characteristic times and Arrhenius energies. We also note that almost perfect Arrhenius behavior of characteristic times is observed over the probed temperature range (see Supplemental Material [27]). The identified Arrhenius behavior allows prediction of relaxation time scales for lower T. The nucleation process with the higher $E_{\text{eff}} \approx 1.1$eV will be rate controlling, implying that, e.g., $\tau_{\text{relax}} = \tau_{100} \approx 10^{-3.6}, 10^{-0.8}$, and $10^{3.8}$s at 500, 400, and $300K$, respectively, for $N = 1584$, choosing $\nu = 10^{12.5\text{s}^{-1}}$. These estimates are actually lower bounds as E_{eff} should increase somewhat for lower T (see above).

Finally, we roughly assess size scaling of τ_{relax} based on just two NC sizes: $N = 586$ and 1584. Analysis of $\tau_{\text{relax}} \sim N^{\beta}$ corresponding to the late stages of the process yields β increasing for decreasing T from $\beta \approx 1.3$ at $1000K$ to $\beta \approx 1.7$ at $800K$. Deviations for lower T below the classic continuum value of $\beta = 4/3$ indicate the presence of a nucleation-mediated process with finite effective barrier [19,21]. This observation is consistent with our assessment that the evolution of h_{100}, and specifically that the Arrhenius energy extracted from τ_{100}, is controlled by the nucleation of new {100} layers.

5.3.2 Pinch-off of Ag nanorods

Within the framework of continuum modeling, shape evolution of objects mediated by surface or periphery diffusion, which is of relevance here, can differ qualitatively from curvature-driven evolution [46]. In addition, it can differ from evolution mediated by inhibited attachment-detachment (also described as evaporation-condensation), which is also controlled by local curvature. For 2D systems, Grayson's theorem [47] shows that pinch-off is not possible for curvature-driven evolution, and it has been argued that the same is true for the evaporation-condensation mechanism [48]. However, pinch-off can occur for evolution mediated by periphery diffusion in 2D systems, as has been observed in experiment and modeling for metallic surface systems [48]. For 3D systems, Grayson's theorem does not prohibit pinch-off for curvature-driven evolution, and no doubt pinch-off can also occur for evaporation-condensation. Furthermore, one anticipates that the propensity for pinch-off in three dimensions is substantially greater for evolution mediated by surface diffusion versus curvature. Indeed, analysis of the evolution of near-cylindrical rods via continuum theory for isotropic surface energy and diffusivity indicates an instability with wavelength $\lambda \approx 4.45\times$ rod diameter [11]. Such behavior is reminiscent of the Rayleigh-Plateau for fluid steams or jets. This result implies that elongated structures with sufficiently large aspect ratio, $\mathscr{R}$, will also pinch off, and provides a prediction of the critical aspect ratio of about $\mathscr{R}_c = 4.5$. Certainly, behavior on the nanoscale will differ quantitatively from the above continuum predictions. However, it is reasonable to expect that qualitative features such as pinch-off will be preserved.

NC synthesis can produce elongated nanorods for various metals, so it is natural to explore if postsynthesis evolution leads to pinch-off, and to determine the associated $\mathscr{R}_c$. Indeed, experiments involving metallic nanowires [16], theory [14], and atomistic simulation (but based on evaporation-condensation and not satisfying detailed balance) [17], indicate the existence of a pinch-off instability for large $\mathscr{R}$. However, it is appropriate to recognize that the key feature in evolution of nanorods is the presence of strong fluctuations. As

a result, evolution for a range of initial aspect ratios, $\mathscr{R}$, has a significant probability for either pinch-off or achieving a single compact Wulff shape. For this reason, we introduce the concept of a pinch-off probability, $P(\mathscr{R})$, which will increase monotonically with initial aspect ratio $\mathscr{R}$. We can determine $P(\mathscr{R})$ by running multiple independent simulations of nanorod evolution, and assessing the fraction of times that pinch-off occurs.

We consider this issue by applying our model to analyze specifically the evolution of readily synthesized octagonal Ag nanorods which have alternating {100} and {110} side facets, and {100} end facets [1]. An example of simulated evolution for $\mathscr{R} = 7.16$ which leads to pinch-off is shown in Fig. 5.3. Multiple simulations for nanorods with this and many other $\mathscr{R}$ values (while retaining a fixed nanorod width) lead to the results for $P(\mathscr{R})$ versus R shown in Fig. 5.4. Naturally defining a critical aspect ratio, $\mathscr{R}_c$, via $P(\mathscr{R}_c) = 1/2$ leads to the estimate of $\mathscr{R}_c = 6.9$ somewhat above the classical continuum value.

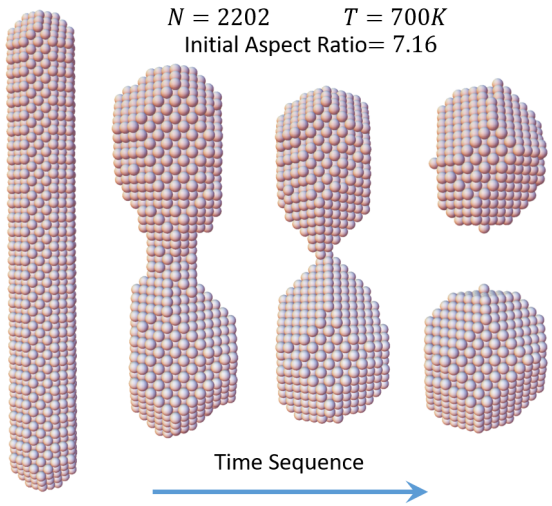

Figure 5.3: Pinch-off of an octagonal Ag nanorod with $N = 2202$ at $T = 700K$.

As an aside, we have also considered pinch-off for elongated Ag nanobars with a square cross-section and all faces corresponding to {100} facets. In this case, the critical aspect ratio is $\mathscr{R}_c \approx 8 - 9$ for the selected cross-section side length of about 1.7nm.

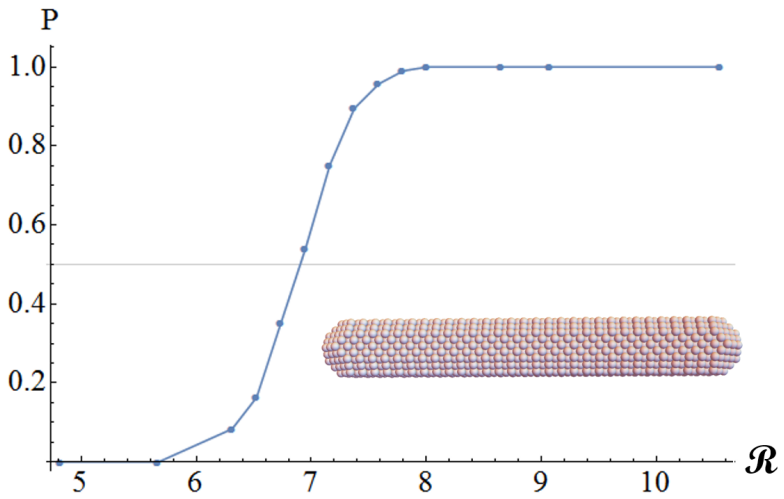

Figure 5.4: Simulated pinch-off probability of Ag nanorods at $700K$ as a function of initial aspect ratio.

5.4 Sintering of Oriented Pairs of Ag and Au Nanoclusters

Sintering of pairs of roughly equal-sized NCs with equilibrated Wulff shapes can follow oriented attachment [37, 38] which could involve alignment of either {100} facet planes or {111} facet planes, and where in addition there is azimuthal alignment so the combined attached NC pair has a single-crystal fcc structure. This latter feature is necessary in order to apply our modeling formalism. Before applying our atomistic-level model to analyze evolution during the sintering process following such attachment, it is instructive to show simple geometric schematics which illustrate the anticipated shape evolution, and which we note is distinct for aligned {100} versus {111} facets. Figure 5.5 illustrates the initial configuration just after oriented attachment, the facets which are present upon filling in the neck region to first create an overall convex shape, as well as the ultimate Wulff shape. On the nanoscale, which we consider, fluctuations will inhibit the formation of such simple geometric shapes with well-defined facets. However, we shall find that some of the qualitative features shown in Fig. 5.5 are still evident.

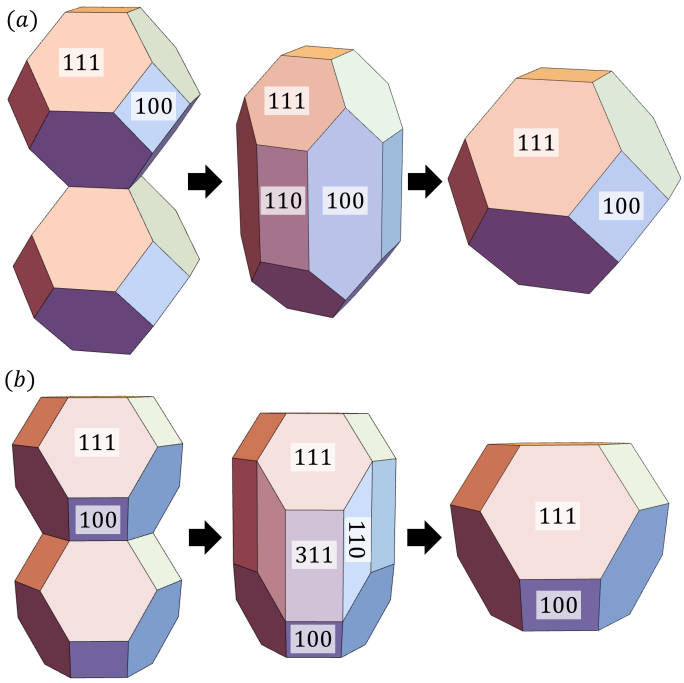

Figure 5.5: Schematic of geometric evolution during sintering of NCs with (a) aligned {100} facets and (b) aligned {111} facets.

5.4.1 Sintering of equal-sized Ag Wulff nanoclusters

We first consider sintering for equal-sized Ag Wulff NCs initially joined by oriented attachment with aligned {100} facets. Simulated evolution at $T = 600K$ is shown in Fig. 5.6(a) for sintering of a pair of NCs each with $a_{100} = a_{111} = 4$ and $N_W(4,4) = 586$, so that the total size equals $N = 2N_W = 1172$ atoms. Initial rapid evolution involves transfer of atoms from the ends of the NC pair to the concave neck region where they are readily captured at existing step edges. See Fig. 5.6(ai). When the neck is filled in, one obtains a convex elongated structure as shown in Fig. 5.6(aii), the sides of which ideally correspond to alternating {100} and {110} facets as illustrated in Fig. 5.5(a). Late-stage equilibration involves transfer of atoms from the ends of the convex elongated shape, nucleating new {100} layers on the {100} side facets, and eliminating {110} side facets. See Fig. 5.6(aiii).

Traditional continuum treatments of surface diffusion mediated sintering of spherical

particles focused growth on radius of the neck $r \sim t^{\alpha}$ predicting that [6, 12] $\alpha = 1/7$. This exponent reflects the initial singular cusplike nature of the neck region in this classic continuum problem, and thus it should not apply for our system. Nonetheless, we analyze neck growth considering the average number of atoms, A, in each of the two {100} planes at the center of the NC pair orthogonal to their long axis. Thus, A measures the neck area, and $A^{1/2}$ reflects the "radius" r. We estimate the limiting value, A_∞, of A as $t \to \infty$, from the Wulff-like equilibrium cluster. Figure 5.6(b) shows the evolution of A/A_∞ for $N = 1172$ and various T. The first stage leading to formation of a convex-shaped NC is facile with no evidence of classic scaling, and ends when A/A_∞ reaches around 0.6. A sharp transition from this first stage to the late stage of evolution (which we show to be nucleation mediated) is only evident below $750K$ [see Fig. 5.6(b)].

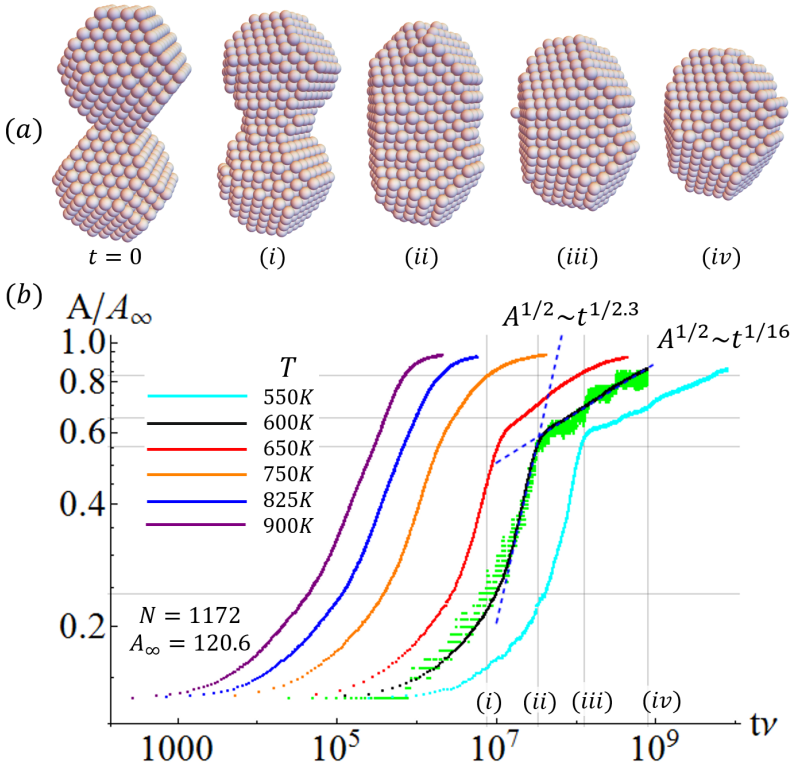

Figure 5.6: (a) Sintering Ag Wulff NC pair with aligned {100} facets and with $N_W = 586$ and $2N_W = 1172$ at $600K$. (b) Evolution of the scaled neck area for $N = 1172$ and various T averaging over 400 trials (35 trials at $550K$). Green data points: single trial at $600K$.

Despite the lack of classic scaling $A^{1/2} \sim t_\alpha$ with $\alpha = 1/7$ for short t, we extract an effective exponent, α_{fill}, based upon the slope of the log-log plot in Fig. 5.6(b) at the inflection point corresponding to the neck filling regime (just below the elbow for lower T). For $N = 1172$, we obtain values from $\alpha_{\text{fill}} \approx 0.43$ at $600K$ to $\alpha_{\text{fill}} \approx 0.24$ at $900K$. An effective $\alpha_{\text{nuc}} \approx 0.06$ is extracted for the late-stage regime at $600K$ similar to the analysis in Ref. [21], although we discount its significance. From the trajectory of a single simulation at $600K$ (green data), it is evident that the increase in A involves distinct steps in the late-stage regime corresponding to nucleation of new layers (thus justifying our description of this regime as nucleation mediated).

For a more complete analysis, we introduce characteristic times: τ_{fill} determined when $A/A_\infty = 0.45$ (reflecting the neck filling stage) and τ_{nuc} determined when $A/A_\infty = 0.85$ (reflecting the final nucleation-mediated stage). Arrhenius analysis for τ_{fill} yields $E_{\text{eff}} \approx$ 0.75eV. In a simplistic analysis, a corner atom of the {100} facet transfers to the {111} facet. The barrier for just the first step is $E_{\text{act}} = 0.75$eV. However, in the second step to reach the final adsorption site on the {111} facet which is $\Delta E = +3\phi$ above the initial site energy, the atom must surmount a barrier of energy $c_{111\text{TD}} + \delta_{\text{ES}}$ above the final-state energy. Thus, the effective barrier for atom transfer is $E_{\text{act}} = c_{111\text{TD}} + \delta_{\text{ES}} + \Delta E = 0.875$eV, comparable to the simulation result, given our neglect of entropic effects. Arrhenius analysis for τ_{nuc} yields Eeff ranging from 0.85eV for $N = 402$ to 1.10eV for $N = 1172$, and our simulation results indicate slightly higher values for $N = 1172$ at lower T. The value for $N = 1172$ is similar to the barrier nucleation of {100} facets for nanocube equilibration and that analysis also applies here.

Finally, we have also analyzed size scaling, $\tau_{111} \sim N^\beta$, for the neck filling regime where β roughly matches the classic continuum value of $\beta = 4/3$ for all T. For the late-stage regime, the exponent, β, instead defined by $t_{\text{nuc}} \sim N^\beta$, increases upon decreasing T from around the classic value of $\beta = 4/3$ for very high T to $\beta \approx 1.5 - 1.6$ at $900K$ to $\beta \approx 2.8$ at $600K$. This is behavior analogous to that for nucleation-mediated nanocube reshaping.

We emphasize that the results for evolution of neck area, A, shown in Fig. 5.6 are typically obtained from several hundred simulation trials. This reduces statistical uncertainty and allows precise extraction of characteristic times, which we find exhibit near-perfect Arrhenius behavior for the range of T which is considered. This allows reliable determination of the associated Arrhenius energy.

We have also considered sintering of equal-sized Ag NCs initially joined with aligned $\{111\}$ facets retaining $N = 1172$. In this case, no transition to late-stage nucleation-mediated evolution occurs even for lower T. This feature is expected as no low-index $\{100\}$ side planes are formed, and no nucleation upon such facets is required (see Ref. [21] and Supplemental Material [27]). Sintering is faster by a factor of 23 at $600K$ than for aligned $\{100\}$ facets, $E_{\text{eff}} \approx 0.70 - 0.71\text{eV}$ is somewhat below that for the filling stage for aligned $\{100\}$ facets, and $\beta \approx 4/3$ for all T consistent with the feature that that evolution is not nucleation mediated (see Supplemental Material [27]). Finally, we remark that our analysis for both aligned $\{100\}$ and $\{111\}$ facets should be compared with the comprehensive IVA modeling in Ref. [21], which considers larger NCs than those treated here.

5.4.2 Sintering of Au nanoclusters: Comparison with HRTEM observations

A key aim of modeling studies should be direct comparison with experiment, both for validation of the modeling and also to elucidate experimental observations. In situ liquid-cell HRTEM studies are providing increasingly detailed data enabling such comparison, although caution in interpretation is required, e.g., given possible e-beam effects. One such previous study presented HRTEM imaging of the sintering of "large" $10 - \text{nm}$ Au nanoparticles and utilized IVA modeling to elucidate observed behavior [7]. As noted in Sec. 5.1, IVA includes a free parameter which was adjusted in this analysis to match the experimental time scale of evolution. In contrast, one key goal of our modeling with realistic surface diffusion kinetics is to reliably predict this time scale. Our focus is also on substantially smaller NCs than those considered above. Fortunately, recent HRTEM

imaging has provided appropriate data on shape evolution for such smaller NCs [8, 9]. We apply our model to analyze sintering of *sim*4-nm Au NCs slightly laterally displaced as monitored in recent HRTEM studies by Yuk *et al.* [9]. In general, when Au NCs merge, they are not aligned, but a single-crystal structure is subsequently achieved by grain boundary migration or by NC rotation. However, in one data set from Ref. [9] partly reproduced in Fig. 5.7(a), the NCs are almost perfectly aligned upon merging, so we model subsequent evolution in this case.

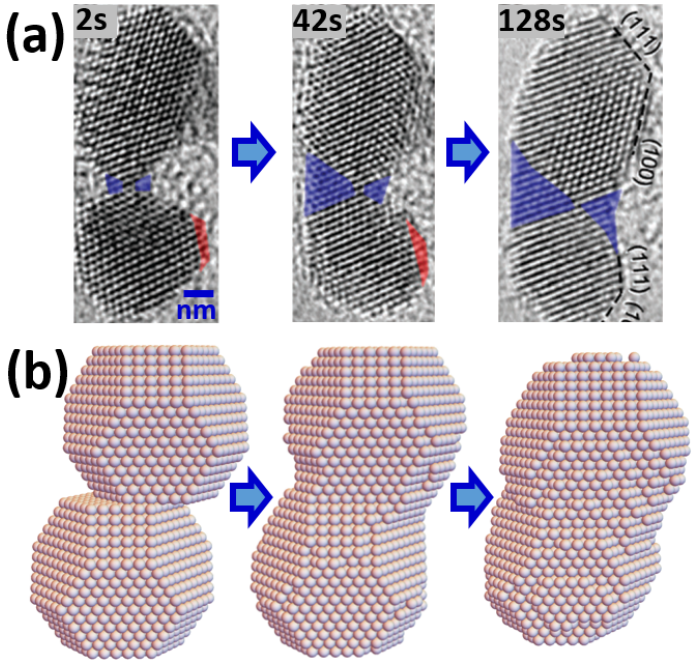

Figure 5.7: Sintering of $\sim$ 4–nm Au NCs. (a) HRTEM at $300K$. Adapted from Ref. [9] with permission from The Royal Society of Chemistry. The initial (final) image is 2s (128s) after impingement. (b) Simulated evolution for $N = 4812$ at $600K$.

However, for this modeling, it is necessary to first prescribe appropriate Au model parameters. We select $c_{100TD} = 0.60$eV,$c_{111TD} = 0.125$eV,$c_{111A} = 0.35$eV, and $c_{111B} = 0.40$eV for Au. This choice is based on density functional theory (DFT) analysis of terrace diffusion barriers [49], and general trends relating terrace and edge diffusion barriers [28]. We select $\delta_{\rm ES} = 0.12$eV based on studies of Au surface dynamics [50] and semiempirical energetics [51]. An effective $\phi = 0.22$eV is consistently selected based on either DFT analysis

of NC energetics [39] or DFT analysis of Au surface energies [52].

For the HRTEM data shown in Fig. 5.7(a), the $\sim$ 4-nm Au NCs appear to be slightly laterally displaced or misaligned upon attachment. We mimic this situation in our simulations, where we also choose a total size of $N = 4812$ roughly matching experiment. We have shown that the offset somewhat increases the initial rate of neck growth, not surprisingly since this makes the neck region a stronger sink for capturing atom diffusion from the ends on the NC pair. Even though we utilize KMC simulation rather than molecular dynamics, it is still computationally demanding to directly simulate evolution for this larger system at the experimental $T = 300K$ over the time scale needed to follow the overall sintering process (which is hundreds of seconds at $300K$). However, simulation is much more efficient at higher T. For purposes of illustration, results for shape evolution at $600K$ are shown in Fig. 5.7(b). To connect with experiment, our strategy is to perform simulation for a range of higher T to determine the relaxation time τ_{fill} (using $A/A_\infty = 0.6$) versus T. See Fig. 5.8. From these results, we extract an effective Arrhenius energy, $E_{\text{eff}} \approx 0.77$eV, for τ_{fill}. These results are then extrapolated to estimate $\tau_{\text{fill}} \sim 130$s at $300K$ where we choose a conventional attempt frequency of $\nu = 10^{13}\text{s}^{-1}$. This prediction for the time to achieve a convex shape is consistent with experiment [9].

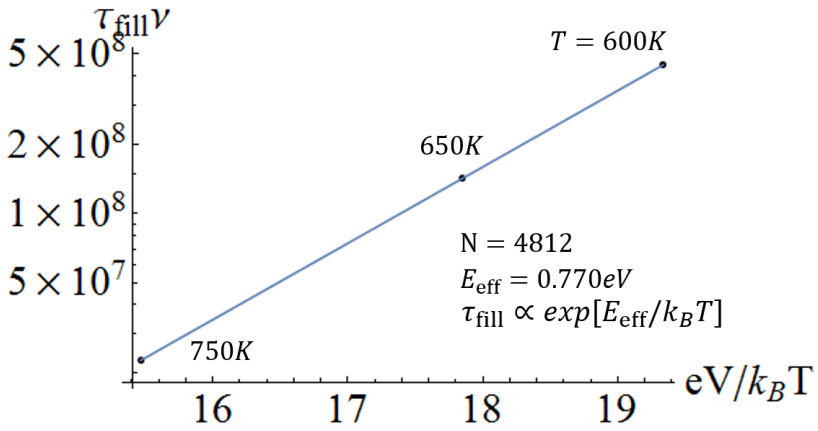

Figure 5.8: Arrhenius behavior of the characteristic time, τ_{fill}, for neck filling for the sintering of $\sim$ 4-nm Au NCs with aligned but laterally offset {111} facets for $N = 4812$.

5.5 Summary

In summary, we have developed a predictive atomistic-level stochastic model for far-from-equilibrium shape evolution of fcc metal NC shapes mediated by surface diffusion. Significantly, our modeling incorporates a realistic prescription of surface diffusion kinetics. This requires accurate description of diffusion barriers for a diversity of local environments. This paper contrasts previous more generic stochastic atomistic modeling with unphysical prescription of barriers and thus kinetics, and also classic continuum modeling which exhibits fundamental shortcomings in describing behavior on the nanoscale. Our model is primarily applied to reliably describe reshaping and sintering of faceted Ag NCs. Significantly, for the effective Arrhenius energies controlling the T dependence of relaxation times, we are able to provide an atomistic-level interpretation and analysis. For example, for the characteristic time for reshaping on Ag nanocubes, we associate the Arrhenius energy with the effective barrier to nucleation of relatively stable square tetramers on {100} facets. In addition, in contrast to generic modeling, our approach allows prediction of the absolute time scale from reshaping, which is key in assessing the robustness of NCs synthesized with targeted nonequilibrium shapes. This capability is demonstrated by prediction of the time for sintering of $\sim$ 4-nm Au NCs as observed in HRTEM studies.

5.6 Acknowledgments

This work was supported by the U.S. Department of Energy (USDOE), Office of Science, Basic Energy Sciences, Division of Chemical Sciences, Geosciences, and Biosciences through the Ames Laboratory Chemical Physics program. The work was performed at Ames Laboratory, which is operated for the USDOE by Iowa State University (ISU) under Contract No. DE-AC02-07CH11358. Partial support is also acknowledged from an ISU Presidential Interdisciplinary Research Seed grant.

5.7 Appendices

5.7.1 Appendix A: IVA versus realististic surface diffusion barriers

As noted in Sec. I, accurate description of surface diffusion kinetics, including both terrace and step edge diffusion, is necessary for realistic and predictive modeling of 3D NC evolution. Furthermore, the formulation must simultaneously provide an accurate description of behavior on both {100} and {111} facets, noting that these are most prominent on fcc NCs. Our formulation, used for simulation of surface diffusion mediated 3D NC evolution, is crafted to incorporate the flexibility to include desired values for both terrace diffusion and edge diffusion barriers via appropriate selection of $c_{100\text{TD}}$, $c_{111\text{TD}}$,c_{111A}, and c_{111B}. These values may be obtained from appropriate assessment of experimental data or directly from ab initio DFT analysis. In contrast, previous IVA based modeling does not include this flexibility. In fact, we clarify here that IVA imposes extremely unrealistic values for barriers for these key diffusion processes.

The IVA atom hop rates have the form $h = \nu \exp\left[-E_{\text{act}}/(k_B T)\right]$, with $E_{\text{act}} = C_{\text{IVA}} + n_i\phi$ for initial coordination number n_i, includes the free parameter C_{IVA}. For modeling of processes on a specific low-index extended surface, C_{IVA} is typically chosen to ensure that IVA recovers the terrace diffusion barrier for that low-index surface [28, 53]. However, a different choice is required for each different low-index surface, so it is not possible to correctly describe simultaneously terrace diffusion on different facets of 3D nanoclusters.

Consider the case of Ag selecting a NN interaction strength $\phi = 0.225$eV. First, consider modeling targeting Ag diffusion on Ag {100} surfaces. If one wants to recover a reasonable terrace diffusion barrier of, say, $E_d\{100\} = 0.425$eV [28,31], then since $E_d\{100\} = C\text{IVA} + 4\phi$ one must select $C_{\text{IVA}} = -0.475$eV. Consequently, this formulation of IVA imposes a diffusion barrier on {111} facets of $E_d\{111\} = C_{\text{IVA}} + 3\phi = 0.20$eV, which is double the true barrier of $E_d\{111\} = 0.1$eV [28,54].

Even ignoring this serious failure of IVA to simultaneously describe terrace diffusion

on different facets, there are additional major shortcomings in the description of key edge diffusion barriers. For example, there is a dramatic failure to describe step edge diffusion on Ag{100} surfaces even choosing $C_{\rm IVA}$ to recover terrace diffusion on a Ag{100} facet. Specifically, the IVA edge diffusion barrier along close packed steps satisfies $E_e(100) = C_{\rm IVA} + \delta + 5\phi = 0.650$eV (i.e., 53% higher than the terrace diffusion barrier) with the above choice of $C_{\rm IVA} = -0.475$eV. However, a reasonable estimate of the actual barrier is given by $E_e = 0.275$eV (i.e., 35% lower than the terrace diffusion barrier) [22, 28, 35]. Thus, these edge diffusion hopping rates predicted by this version of IVA are typically orders of magnitude lower than actual rates.

Second, for modeling targeting Ag diffusion on Ag{111} surfaces, since $E_d(111) = C_{\rm IVA} + 3\phi$, one must now choose $C_{\rm IVA} = -0.575$eV to recover a reasonable value of $E_d(111) = 0.10$eV [28,54]. It follows that this IVA prescription enforces $E_d(100) = C_{\rm IVA} + 4\phi = 0.325$eV substantially below the more realistic value of $E_d(100) = 0.425$eV noted above. Even if we just consider diffusion on the Ag{111} surface within this IVA formulation, there are still significant shortcomings in the description of step edge diffusion. One has that $E_e(111) = C_{\rm IVA} + 5\phi = 0.550$eV, which is the same for A- and B-type steps, and is well above the realistic and distinct estimates of $E_e(111)|_A = 0.275$eV and $E_e(111)|_B = 0.300$eV for the two different types of step edges [33].

The severe consequences of this failure of IVA kinetics (and the success of our treatment) are illustrated by the results of KMC simulations for the formation during deposition of 2D epitaxial Ag nanoclusters on low-index {100} and {111} Ag surfaces. Given the artificially high step edge diffusion barriers in the IVA prescription, this formulation predicts fractal island structure whereas the actual structure is compact as confirmed by scanning tunneling microscopy experiments or realistic modeling. See Supplemental Material [27].

Another clear and serious shortcoming of the IVA formulation regarding reshaping of 3D nanoclusters is that the formulation does not and cannot include any ES barriers. However, these additional barriers are important in controlling the rate of mass flow between layers

and facets [28].

5.7.2 Appendix B: Thermodynamics of fcc metal nanoclusters

Our prescription of the energetics of various NC configurations via a lattice-gas model with NN pairwise interactions of effective strength, ϕ, is applied to evaluate differences, $E_f - E_i$, between energies of initial and final configurations. As noted in Sec. 5.2, support for the effectiveness of this simple prescription comes from a recent DFT analysis of the energetics of fcc NCs [39]. The key idea in this paper is that the total energy of the NC can be decomposed into a sum of energies for the individual atoms, E_n, where these energies depend solely on the coordination, n, of the atom. These coordination-dependent single atom energies are determined in a systematic fashion from DFT calculations considering mainly atoms at surfaces with different local configurations and coordination numbers. The key result for various metals is that E_n varies nearly linearly with n, i.e., $E_n \approx A - Bn$ (with $B > 0$), over the considered coordination range, $n \geq 3$.

Given this behavior, reliable determination of $E_f - E_i$ can be achieved by a model with NN pairwise interactions if one chooses $\phi = 2B$. (Here we note that an atom with coordination n is regarded as having n shared bonds of strength ϕ with NN atoms, so the energy of half of each of these bonds is associated with the atom.) Such an analysis of results from Ref. [39] indicates that the effective $\phi \approx 0.20$, 0.28, 0.38, 0.40, and 0.64eV for Ag, Cu, Ni, Pt, and Ir, respectively. For Au, E_n versus n deviates more from linearity with higher (lower) values of the effective ϕ for smaller (larger) n, and we select $\phi = 0.22$eV.

We argue that these values predominantly reflect the NC surface rather than bulk thermodynamics. This feature is supported by the observation that similar values for the effective ϕ can be extracted from DFT results for {111} and {100} surface energies using $\gamma_{111} = \sqrt{3}\phi/a^2$ and $\gamma_{100} = 2\phi/a^2$ for the NN interaction model. Here, a denotes the surface lattice constant. From results of DFT analysis for γ_{111} using the Perdew-Burke-Ernzerhof functional [52] one obtains $\phi = 0.23$, 0.31, 0.43, 0.41, and 0.61eV for Ag, Cu, Ni, Pt, and

Ir, respectively. For Au, one obtains $\phi = 0.22$eV. Quite similar values are obtained using DFT values for γ_{100}, e.g., yielding $\phi = 0.21$eV for Ag and $\phi = 0.23$eV for Au.

As already indicated in Sec. 5.2, if E_c denotes the bulk cohesive energy, then the above values for effective ϕ are far from the choice $\phi(\text{bulk}) = E_c/6$ which would recover the bulk thermodynamics. Specifically, one has that $\phi(\text{bulk}) = 0.49$, 0.58, 0.74, 0.97, and 1.16eV for Ag, Cu, Ni, Pt, and Ir, respectively, and $\phi(\text{bulk}) = 0.64$eV for Au.

5.8 Supplementary Material

See Supplementary Material at for further description of: IVA vs realistic simulations of 2D epitaxial NC growth (S1); Ag nanocube reshaping (S2); pinch-off of Ag nanorods (S3); sintering of Ag NCs with aligned {100} (S4) and {111} (S5) facets; sintering of Au NCs (S6).

Bibliography

[1] Younan Xia, Yujie Xiong, Byungkwon Lim, and Sara E. Skrabalak. Shape-Controlled Synthesis of Metal Nanocrystals: Simple Chemistry Meets Complex Physics? *Angew. Chem. Int. Ed.*, 48(1):60–103, 2009.

[2] L. D. Marks and L. Peng. Nanoparticle shape, thermodynamics and kinetics. *J. Phys.: Condens. Matter*, 28(5):053001, 2016.

[3] Lorenz Ratke and Peter W Voorhees. *Growth and coarsening: Ostwald ripening in material processing*. Springer Science & Business Media, 2013.

[4] Nguyen T. K. Thanh, N. Maclean, and S. Mahiddine. Mechanisms of Nucleation and Growth of Nanoparticles in Solution. *Chem. Rev.*, 114(15):7610–7630, 2014.

[5] W. W. Mullins. Theory of Thermal Grooving. *J. Appl. Phys.*, 28(3):333–339, 1957.

[6] Jens Eggers. Coalescence of Spheres by Surface Diffusion. *Phys. Rev. Lett.*, 80(12):2634–2637, 1998.

[7] Teck H. Lim, David McCarthy, Shaun C. Hendy, Kevin J. Stevens, Simon A. Brown, and Richard D. Tilley. Real-Time TEM and Kinetic Monte Carlo Studies of the Coalescence of Decahedral Gold Nanoparticles. *ACS Nano*, 3(11):3809–3813, 2009.

[8] Jong Min Yuk, Jungwon Park, Peter Ercius, Kwanpyo Kim, Daniel J. Hellebusch, Michael F. Crommie, Jeong Yong Lee, A. Zettl, and A. Paul Alivisatos. High-Resolution EM of Colloidal Nanocrystal Growth Using Graphene Liquid Cells. *Science*, 336(6077):61–64, 2012.

[9] Jong Min Yuk, Myoungho Jeong, Sang Yun Kim, Hyeon Kook Seo, Jihyun Kim, and Jeong Yong Lee. In situ atomic imaging of coalescence of Au nanoparticles on graphene: rotation and grain boundary migration. *Chem. Commun.*, 49(98):11479–11481, 2013.

[10] Lise-Marie Lacroix, Raul Arenal, and Guillaume Viau. Dynamic HAADF-STEM Observation of a Single-Atom Chain as the Transient State of Gold Ultrathin Nanowire Breakdown. *J. Am. Chem. Soc.*, 136(38):13075–13077, 2014.

[11] Xingchen Ye, Matthew R. Jones, Layne B. Frechette, Qian Chen, Alexander S. Powers, Peter Ercius, Gabriel Dunn, Grant M. Rotskoff, Son C. Nguyen, Vivekananda P. Adiga, Alex Zettl, Eran Rabani, Phillip L. Geissler, and A. Paul Alivisatos. Single-particle mapping of nonequilibrium nanocrystal transformations. *Science*, 354(6314):874–877, 2016.

[12] G. C. Kuczynski. Study of the Sintering of Glass. *J. Appl. Phys.*, 20(12):1160–1163, 1949.

[13] C Herring. Chapter 8 in the physics of powder metallurgy. *MacGraw-Hill, New-York*, page 143, 1951.

[14] F. A. Nichols and W. W. Mullins. Morphological Changes of a Surface of Revolution due to Capillarity-Induced Surface Diffusion. *J. Appl. Phys.*, 36(6):1826–1835, 1965.

[15] C. Bréchignac, Ph. Cahuzac, F. Carlier, C. Colliex, J. Leroux, A. Masson, B. Yoon, and Uzi Landman. Instability Driven Fragmentation of Nanoscale Fractal Islands. *Phys. Rev. Lett.*, 88(19):196103, 2002.

[16] Alexander Volk, Daniel Knez, Philipp Thaler, Andreas W. Hauser, Werner Grogger, Ferdinand Hofer, and Wolfgang E. Ernst. Thermal instabilities and Rayleigh breakup of ultrathin silver nanowires grown in helium nanodroplets. *Phys. Chem. Chem. Phys.*, 17(38):24570–24575, 2015.

[17] Vyacheslav Gorshkov and Vladimir Privman. Kinetic Monte Carlo model of breakup of nanowires into chains of nanoparticles. *J. Appl. Phys.*, 122(20):204301, 2017.

[18] S. V. Khare and T. L. Einstein. Unified view of step-edge kinetics and fluctuations. *Phys. Rev. B*, 57(8):4782–4797, 1998.

[19] Nicolas Combe, Pablo Jensen, and Alberto Pimpinelli. Changing Shapes in the Nanoworld. *Phys. Rev. Lett.*, 85(1):110–113, 2000.

[20] William W. Mullins and Gregory S. Rohrer. Nucleation Barrier for Volume-Conserving Shape Changes of Faceted Crystals. *J. Am. Ceram. Soc.*, 83(1):214–16, 2000.

[21] David N. McCarthy and Simon A. Brown. Evolution of neck radius and relaxation of coalescing nanoparticles. *Phys. Rev. B*, 80(6):064107, 2009.

[22] C. R. Stoldt, A. M. Cadilhe, C. J. Jenks, J.-M. Wen, J. W. Evans, and P. A. Thiel. Evolution of Far-From-Equilibrium Nanostructures Formed by Cluster-Step and Cluster-Cluster Coalescence in Metal Films. *Phys. Rev. Lett.*, 81(14):2950–2953, 1998.

[23] P. Jensen, N. Combe, H. Larralde, J. L. Barrat, C. Misbah, and A. Pimpinelli. Kinetics of shape equilibration for two dimensional islands. *Eur. Phys. J. B*, 11(3):497–504, 1999.

[24] Da-Jiang Liu and J. W. Evans. Sintering of two-dimensional nanoclusters in metal(100) homoepitaxial systems: Deviations from predictions of Mullins continuum theory. *Phys. Rev. B*, 66(16):165407, 2002.

[25] Pablo Jensen. Growth of nanostructures by cluster deposition: Experiments and simple models. *Rev. Mod. Phys.*, 71(5):1695–1735, 1999.

[26] Vyacheslav Gorshkov, Vasyl Kuzmenko, and Vladimir Privman. Nonequilibrium kinetic study of sintering of dispersed nanoparticles. *CrystEngComm*, 15(36):7177–7191, 2013.

[27] See Supplemental Material at http://link.aps.org/supplemental/10.1103/PhysRevMaterials.3.026001 for further description of IVA versus realistic simulations of 2D epitaxial NC growth (S1), Ag nanocube reshaping (S2), pinch-off of Ag nanorods (S3), sintering of Ag NCs with aligned 100 (S4) and 111 (S5) facets, and sintering of Au NCs (S6).

[28] J. W. Evans, P. A. Thiel, and M. C. Bartelt. Morphological evolution during epitaxial thin film growth: Formation of 2D islands and 3D mounds. *Surf. Sci. Rep.*, 61(1):1–128, 2006.

[29] Thomas Michely and Joachim Krug. *Islands, mounds and atoms*, volume 42. Springer Science & Business Media, 2012.

[30] S. K. Xiang and Hanchen Huang. Ab initio determination of Ehrlich–Schwoebel barriers on Cu{111}. *Appl. Phys. Lett.*, 92(10):101923, 2008.

[31] S. Frank, H. Wedler, R. J. Behm, J. Rottler, P. Maass, K. J. Caspersen, C. R. Stoldt, P. A. Thiel, and J. W. Evans. Approaching the low-temperature limit in nucleation and two-dimensional growth of fcc (100) metal films Ag/Ag(100). *Phys. Rev. B*, 66(15):155435, 2002.

[32] K. J. Caspersen, A. R. Layson, C. R. Stoldt, V. Fournee, P. A. Thiel, and J. W. Evans. Development and ordering of mounds during metal(100) homoepitaxy. *Phys. Rev. B*, 65(19):193407, 2002.

[33] Erik Cox, Maozhi Li, Po-Wen Chung, C. Ghosh, T. S. Rahman, C. J. Jenks, J. W. Evans, and P. A. Thiel. Temperature dependence of island growth shapes during submonolayer deposition of Ag on Ag(111). *Phys. Rev. B*, 71(11):115414, 2005.

[34] Maozhi Li, P.-W. Chung, E. Cox, C. J. Jenks, P. A. Thiel, and J. W. Evans. Exploration of complex multilayer film growth morphologies: STM analysis and predictive atomistic modeling for Ag on Ag(111). *Phys. Rev. B*, 77(3):033402, 2008.

[35] Yong Han, Conrad R. Stoldt, Patricia A. Thiel, and James W. Evans. Ab Initio Thermodynamics and Kinetics for Coalescence of Two-Dimensional Nanoislands and Nanopits on Metal (100) Surfaces. *J. Phys. Chem. C*, 120(38):21617–21630, 2016.

[36] Aleksey Ruditskiy and Younan Xia. Toward the Synthesis of Sub-15 nm Ag Nanocubes with Sharp Corners and Edges: The Roles of Heterogeneous Nucleation and Surface Capping. *J. Am. Chem. Soc.*, 138(9):3161–3167, 2016.

[37] Marijn A. van Huis, Lucas T. Kunneman, Karin Overgaag, Qiang Xu, Gregory Pandraud, Henny W. Zandbergen, and Daniël Vanmaekelbergh. Low-Temperature Nanocrystal Unification through Rotations and Relaxations Probed by in Situ Transmission Electron Microscopy. *Nano Lett.*, 8(11):3959–3963, 2008.

[38] Hengzhong Zhang, James J. De Yoreo, and Jillian F. Banfield. A Unified Description of Attachment-Based Crystal Growth. *ACS Nano*, 8(7):6526–6530, 2014.

[39] Luke T. Roling, Lin Li, and Frank Abild-Pedersen. Configurational Energies of Nanoparticles Based on Metal–Metal Coordination. *J. Phys. Chem. C*, 121(41):23002–23010, 2017.

[40] Claude R. Henry. Morphology of supported nanoparticles. *Prog. Surf. Sci.*, 80(3):92–116, 2005.

[41] T. P. Martin. Shells of atoms. *Phys. Rep.*, 273(4):199–241, 1996.

[42] J. N. Bronsted. Acid and Basic Catalysis. *Chem. Rev.*, 5(3):231–338, 1928.

[43] M. G. Evans and M. Polanyi. Inertia and driving force of chemical reactions. *Trans. Faraday Soc.*, 34(0):11–24, 1938.

[44] Lin Li, Philipp N. Plessow, Michael Rieger, Simeon Sauer, Roel S. Sánchez-Carrera, Ansgar Schaefer, and Frank Abild-Pedersen. Modeling the Migration of Platinum Nanoparticles on Surfaces Using a Kinetic Monte Carlo Approach. *J. Phys. Chem. C*, 121(8):4261–4269, 2017.

[45] Madeline Vara, Luke T. Roling, Xue Wang, Ahmed O. Elnabawy, Zachary D. Hood, Miaofang Chi, Manos Mavrikakis, and Younan Xia. Understanding the Thermal Stability of Palladium–Platinum Core–Shell Nanocrystals by In Situ Transmission Electron Microscopy and Density Functional Theory. *ACS Nano*, 11(5):4571–4581, 2017.

[46] Harald Garcke. Curvature Driven Interface Evolution. *Jahresber. Dtsch. Math. Ver.*, 115(2):63–100, 2013.

[47] Matthew A. Grayson. The heat equation shrinks embedded plane curves to round points. *Journal of Differential Geometry*, 26(2):285–314, 1987.

[48] Woei Wu Pai, John F. Wendelken, C. R. Stoldt, P. A. Thiel, J. W. Evans, and Da-Jiang Liu. Evolution of Two-Dimensional Wormlike Nanoclusters on Metal Surfaces. *Phys. Rev. Lett.*, 86(14):3088–3091, 2001.

[49] Luke T. Roling and Manos Mavrikakis. Toward rational nanoparticle synthesis: predicting surface intermixing in bimetallic alloy nanocatalysts. *Nanoscale*, 9(39):15005–15017, 2017.

[50] P. M. Spurgeon, K. C. Lai, Y. Han, Evans J. W., and Thiel P. A. Fundamentals of Au(111) Surface Dynamics: Coarsening of 2D Au Islands. *J. Phys. Chem. C*, 2020.

[51] P. Stoltze. Simulation of surface defects. *J. Phys.: Condens. Matter*, 6(45):9495–9517, 1994.

[52] Richard Tran, Zihan Xu, Balachandran Radhakrishnan, Donald Winston, Wenhao Sun, Kristin A. Persson, and Shyue Ping Ong. Surface energies of elemental crystals. *Sci. Data*, 3(160080):1–13, 2016.

[53] Shaun Clarke and Dimitri D. Vvedensky. Growth kinetics and step density in reflection high-energy electron diffraction during molecular-beam epitaxy. *J. Appl. Phys.*, 63(7):2272–2283, 1988.

[54] Harald Brune, Karsten Bromann, Holger Röder, Klaus Kern, Joachim Jacobsen, Per Stoltze, Karsten Jacobsen, and Jens Norskov. Effect of strain on surface diffusion and nucleation. *Phys. Rev. B*, 52(20):R14380(R)–R14383, 1995.

CHAPTER 6. COMPLEX OSCILLATORY DECREASE WITH SIZE IN DIFFUSIVITY OF {100}-EPITAXIALLY SUPPORTED 3D FCC METAL NANOCLUSTERS

A paper published in *Journal of Physical Chemistry C*

King Chun Lai[1,2], James W. Evans[1,2]

[1]*Department of Physics and Astronomy, Iowa State University, Ames, Iowa 50011, USA*

[2]*Ames Laboratory-USDOE, Iowa State University, Ames, Iowa 50011, USA*

(Received 10 July 2019; published 8 September 2019)

Abstract

Diffusion and coalescence of supported 3D metal nanoclusters (NCs) leads to Smoluchowski Ripening (SR), a key pathway for catalyst degradation. Variation of the NC diffusion coefficient, D_N, with size N (in atoms) controls SR kinetics. Traditionally, a form $D_N \sim N^{-\beta}$ was assumed consistent with mean-field analysis. However, KMC simulation of a stochastic model for diffusion of {100}-epitaxially supported fcc NCs mediated by surface diffusion reveals instead a complex oscillatory decrease of D_N with N. Barriers for surface diffusion of metal atoms across and between facets, along step edges, etc., in this model are selected to accurately capture behavior for fcc metals. (This contrasts standard bond-breaking prescriptions which fail dramatically.) For strong adhesion, equilibrated NCs are truncated pyramids (TP). Local minima of D_N sometimes but not always correspond to sizes, $N_{\rm TP}$, where these have a closed-shell structure. Local maxima generally correspond

to $N \approx N\text{TP} + 3$ for $N = O(10^2)$. For weak adhesion, equilibrated NCs are truncated octahedra (TO), and local minima of D_N occur for sizes close or equal to those of just a subset of closed-shell structures. Analytic characterization of energetics along the NC diffusion pathway (which involves dissolving and reforming outer layers of facets) provides fundamental insight into the behavior of D_N, including the strong variation with N of the effective NC diffusion barrier.

DOI: 10.1039/c9nr05845a

6.1 Introduction

Smoluchowski Ripening (SR) involving diffusion and coalescence of supported 3D metal nanoclusters (NCs), also known as Particle Migration & Coalescence (PMC), is of central importance as a pathway for catalyst degradation. [1–5] Classic studies have analyzed SR kinetics which is controlled by the size-dependence of NC diffusivity. [1, 2] Consequently, there has been sustained interest in the variation of the NC diffusion coefficient, D_N, with size N (in atoms). [2, 6] The traditional perception was that D_N decreases monotonically with N. This behavior is consistent with a mean-field analysis for NC diffusion mediated by uncorrelated hopping of individual atoms across the surface of the NC with single characteristic rate, h. In this scenario, each hop of a surface atom shifts the NC center of mass (CM) by $\delta R_{\text{CM}} \sim a/N$, where "$a$" is the surface lattice constant. The dimensionless NC surface area, A, scales like $A \sim N^{2/3}$, and the total rate of surface atom hopping like $H \sim hA$. It is convenient to set $h = \nu \exp\left[-E_s/(k_B T)\right]$, and $D^{\text{o}} = a^{\nu}$. Here, ν is an attempt frequency, Es is the assumed single surface hopping barrier, k_B is the Boltzmann constant, and T is the surface temperature. Then, the mean-field treatment predicts that

$$D_N \sim H(\delta R_{\text{CM}})^2 \sim D^{\text{o}} \exp\left[-E_{\text{eff}}/(k_B T)\right] N^{-\beta}$$
$$\text{with } E_{\text{eff}} = E_s \text{ and } \beta = \beta_{\text{MF}} = 4/3. \tag{6.1}$$

Our focus is on diffusion of epitaxially supported 3D NCs where diffusivity is generally lower than for non-epitaxially supported 3D NCs. [6] Detailed analysis of the epitaxially supported case is limited. One Kinetic Monte Carlo (KMC) simulation study for 3D epitaxial NCs, [7] and another for the analogous 2D case, [8] found an oscillatory variation of D_N with N, and suggested that minima correspond to sizes with closed-shell structures. However, subsequent analysis revealed a much more complex scenario for the 2D case, [9, 10] and no detailed analysis exists in 3D. Thus, our goal here is to characterize and provide fundamental insight into the "fine structure" in the variation of D_N with N for 3D epitaxial NCs.

Specifically, we develop a stochastic lattice-gas model for diffusion of {100}-epitaxially supported metallic fcc NCs mediated by diffusive transport of metal atoms across the surface of the NC. We emphasize that for realistic modeling, not just NC thermodynamics, but also the multiple barriers for surface diffusion across facets, along step edges and around kinks or corners, between layers or facets, etc., must be chosen to realistically capture behavior for fcc metals. [5, 11] KMC simulation of such stochastic modeling allows direct access to the relevant time scale for surface diffusion, and precise characterization of the variation of D_N with size N and other key control parameters such as temperature, T. However, for deeper insight into the observed complex behavior, we also identify NC diffusion pathways (which involve dissolving and reforming outer layers of facets). We provide an analytic assessment of the associated variation of atomistic-level NC energetics along such minimum energy pathways, as well as a corresponding coarse-grained continuum analysis.

This article is organized as follows. The stochastic model is described in the next section, as well as procedure for reliable extraction of NC diffusion coefficient, D_N. Then, we present detailed KMC results for D_N versus N for the case of strong NC adhesion to the substrate, as well as a complementary analytic characterization. Next, we more briefly analyze NC diffusion behavior for the case of weak NC adhesion. Finally, we provide additional Discussion including assessment of related systems, and brief Conclusions.

6.2 Modeling and Methods

6.2.1 Model information

The following provides a description our realistic stochastic lattice-gas model for diffusion of {100}-epitaxially supported metallic fcc NCs. NC diffusion is mediated by diffusive transport of individual metal atoms across the surface of the NC. This surface diffusion is described by hopping of under-coordinated atoms to available nearest-neighbor (NN) fcc sites still connected to the cluster. Thus, we exclude atom detachment particularly from the contact line at the base of the NC, thereby preserving NC size. With regard to NC thermodynamics, interactions within the fcc metal NC cluster are described by an effective NN attraction of strength $\phi > 0$. This prescription was shown in recent DFT analysis to effectively capture NC surface energetics for many fcc metals. [12] In fact, the value of ϕ extracted from this DFT analysis reasonably recovers surface energies, but is much weaker than that extracted from bulk energetics as one sixth of the cohesive energy, E_c (e.g., $\phi = 0.225$eV versus $E_c/6 = 0.49$eV for Ag). [11] In fact, the bulk cohesive energy is not incorporated as a parameter into our model. This is not unreasonable since NC diffusion is controlled by surface rather than bulk thermodynamics and kinetics. Each atom in the bottom {100} NC layer is regarded as supported by 4 atoms in the top {100} substrate layer. Adhesion is described by a NN attraction of strength $\phi_s = f\phi$ between NC and substrate atoms. Thus, f measures the strength of adhesion, and $f = 1$ corresponds to homoepitaxy. We focus on the regime of strong adhesion choosing $f = 0.75$ (where supported NCs resemble truncated pyramids), but for contrast more briefly consider weak adhesion where $f \leq 0.05$ (where the supported NCs resemble unsupported Wulff shapes).

The total NC energy, $E_N < 0$, is obtained as the sum of the total interaction energy within the NC, and the total adhesion energy. Ground state NC configurations have the minimum E_N. Equilibrated NCs exist in excited states with finite probability as determined by a Boltzmann factor based on E_N. In the large-size continuum limit, fluctuations around a

well-defined equilibrium shape vanish. For negligible adhesion ($f \approx 0$), this equilibrium NC shape corresponds to the Wulff shape of an unsupported NC. For our model, the Wulff shape corresponds to a regular truncated octahedron (TO) where all edges have equal length. [13] Equilibrium shapes of {100}-epitaxially supported NCs with significant adhesion are determined from the Winterbottom construction which truncates a portion of the unsupported Wulff cluster adjacent to a {100} facet. [13] Specifically, in the continuum regime, when measured from the center of the unsupported Wulff cluster, the distance to the top {100} facet, h_{100}, and to the substrate, $h_{\rm sub}$, are related by $h_{100}/\gamma_{100} = h_{\rm sub}/(\gamma_{100} - \beta_{\rm ad})$. Here, $\gamma_{100} = 2\phi a^{-2}$ denotes the surface energy of {100} facets, and $\beta_{\rm ad} = 4\phi_s a^{-2}$ denotes the adhesion energy. It follows that $h_{\rm sub}/h_{100} = 1 - 2f$. Negative values mean that the location of the substrate for the supported NC is above the center of the unsupported NC. See Fig. 6.1. In our atomistic model, equilibrium shapes mimic continuum shapes. See below.

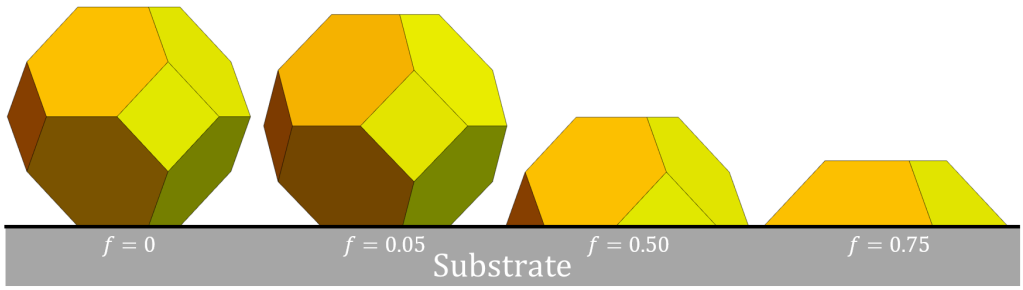

Figure 6.1: Schematics of equilibrium Winterbottom NC shapes for $f = 0$, 0.05, 0.5, and 0.75.

Diffusion of supported NCs is sensitively dependent on the prescription of the kinetics of adatom surface diffusion. In stochastic lattice-gas modeling, often a simple IVA bond-breaking prescription is applied to determine the activation barriers for hopping in diverse local surface environments. [14, 15] However, these (and alternative Metropolis type prescriptions) fail dramatically to describe key features of surface diffusion barriers on fcc metal surfaces, e.g., the relative magnitude of terrace diffusion on different facets, of terrace versus step edge diffusion, and of intra- versus inter-layer diffusion. [11] Consequently, we

apply a refined BEP formalism with sufficient flexibility to capture all key diffusion barriers, as described in the next subsection. [5,11]

For specificity, our model parameters are chosen to correspond to Ag. Supported 3D Ag NCs have been studied on graphite, [16] and on various oxide surfaces [17,18] including Al_2O_3, [19,20] TiO_2, [21,22] and MgO. [23] Theoretical analysis indicates that Ag NC on MgO(001) exhibits cube-on-cube {100} epitaxy at least for $N = 40$ to 2800, rather than {111} epitaxy or a decahedral structure. [24] Thus, Ag/MgO(001) falls within the class of systems described by our model.

6.2.2 Prescription of surface diffusion kinetics for fcc metal NCs

Realistic prescription of the surface diffusion kinetics is more challenging than that of NC thermodynamics. [5,11] Rates for hopping of surface atoms to NN sites have an Arrhenius form, $h = \nu \exp\left[-E_{\rm act}/(k_B T)\right]$, where the activation barrier, Eact, depends sensitively on the local environment (for which there are many possibilities). Again T denotes the surface temperature, and ν is a vibrational attempt frequency. (Typically, one finds that $\nu \approx 10^{12.5}{\rm s}^{-1}$ for fcc metal systems, although the value of this prefactor will not affect the results presented here.) Below E_i (E_f) denote the energies associated with an atom in the initial (final) state before (after) a NN hop. A conventional IVA bond-breaking form, $E_{\rm act} = E_0 - E_i$ is typically chosen, but this fails dramatically describe fcc metal surfaces. [5, 11] Thus, we instead choose a generalized symmetric BEP form [11]$E_{\rm act} = C_\alpha + 1/2(E_f - E_i)$ with distinct C_α for different classes α of hops, e.g., α = TD terrace diffusion + attachment/detachment at steps and ED step edge diffusion, and with separate subclasses for {111} and {100} facets, and also for intra- and interlayer diffusion. Each class includes the reverse process for every forward process (e.g., detachment as the reverse of attachment to step edges) in order to satisfy detailed-balance.

The C_α are selected to recover precise value for terrace, edge, and interlayer diffusion for the metal of interest. See the ESI sec. 1. For Ag, we select $C_{\rm TD100} = 0.425$eV,

$C_{\mathrm{TD111}} = 0.10\mathrm{eV}$, $C_{\mathrm{ED111}B} = 0.30\mathrm{eV}$, and $C_{\mathrm{ED111}A} = C_{\mathrm{ED100}} = 0.275\mathrm{eV}$ for intralayer diffusion. [11] Here, A and B indicate close-packed {100}- and {111}-microfaceted steps on {111} facets, respectively. The local geometry of the former is the same as for close-packed steps on {100} facets. For interlayer diffusion for Ag, our C_α also incorporate an additional Ehrlich-Schwoebel barrier for downward interlayer diffusion of $\delta_{\mathrm{ES}} = 0.1\mathrm{eV}$ for close-packed (but not kinked) steps on {100} facets, and for A (but not B) steps on {111} facets. We use the same C_α for hopping between the lowest and next highest layer of the NC. For atoms at the periphery of the lowest layer hopping around the contact line of the NC: (i) the same C_α are used for strong adhesion; and (ii) C_α are selected by neglecting substrate atoms for weak adhesion. We also allow atoms to hop to second NN sites in order to round corners of the contact line base the NC.

As indicated above, our model dynamics allows diffusion of metal atoms across the NC surface, but not detachment of atoms from the NC at its base (which would be followed by diffusion across the substrate, and possible reattachment to the NC). The rationale is as follows. The effective barrier for NC surface diffusion (detachment) is determined by the sum of: (i) the energy change upon moving an atom at a kink site on the NC to a facet on the NC (to the substrate); and (ii) the terrace diffusion barrier across the facet (across the substrate). The effective barrier is significantly higher for detachment justifying our neglect of this process. See the ESI sec. 2 for further discussion.

6.2.3 KMC simulation of NC diffusion

KMC simulation, which implements the various hopping processes with probabilities proportional to their physical rates, allows tracking of the evolution of the configuration of the NC as it diffuses across the surface. From such simulations, one can extract the lateral position, $r_{\mathrm{CM}}(t)$, of the NC center of mass (CM) at time t. Then, $\delta\mathbf{r}_{\mathrm{CM}}(\delta t) = \mathbf{r}_{\mathrm{CM}}(t + \delta t) - \mathbf{r}_{\mathrm{CM}}(t)$ gives the CM displacement in a time interval δt. One defines a time-dependent diffusion coefficient for the NC of N atoms as $D_N(\delta t) = \langle \mathbf{r}_{\mathrm{CM}}(\delta t) \cdot \mathbf{r}_{\mathrm{CM}}(\delta t) \rangle / (4\delta t)$. Gen-

erally, $D_N(\delta t)$ decreases from a "high" value for short δt to a plateau value as $\delta t \to \infty$, which corresponds to the true diffusion coefficient, $D_N = \lim \delta t \to \infty D_N(\delta t)$. The decrease in $D_N(\delta t)$ corresponds to subtle "back-correlations" in the walk of the cluster CM. [10] Simulations readily yield extensive statistics and thus precise values for $D_N(\delta t)$ for small δt, but not so readily for $\delta t = \delta t_p$ sufficiently large that $D_N(\delta t_p)$ has reached its plateau value. See ESI sec. 3. Thus, it is necessary to run simulations for an extended total time of 200 δt_p in order to precise determination NC diffusivity.

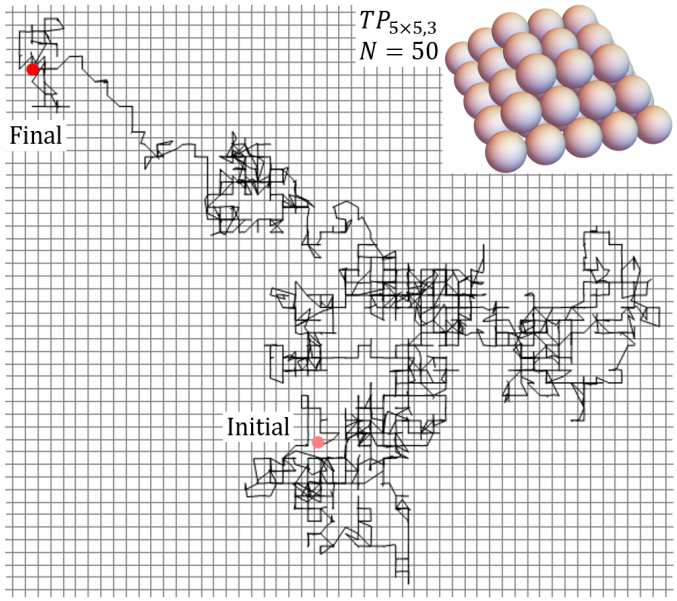

Figure 6.2: Diffusion trajectory from KMC simulation for a closed-shell Ag TP with size $N = 50$ for the case of strong adhesion with $f = 0.75$ at $900K$.

Fig. 6.3 shows KMC simulation results for a typical diffusion trajectory for the CM of an NC of size $N = 50$ atoms for the case of strong adhesion with $f = 0.75$ at $900K$. During diffusion, the NC can be regarded as remaining in equilibrium state. However, as noted above, the NC in this state does not just correspond to a fixed ground state NC configuration, but rather samples excited states. In the ESI sec. 4, we show snapshots which illustrate the NC evolving through a sequence of configurations during diffusion, and we also provide a movie of NC diffusion. Further discussion of key configurations accessed during

diffusion is provided in sec.6.3 and 6.4. For the system under consideration here, our analysis will reveal a complex dependence of D_N on size N. It will prove instructive to consider an effective activation barrier, $E_{\text{eff}} > 0$, for NC diffusion where $D_N \sim \exp\left[-E_{\text{eff}}/(k_B T)\right]$ for fixed N at various T. In contrast to the MF treatment, $E\text{eff} = E_{\text{eff}}(N)$ will depend strongly on N, and this dependence will in fact induce the complex variation of D_N with N.

6.3 Results for Strong Adhesion $f = 0.75$

6.3.1 Ground-state NC shapes with strong adhesion with $f = 0.75$

The adhesion energy per atom in the lowest NC layer is $4f\phi$ given the four supporting substrate atoms, which equals 3ϕ for $f = 0.75$. Thus, conveniently, the total NC energy E_N is an integer multiple of ϕ. The continuum Winterbottom NC shape is a truncated square pyramid (TP) where the length of the edges of the top square {100} facet equals that of the edges between {111} side facets. See Fig. 6.1. For the atomistic model, ground state structures tend to mimic the continuum shape. Particularly stable ground state structures correspond to a subset of closed-shell k-layer TP with bases of $m \times n$ atoms, denoted by $\text{TP}_{m\times n,k}$. For these $\text{TP}_{m\times n,k}$ structures, the total number of atoms, $N = N_{m\times n,k}$, is given by

$$\begin{aligned} &N_{m\times n,k} = a_k mn - b_k(m+n) + c_k, \\ &\text{where } a_k = k, b_k = k(k-1)/2, \text{ and } c_k = (2k-1)k(k-1)/6, \end{aligned} \tag{6.2}$$

and the total NC energy, $E_N = E_{m\times n,k} < 0$, is given by

$$\begin{aligned} &E_{m\times n,k} = -\left[A_k mn - B_k(m+n) + C_k\right]\phi \\ &\text{where } A_k = 6k-1, B_k = (3k-2)k, \text{ and } C_k = 2k^2(k-1). \end{aligned} \tag{6.3}$$

Ground state $\text{TP}_{m\times n,k}$ structures have $m = n$ square or $m = n+1$ near-square bases, and also $k \le \min(n,m) - 1$ so that the top layer is 2×2 or larger. Corresponding, ground states sizes in bold font are:

$N_{m\times n,1} = 4, 6, 9, 12$ (degen), (but not 16,...) for $m \times n = 2\times 2, 3\times 2, 3\times 3, 4\times 3$, (but not 4×4,...);

$N_{m\times n,2} = 13, 18, 25, 32, 41,$ (but not 50,...) for $m \times n = 3\times 3, 4\times 3, 4\times 4, 5\times 4, 5\times 5$ (but not 6×5,...);

$N_{m\times n,3} = 29, 38, 50, 62, 77, 92, 110, 128, 149$ (degen), (but not 170,...) for $m\times n = 4\times 4, ..., 5$ (but not 9×8,...);

$N_{m\times n,4} = 54, 68, 86, 104, 126, 148, 174,$ for $m \times n = 5\times 5, ..., 8\times 8$,...);

$N_{m\times n,5} = 135, 160,$ (but not 90 or 110) for $m\times n = 7\times 7, 8\times 7, ...$ (but not 6×6 or 7×6...) etc.

for single- double-, triple-, quadruple, quintuple-layer NCs, etc. The particular stability of these sizes is quantified below. Sizes are also indicated which are not ground states, and $N = 12$ & 149 are degenerate with higher-layer structures.

6.3.2 KMC results for D_N versus N

Analysis of the type of simulation data for the trajectories of {100}-epitaxially supported 3D Ag NCs for strong adhesion with $f = 0.75$ shown in Fig. 6.2 produces the results shown in Fig. 6.3 (middle frame) for the variation of D_N with N up to $N \sim 190$. Behavior for larger sizes is reported in the ESI sec. 5, and is briefly discussed in sec. 6.3.5. A complex oscillatory variation is most evident at the lowest temperature shown, $T = 700K$. These features are diminished by entropic effects at higher T, as shown for $T = 800K$ and $900K$. The vertical lines mark the sizes for the non-degenerate closed-shell ground state TPs listed above with sizes denoted $N = N_{\rm TP}$. Often, but not always, these correspond to local minima in D_N. Often, local maxima in D_N correspond to $N = N_{\rm TP} + 2$ or $N_{\rm TP} + 3$ in the size range shown. Closed-shell TPs are expected to be relatively stable. Indeed, a measure, $\delta E = \delta E_N$, of the deviation from the continuum form of the energy per atom, also shown in Fig. 6.3 (top), correlates with the variation of D_N (i.e., relatively high average coordination per atom implies relatively low diffusivity). From the variation of D_N with T for fixed N,

we can extract from KMC data an effective barrier, $E_{\text{eff}}(N)$, for NC diffusion for each N as is also shown in Fig. 6.3 (bottom). It is instructive to compare E_{eff} for different classes of NCs where $N = N_{\text{TP}} + n$ for small n: $E_{\text{eff}}(N_{\text{TP}} + n) \approx 1.5$, 1.1, 0.85, 0.75eV decreases as n increases from $n = 0$, 1, 2, and 3, respectively, as is most clearly evident for $N_{\text{TP}} = 50$, 62, 77, and 92.

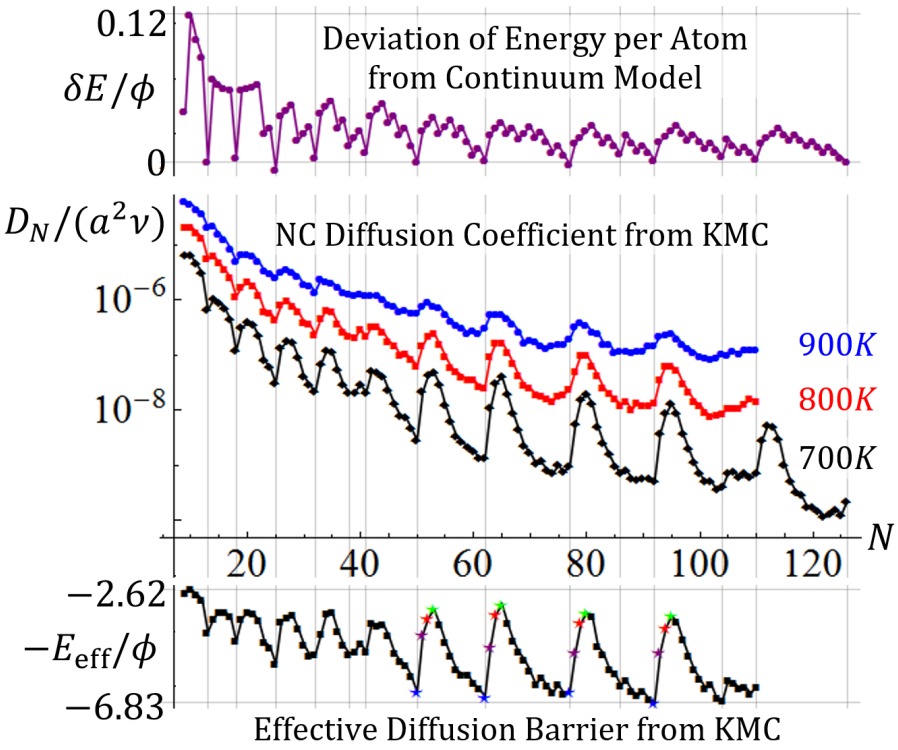

Figure 6.3: Top: $\delta E = [E_N - E_N(\text{cont})]/N$ where $E_N(\text{cont})/\phi = 0.529 - 1.496N^{1/3} + 3.977N^{2/3} - 6N$ recovers E_N for $\text{TP}_{3\times3,3}$, $\text{TP}_{5\times5,3}$, $\text{TP}_{7\times7,4}$, and $\text{TP}_{9\times9,5}$. Middle: KMC results for D_N versus N for an Ag NCs with $f = 0.75$. Bottom: Effective barrier versus N for NC diffusion extracted from the T-dependence of D_N from KMC highlighting several cases for N_{TP} (blue), $N_{\text{TP}} + 1$ (purple), $N_{\text{TP}} + 2$ (red), $N_{\text{TP}} + 3$ (green); $-E_{\text{eff}}$ is plotted so that peaks and valleys correspond to those of D_N. Note: vertical lines correspond to sizes for closed-shell ground state truncated pyramids.

Finally, we note that while many previous studies of NC diffusion have focused on simple size scaling, $D_N \sim N^{-\beta}$, such a routine analysis is not applicable here given the complex oscillatory behavior. However, one could consider the partial scaling of D_N with N, e.g.,

restricting N to local maxima (max) of D_N. Based on the three maxima at $N = 65$, 80, and 95 in Fig. 6.3, one obtains $\beta_{\max} \approx 3.1$, 2.6, and 2.1 at $700K$, $800K$, and $900K$, respectively, which are higher than but shifting towards $\beta_{\mathrm{MF}} = 1.33$ for increasing T.

6.3.3 Mechanism & energetics for NC diffusion

To elucidate the behavior of D_N, we first describe the mechanistic pathway leading to long-range NC diffusion for the case where NC ground states are closed-shell TPs. The pathway involves dissolution of an outer layer of the NC on a single facet, transfer of those atoms to another side of the NC, and formation of a new complete outer layer on that side. Specifically, for a square n n base, the outer layer is transferred to the opposite side. For a rectangular $n \times (n + 1)$ base, the outer layer on a short side is transferred to one of the other three sides. Atom transfer between facets generally occurs across edges between adjacent side {111} facets, rather than across the top {100} facet or around the base of the NP. The latter are kinetically inhibited by high diffusion barriers in our model (a feature which dominates the thermodynamic preference for adatoms to reside on {100} versus {111} facets). Complete transfer of an outer layer recovers the initial closed-shell ground-state structure, but with shifted CM, thereby leading to long-range NC diffusion.

The above process can be quantified analytically by tracking the energy change, $\Delta E(q)$, as a function of the number, q, of atoms transferred between different sides of the NC for the minimum energy path (MEP). The MEP has the smallest $\Delta E(\max) = \max_q \Delta E(q)$. By symmetry, $\Delta E(q) = \Delta E(q_{\mathrm{tot}} - q)$, where $q_{\mathrm{tot}} = k(2n - k + 1)/2$ is the total number of atoms in the facet supplying atoms with base with of n atoms and height of k layers. Examples are provided in Fig. 6.4 (black curves) for $\mathrm{TP}_{5\times5,3}$ ($N_{\mathrm{TP}} = 50$), $\mathrm{TP}_{7\times6,4}$ ($N_{\mathrm{TP}} = 104$), and $\mathrm{TP}_{8\times8,5}$ ($N_{\mathrm{TP}} = 190$) with $\Delta E(\max) = 4\phi$, 5ϕ, and 6ϕ, respectively. $\Delta E(\max)$ gives a measure of the difficulty of mass transfer, and thus of NC diffusion (but it does not account for the details of surface diffusion kinetics or entropic effects).

Analysis is more complex for non-closed or open-shell TPs which one generally can

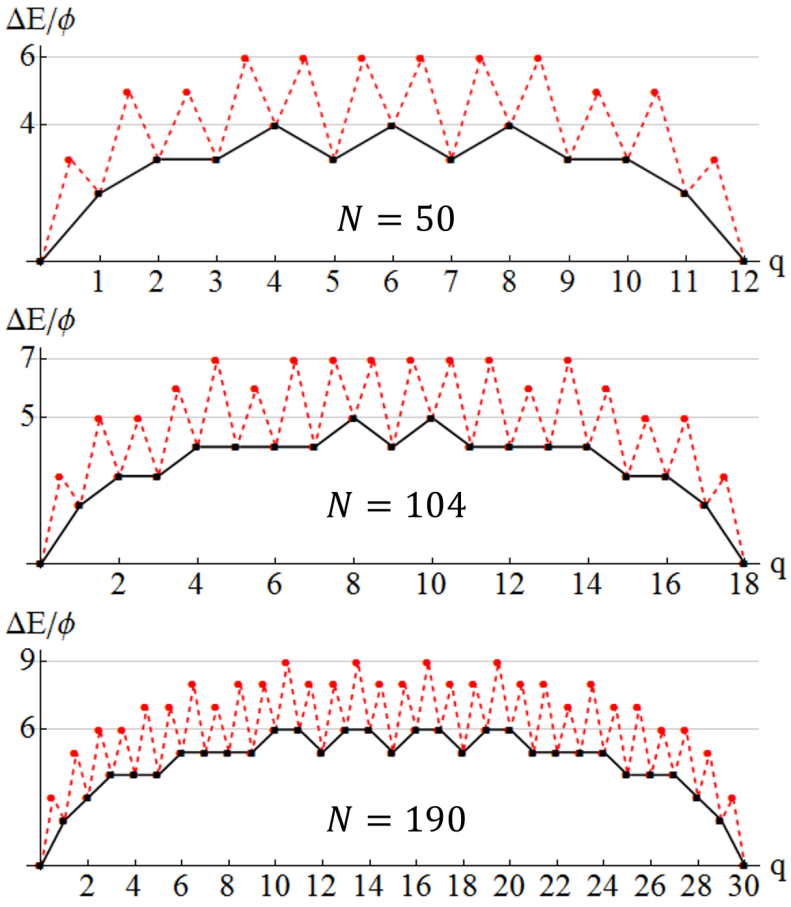

Figure 6.4: Analytic determination of $\Delta E(q)$ versus q for close-shell NCs with $N_{\rm TP} = 50$, 104, and 190. Black curves show ΔE by comparing states before and after an atom transit. Red dashed curves shows ΔE during an atom move between facet 1 and 2.

regard as a closed-shell TP with an additional incomplete layer on one facet. Consider the following two-stage diffusion pathway. In the first stage, atoms are transferred to complete an incomplete 2D layer on a facet labeled 2 from a complete facet labeled 1 on the opposite side. In the second stage, the incomplete layer now existing on facet 1 is transferred to facet 2. Then, the original NC structure is recovered, but with shifted CM. $\Delta E(q)$ versus q has a different form in each stage, but vanishes at the end of each stage. See below. Other cases involve shifting the incomplete layer to an adjacent (rather than the opposite) side facet. Even more complicated scenarios can occur in some cases where the ground state

NC structure is k-layer, but the diffusion path with the lowest $\Delta E(\max)$ goes through a $(k-1)$-layer NC configurations. One example is for $N = 66$ where the ground state is a 4-layer structure, but the optimum diffusion pathway goes through 3-layer structures. See ESI sec. 6.

Fig. 6.5 provides comprehensive analytic results for $\Delta E(\max)$ versus N up to $N = 110$ for both open- and closed-shell TPs. $\Delta E(\max)$ for closed-shell TPs correspond to local maxima, and the $\Delta E(\max)$ variation with N correlates reasonably with that of D_N. Fig. 6.5 also indicates a slow increase in $\Delta E(\max)$ with N, somewhat obscured by the strong oscillatory behavior. This feature will be elucidated below. $\Delta E(\max)$ just characterizes the thermodynamics rather than the kinetics of the NC diffusion process.

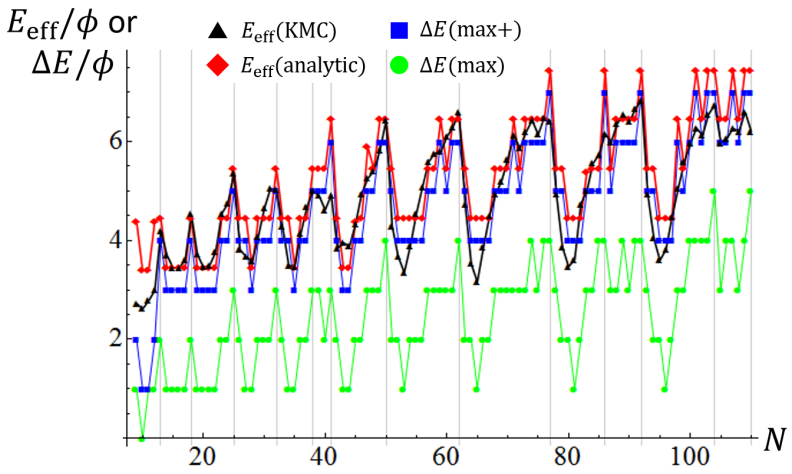

Figure 6.5: Variation of $\Delta E(\max)$, $\Delta E(\max+)$, E_{eff}(analytic), and E_{eff}(KMC) with N. Vertical lines indicate sizes for closed-shell ground state TPs.

To assess kinetics, we note that $\Delta E(q)$ just describe energies relative to the ground state after each transfer of an adatom between facets and incorporation into a growing 2D layer. Thus, naturally the system energy is higher mid-atom transfer, and thus the actual energy barrier which the system must surmount for NC diffusion is higher. For large NCs, the increased barrier will reflect energy difference of 3ϕ between an isolated atom in transit at a 3fh site on a {111} facet and that atom incorporated into a kink site at the periphery of

an incomplete layer. However, for smaller NCs, this energy difference is often 2ϕ. Fig. 6.4 also shows the energy profile along the MEP incorporating energies mid-atom transfer as a dashed red line, and Fig. 6.5 also shows the corresponding boosted $\Delta E(\max+)$ versus N. Finally, the actual effective barrier for Eeff for the above process must add a diffusion barrier which is typically but not always equal to that for terrace diffusion on {111} facets of 0.1eV for Ag. This analytic estimate of E_{eff}(analytic) versus N is also shown in Fig. 6.5. Again we caution that this analysis does not account for entropic effects. The analytic treatment is successful in capturing the key features of our KMC estimate, E_{eff}(KMC) (reproduced from Fig. 6.2).

6.3.4 Continuum analysis of energetics

Fig. 6.5 indicates a slow increase in $\Delta E(\max)$ with N, somewhat obscured by the strong oscillatory behavior. To elucidate this trend, and the variation of $\Delta E(q)$ with q, it is instructive to perform a continuum analyses for behavior in the large NC size regime. For a closed-shell (CS) TP, Fig. 6.6 shows schematically the process of transferring atoms from an initially complete outer layer on one facet to another facet. One issue is the shape of 2D island constituting the incomplete layer. This island is bounded by close-packed step edges on the sides and top as shown in Fig. 6.6, and these have the same step energy $\sigma = \phi/a$. For our model with $f = 0.75$, the higher coordination of atoms on the bottom step at the contact line with substrate atoms dominates the weaker binding strength to those atoms resulting in a vanishing effective step energy. See ESI sec. 7. With these step energies, minimization of total 2D island step energy for fixed island area reveals that the minimum energy shape has equal length step edges on the sides and top, and double that length on the bottom. Thus, the equilibrium 2D island shape is identical to the overall side facet shape of the TP. Given this island shape, it is straightforward to determine the change in system energy,

$$\Delta E(x)|_{\text{CS}} = 3\sigma l \left[(1-x)^{1/2} + +x^{1/2} - 1\right] \text{ with } x = a/a_{\text{tot}}, \tag{6.4}$$

as a function the fraction, x, of atoms transferred to the new facet. This form shown in Fig. 6.6 mimics that of the discrete model in Fig. 6.3. It follows that the maximum $\Delta E(x)$ for $x = 1/2$ satisfies

$$\Delta E(\max)|_{\mathrm{CS}} = (\sqrt{2} - 1)3\sigma l \approx 1.24\sigma l \sim N^{1/3}, \tag{6.5}$$

reasonably tracking actual values in Fig. 6.5, and elucidating the slow increase in $\Delta E(\max)$ with N.

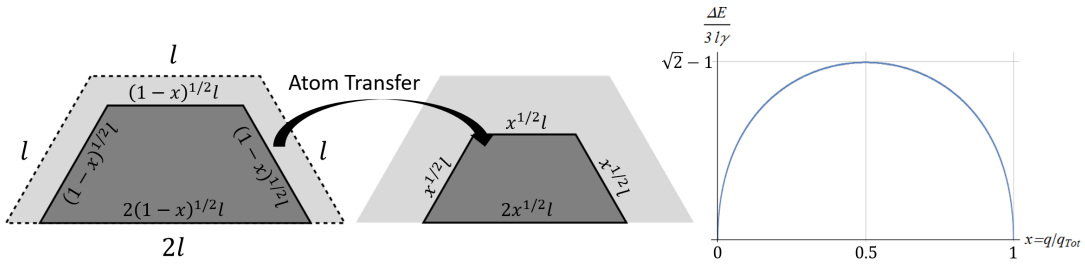

Figure 6.6: Continuum analysis of energy change upon atom transfer for a closed-shell TP. Dashed line shows initial complete side facet layer on the TP which shrinks during atom transfer (dark gray) leading to growth of an incomplete layer (also dark gray) on the other facet. The variation in energy is also shown (right).

Next, we more briefly present a continuum treatment for open-shell (OS) TPs. As discussed above, the mechanism for mass transfer leading to NC diffusion has two stages. First, atoms are transferred from a complete facet 1 to grow an initially incomplete layer on facet 2 (which becomes complete). Second, the incomplete layer remaining on facet 1 is transferred to facet 2. Fig. 6.7 shows the case where the dimensions of the initial incomplete layer are smaller by a factor of r than those of the complete facet. Here, x_1 (x_2) denotes the fraction of atoms transferred in the first (second) stage. Evaluating the energy change as a function of the amount of material transferred (see ESI sec. 8), one finds that $\Delta E(\max 1)|_{\mathrm{OS}} = \left[\sqrt{2}(1 + r^2)^{1/2} - r - 1\right] 3\sigma l$ in the first stage, and $\Delta E(\max 2)|_{\mathrm{OS}} = 3(\sqrt{2} - 1)r\sigma l$ in the second. The effective barrier $\Delta E(\max)|_{\mathrm{OS}} = \max\, j\Delta E(\max\, j)|_{\mathrm{OS}}$ for the open-shell TP is below $\Delta E(\max)|_{\mathrm{CS}}$ for a closed-shell TP for all $0 < r < 1$, consistent

with the lower $\Delta E(\max)$ for open-shell TPs shown in Fig. 6.5. The smallest value of $\Delta E(\max)|_{\rm OS} = 3(\sqrt{2}-1)\sigma l/(2\sqrt{2}) \approx 0.439\sigma l$ occurs for $r = 1/(2\sqrt{2}) \approx 0.354$.

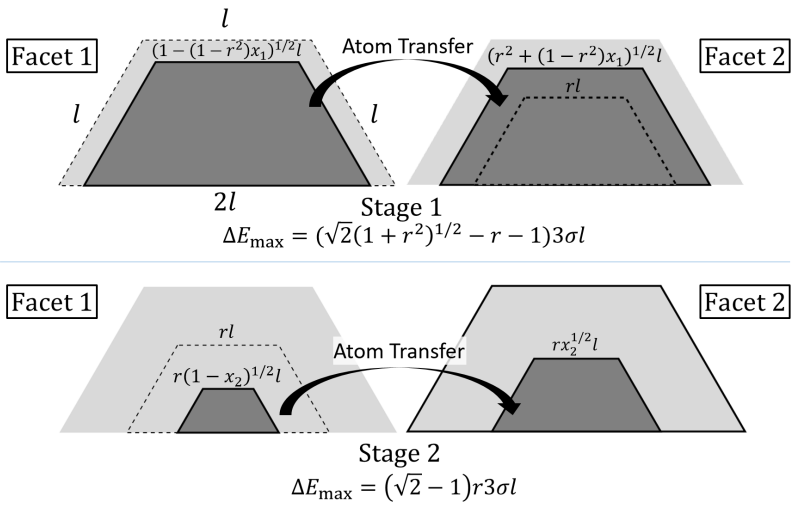

Figure 6.7: Continuum analysis of energy change upon atom transfer for an open-shell TP. Dashed lines in stage 1 show initial complete layer (incomplete layer) on facet 1 (2) which shrinks (grows) during atom transfer. Dashed lines in stage 2 show initial incomplete layer on facet a which shrinks during atom transfer.

6.3.5 Local minima and maxima of D_N

As noted in sec. 6.1, a general expectation in previous studies [7,8] both for 2D and 3D epitaxially supported NCs is that NCs with closed-shell ground state correspond to local minima in diffusivity. However, this expectation is not realized in 2D, [9,10] and needs critical assessment in 3D. The above analysis of energetics 3D {100}-epitaxially supported Ag NCs shows that generally closed-shell ground state TPs correspond to local maxima in $\Delta E(\max)$ and related quantities, at least for smaller N. This feature is compatible with local minima in DN occurring for these sizes $N = N_{\rm TP}$. Nonetheless, our precise KMC results for D_N in Fig. 6.2 reveal that local minima in D_N can occur for sizes other than $N = N_{\rm TP}$. Specifically, these sizes include $N = N_{\rm TP} - 1$ and $N_{\rm TP} - 3$ (at least for larger $N_{\rm TP}$). To explain this behavior, note that for $N_{\rm TP} = 104$, 110 or 126, $E_{\rm eff}$(analytic) actually has the same local maximum value for $N = N_{\rm TP}$ and $N_{\rm TP} - 1$. Also, if Ω_0 denotes the

ground state degeneracy, then one has $\Omega_0 = 1$ for $N = N_{\rm TP}$ with a square base versus $\Omega_0 = 8$ for $N = N_{\rm TP} - 1$. Finally, let $\Omega_{\rm TS}$ denote the degeneracy in the transition state at $q \approx q_{\rm tot}/2$ where half a complete layer has been transferred from one side of the NC to another. Then, based upon the heuristic estimate [25]

$$D_N \sim (\Omega_{\rm TS}/\Omega_0) \exp\left[-E_{\rm eff}({\rm analytic})/(k_B T)\right], \tag{6.6}$$

it follows that the higher ground state degeneracy for $N = B_{\rm TP} - 1$ results in lower D_N relative to $N = N_{\rm TP}$. Here, we use that the variation of $\Omega_{\rm TS}$ between $N = N_{\rm TP}$ and $N{\rm TP}-1$ is not as great as for Ω_0 (see ESI sec. 9). The same argument applies comparing D_N for $N_{\rm TP} = 104$ and $N_{\rm TP} - 3 = 101$. There are examples where $E_{\rm eff}$(analytic) for $N = N_{\rm TP} - n$ with small n is lower than for $N = N_{\rm TP}$, and yet D_N is also lower. In these cases, strong entropic effects must predominate.

As noted above, local maxima in D_N tend to occur for $N = N_{\rm TP} + 3$ for larger sizes with $N = O(10^2)$. Consistently, $E_{\rm eff}$ displays a local minima for these sizes corresponding to local minimum in $\Delta E(\max)$ for $N_{\rm TP} + 3$ or $N{\rm TP} + 4$. For these sizes, the ground state corresponds to a small 2D cluster of $1, 2, 3,...$ atoms on a facet of a closed-shell TP. The presence of this small 2D cluster naturally facilitates initial transfer of atoms from another complete side of the NC, thereby reducing $\Delta E(q)$, $\Delta E(\max)$, and related quantities.

Finally, we briefly comment of behavior of D_N for larger sizes, which is reported in the ESI sec. 5. The basic features observed in the smaller size range up to $N \approx 190$ are preserved, i.e., complex oscillatory decay of D_N versus N. However, it should be noted that local minima in D_N do not occur for all sizes with closed-shell ground states, but only at or near a subset of these. A similar feature is manifested for the case of weak adhesion described in sec. 6.4. An effective criterion to assess the subset of closed-shell sizes corresponding to local minima in D_N is again provided by (the occurrence of local minima in) the readily calculated quantity δE. See ESI sec. 5.

6.4 Results for Weak Adhesion $f \leq 0.05$

6.4.1 Ground-state NC shapes with weak adhesion where $f \approx 0$

The Winterbottom shapes for smaller sizes $N = O(10^2)$ when $f \approx 0$ will roughly correspond to that of unsupported Wulff clusters. For certain sizes, these correspond to closed-shell Truncated Octahedra (TO) bounded by {111} and {100} facets. Let n_{111} (n_{100}) denote the number of atoms on edges between adjacent {111} facet pairs (adjacent {111} and {100} facets). Then, the symmetric regular TO where $n_{111} = n_{100} = n$ with magic sizes [26]

$$N^{\mathrm{TO}}(n) = 16n^3 - 33n^2 + 24n - 6 = \mathbf{38}, \mathbf{201}, \mathbf{586}, ... \text{ for } n = 2, 3, 4, ... \tag{6.7}$$

are especially stable. Also particularly stable are asymmetric TO, denoted TO+, where $n = n_{111} = n_{100} + 1$ and [27]

$$N^{\mathrm{TO+}}(n) = 16n^3 - 63n^2 + 84n - 38 = \mathbf{79}, \mathbf{314}, \mathbf{807}, ... \text{ for } n = 3, 4, 5, ... \tag{6.8}$$

A recent analysis revealed 49 additional sizes of various asymmetric closed-shell TO (including TO+) between each consecutive pair of magic regular TO sizes, which are also relatively stable compared to non-closed-shell structures. [28] For each of these sizes between $N^{\mathrm{TO}} = 38$ and 201, there is a corresponding size between $N^{\mathrm{TO}} = 201$ and 586, etc., so structures repeat quasi-periodically. For example, the closed-shell structure for $N = 244$ corresponds to that for $N = 52$; the $N = 314$ TO+ corresponds to the $N = 79$ TO+.

Excitation of a closed-shell structure by moving a corner atom to a {111} ({100}) facet increases the energy by $E_{\mathrm{ex}} = 3\phi$ (2ϕ). Given the restricted number, M, of adsorption sites on facets for the NC sizes considered here, it follows that $\exp\left[-E_{\mathrm{ex}}/(k_B T)\right] M \ll 1$ so the ground state structure predominates for $700K$.

6.4.2 KMC results for D_N versus N

Next, we describe briefly analysis of diffusion of supported NCs with weak adhesion corresponding to $f \leq 0.05$. Fig. 6.8 (middle frame) shows the variation of D_N with N

for {100}-epitaxially supported 3D Ag NCs at $T = 700K$ for weak adhesion with $f = 0.05$ (and with $f = 0$ where the NC is constrained to be attached to the substrate). A complex oscillatory variation is evident. The vertical lines mark the sizes for the symmetric TO and TO+ listed in sec. 6.3, as well as all other less symmetric ground state closed-shell TO. Sizes associated with (or sometimes close to) symmetric regular TO and to TO+ correspond to strong local minima in D_N, and sizes close to a restricted subset of the other closed-shell ground state TO correspond to less prominent local minima. For sizes associated with these minima, the closed-shell TOs are relatively stable. A measure, δE_N, of the relative energy per atom, also shown in Fig. 6.8 (top), correlates reasonably with the variation of D_N with N.

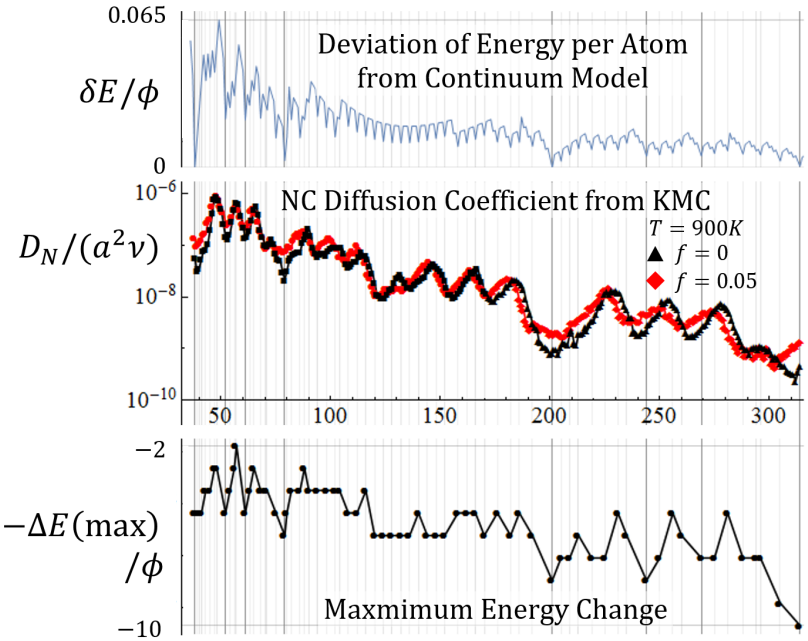

Figure 6.8: Top: $\delta E = [E_N - E_N(\text{cont})]/N$ where [28]$E_N(\text{cont})/\phi = -1.59 + 0.061N^{1/3} + 7.554N^{2/3} - 6N$ recovers E_N for regular TO with $N = 38$, 201, 586, and 1289. Middle: KMC results for D_N versus N for an Ag TO at $700K$ for $f = 0.05$ (black) and $f = 0$ (red). Bottom: Analytic results for $-\Delta E(\max)/\phi$, where the negative sign is included so that peaks and valleys correspond to those of D_N. Note: vertical lines correspond to sizes for closed-shell structures, with those for TO, TO+, and other particularly stable structures, indicated as thicker lines.

6.4.3 Mechanism & energetics for NC diffusion and continuum analysis

To elucidate the behavior of D_N, we first discuss the mechanistic pathway for long-range NC diffusion where ground states are closed-shell regular TOs. One pathway involves dissolution of the outer layer of two vertical {100} facets (on the left and center in Fig. 6.1) and two {111} facets (on the left in Fig. 6.1), transfer of those atoms around the NC surface, and formation of a new complete outer layer on the other two vertical {100} facets and on the two {111} facets on the opposite side from those donating atoms. (There are four other {111} facets which remain largely unchanged.) Clearly, this process is more complex than that described for diffusion of closed-shell TP with $f = 0.75$. Nonetheless, analytical quantification is still possible tracking the energy change, $\Delta E(q)$, as a function of the number, q, of atoms transferred along the MEP. By symmetry for regular TO, $\Delta E(q) = \Delta E(q_{\text{tot}} - q)$, where q_{tot} is the total number of atoms transferred. The maximum value, $\Delta E(\text{max})$, of $\Delta E(q)$, again gives a measure of the difficulty of the process (not accounting for the details of surface diffusion kinetics or entropic effects).

The additional challenge here compared to the analysis for TP with $f = 0.75$ is the variety of possibilities for transferring atoms which must be considered to determine the MEP and $\Delta E(\text{max})$. The general principle, as for $f = 0.75$, is to select atoms to transfer which break the minimum number of bonds and to arrange them on the receiving facet to create the maximum number of bonds. As an example, for $N^{\text{TO}} = 38$, one removes atoms from a {111} then a {100} then a {111} and finally a {100} facet, and builds up layers in the reverse sequence (first on a {100} facet, etc.) to obtain $\Delta E(\text{max}) = 5\phi$. See ESI sec. 10 for further discussion and detailed analysis for $N^{\text{TO}} = 201$.

For the less symmetric closed-shell TO, {100} facets generally have multiple different sizes and shapes. In this case, a separate analysis of $\Delta E(q)$ is performed for each possible type of supporting facet. The minimum $\Delta E(\text{max})$ from these different possibilities is selected. Results from extensive analysis of $\Delta E(\text{max})$ for regular and less symmetric closed-shell ground state TO are reported in Fig. 6.8 (lower frame).

We do not present a detailed continuum analysis here. However, from the formalism presented for $f = 0.75$, it is clear that irrespective of the detailed pathway for atom transfer, one has that $\Delta E(\max) \propto \phi l/a \sim N^{1/3}$. This slow increase in $\Delta E(\max)$ with N is reflected in Fig. 6.8 (bottom), again somewhat hidden by oscillatory structure.

6.4.4 Local maxima and minima of D_N

Regular TO for $N = 38, 201$, etc. and TO+ for $N = 79, 314$, etc., are well recognized as being particularly stable, so it is not surprising that D_N has prominent local minima reflecting these sizes. However, the prominent oscillatory structure of D_N is not determined by TO and TO+ alone, but by augmenting these with a subset of less symmetric closed-shell ground state TO. These less symmetric closed-shell TO still have enhanced stability measured by prominent local minima in δE, and prominent local maxima in $\Delta E(\max)$, relative to nearby closed-shell TO. Examples include $N = 52$ and 244 which correspond to "elongated" TO, and $N = 61$ and 269 which have a slab-like structure with 3-fold symmetry. See ESI sec. 11. The variation in D_N repeats quasi-periodically matching the repeat of closed-shell ground states described above between each pair of magic sizes. Thus, prominent minima at $N = 38, 52, 61$, and 79 are repeated at $N = 201, 244, 269$, and 314, respectively. Prominent local maxima in D_N often correspond to inhibited stability as measured by δE, and somewhat more prominent local minima in $\Delta E(\max)$. These also repeat quasi-periodically.

6.5 Discussion

Complex oscillatory decay of diffusivity, D_N, with N is evident in the above analyses for both strong and weak adhesion. In fact, this behavior applies more generally. We have also considered moderate adhesion with $f = 0.5$ where the continuum Winterbottom shape of supported NC corresponds to half of a Wulff cluster. See Fig. 6.1. Closed-shell ground state structures for $f = 0.5$ in the atomistic model up to $N = O(10^2)$ sometimes

correspond to TP, and sometimes to TP with lower corner atoms removed. KMC reveals oscillatory decay of D_N. Local minima do not always correspond to closed-shell ground states. Here, we find that $\Delta E(\max)$ and E_{eff} exhibit "flat" local maxima corresponding several consecutive N (rather than maxima just occurring just at isolated sizes with close-shell ground states), explaining why open-shell structures can have the lowest D_N. On the other hand, local minima in $\Delta E(\max)$ and E_{eff} often occur for a single N, or consecutive pair of N, and correspond to local maxima in D_N. See ESI sec. 12. In addition, we assess behavior for smaller $f = 0.17$ corresponding to the relatively weak adhesion of Ag NCs on MgO(001). [18] In this case, the oscillatory decay of D_N with N is similar to that found for $f \leq 0.05$. See ESI sec. 13.

The observed oscillatory decay of D_N with N appears in marked contrast to the traditional picture of algebraic scaling $D_N \sim D^{\text{o}} \exp\left[-E_{\text{eff}}/(k_B T)\right] N^{-\beta}$, where mean-field analysis gives that E_{eff} is size-independent, and $\beta_{\text{MF}} = 4/3$. In fact, our analysis shows that the effective barrier for diffusion has a strong oscillatory size dependence, with an overall increase with N like $E_{\text{eff}} \sim N^{1/3}$. This corresponds to faster than algebraic asymptotic decay of D_N for large N. Analogous observations have been made for NC reshaping. [14, 29] Despite this feature, we have shown that for strong adhesion, $f = 0.75$, an effective β can be reasonably extracted from selected peaks of D_N (for a fixed range of sizes). Reported results show this βeff decreasing from 3.1 at $700K$ to 2.1 at $900K$. Furthermore, oscillations in D_N disappear for sufficiently high T, and classic mean-field scaling $\beta_{\text{eff}} \to 4/3$ of D_N is recovered. This behavior can be understood given that the structure of supported NCs become less facetted and more irregular with a randomly rough surface as T increases. In this regime, surface hopping becomes uncorrelated as assumed in the mean-field analysis. This type of recovery of mean-field behavior for increasing T is a general phenomenon applying for any adhesion strength.

As an aside, for diffusion of 2D epitaxial NCs, mean-field scaling is recovered asymptotically as $N \to \infty$ for any T (not just as $T \to \infty$). This fundamental difference arises from

the feature that 2D NCs, in contrast to 3D NCs, are not facetted in the large-N continuum regime.

One could consider {111}- rather than {100}-epitaxially supported 3D fcc metal NC. Now, each atom in the lowest layer is regarded as supported by three atoms in the substrate, again with an effective NN substrate-NC atom attraction of $\phi_s = f\phi$. Then, the distance to the top {111} facet, h_{111}, and to the substrate, $h_{\rm sub}$, are related by $h_{\rm sub}/h_{111} = 1 - 2f$. By analogy with $f = 0.75$ for the {100}-supported case, the Winterbottom shape for $f = 2/3$ is a truncated hexagonal pyramid where the edge length for the top hexagonal {111} facet matches that of the edges between the six alternating {100} and {111} side facets. For $f \approx 0$, the equilibrium shape is a Wulff TO, now supported on a {111} facet. Behavior of diffusivity in these cases is analogous to that for {100}-supported NCs with complex oscillatory decay in D_N versus N, and where again detailed insight comes from an atomistic-level analysis of energetics along the MEP or from a continuum analysis.

Finally, some additional comments are appropriate on T-dependence of D_N, and in particular on the disappearance of oscillations for high T. Oscillatory structure relies on the distinction between closed-shell and other NC structures. For sufficiently low T, NCs with closed-shell ground states will most likely be found in those configurations as discussed above accounting for excited-state Boltzmann factors and configurational degeneracy. However, for high T, the NC will most likely be in a non-closed-shell excited state. This type of entropic effect diminishes distinction between open- and closed-shells, and thus degrades the oscillatory fine structure of D_N versus N.

6.6 Conclusion

Our KMC simulation analysis of the diffusion of epitaxial supported 3D NCs reveals a ubiquitous oscillatory decay of D_N versus N. This behavior is in marked contrast to the traditional picture of algebraic decay, $D_N \sim N^{-\beta}$. While KMC simulation precisely quantifies D_N, it does not necessarily offer fundamental insight into the origin of behavior.

However, such insight is provided by our identification of the mechanistic pathway for NC diffusion, i.e., facet dissolution and reformation, together with a comprehensive analytical characterization of the energetics along the minimum energy pathway (MEP) for this process. A coarse-grained continuum analysis of MEP energetics provides additional insight, particularly regarding the increase in the effective barrier for NC diffusion with size.

For diffusion of either supported 2D or 3D epitaxial NCs exhibiting oscillatory decay, it is natural to anticipate that local minima correspond to sizes with closed-shell NC ground state structures with sizes $N = N_{\mathrm{CS}}$. [7,8] Our analysis does reveal some correlation between local minima in D_N and closed-shell structures. However, for strong adhesion, we find local minima for sizes $N = N_{\mathrm{CS}} - 1$ and $N_{\mathrm{CS}} - 3$ and explain this feature as due to higher ground state degeneracy for these sizes relative to closed-shell NCs. For moderate and weak adhesion, local minima only correlate strongly with a subset of closed-shell structures. Thus, a comprehensive and fundamental understanding of the fine structure of D_N versus N necessarily requires the type of analytic characterization of energetics along MEP for diffusion provided here.

Finally, we remark that our results for D_N versus N can provide input to analysis of SR kinetics of distributions of supported NCs. We have noted the importance of this process for catalyst degradation. However, it might also be noted that under reaction conditions, adsorption of reactants on the NC surface can alter both NC surface thermodynamics and diffusion kinetics, and thus NC diffusivity. Nonetheless, the current study of NC diffusion in a vacuum environment is a valuable precursor to understanding of such behavior in more complex environments.

6.7 Acknowledgments

We thank Alex Travesset for discussions on TO, TO+ and related structures for unsupported NCs. This work was supported by the U.S. Department of Energy (USDOE), Office of Science, Basic Energy Sciences, Division of Chemical Sciences, Geosciences, and

Biosciences through the Ames Laboratory Chemical Physics program. The work was performed at Ames Laboratory which is operated for the USDOE by Iowa State University (ISU) under Contract No. DE-AC02-07CH11358.

6.8 Footnote

Electronic supplementary information (ESI) available. See DOI: 10.1039/c9nr05845a

Bibliography

[1] E. Ruckenstein and B. Pulvermacher. Kinetics of crystallite sintering during heat treatment of supported metal catalysts. *AlChE J.*, 19(2):356–364, 1973.

[2] P. Wynblatt and N. A. Gjostein. Supported metal crystallites. *Prog. Solid State Chem.*, 9:21–58, 1975.

[3] Thomas W. Hansen, Andrew T. DeLaRiva, Sivakumar R. Challa, and Abhaya K. Datye. Sintering of Catalytic Nanoparticles: Particle Migration or Ostwald Ripening? *Acc. Chem. Res.*, 46(8):1720–1730, 2013.

[4] Yunqian Dai, Ping Lu, Zhenming Cao, Charles T. Campbell, and Younan Xia. The physical chemistry and materials science behind sinter-resistant catalysts. *Chem. Soc. Rev.*, 47(12):4314–4331, 2018.

[5] King C. Lai, Yong Han, Peter Spurgeon, Wenyu Huang, Patricia A. Thiel, Da-Jiang Liu, and James W. Evans. Reshaping, Intermixing, and Coarsening for Metallic Nanocrystals: Nonequilibrium Statistical Mechanical and Coarse-Grained Modeling. *Chem. Rev.*, 119(11):6670–6768, 2019.

[6] Pablo Jensen. Growth of nanostructures by cluster deposition: Experiments and simple models. *Rev. Mod. Phys.*, 71(5):1695–1735, 1999.

[7] Lin Li, Philipp N. Plessow, Michael Rieger, Simeon Sauer, Roel S. Sánchez-Carrera, Ansgar Schaefer, and Frank Abild-Pedersen. Modeling the Migration of Platinum Nanoparticles on Surfaces Using a Kinetic Monte Carlo Approach. *J. Phys. Chem. C*, 121(8):4261–4269, 2017.

[8] J. Heinonen, I. Koponen, J. Merikoski, and T. Ala-Nissila. Island Diffusion on Metal fcc (100) Surfaces. *Phys. Rev. Lett.*, 82(13):2733–2736, 1999.

[9] King C. Lai, James W. Evans, and Da-Jiang Liu. Communication: Diverse nanoscale cluster dynamics: Diffusion of 2D epitaxial clusters. *J. Chem. Phys.*, 147(20):201101, 2017.

[10] King C. Lai, Da-Jiang Liu, and James W. Evans. Diffusion of two-dimensional epitaxial clusters on metal (100) surfaces: Facile versus nucleation-mediated behavior and their merging for larger sizes. *Phys. Rev. B*, 96(23):235406, 2017.

[11] King C. Lai and James W. Evans. Reshaping and sintering of 3D fcc metal nanoclusters: Stochastic atomistic modeling with realistic surface diffusion kinetics. *Phys. Rev. Mater.*, 3(2):026001, 2019.

[12] Luke T. Roling, Lin Li, and Frank Abild-Pedersen. Configurational Energies of Nanoparticles Based on Metal–Metal Coordination. *J. Phys. Chem. C*, 121(41):23002–23010, 2017.

[13] Claude R. Henry. Morphology of supported nanoparticles. *Prog. Surf. Sci.*, 80(3):92–116, 2005.

[14] Nicolas Combe, Pablo Jensen, and Alberto Pimpinelli. Changing Shapes in the Nanoworld. *Phys. Rev. Lett.*, 85(1):110–113, 2000.

[15] Teck H. Lim, David McCarthy, Shaun C. Hendy, Kevin J. Stevens, Simon A. Brown, and Richard D. Tilley. Real-Time TEM and Kinetic Monte Carlo Studies of the Coalescence of Decahedral Gold Nanoparticles. *ACS Nano*, 3(11):3809–3813, 2009.

[16] I. M. Goldby, L. Kuipers, B. von Issendorff, and R. E. Palmer. Diffusion and aggregation of size-selected silver clusters on a graphite surface. *Appl. Phys. Lett.*, 69(19):2819–2821, 1996.

[17] Mingshu Chen and D. Wayne Goodman. Chapter 5 Oxide-supported metal clusters. *Chemical Physics of Solid Surfaces*, 12:201–269, 2007.

[18] Stephanie L. Hemmingson and Charles T. Campbell. Trends in Adhesion Energies of Metal Nanoparticles on Oxide Surfaces: Understanding Support Effects in Catalysis and Nanotechnology. *ACS Nano*, 11(2):1196–1203, 2017.

[19] N. Nilius, N. Ernst, and H.-J. Freund. Photon Emission Spectroscopy of Individual Oxide-Supported Silver Clusters in a Scanning Tunneling Microscope. *Phys. Rev. Lett.*, 84(17):3994–3997, 2000.

[20] W. Benten, N. Nilius, N. Ernst, and H.-J. Freund. Photon Emission Spectroscopy of Single Oxide-Supported Ag-Au Alloy Clusters. *Phys. Rev. B*, 72(4):045403, 2005.

[21] D. A. Chen, M. C. Bartelt, S. M. Seutter, and K. F. McCarty. Small, uniform, and thermally stable silver particles on TiO2(110)-(1×1). *Surf. Sci.*, 464(1):L708–L714, 2000.

[22] K. Luo, T. P. St. Clair, X. Lai, and D. W. Goodman. Silver Growth on TiO2(110) (1 × 1) and (1 × 2). *J. Phys. Chem. B*, 104(14):3050–3057, 2000.

[23] J. H. Larsen, J. T. Ranney, D. E. Starr, J. E. Musgrove, and C. T. Campbell. Adsorption energetics of Ag on MgO(100). *Phys. Rev. B*, 63(19):195410, 2001.

[24] Riccardo Ferrando, Giulia Rossi, Andrea C. Levi, Zdenka Kuntová, Florin Nita, Andrei Jelea, Christine Mottet, Giovanni Barcaro, Alessandro Fortunelli, and Jacek Goniakowski. Structures of metal nanoparticles adsorbed on MgO(001). I. Ag and Au. *J. Chem. Phys.*, 130(17):174702, 2009.

[25] J. H. Larsen, J. T. Ranney, D. E. Starr, J. E. Musgrove, and C. T. Campbell. Adsorption energetics of Ag on MgO(100). *Phys. Rev. B*, 63(19):195410, 2001.

[26] Riccardo Ferrando, Giulia Rossi, Andrea C. Levi, Zdenka Kuntová, Florin Nita, Andrei Jelea, Christine Mottet, Giovanni Barcaro, Alessandro Fortunelli, and Jacek Goniakowski. Structures of metal nanoparticles adsorbed on MgO(001). I. Ag and Au. *J. Chem. Phys.*, 130(17):174702, 2009.

[27] Robert L. Whetten, Joseph T. Khoury, Marcos M. Alvarez, Srihari Murthy, Igor Vezmar, Z. L. Wang, Peter W. Stephens, Charles L. Cleveland, W. D. Luedtke, and Uzi Landman. Nanocrystal gold molecules. *Adv. Mater.*, 8(5):428–433, 1996.

[28] King C. Lai, Xun Zha, James W. Evans, and Alex Travesset. Structure of Polydisperse fcc Nanocrystals: Implications for Crystal Fractionalization. *J. Phys. Chem. C*, 123(14):9528–9537, 2019.

[29] William W. Mullins and Gregory S. Rohrer. Nucleation Barrier for Volume-Conserving Shape Changes of Faceted Crystals. *J. Am. Ceram. Soc.*, 83(1):214–16, 2000.

CHAPTER 7. GENERAL CONCLUSIONS

In this work, we explored important issues about Smoluchowski ripening (particle migration and coalescence). As we stressed, such ripening process is a key mechanism mediating the coarsening and degradation of catalysis or other optical array of nanoparticles. Kinetic Monte Carlo simulations were applied to various systems to compare and verify our theoretical approaches.

Our discussion started with 2D nanoislands on (100)-expitaxial surface with a focus on size N dependence of diffusion coefficient D_N in Chapter 2. The dependence of size $9 \leq N \leq O(10^2)$ with parameters modeling Ag nanoislands were studied. Instead of a monotonic decrease with size increases predicted by classical mean field theory $D_N \sim N^{-\beta}$, we discovered a complex oscillatory feature of D_N. First of all, two types of diffusion pathways with different effective activation energy barriers E_{eff} are identified: facile diffusion (FA) and nucleation-mediated diffusion (NM). FA with $E_{\text{eff}} = E_e + 2\phi + \delta$ was observed for the sizes $N_p + 1$ and $N_p + 2$, with N_p be sizes of a square or rectangle island. Such diffusion pathway leads to a higher diffusion coefficient compared to NM with $E_{\text{eff}} = E_e+$. All other sizes $N \neq N_p + 1$ nor $N_p + 2$ diffuse through NM pathways. Further against intuition, size $N_p + 3$ instead of N_p have a lower D_N among comparable sizes. Through utilizing integer partition function, we performed combinatorial analysis of the number of the ground-state and low-lying state cluster configurations. With this, impact of the entropic effect on D_N was accounted and predicting the oscillatory features precisely. Furthermore, the classic value of $\beta = 3/2$ is recovered for $N \sim O(10^3)$ with Ag parameters in room temperature. The analysis was extended in Chapter 3 to periphery diffusion diffusion of 2D nanopit (or

vacancy island). The oscillatory behavior is also observed but with absence of FA diffusion due to the absence of low excitation diffusion pathway for nanopit. In this work, we further compare our simulation results with data from more than one experimental groups. We find effective size-scaling exponents of $\beta_{\text{eff}} \approx 1.05$ for island, $\beta_{\text{eff}} \approx 1.17$ for nanopits consistent to $\beta_{\text{eff}} \approx 1.15$ for island diffusion from ORNL experiment.

From 2D system, we move on to 3D systems in the rest of the thesis. Starting with a study of equilibrium shape of nanocrystals (NCs) in Chapter 4. Beyond the continuous regime, the traditional Wulff construction approach is not sufficient to predict all energetically favorable closed-shell structures. We identified exactly 49 sizes N with some degeneracy for a 70 distinct closed-shell structures in total between two major Wulff magic sizes. Each of the sizes correspond to a local minima of the energy per atom, which is compatible with other theoretical studies through different approaches. Besides giving us insight in future studies related to SR, the result leads to a realistic description of polydisperse NC distribution reflecting thise utilized in self-assembly experiments.

With the understanding of equilibrium shape in discrete regime, we explored the reshaping processes of 3D NCs in Chapter 5. In this work, we developed a stochastic model in atomistic-level for the surface diffusion of fcc metal NC. Instead of the generic modeling (simple bond counting approach) with unphysical prescription of barriers of kinetics. Our models incorporates with realistic prescriptions based on experiments observations, giving description of energy barriers of surface diffusion depending on various local atomistic environments. It covers three types of far-from-equilibrium systems. First type of process presented was reshaping of a single far-from-equilibrium Ag nanocube. Relaxation time of the process was obtained with Arrhenius analysis and matching theoretical expectations. Next, the sintering process of two individual NCs was simulated. Besides theoretical approaches, we performed simulations for Au NCs and compared to HRTEM experiment. The relaxation time of the sintering process was recovered, demonstrating the prediction power of our model by good agreement. The third system covered is the fragmentation or pinch-off

of Ag nanorod., showing the dependence of pinch-off probability on aspect ratio $\mathscr{R}$.

In Chapter 6, We also applied the stochastic model to the diffusion of epitaxial supported 3D NCs. Though similar oscillatory decay of D_N was observed like Chapter 2 and Chapter 3, the nature of the size dependence is fundamentally different. To elucidate behavior, we identified optimal diffusion pathways, which involve two major processes, i.e. dissolution and reformation of surface layers of the NCs. From those optimal pathways, the minimum excitation required for long range diffusion were extracted, which the gave effective activation barrier of different sizes N. Our atomistic prediction of barriers matches well with the kMC simulation and recovers the oscillating features of size dependence. For strong adhesion, minima at $N_{\mathrm{CS}} - 3 \leq N \leq N_{\mathrm{CS}} - 1$ instead of N_{CS}, due to the high ground state degeneracy of these sizes relative to N_{CS}. For weak adhesion, the local minima correlates with closed-shell structure much more significantly. We also approach the problem with coarse-grained continuum regime, providing insight of the increasing effective barrier with size in a larger scale of size. Overall, the long range diffusion thus SR of these systems are important to understanding catalytic degradation. This study may lead to further understanding of more complex environments in conditions.

APPENDIX EQUILIBRIUM SHAPES OF UNSUPPORTED, SUPPORTED, AND INTERCALATED THREE-DIMENSIONAL METAL NANOCLUSTERS

For unsupported (or free-standing) crystalline clusters of atoms, the equilibrium crystal shape is determined by the classic Wulff construction [1] which is a continuum theory rather than a discrete atomistic formulation. The exposing surface of these equilibrium shapes are generally composed of different crystalline facets, and the Wulff construction states that the distance from the center of the cluster to the facet surface is proportional to the surface energy for that facet. Furthermore, the proportionality constant is the same for all facets orientations. As a natural consequence, the crystal surface is dominated by the facets with the lowest surface energies, and facets with sufficiently high surface energy can be completely absent. To implement Wulff construction, one must have access to the relevant facet surface energies. For metallic systems, earlier studies often obtained these from semi-empirical potentials for the interaction between metal atoms (e.g., the Embedded Atom Method). However, more recent studies including our analyses discussed below obtain these values from a higher-level theory, Density Functional Theory (DFT). We will not provide the details of the DFT analysis here, but instead just quote the results and focus on presenting the corresponding Wulff shapes.

One example of the above analysis for the case of unsupported NiAl binary alloy crystals with a 1:1 Ni:Al stoichiometric ratio is shown in Ref. [2]. For such a system, there is an additional complication in that for facet orientations corresponding to (111) or (100) surfaces, the surface can be either Al or Ni terminated. The termination exposed naturally

depends on the surface energies, which depends on the environment of the cluster. Specifically, it is characterized by specifying the Ni chemical potential relative to its bulk value, $\Delta\mu_{\mathrm{Ni}}$. Higher values correspond to a preference for Ni termination. The results for surface energies γ of (111), (100), and (110) terminations as a function of $\Delta\mu_{\mathrm{Ni}}$ are shown in Fig. A.1. Fig. A.2 shows the corresponding NiAl crystal shapes under different $\Delta\mu_{\mathrm{Ni}}$.

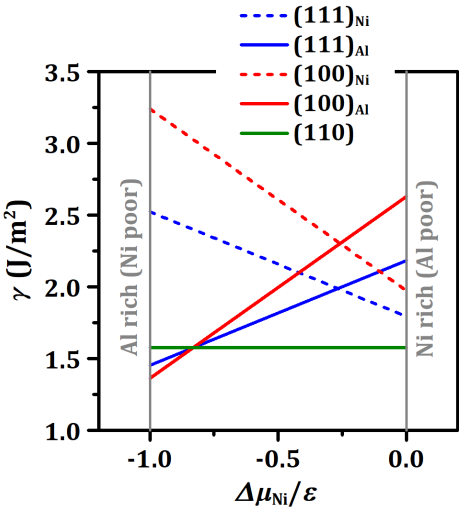

Figure A.1: Surface energy phase diagram from DFT calculations for three low-index NiAl surface or facets (110), (100), and (111). $(100)_{\mathrm{Ni(Al)}}$ denotes the Ni (Al) termination of the (100) surface, and $(111)_{\mathrm{Ni(Al)}}$ denotes the Ni (Al) termination of the (111) surface. (110) has a single mixed termination. Here $\epsilon = \sigma_{\mathrm{Ni}} + \sigma_{\mathrm{Al}} - \sigma_{\mathrm{NiAl}} = 1.324\mathrm{eV}$ (a difference in bulk chemical potentials). [2]

For supported 3D clusters, in addition to the surface energies of different facets, the equilibrium shape also naturally depends on the strength of adhesion β to the substrate. The stronger the adhesion, the greater the degree of wetting of the substrate, and the "flatter" the equilibrium shape. In an extreme case for strong adhesion, the equilibrium shape will be a flat 2D monolayer atoms. As an extension of Wulff construction, the Kaischew construction [3] or the Winterbottom construction [4] determines the equilibrium shape of these supported clusters, again within a continuum framework. Essentially, it corresponds to the Wulff shape of the unsupported cluster, except that a portion of the cluster adjacent to the supporting facet is removed. See Fig. A.3.

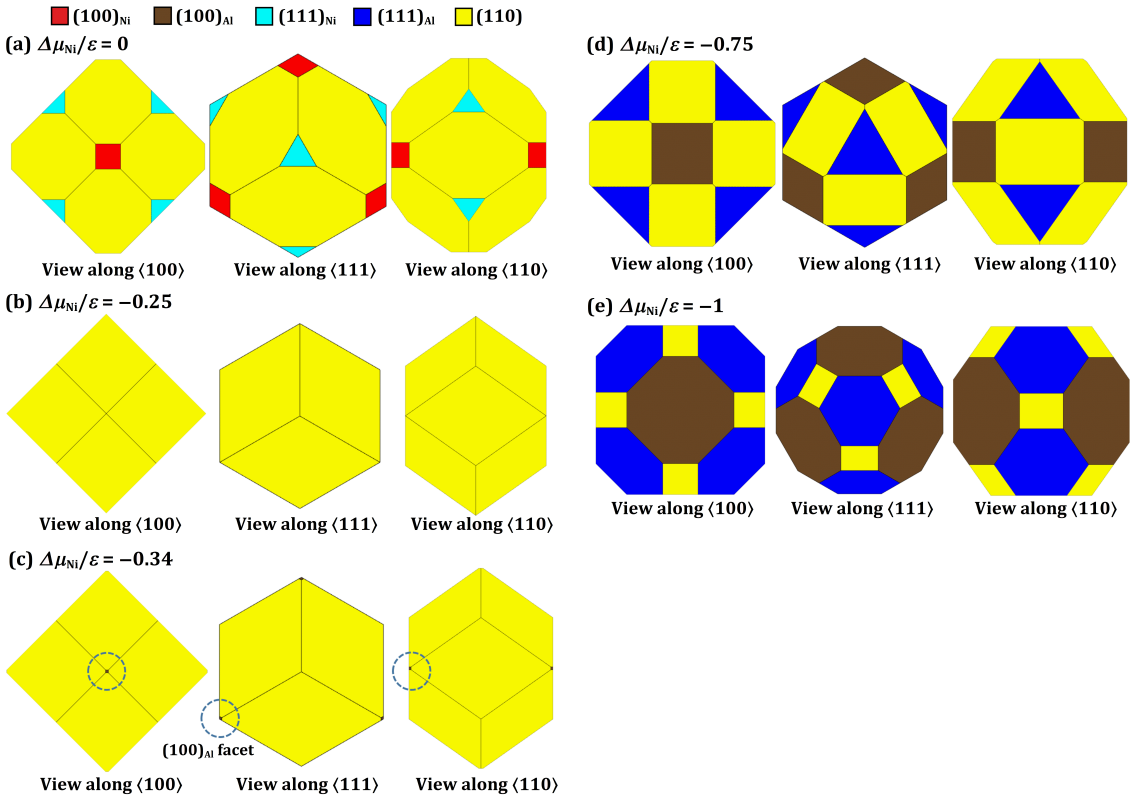

Figure A.2: Equilibrium shapes for NiAl crystals from the Wulff construction for various given $\Delta\mu_{\mathrm{ni}} = 0$ (a); -0.25 eV (b); -0.34 eV (c); -0.75 eV (d); -1.0 eV (e). Colors differentiate orientations and surface terminations of crystal facets. The left, middle, and right columns show the top view orientations along the {100}, {111}, and {110} directions, respectively, as indicated. [2]

We apply this analysis to determine the equilibrium shapes of Cu clusters supported on (111) facets on highly-oriented pyrolytic graphite (HOPG) and on the layered material MoS_2. For Cu on HOPG, we consider only the (111) and (100) facets to be present, with surface energies $\gamma_{\mathrm{Cu}(111)} = 1.292 J/m^2$, $\gamma_{\mathrm{Cu}(100)} = 1.438 J/m^2$, and adhesion energy of $\beta = 0.405 J/m^2$ [6]. The results of the corresponding Winterbottom construction are shown in Fig. A.4. However, in a discrete atomistic model, one cannot exactly recover the continuum

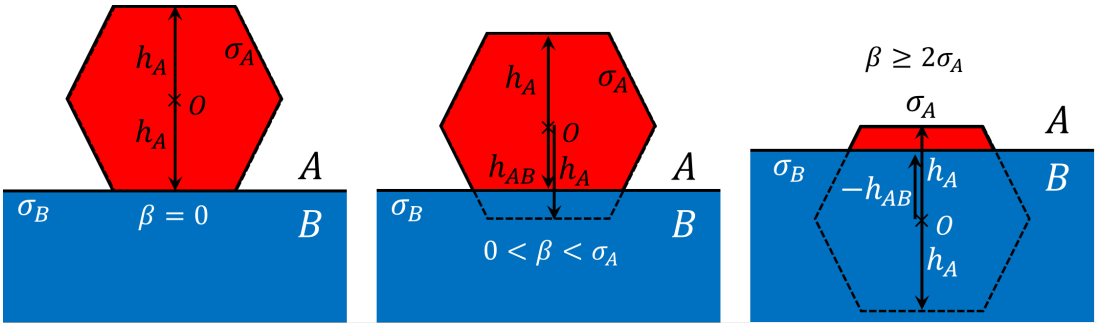

Figure A.3: Equilibrium shapes of supported crystalline clusters with different adhesion β. σ_A denotes the surface energy of the cluster material A, and β denotes the adhesion energy between A and the substrate B [5].

Winterbottom shape. In Fig. A.5 we show clusters for two discrete sizes of N atoms, where the continuum shape is relatively closely recovered by a truncated octahedral structure. For Cu on MoS_2, we retain not just (111) and (100) facets, but five other facet orientations which higher surface energies and which are present to a correspondingly smaller degree [7]. Results for these multiple surface energies come from a published database [8]. We use the value for the ratio of adhesion energy to (111) surface energy of $\beta/\gamma_{\mathrm{Cu(111)}} = 0.543$ based on DFT analysis. Results of the corresponding Winterbottom construction are shown in Fig. A.6.

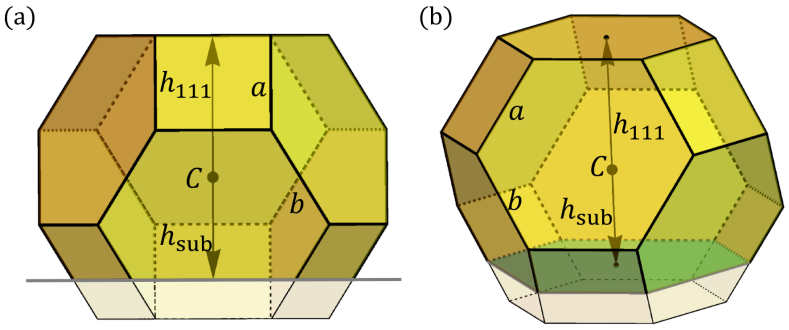

Figure A.4: Orthographic projections of the Winterbottom construction for the equilibrium shape of Cu supported on HOPG. The substrate surface is shown as an extended grey line. The potion of the cluster below that grey line is removed. (111) [(100)] facets have full or truncated hexagonal [square] borders. [6]

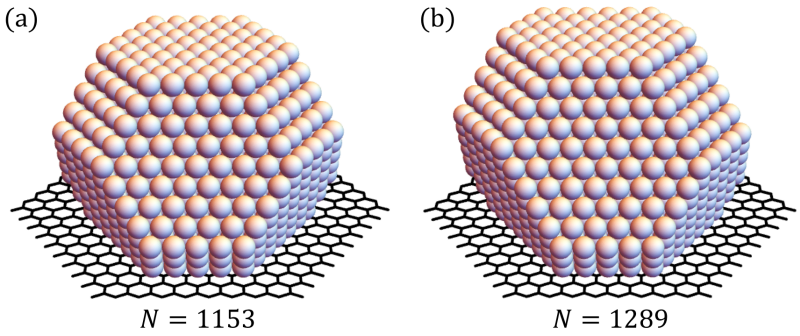

Figure A.5: Supported equilibrium Cu clusters on HOPG with a discrete number of atoms $N = 1153$ (a) and $N = 1289$ (b) close to the continuum Winterbottom shape. [6]

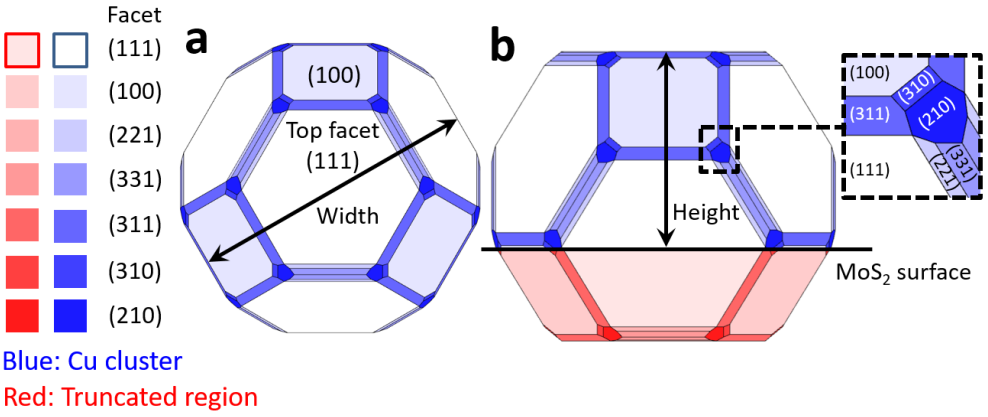

Figure A.6: Supported equilibrium Cu cluster on MoS_2. [7]

Next, we consider the case of supported Fe clusters on HOPG [9]. An additional complication here is that the crystal structure of Fe is not clear at least for smaller nanoscale supported clusters. For this reason we have determined Winterbottom shapes for both hcp and fcc structures. However, here we report results just for the hcp case which seems to correspond to experimental observations. Again we consider the possibility that six distinct surface facets with lower surface energies are present. These surface energies are taken from a published data base [8]. The additional parameter needed is the ratio of adhesion to surface energy which is taken as $\beta/\gamma_{0001} = 0.146$ based on DFT analysis. Results of the corresponding Winterbottom construction are shown in Fig. A.7a.

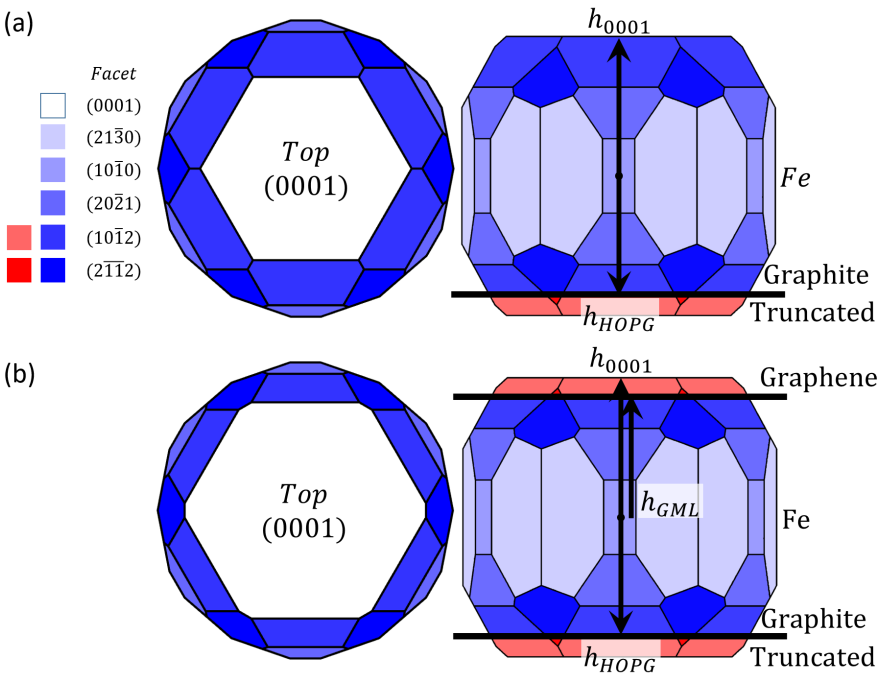

Figure A.7: Equilibrium shape of an hcp Fe cluster: (a) supported on HOPG (Winterbottom); (b) intercalated beneath the top graphene layer of HOPG (double Winterbottom) Red colored regions above or below the thick black line are removed. [9]

Next, we comment on the case of metal clusters intercalated under the top layer(s) of layered materials such as graphite or MoS_2 [9]. The possibility for form such clusters has only been recognized in the last few years. It is of interest not just as a pathway to tune the properties of the layered material, but also as a possible mechanism to protect the metal nanocluster from oxidation, etc. One could anticipate that the upper layer(s) of the layered material which forms a protective blanket over the nanocluster is subject to significant strain (due to stretching) and exerts significant pressure on the nanocluster, and this is the case. However, for an initial analysis of equilibrium shape of intercalated clusters, we have neglected such strain effects. Then, we propose that the equilibrium shape is determined by what we describe as a "double Winterbottom" construction where one removed a portion of the cluster adjacent to both the underlying supporting substrate (as in the standard Winterbottom construction), but now also a portion adjacent to the covering blanket. The

amount removed depends on the strength of the corresponding adhesion energy relative to the metal surface energies just as in the standard Winterbottom construction. The results of such a double Winterbottom construction are shown for hcp Fe clusters intercalated under the surface of HOPG in Fig. A.7b.

Finally, we note again that experimental data indicates that the protective blanket does exert significant pressure on the intercalated nanocluster. Thus, it is reasonable to anticipate that the actual equilibrium shape is squeezed flatter than that predicted by the double Winterbottom construction. This is the case, and we have developed an appropriate theory to determine these squeezed shapes. We are still refining this theory for journal publication, so results are not presented here.

Bibliography

[1] G. Wulff. XXV. Zur Frage der Geschwindigkeit des Wachsthums und der Auflösung der Krystallflächen. *Zeitschrift für Kristallographie - Crystalline Materials*, 34(1-6):449–530, 1901.

[2] Linxia Wang, King C. Lai, Li Huang, James W. Evans, and Yong Han. Low-index surface energies, cleavage energies, and surface relaxations for crystalline NiAl from first-principles calculations. *Surf. Sci.*, page 121532, 2019.

[3] R. Kaischew. Uber eine Verallgemeinerung des Wulffschen Satzes und uber die Kristallbildung auf fremden Oberflachen. *Arbeitstagung Festkrperphysik.*, 73(19):81, 1952.

[4] W. L. Winterbottom. Equilibrium shape of a small particle in contact with a foreign substrate. *Acta Metall.*, 15(2):303–310, 1967.

[5] King C. Lai, Yong Han, Peter Spurgeon, Wenyu Huang, Patricia A. Thiel, Da-Jiang Liu, and James W. Evans. Reshaping, Intermixing, and Coarsening for Metallic Nanocrystals: Nonequilibrium Statistical Mechanical and Coarse-Grained Modeling. *Chem. Rev.*, 119(11):6670–6768, 2019.

[6] Yong Han, King C. Lai, Ann Lii-Rosales, Michael C. Tringides, James W. Evans, and Patricia A. Thiel. Surface energies, adhesion energies, and exfoliation energies relevant to copper-graphene and copper-graphite systems. *Surf. Sci.*, 685:48–58, 2019.

[7] Dapeng Jing, Ann Lii-Rosales, King C. Lai, Qiang Li, Jaeyoun Kim, Michael Tringides, James W. Evans, and Patricia A. Thiel. Non-equilibrium growth of metal clusters on a layered material: Cu on MoS_2. *New J. Phys.*, 2020. Accepted.

[8] Richard Tran, Zihan Xu, Balachandran Radhakrishnan, Donald Winston, Wenhao Sun, Kristin A. Persson, and Shyue Ping Ong. Surface energies of elemental crystals. *Sci. Data*, 3(160080):1–13, 2016.

[9] Ann Lii-Rosales, Yong Han, King C. Lai, Dapeng Jing, Michael C. Tringides, James W. Evans, and Patricia A. Thiel. Fabricating Fe nanocrystals via encapsulation at the graphite surface. *Journal of Vacuum Science & Technology A: Vacuum, Surfaces, and Films*, 37(6):061403, 2019.